Spectroscopic Studies of the Critical Phenomena and Composition of Confined Fluids

Ashley Love MSci

Thesis submitted to the University of Nottingham
for the degree of Doctor of Philosophy

August 2016

Declaration

I hereby declare that this Thesis and the work presented in it are my own, unless acknowledged otherwise.

A. G. Love

Ashley Love

August 2016

Acknowledgements

Firstly I would like to thank my supervisor Prof. Mike George, for both giving me this opportunity and his continued guidance throughout these past years, making this work possible.

I am particularly grateful to Drs. James Calladine, Jie Ke and Xue Han who showed me the ropes at the start of this work and offered essential input throughout.

Thanks must also be given to Peter Fields and Richard Wilson of the mechanical workshop, who not only came to the rescue when any one of many technical difficulties reared its ugly head, but also for producing much of the excellent apparatus used in this Thesis.

I would also like to thank Prof. Robert Mokaya and his group past and present, particularly Drs. Beatrice Adeniran and Wantana Sangchoom, for providing me with many of the porous materials that this work required, along with the gas sorption measurements used to characterise them. I am also very grateful to Drs. Richard Wheatley and Hainam Do for providing invaluable discussion and carrying out the demanding theoretical work presented in this Thesis.

Furthermore the rest of the George group past and present also deserves a big thank you for providing help and advice and making this time a thoroughly enjoyable one, be it through a lively discussion or a quick drink.

Finally, I would like to thank my friends and family for their continued support, and Catherine for her support, patience and love.

Abstract

Chapter 1

This Chapter will provide an introduction to this Thesis, describing the concept of supercritical fluids and future applications that can be provided through the understanding of a substance's phase characteristics confined in nanoporous media. This Chapter also details some current implementations of confined supercritical fluids, particularly the production of microelectronics by means of supercritical fluid electrodeposition, carbon capture and storage, petrochemical extractions and catalysis. This Chapter will also briefly introduce the porous media and spectroscopic techniques utilised in this Thesis.

Chapter 2

Vibrational spectroscopy has been used to study fluids in nanopores to provide an insight into the unique phase characteristics of pore confined fluids. These investigations rely on near-infrared (NIR) spectroscopy to analyse the effect of confinement in nanoporous materials on the critical temperature (T_c) of both carbon dioxide and difluoromethane, in pore sizes ranging from 3.2 to 100 nm. The materials used in this study are in the form of MCM-41 (Mobil^{TM} Crystalline Materials-41) and MSU-H (Michigan State University-Hexagonal) silica, as well as aluminosilicates and larger pore uniform anodic alumina oxide (AAO) films. The results presented in this Chapter show that, when confined in these materials, both carbon dioxide and difluoromethane behave as supercritical fluids under bulk subcritical conditions, exhibiting a significant depression in the critical temperature. The mean critical temperature of both fluids has been measured in these materials, with evidence of a range of critical temperatures lower than the bulk value, due to the distribution of pore sizes within each material. The pore critical temperature (T_{cp}) was found to increase in a non-linear fashion as the pore size increased, with a plateau in T_{cp} evident for both fluids in the *ca.* 5–12 nm range. Following the plateau, the T_{cp} then increases a linear fashion to the bulk critical temperature value in the largest pore sizes investigated ($\geq$ 18 nm). In order to investigate the observation of a plateau in T_{cp} further, a closer look was then taken into the role of the adsorbate molecule in this phenomenon. This was achieved by studying the critical temperature of pore confined ethane, a non-polar weakly interacting adsorbate due it its low polarisability. The critical temperature for ethane in the range of pore sizes studied previously has also been determined. The relationship between mean pore diameter and the pore critical temperature for ethane was found to differ to that seen with both carbon dioxide and difluoromethane. The dependence of the T_{cp} for ethane as a function of pore diameter was found to exhibit a more linear relationship than that seen with carbon dioxide and difluoromethane, with an absence of an obvious plateau as observed for these other fluids. This provides evidence that the polarity or polarisability of the molecule and therefore the fluid-pore interaction potential is responsible for large plateau in critical temperature in the *ca.* 5–12 nm pore size range observed with the other two adsorbates.

Chapter 3

Chapter 3 details complimentary Raman spectroscopic studies which have been undertaken on these fluids in nanopores. Raman spectroscopy has been used to analyse the phase characteristics of carbon dioxide, difluoromethane and ethane in the presence of the nanoporous silica, as well as aluminosilicates and anodic alumina templates. The results support those that are presented in Chapter 2, with the mean pore critical temperature of these fluids again having been determined. The results obtained by both near-infrared and Raman spectroscopic studies are then compared and both methods are assessed on their merits. This Chapter concludes with a theoretical study utilising grand canonical Monte Carlo simulations in order to calculate the critical temperature of carbon dioxide in pores. The pore sizes studied range from 3–8 nm, with the carbon dioxide confined within these pores exhibiting a significant depression in T_c, which is in agreement with experimental observations. Although the absolute T_c values determined were higher than those measured through experimental studies, the general trend of T_{cp} as a function of pore diameter displayed similar behaviour to that measured by the work in this Thesis. Simulations were then carried out in pores with no fluid-pore interaction potential to probe the effect of confinement only. This was in order to elucidate properties of weakly or non-interacting adsorbates, for example ethane. It was found that by removing the wall potential of the pore a significant effect is observed on the confined substances density and chemical potential. Also, removal of the pore wall potential was found to raise the critical temperature of the confined carbon dioxide across the range of the pore sizes studied and produced a more linear relationship between T_{cp} and pore diameter, reminiscent of ethane, a weakly binding adsorbate. This supports the idea that the T_{cp} versus pore diameter trend exhibited by a fluid, is influenced by the attractive effects of a pore wall surface on the adsorbate.

Chapter 4

Chapters 2 and 3 have examined the effect of confinement on a pure fluid. This Chapter will examine the behaviour of binary mixtures in nanopores that have applications in the supercritical fluid electrodeposition process, using both near-infrared and Raman spectroscopic techniques. The change in equilibrium mixture composition has been assessed in a range of pore sizes for both carbon dioxide/acetonitrile and difluoromethane/tetrabutylammonium tetrafluoroborate mixtures. The materials selected for this study were nanoporous silica templates and anodic alumina, with pore sizes ranging from 3.2 to 18 nm in the form of MCM-41, MSU-H and SM-18-100-13 AAO. It was found that one component of the binary mixture was favourably taken into the pore for all mixture compositions, with the largest deviation from the bulk mixture composition occurring in mixtures with the lowest proportion of the preferred component. For both mixtures the preferred component was the more polar/polarisable compound or the component that offered the strongest interaction potential with the pore walls.

Chapter 5

Chapter 5 presents a summary of the findings in this Thesis. The implications of this work and how they relate to real world applications is also discussed. Finally future work required to be carried out in order to build on this knowledge is suggested. This will enable a greater understanding of confined fluids, enabling them to be exploited in future applications.

Chapter 6

This Chapter will describe the experimental procedures, samples preparations, materials and apparatus used in this Thesis to undertake its studies. It describes the use of a cryostat in conjunction with near-infrared and Raman spectroscopy to study the phase behaviour and critical temperature of pore confined fluids for the first time. Furthermore the experimental procedure used to study pore mixture component selectivity by the use of a variable volume view cell and vibrational spectroscopy is also described.

Contents

Abbreviations

AAO	Anodic Alumina Oxide
Abs	Absorbance
ATR	Attenuated Total Reflectance
BPR	Back Pressure Regulator
BJH	Barett-Joyner-Halenda
CARS	Coherent Anti-stokes Raman Spectroscopy
$\mathbf{cm}^{-1}$	Wavenumbers
$\mathbf{D}_c$	Critical Density
DFT	Density Functional Theory
DR	Differential Refractometry
EMP2	Elementary Physical Model 2
FEG-SEM	Field Emission Gun-Scanning Electron Microscopy
FTIR	Fourier Transform Infrared Spectroscopy
FWHM	Full Width at Half Maximum
G	Gibb's Free Energy
GAI	General Adsorption Isotherm Equation
GCMC	Grand Canonical Monte Carlo
GC-TMMC	Grand Canonical-Transition Matrix Monte Carlo
HiP	High Pressure Equipment Inc.
I	Intensity

IUPAC	International Union of Pure and Applied Chemistry
M	Molar
MC	Monte Carlo
MCM-41	Mobil^{TM} Crystalline Materials-41
MPa	Mega Pascals
MSU-H	Michigan State University-Hexagonal
NDE	Non-linear Dielectric Effect
NIR	Near-Infrared
NIST	National Institute of Standards and Technology
NLDFT	Non-Local Density Functional Theory
NMR	Nuclear Magnetic Resonance
P	Pressure
$\mathbf{P}_c$	Critical Pressure
$\mathbf{P}_{cp}$	Pore Critical Pressure
PEEK	Polyether Ether Ketone
PFG NMR	Pulsed Field Gradient Nuclear Magnetic Resonance
psi	Pounds per Square Inch, 1 psi = 0.00689 Mpa
SANS	Small Angle Neutron Scattering
SCF	Supercritical Fluid
SEM	Scanning Electron Microscopy
SSI	Scientific Systems Inc.
T	Temperature
$\mathbf{TBA.BF}_4$	Tetrabutylammonium Tetrafluoroborate
$\mathbf{T}_c$	Critical Temperature
$\mathbf{T}_{ch}$	Hysteresis Critical Temperature
$\mathbf{T}_{cp}$	Pore Critical Temperature
USANS	Ultra Small Angle Neutron Scattering
V	Volume
V_m	Molar Volume

XRD	X-ray Diffraction
Z	Compressibility
$\Delta\mathbf{T}_{rp}$	Decrease in Reduced Pore Critical Temperature
ε_r	Dielectric Constant
ξ	Correlation Length

Chapter 1

Introduction

1.1 Supercritical Fluids

The work in this Thesis concerns the unique phase phenomena of pore fluids and how this influences their critical parameters, as well as the composition of mixtures in nanopores above the critical point. Many new and future applications of confined fluids require an understanding of their phase properties and in particular critical behaviour in order to be exploited. Therefore the definition and general properties of a supercritical fluid and how it relates to other phases of matter will be explored in this section. Supercritical fluids (SCFs) are defined as any substance with a temperature and pressure exceeding the critical temperature and pressure (T_c and P_c), as shown on the phase diagram displayed in Figure 1.1.[1,2] They can be treated as a hybrid of gases and liquids as their physical properties are an intermediate between the two in terms of density, viscosity and diffusivity.[3–7] However a third parameter, the critical density (D_c) is required to be reached for the fluid to exhibit the non-ideal properties that are associated with being a SCF, for example a substance below its critical density will lack the ability to dissolve solids. To ensure a SCF has the ability to dissolve a similar quantity of other compounds when compared to traditional solvents, it must have a density close to or higher than its critical density.[2]

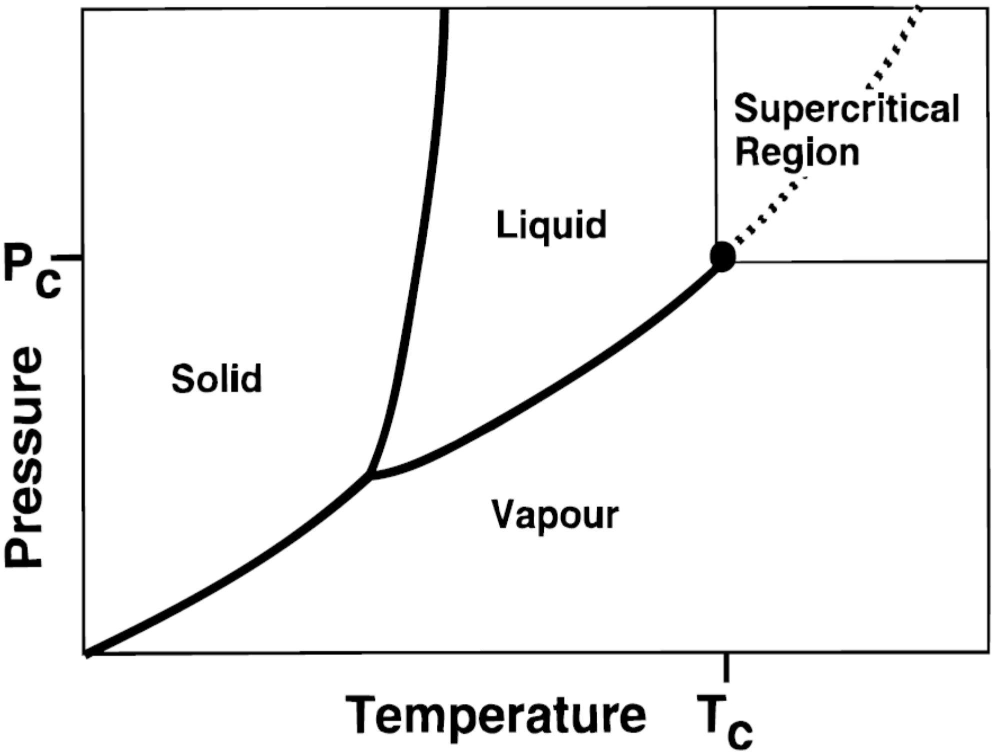

FIGURE 1.1: A phase diagram of a pure substance reproduced from reference 2.

In a physical system, the critical temperature can be identified as the point at which the two phases in coexistence have equal free energies and chemical potential.[8] Therefore in the case of fluids the distinct gas-liquid phase boundary ceases to exist. Below the critical temperature the system can undergo a first order phase transition, this is a sharp, discontinuous change in a suitable order parameter, a thermodynamic function that is different in each phase such as density or composition. Above the critical temperature this phase transition takes a second order form and has a continuous change in the order parameter (Figure 1.2).[9]

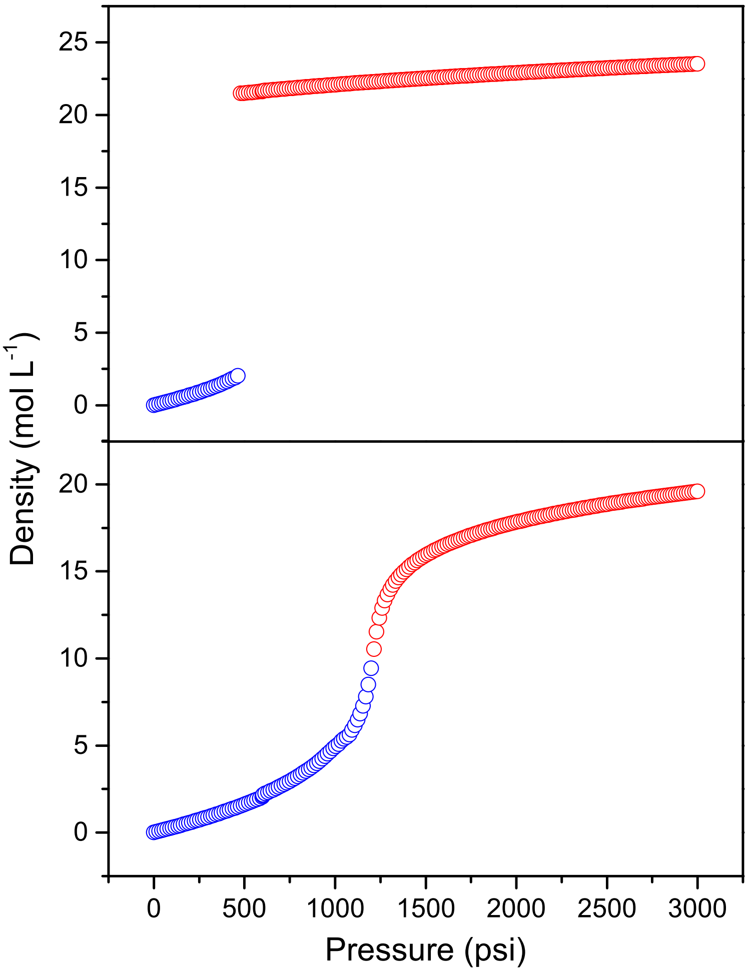

FIGURE 1.2: A diagram of how the order parameter (density) of CO_2 changes with pressure. **(Top)** First order gas to liquid phase transition at 270 K below the critical temperature. **(Bottom)** Continuous gas to supercritical fluid phase transition at 310 K above the critical temperature. Data taken from the National Institute of Standards and Technology (NIST) database.[10]

According to Ehrenfest's classification scheme the order of a phase transition is the lowest order of the differential of a thermodynamic potential, such as Gibb's free energy (G), which shows discontinuity with respect to temperature (T) or pressure (P).[11–13] The first derivative of G with respect to P shows a discontinuity in volume (V) as a function of pressure for a gas–liquid phase change (Equation 1.1 **(a)**). The second differential of G which is the compressibility of the substance (Z) with respect to pressure shows a discontinuity for a gas–SCF phase change (Equation 1.1 **(b)**).

$$a)\quad \left(\frac{\delta G}{\delta P}\right)_T = V \qquad\qquad b)\quad \left(\frac{\delta^2 G}{\delta P^2}\right)_T = \left(\frac{\delta V}{\delta P}\right)_T = Z \tag{1.1}$$

In the case of a pure fluid coexisting with its gas phase, the order parameter (density) fluctuations in each phase increasingly grow as the critical point is approached and diverge at the critical point.[14] The spatial extent of these fluctuations known as the correlation length (ξ), are a measure of how far a single particle's influence propagates through the system. The correlation length increases as the critical point is approached leading to larger density fluctuations in a fluid which begin to exceed the molecular scale. This is a key property of criticality in fluids. This means that the physical properties of a fluid near or at the critical point depend on these order parameter fluctuations and the spatial dimension of the system, which limits the correlation length to the size of the system. This leads to increased deviation from bulk properties of near-critical fluids in confined spaces, where even small fluctuations dominate the entire system.[15]

These critical and near-critical effects are apparent in many physical systems and have an anomalous influence on properties such as magnetic susceptibility.[16] This divergence of the correlation length also explains the observation of critical opalescence or turbidity in mixtures, which are the result of increasingly large concentration fluctuations as the critical point is approached, scattering light and making a usually transparent solution cloudy in appearance.[17]

Unlike conventional solvents, the physical properties of SCFs can be easily tuned by changing temperature and pressure, making them more gas or liquid-like. This attribute has been harnessed in supercritical fluid extraction porcesses and in supercritical fluid reactions.[18–22] By changing pressure and temperature, different products can be isolated as the density of the fluid is no longer sufficient to dissolve them, allowing them to be extracted from the reaction mixture. This has been used to great effect allowing a high yield and selectivity to be achieved for a variety of reagents and natural products. By fixing the temperature of a substance above its T_c it can be transformed between a gas and SCF by simply applying or releasing pressure to cross the gas–supercritical fluid phase boundary. This property has allowed the development of a supercritical drying process with applications in porous material production.[23–25] This drying process has been utilised in applications such as the preparation of free-standing arrays of CdS nanowires, where the diffusivity of the SCF allows it penetrate deep into to nanoscale structure.[26] This enables the sample to be purged without the surface tension of the liquid-vapour interface of a drying liquid deforming their uniform arrangement. New applications which utilise the anomalous phase characteristics of pore confined SCFs and their ability effuse deep into to nanoscale structures will be discussed in the upcoming sections.

1.2 Supercritical Fluid Electrodeposition

Electrodeposition deposits dissociated ions from a solution by the transfer of electrons through the use of electrodes in the deposition bath.[27] It allows deposition onto and into large complex objects whilst retaining their topography and spatially defined growth, allowing deposition onto complex structures through the placement of electrodes. Direct control over the driving force of the process is enabled through the applied potential.[28,29] Recent developments have led to electrodeposition from supercritical fluids.[30–34] These fluids include supercritical water (scH_2O) and ammonia (scNH_3),[30–32] and more recently less polar fluids such as supercritical carbon dioxide (scCO_2) in the presence of a co-solvent,[33,34] as well as supercritical difluoromethane (scR32/scCH_2F_2).[35–37] These SCFs are used as the solvent in the deposition bath.[34] Supercritical fluids have a range of properties that can be exploited for this particular purpose such as a wide electrochemical window and zero or negligible surface tension.[35,38,39]

A wide electrochemical window allows for a large range of chemical species to be dissolved within the fluid and then subsequently deposited *via* an electric potential before the solvent itself is oxidised or reduced.[40] This is a benefit as oxidisation or reduction of the solvent prevents the electrochemical energy from being passed to the intended chemical species within the solvent. The lack of surface tension exhibited by supercritical fluids is a key property, allowing the fluid to penetrate deep into nanoporous structures and templates. An example of this is in the case of chemical fluid deposition (CFD) of copper and nickel into high aspect ratio trenches using $scCO_2$.[41] This allows for deposition to take place within the confines of a pore, avoiding material deposition limited only to the pore entrance.[33,41] The lower density of the supercritical fluid and the lack of surface tension contribute to a greater effusion rate of the fluid and therefore a higher mass transport rate of the species dissolved within it,[42] again making it an ideal solvent for electrodeposition into nanoporous templates. Another benefit is the availability of supercritical fluids that posses a high chemical stability. This stability has allowed for the deposition of reactive materials such as germanium at high temperatures, improving the quality (crystallinity) of the deposited material.[37,43] A diagram of the supercritical fluid electrodeposition process, depositing material into a nanoporous template is shown in Figure 1.3.

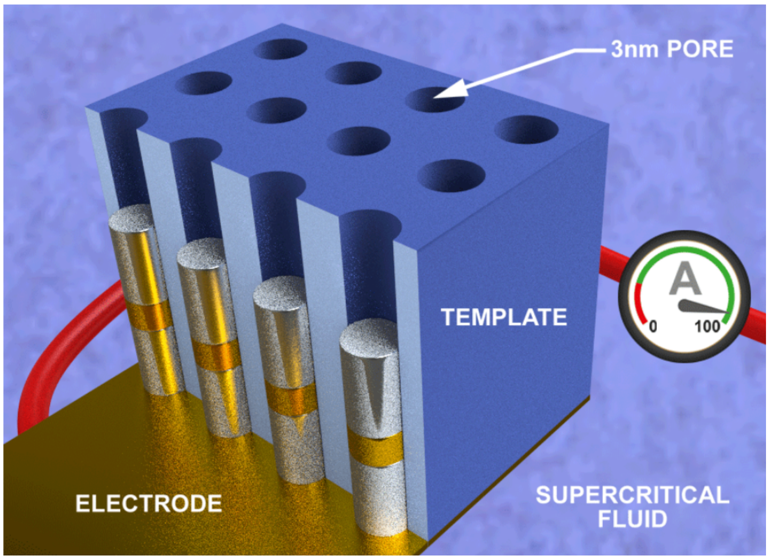

Figure 1.3: A diagram illustrating the supercritical fluid electrodeposition process into a nanoporous template. Reproduced from 44.

By exploiting these key advantages, supercritical fluid electrodeposition has allowed for the production of ordered templated nanowires.[45–47] This is particularly interesting in terms of the microelectronics industry as it offers an alternative methodology for microchip or integrated circuit manufacture. These devices are traditionally manufactured *via* photolithography, which exposes a light sensitive photoresist to monochromatic light to etch or pattern conductive channels or circuitry. The size of the channels produced by this process however is limited by the wavelength of the light used to etch the photoresist, with the etching only achieving down to 50 nm resolution with developments in UV (ultraviolet) excimer laser technology.[48] This has been improved with the use of extreme UV laser etching,[49] x-ray lithography and the introduction of multiple patterning methods.[50,51] However these solutions are much more cost and time intensive and require tuning of the photoresist absorption to maximise effectiveness.[50] This is very much a top down approach for microelectronics manufacture, where material is taken away from a blank *via* photolithography producing the device. A bottom up approach however would be to manufacture the devices in-situ utilising electrodeposition of conductive materials into templates. This can produce better size resolution as porous materials that can be used for templates can possess pores with sub-nanometer diameters,[52] offering the possibility of production for a wide range of nanosized components. These devices include semiconductors, transistors, diodes or nanowires which have applications in optoelectronics, sensors, and electronic circuits.[53] An example of a device that could be produced using this methodology is shown in Figure 1.4. Electrodeposition is advantageous in this case as compounds can be selectively deposited from the deposition bath by adjusting the potential,[54] creating a structure consisting of more than one compound. This allows the production of components with heteroatom junctions, an important feature of devices such as semiconductors.[55]

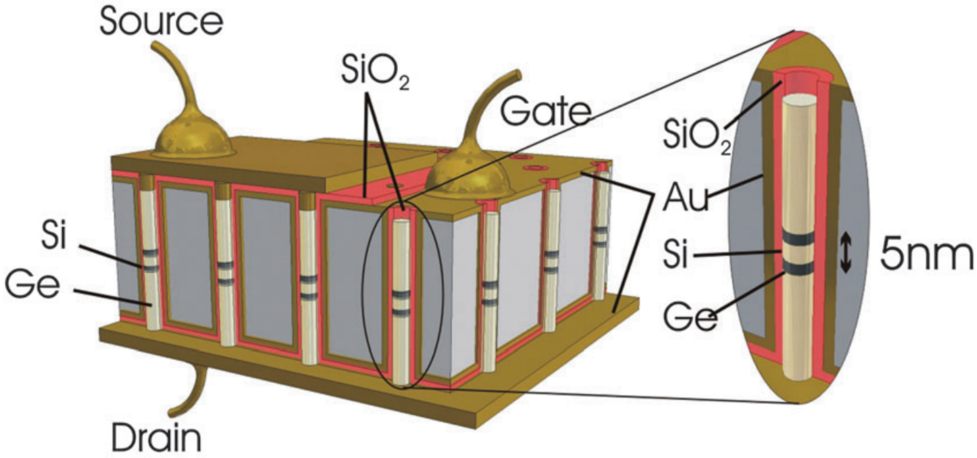

FIGURE 1.4: Concept of a multi-state logic device which may be produced by supercritical fluid electrodeposition in the future. The advantages of electrodeposition mean it is particularly suited to the production of axial heterostructures like the Si/Ge quantum dot structure shown. Reproduced from 37.

Previous work in this area has shown successful electrodeposition of copper, silver, cobalt, and germanium from a single-phase of $scCO_2$ with a co-solvent, as well as supercritical HFC's (hydroflurocarbons).[34,37,43,47] An example of silver nanowires produced using this process from a $scCO_2/CH_3CN$ bath is shown in Figure 1.5. Supercritical CO_2 itself does not have a high dielectric constant (ε_r=1.5 at 308.15 K and 10 MPa),[56] making it a less than ideal solvent for electrodeposition (for comparison supercritical difluoromethane has an ε_r=4.9 at 351.26 K and 5.8 MPa).[57] This means that its ability to carry charge to the species dissolved within it for oxidation and reduction to take place is not optimal for electrodeposition.

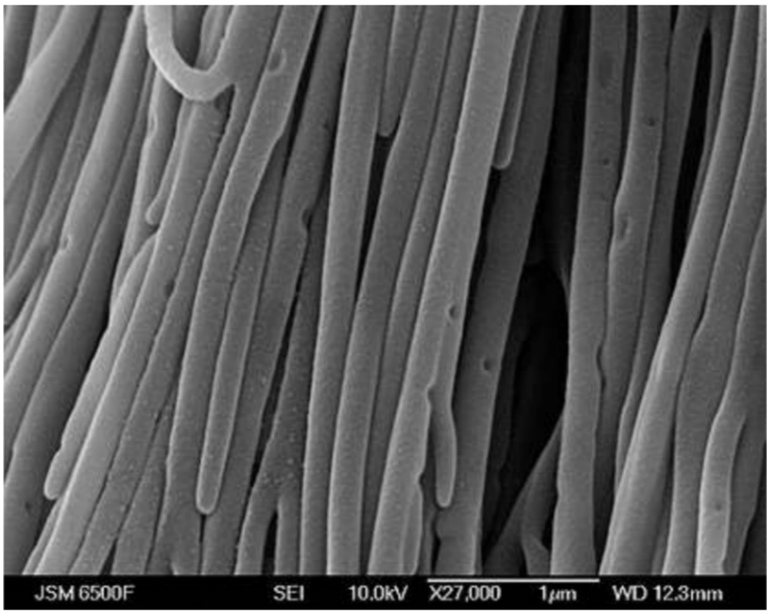

FIGURE 1.5: FEG-SEM (Field Emission Gun-Scanning Electron Microscopy) image of silver nanowires on a partially dissolved 200 nm anodic alumina template. The wires were deposited from 4.8 mM $[Ag(CH_3CN)_4][BF_4]$ in scCO2/CH_3CN, with a 20 mM $[nBu_4N][BF_4]$ electrolyte at 309 K and 1856 psi. Reproduced from reference 47.

A co-solvent has to be added to the mixture in a relatively small proportion to improve its dielectric constant, conductivity and ion solubility, with acetonitrile proving suitable in the past.[58,59] To maintain the homogeneity throughout the supercritical mixture, keeping it monophasic and therefore retaining its desired properties, as little acetonitrile is added as possible to provide the conductivity and ion solubility needed. A composition in the region of 12% CH_3CN, 87.4% CO_2 by weight has been found to be appropriate, with the remaining 0.6% consisting of the supporting electrolyte which improves conductivity.[34,45] This small proportion is used because the properties of the mixture are a weighted average of each component, those being the supercritical fluid, co-solvent and the electrolyte. Supercritical difluoromethane does not need a co-solvent as its dielectric constant is high enough for deposition to take place as long as a suitable electrolyte is present, with past work showing that many polar HFC's including difluoromethane are ideal for this purpose.[34,37,59] The fact that supercritical fluid electrodeposition takes place from a mixture of compounds demonstrates the importance of understanding how mixture composition may be affected when confined in a nanopore. If confinement of the electrodeposition bath changes its properties, this could have a knock on effect in terms of its physical attributes including conductivity, viscosity and diffusivity, which are important to determining the success of deposition.[60,61] It is therefore important to understand how mixture composition changes when confined in a nanopore, as electrodeposition has to take place from a multi-component bath. A grasp of the phase behaviour within nanopores will allow the properties of these fluids to be tuned *via* changes to temperature or pressure of the deposition conditions and perhaps co-solvent choices or electrolyte quantities. This will allows for optimal electrodeposition to take place into a nanochannel.

1.3 Gas Storage, Extraction and Catalysis

The experiments described in this Thesis have implications that reach beyond supercritical fluid electrodeposition. Phase behaviour in pores has become an important avenue of research in the area of gas storage and oil/natural gas extraction processes. An example of which is the storage of CO_2 in coal beds. In the case of CO_2 storage it is important to determine the storage capacity of high pressure CO_2 in the nanosized pores of the coal and rock, which depends on the tempreture and pressure and therefore the phase of the CO_2.[62,63] Injected CO_2 also displaces CH_4 present in the coal, which contributes to improved methane recovery in basins with coalbed methane.[64] To maxmise the efficiency of these processes, an understanding of the phase behaviour, selectivity and sorption mechanisms of these confined species within geological nanopores during this exchange process is required.[65]

Pore wetting, which is the ability for a fluid to spread over the surface of a pore wall and adhere to it, is also a significant factor in the CO_2 storage and oil recovery processes in nanopores.[66] The wettability depends highly on the CO_2 phase, therefore any shift in critical parameters within the pores will have an effect on this behaviour and the storage process.[67] This property can be determined by measuring the contact angle of the fluid droplet with the surface of the pore wall, giving indications to the surface tension of the droplet and its interfacial properties. Pore wetting is influenced by the fluid-wall interaction strength and pore geometry. A firm grasp of the phase behaviour of the compounds contained within the small pores of geological formations, along with an understanding of how wetting changes in various pore types and how different phases of matter can affect wetting phenomena is necessary to maximise both the efficiency and safety of these applications. In the case of oil recovery it is vital to understand these effects, as processes that extract oil droplets in geological capillary tubes are dominated by this behaviour, where the degree of wetting and the phases of water present under these conditions have a profound effect on the fluid dynamics, viscosity and diffusivity and therefore extraction efficiency.[68] It has also been shown that contact angle will increase with density and pore diameter.[67]

CO_2 geological storage has also become one of the most promising technologies to control greenhouse gas emissions, with the CO_2 being stored in depleted oil reservoirs or aquifers.[69] Again the efficiency and safety of the CO_2 storage process depend on the fluid-fluid and rock-fluid interactions, wettability, physical and chemical properties of fluids, temperature, pressure, pore surfaces, pore structure and saturation of the pores.

Mesoporous materials are in high demand for catalytic applications, they allow for the transformation of homogeneous systems into heterogeneous catalysis systems. Mesoporous materials offer a method of encapsulation of catalytic nanoparticles with high stability and low rates of degradation, preventing nanoparticle coagulation to achieve excellent catalyst recovery.[70,71] The high surface area, tunable pore sizes for reactant selectivity and the ease of diffusion into the pore are attractive features for preforming reactions confined within nanopores. In order to fully exploit the benefits of confined catalytically active sites within these materials, a firm grasp of the phase behaviour, component selectivity, wall-adsorbate interactions, and wetting behaviour has to be understood.

The exact phase behaviour of both sub-critical and supercritical fluids within the nanopores is yet to be fully understood. However a depression in the critical temperature of pore confined fluids has already been measured *via* gas sorption and nuclear magnetic resonance (NMR) spectroscopic studies.[72–80] This has been demonstrated for a number of porous materials and fluids where the change in

T_c is dependent on the pore size, structure and fluid. How P_c changes in the presence of a porous material has yet to be thoroughly studied experimentally. It is assumed that the confinement of a fluid will indeed have an effect on the P_c and saturation properties of the fluid, as observed for T_c. Theoretical studies have already sought to develop an equation of state for pure confined fluids by introducing parameters to account for molecular interactions and the porosity of the confinement medium.[81,82] These have shown good agreement with the previous experimental results from carbon dioxide absorption into silica aerogel. The unique phase properties exhibited by pore confined fluids are due to the fact that the confinement size is very similar to the molecular size (on the nanoscale). The mean free path of the confined molecule will be greatly reduced compared to its bulk counterpart, so the attractive interactions of the fluid with the confinement medium and the decreased coordination of neighbouring fluid molecules due to the confines of the pore have a significant effect on its phase behaviour.[81–85]

1.4 Porous Materials

Applications that utilise confined fluids often require a porous matrix or template in which a substance can be confined, in order for it to be used or even have its phase characteristics studied. These porous materials can be often divided into the categories of crystalline regular structured materials and amorphous materials. Crystalline structures include for example, mesoporous silica,[86] aluminosilicates,[87] aluminophosphates[88] and carbon nanotubes.[89] The atomic structures and coordinates of these materials can usually be reliably determined using x-ray or neutron diffraction.[90,91] Often due to their challenging preparation, materials with pore diameters of several nanometers are rarely produced in a completely uniform state. Therefore the production of these larger pore materials often results in a pore size distribution in the material. This can be seen in the example of MCM-41 (Mobil^{TM} Crystalline Materials-41) which is traditionally prepared by a liquid crystal technique, where the chain length of the liquid crystal influences the pore size during synthesis.[92,93] Amorphous nanoporous materials such as controlled pore and vycor glasses, can widely vary in their micro-structure and regularity and are difficult to characterise completely. They have roughly cylindrical pores with circular pore cross sections. However, electron micrographs have shown that these materials have a networked structure of winding pores. A further example of an amorphous material is silica aerogels, in which the liquid phase of the gel has been replaced by gas. Although the pore networks are quite regular the structure surrounding them can be random hence their lack of crystallinity.

A separate class of porous materials are highly ordered anodic alumina oxide templates (AAO) (Figure 1.6). AAO templates are usually produced by a two step anodization process.[94,95] This anodization process involves the exposure of high-purity aluminium to an acid solution at a constant voltage. The aluminium is etched away electrochemically in stages, with the anodization voltage and time determining the final pore diameter. The first anodization produces a layer of alumina which is then stripped off using an acid mixture (*e.g.* phosphoric and chromic acid). The concave patterns on the surface of the aluminium left behind on the substrate act as self-assembled masks for the second anodization process. The remaining aluminium substrate is removed with a metal salt solution (*e.g.* $CuCl_2$ or $HgCl_2$ with H_2O and HCl) and the bottom of the pores are then opened up with a suitable acid (*e.g.* 0.1 M phosphoric acid). A polymer film can then be applied to the template for protection which can be removed later by hand.

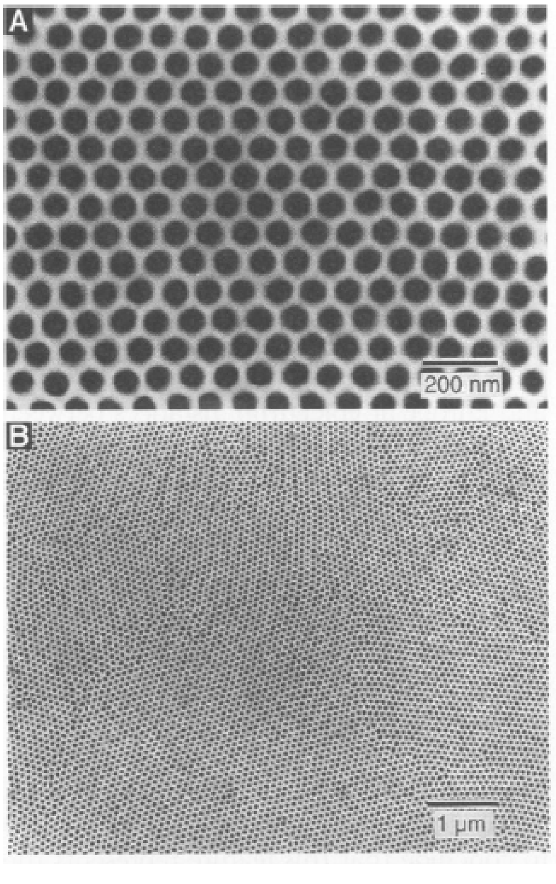

Figure 1.6: **(A)** Scanning electron microscope (SEM) view of an AAO surface in high magnification and **(B)** lower magnification. Reproduced from reference 94.

1.4.1 Pore Size Measurements

As mentioned previously, x-ray diffraction (XRD) can be used to characterise porous materials and determine pore dimensions.[90] This provides highly accurate atomic coordinates and characterisation of the lattice atoms, therefore pore diameters. However, XRD is only suited to very ordered materials as it does not provide a statistical measure of the varying pore geometries and parameters. Also pore diameters have to be determined from lattice spacing which can give erroneous pore diameter values since the pore wall thickness may not be estimated correctly.[96] Gas sorption is the most popular method of pore characterisation as it allows a wide range of pore sizes to be assessed. Gas sorption techniques are convenient to use and are not as cost intensive as other methods. Gas sorption also allows for a statistical analysis of the entire pore size range and gives the proportion of each pore size present in the material. Gas sorption isotherms exhibit characteristics depending on the adsorbent (pore) type and the adsorbate (confined species). Examples of typical isotherms are shown in Figure 1.7.

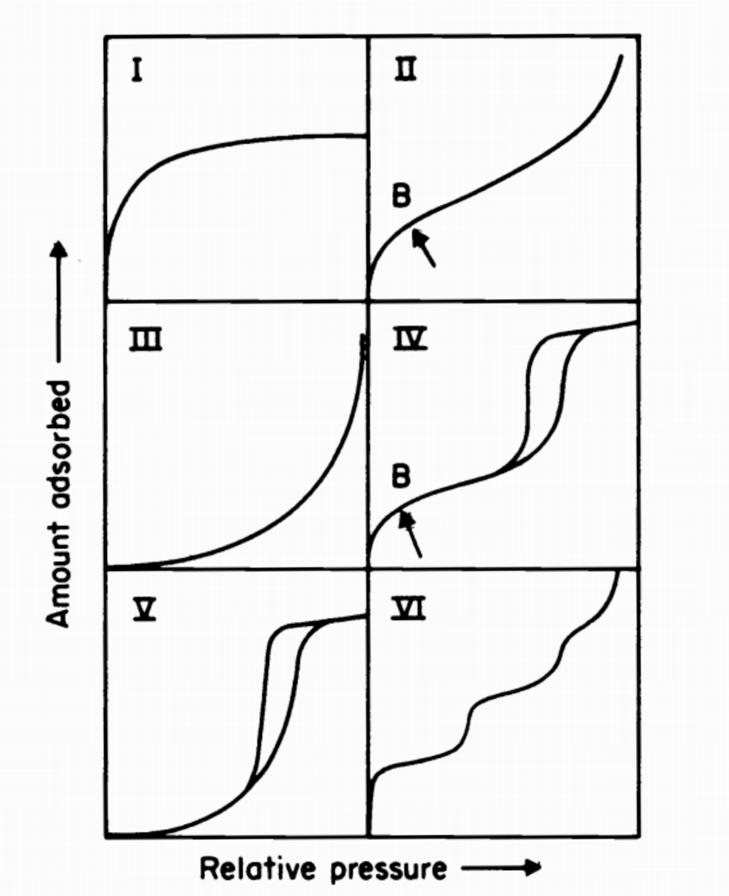

FIGURE 1.7: Characteristic gas sorption isotherm types reproduced from reference 97.

According to the International Union of Pure and Applied Chemistry (IUPAC), isotherms can be classified as six separate types.[97] Each of these indicate the unique properties of the pore or surface. Type I isotherms are characteristic of adsorption into pores which are very narrow and only adsorb a few molecular layers. This behaviour is often observed for microporous materials (< 2 nm). Micropores are filled and therefore exhibit high uptakes at relatively low pressures because of the narrow pore width and the high adsorption potential, since the adsorbate is close to the pore walls. The uptake limit is governed by the accessible micropore volume rather than by the internal surface area. Type

II sorption isotherms are typically obtained in cases of non-porous or macroporous adsorbents, where unrestricted monolayer-multilayer adsorption can occur. Point **B** in Figure 1.7 indicates the stage at which monolayer coverage is complete and multilayer adsorption begins to occur. The type III isotherm is reversible and convex over the entire pressure range and does not exhibit a point where monolayer coverage switches to multilayer coverage indicating that the attractive adsorbate-adsorbent interactions are relatively weak. Type IV isotherms are typical for mesoporous materials. Their characteristic features are the hysteresis loop (difference in adsorption and desorption pressure) which is associated with the occurrence of pore condensation. This phenomena is related to the interactions between the condensed pore fluid and the pore.[98–101] The plateau of the isotherm at high pressures indicates complete pore filling and a fully condensed adsorbate formed under these conditions. The initial steep increase in the amount adsorbed is attributed to monolayer-multilayer adsorption as in the case of the type II isotherm. Type V isotherms again exhibit pore condensation and hysteresis. However, in contrast to type IV the initial part of this sorption isotherm is similar to that of type III, as little adsorption into the pore occurs at low relative pressures. This indicates a relatively weak attractive interaction between the adsorbent and the adsorbate. The type VI isotherm is due to stepwise multilayer adsorption on a uniform non-porous surface. The gradient of the steps observed depend on the homogeneity of the adsorbent surface, the adsorbate and the temperature, therefore it is heavily influenced by the surface-adsorbate interaction energy.

Many pore size analysis techniques that utilise gas sorption make use of the Kelvin equation which relates the equilibrium vapour pressure of a liquid in a capillary or pore (P), to the equilibrium vapour pressure of the same liquid on a planar non-porous surface (Po), known as the saturated vapour pressure.[97,102] For a cylindrical pore the Kelvin equation takes the form of Equation 1.2.

$$ln\frac{P}{P_0} = \frac{-2\gamma V_m}{rRT} \tag{1.2}$$

where γ is the surface tension of the liquid, V_m is the molar volume of the condensed liquid contained in a pore of radius r, R is the ideal gas constant and T is the temperature. However since adsorption onto the pore wall will have already taken place prior to pore condensation, r is not the actual value of the pore radius. The film thickness (l_c) needs to be considered when condensation takes place on the pore wall.[102] The pore radius (r_p) of a cylindrical pore is actually given as:

$$r_p = r + l_c \tag{1.3}$$

This assumes that the film thickness is the same as that on a non-porous surface. The Barett-Joyner-Halenda (BJH) method can be considered as the most popular method for mesopores size analysis that relies on these assumptions.[103] However because this approach is based on modifying the Kelvin equations and assumptions have to be made for the film thickness during pore condensation and evaporation, this approach has a tendency to underestimate the pore diameter. The methods which make use of the modified Kelvin equation are based on the emptying of the mesopores by the step-wise reduction of relative pressure (P/P_0) with an allowance being made for the thinning of the adsorbed film in the pores already emptied of condensate.[104] It is also assumed that the meniscus curvature is controlled by the pore size and shape, the pores are rigid, are in the mesopore size range (2–50 nm pore diameter) and that there are no pore blocking effects by the adsorbate.[104] In narrow pores especially, attractive fluid-wall interactions are dominant and the macroscopic thermodynamic concepts of liquid-vapour interfaces and bulk-like core fluid cannot realistically be applied. In addition, methods based on the modified Kelvin equation do not take into account the influence of the adsorption potential on the relative pressure value of the pore condensation transition. It is also assumed that the pore fluid has the same thermophysical properties as the corresponding bulk fluid for example surface tension, but the surface tension of the pore liquid depends on the radius of the meniscus curvature.

A more advanced approach is to apply theoretical techniques to simulate the pore confined adsorbate, an example of which is non-local density functional theory (NLDFT) which is a theoretical method that is used to accurately calculate the pore size distribution of a porous material. In order to determine the pore size of an adsorbent, a set of isotherms are calculated for a range of pore sizes for a given adsorbate. The isotherms are calculated by integrating the equilibrium density profiles of the fluid in the model pore to generate a set of isotherms called a Kernel.[102] No assumptions are necessary concerning the nature of pore filling and adsorbed film thickness. The equilibrated density profiles of the confined fluid at given temperature and pressure can be directly obtained by DFT and Monte Carlo (MC) calculations (Figure 1.8).[105,106]

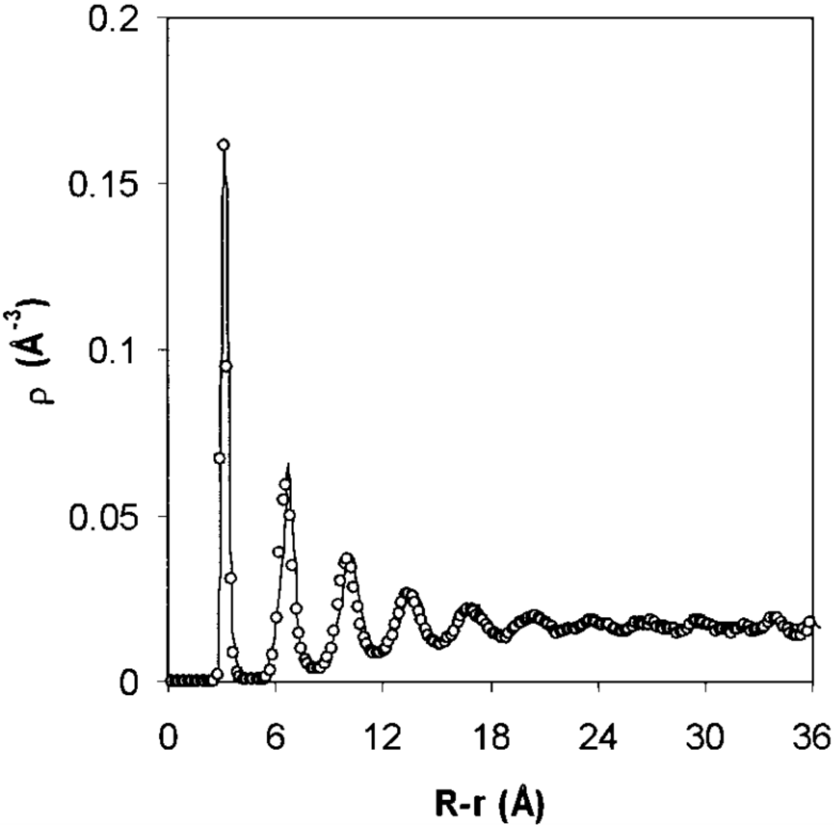

FIGURE 1.8: Nitrogen density profiles in cylindrical pores with a 72 Å pore diameter at 77 K, represented by density as a function of distance from the pore wall. The points = grand canonical Monte Carlo simulations and the lines = NLDFT. Reproduced and adapted from reference 106.

These methods are based on a solution of the generalized adsorption isotherm equation (GAI), which correlates the kernel of theoretical adsorption/desorption isotherms with the measured experimental sorption isotherm of a material (Equation 1.4).[102]

$$N\frac{P}{P_0} = \int_{W_{MAX}}^{W_{MIN}} N(P/P_0, W) f(W) dW \tag{1.4}$$

Where $N(P/P_0)$ is the experimental adsorption isotherm data consisting of the amount adsorbed (N) as a function of relative pressure (P/P_0), W is the width of the pore, $N(P/P_0, W)$ is the isotherm of a single pore of width W and $f(W)$ is the pore size distribution function. The GAI equation assumes that the measured isotherm consists of a number of individual isotherms associated with each pore size, this is then multiplied by their relative distribution $f(W)$. The pore size distribution is then derived by solving the GAI equation numerically. Since the equilibrium density profiles of an adsorbate are known for each pressure along an isotherm, no assumptions about the pore filling mechanism, surface tension or contact angle of the fluid on the pore wall are required as in case of the macroscopic thermodynamic methods discussed previously as this methodology takes into account the density modulations near the pore walls due to the adsorbed layers of molecules and the pore-fluid attractive potential.[106] Therefore NLDFT can describe the adsorption isotherm over the complete range and it is possible to obtain with a single method a pore size distribution which extends over the complete micro-mesopore range.

1.5 Aims

The aim of this Thesis is to investigate the unique phase characteristics of confined fluids utilising spectroscopy. Usually, spectroscopic techniques are used to ascertain the densities of the species present and therefore its phase properties by studying spectral features. The phase behaviour of bulk substances has been studied previously using attenuated total reflectance-Fourier transform infrared spectroscopy (ATR-FTIR),[107] NMR,[108] near-infrared (NIR) spectroscopy,[109–112] and coherent anti-stokes Raman spectroscopy (CARS).[113,114] In the case of confined phase properties spectroscopic techniques such as microwave spectroscopy,[83] NMR,[79,80] ATR-FTIR[115] and CARS have previously been employed in the literature.[116,117]

It is the objective of this study to build on the previous work, using near-infrared and Raman spectroscopy to provide a detailed insight into the nature of confined fluid phase properties. Near-infrared spectroscopy has a multitude of applications, for example in medical settings, due to the fact that NIR radiation can penetrate living tissues and is non-destructive.[118] NIR has also been used as a tool in the detection of cerebral bleeding *in-vivo* when combined with a indocyanine green dye dilution in the blood stream and the determination of cartilage thickness to determine joint health.[118,119] Its non-destructive nature also allows it to be used for manufacturing quality control, for example imaging of drug formulations.[120] It has also found use in the agriculture industry, as water absorption bands are weaker in this region and allow for the evaluation of living or biological materials with relatively large sample thickness. This makes analysis of a variety of sample types possible, for example in the quality control of food.[121,122] The weaker absorption bands have also granted the analysis of dense phases of matter permitting the study of phase behaviour.[109–112,123]

Raman spectroscopy has proven to be a valuable tool for a number of applications. Firstly, because of its differing selection rules compared to infrared spectroscopy, Raman spectroscopy can provide chemical and structural information from moieties that are invisible to infrared spectroscopy.[124] This is because vibrations that have a large change in polarisability will be easily observed in the Raman spectrum even if they have a small or zero change in dipole moment, rendering them weakly absorbing in the infrared spectrum.[124] This property makes Raman an ideal tool for looking at biological materials or living tissues which contain a large proportion of water, as water is strongly infrared absorbing and can hide vibrational modes belonging to other species in the infrared spectrum. Examples of Raman spectroscopy used on these types of samples can be seen in cancer tissue detection,[125–127] through imaging of tissue and the analysis of plant matter.[128–130]

As Raman is a scattering technique and the scattered photons are only collected from the region of the sample upon which the incident light impinges, the drawbacks of traditional transmission infrared spectroscopy is negated. Usually, for infrared transmission measurements, if a sample is above a certain thickness or too strongly absorbing it cannot be analysed, as the light is not transmitted through the sample for a measurement (totally absorbing). This means Raman spectroscopy can be used on a number of samples that are opaque to infrared transmission, such as thick solid state samples or dense liquids, allowing Raman spectroscopy to be used for the study of phase characteristics of substances in dense states and also within solid porous samples.[116,117,131]

Chapter 2

Near-Infrared Investigations of Confined Fluid Critical Temperature

2.1 Introduction

This Chapter will describe the use of near-infrared (NIR) spectroscopy to probe the phase behaviour and in particular the depression in the critical temperature, of fluids confined in pores. Molecules confined in narrow channels, with widths that can be as small as a few molecular diameters, exhibit a wide range of phase phenomena not present in the bulk counterpart. Examples of these are layering and wetting transitions on the pore surface which are driven by fluid-pore interactions,[132,133] and shifts in phase transition parameters such as the freezing temperature.[134] This behaviour is primarily driven by finite size effects,[135] the introduction of a fluid-wall interaction potential,[136,137] and the competition between the fluid-wall and fluid-fluid interactions determining the fluid's properties.[138] It can be demonstrated by a classical mean field treatment of a fluid in a pore that the pore critical temperature (T_{cp}) will be lower than that of the bulk fluid.[81,82,84] The confinement of a fluid reduces the nearest neighbour coordination number (z) and reduces the total maximum interaction energy per molecule, resulting in a lower critical temperature.[82,84] This is demonstrated in Equation 2.1.

$$T_c = c\frac{z\varepsilon}{k} \tag{2.1}$$

where k is Boltzmann's constant, ε is the interaction energy between nearest neighbour fluid molecules and c is a constant of proportionality. Scaling theory of criticality for fluids confined between plates and within pores,[85,139–141] predicts the shift in critical temperature of a fluid in a confined space as:

$$\frac{T_c - T_{cp}}{T_c} \approx \frac{1}{R_c} \tag{2.2}$$

where T_c is the bulk fluid critical temperature, T_{cp} is the pore or confined fluid critical temperature and R_c is the interior radius of the capillary. This parameter can also be substituted with slit width (H) in the case of a slit type pore.[141] This prediction was derived mathematically with a slab density profile, treating the adsorbed fluid as a film possessing uniform density and thickness with the same properties as the bulk condensate at equivalent temperatures.[102,142] This has also been calculated using a density functional approach as a function of wall separation or capillary radius, chemical potential and temperature.[140,141] This scaling theory predicts a linear dependence of the depression in the pore critical temperature with inverse pore or slit width. Theoretical studies have shown that the degree of spatial confinement in a pore is not the only factor influencing the critical temperature of a pore fluid. The magnitude of the pore-fluid interaction potential has also been shown to play a pivotal role in the extent of the depression in T_c, with stronger fluid-pore interactions predicted to result in a lower value of T_{cp} due to an influence on the coexisting pore phases.[85,139,143–145] In order to determine the effect of pore confinement on the critical temperature of a fluid, a number of experimental techniques can also be utilised. A brief overview of this is detailed within this work.

2.1.1 Neutron Scattering Techniques

Small angle neutron scattering (SANS) and ultra-small angle neutron scattering (USANS) have been to shown to provide a reliable method of probing adsorption behaviour of confined fluids. This technique offers good spatial resolution, allowing for the study of interfacial phenomena in pores.[146] Melnichenko *et al.* used SANS and neutron transmission spectroscopy to study the adsorption of $scCO_2$ in aerogels and Vycor glass.[147] The study concluded that there is a formation of a highly densified adsorbed phase with a density of 1.07 $g.cm^{-3}$ at 308.15 K, which is close to the density corresponding to the van der Waals volume of CO_2

of 1.03 g.cm^{-3}. This value is the volume occupied by a single CO_2 molecule and has been determined previously in other studies.[148,149] The excess adsorption of CO_2 is found to be independent of oxidation on the aerogel pore surface but was found to depend strongly on the proximity to the critical point of the bulk fluid. It is proposed that the CO_2 molecules do not adsorb on the pore walls of the Vycor porous glass due to significant suppression of the critical temperature of the confined fluid, preventing adsorbate condensation.

SANS has also been used to investigate the phase behaviour of CO_2 injected into coal and the possible changes in the coal pore structure that may result from this injection.[62] The coals were selected from different geological depths to represent the range of the underground CO_2 conditions (from subcritical to supercritical), which may be present in deep subsurface environments. The study showed that the porous matrix of all coals examined remained unchanged after exposure to CO_2 at pressures up to 200 bar (2901 psi), as there was no significant change in the amount of CO_2 absorption after pressure cycling the coal. CO_2 was observed to condense from gas to liquid within the coal pores, leading to increased average fluid density in the pores. These values are increased by a factor of three to four compared to the density of bulk CO_2 under similar thermodynamic conditions. The intermediate size pores within the coal, with a 200 nm pore diameter, exhibited an average fluid density similar to the density of bulk fluid. This indicates that capillary adsorption does not occur in these pores. In the coal with a very small amount of porosity and relatively large pore sizes there was found to be no significant enhancement in the confined CO_2 density.

Further studies of the phase behaviour of CO_2 confined in porous fractal silica (PFS) were also investigated using SANS and USANS.[63] A range of fluid densities and temperatures corresponding to gaseous, liquid, near critical and supercritical conditions of the bulk fluid were investigated. The results revealed the formation of a dense adsorbed phase in the small pores (< 0.4 nm) at all temperatures. At low pressures it was shown that the average fluid density in pores may exceed the density of bulk fluid up to a factor of 6.5 at 295 K. This “enrichment factor” was shown to decrease with temperature, although a significant fluid densification in the small pores still existed at temperatures far above the critical temperature of bulk CO_2. It was also shown that larger pores are only partially filled with a liquid-like adsorbed layer which coexists with unadsorbed fluid in the pore centre. With increasing pressure, all pores became uniformly filled with fluid showing no measurable enrichment of the CO_2 density (see Figure 2.1).

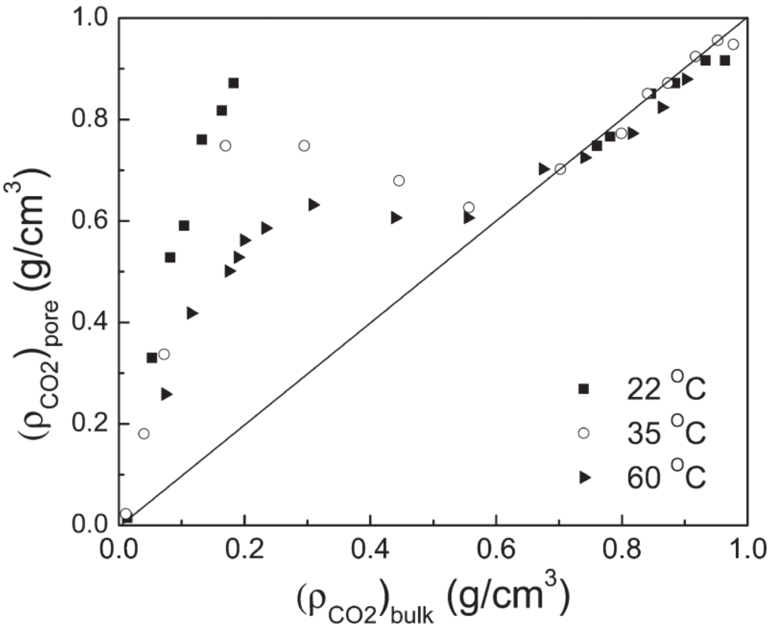

FIGURE 2.1: Average CO_2 density in micropores with a diameter 1.6 nm as a function of the bulk fluid density for a range of temperatures. The solid black line represents (ρCO_2)pore = (ρCO_2)bulk values. Reproduced from reference 63.

SANS has also been used to ascertain the density of hydrogen in carbon nanopores.[150] The density of the adsorbed fluid appears to be dependant on both pore size and pressure, with the confined density of H_2 in narrow nanopores comparable to the density of liquid H_2 at 200 bar (2901 psi), as shown in Figure 2.2. The surface-molecule interactions responsible for the density increase of H_2 within the pores have been estimated to create an environment akin to pressures that exceed the external gas pressure by a factor of ~ 50.

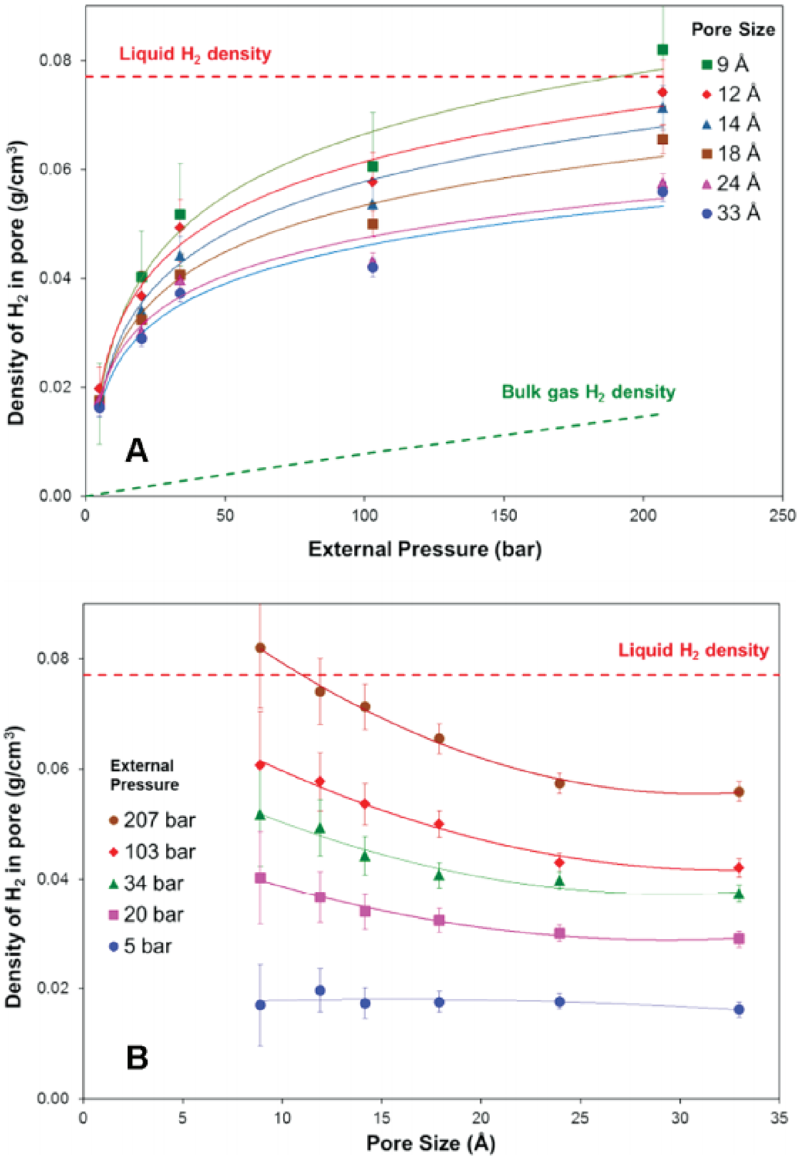

FIGURE 2.2: Room-temperature densities of adsorbed H_2 as functions of **(A)** pressure for selected pore sizes and **(B)** pore size at constant pressures. Reproduced from reference 150.

2.1.2 Nuclear Magnetic Resonance Spectroscopy

A more convenient and chemically sensitive technique than neutron scattering which can be used to study the unique phase properties of confined fluids is nuclear magnetic resonance (NMR) spectroscopy.[79,80,151] The investigation of supercritical xenon confined in a mesoporus zeolite FSM-16, with mean pore diameters of 1.9, 2.7, and 4.1 nm has been conducted by Omi *et al.*[80] The high pressure NMR spectroscopy provides the means to thoroughly study the effect of confinement on the xenon density in a number of different pore sizes. Figure 2.3 shows the ^{129}Xe NMR spectra of xenon in FSM-16 at pressures ranging from 0.3 to 10 MPa (44–1450 psi). The two peaks in the resulting NMR spectrum at 0.3 MPa were assigned to the free xenon gas (0 ppm) and the confined xenon (95 ppm, broad peak).

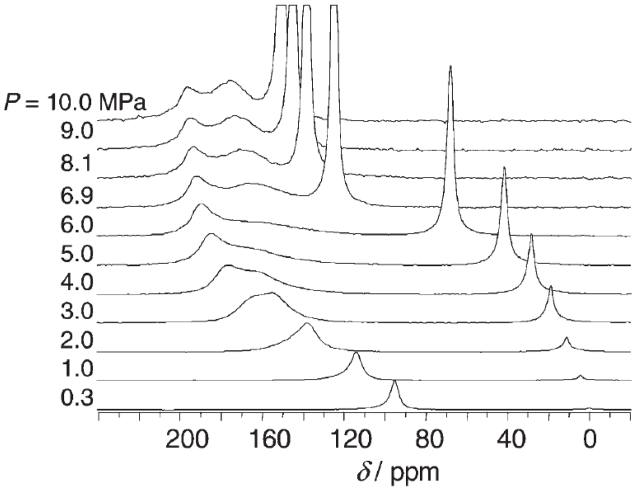

FIGURE 2.3: Changes in the ^{129}Xe resonance chemical shift with Xe pressure in FSM-16, with a mean pore size of 1.9 nm at 295 K. Reproduced from reference 80.

The chemical shift of the free xenon peak in the presence of FSM-16 was in good agreement with the chemical shift values of pure bulk xenon previously determined by Jameson *et al.* across a large density range in their NMR study,[152] where a correlation between density and ^{129}Xe chemical shift value was observed (Figure 2.4).

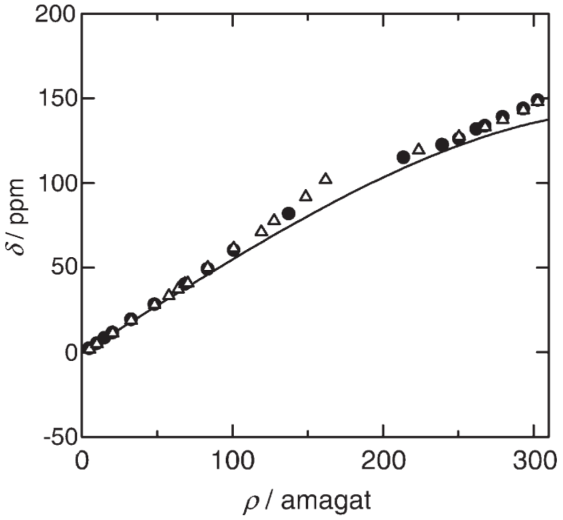

Figure 2.4: The density dependence of the ^{129}Xe NMR chemical shift of pure bulk xenon (△) and free xenon (●) in the presence of 4.1 nm pore diameter FSM-16 at 298 K. Density is given in amagat, where 1 amagat the number of ideal gas molecules per unit volume at 1 atmosphere of pressure. The solid line indicates the xenon density given by Jameson et al.[152] Reproduced from reference 80.

At 295 K, the bulk density showed a much more pronounced effect on the confined Xe chemical shift value in each FSM-16 samples. This effect was evident across the whole density range and was dependent on the pore size, with the density increasing as the pore size decreases (Figure 2.5).

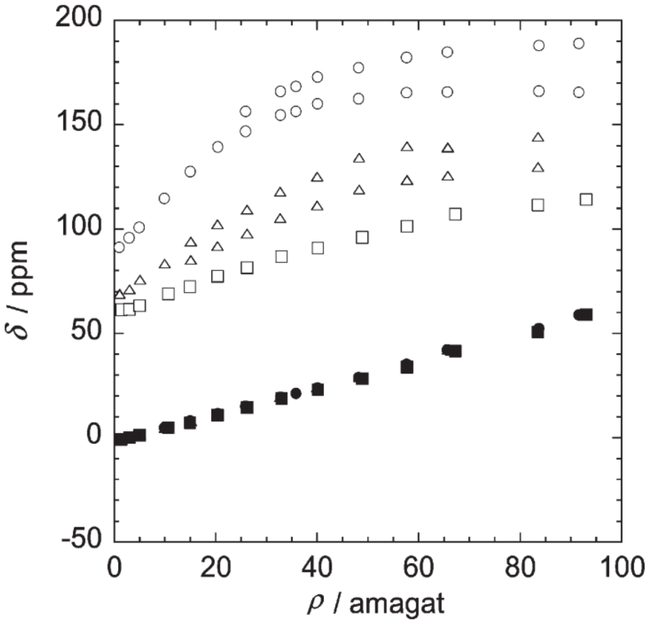

FIGURE 2.5: Density dependence (ρ) of both ^{129}Xe NMR chemical shifts in FSM-16 at 295 K with a mean pore size of 1.9 nm (●: free, ○: confined), 2.7 nm (▲: free, △: confined) and 4.1 nm (■: free, □: confined). Reproduced from reference 80.

Work carried out by Hiejima *et al.* demonstrated the use of ^{19}F NMR spectroscopy to study the phase properties of sulfur hexafluoride (SF_6) confined in Vycor glass, with a mean pore diameter of 7 nm.[151] The ^{19}F NMR spectrum is shown in Figure 2.6, with two signals arising from bulk and confined SF_6 observed. The two signals are distinguishable over a range of temperatures (290–330 K) and pressures (0–12 MPa). The occurrence of two peaks suggests that the exchange of SF_6, inside and outside of the nanopore, is a slow process.

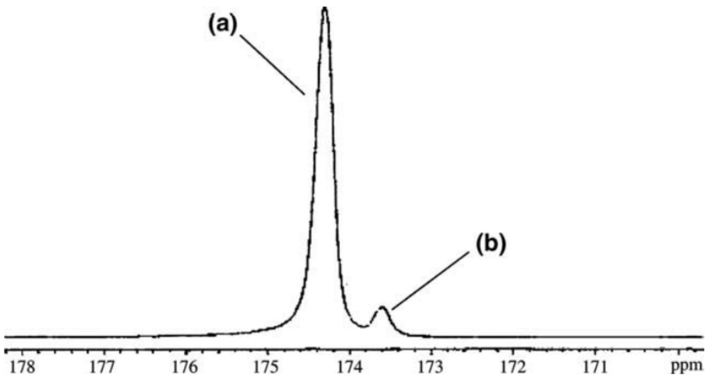

FIGURE 2.6: Typical ^{19}F NMR spectrum of SF_6 in Vycor glass at 330 K and 4.7 MPa. Two signals are observed due to (a) bulk and (b) confined SF_6. Reproduced from reference 151.

The change in the confined SF_6 NMR peak position with pressure is shown in Figure 2.7. This shows the pressure dependence of the observed chemical shift (δ_{obs}). The chemical shift for bulk SF_6 increases with pressure and sharply increases to a larger value at the bulk gas to liquid transition. However, for the confined SF_6 δ_{obs} is observed to decrease with increasing pressure at low pressures of bulk SF_6. Furthermore, the δ_{obs} for the confined SF_6 then increases with pressure gradually at higher bulk pressures and at the bulk gas to liquid transition the change in δ_{obs} is small. The small change in SF_6 chemical shift can be explained by the variation of density as it undergoes a phase transition.

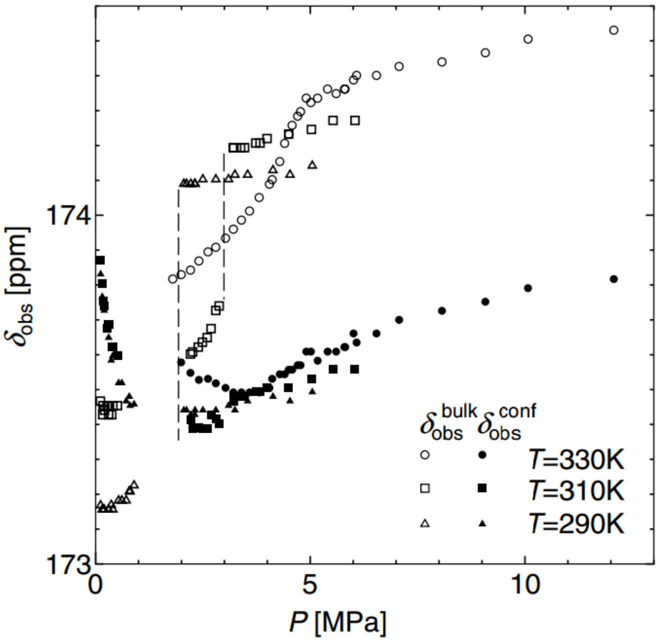

FIGURE 2.7: Pressure dependence of the observed ^{19}F NMR chemical shift for bulk (open symbols) and confined SF_6 (closed symbols) at different temperatures. Reproduced from reference 151.

To establish the density inside of the pore across a range of bulk densities, the authors use the fact that NMR signal intensity is proportional to the number of molecules in a particular chemical environment. The ratio I_{Conf}/I_{Bulk}, which is the intensity ratio of the confined and bulk ^{19}F NMR peaks, can be written as:

$$\frac{I_{Conf}}{I_{Bulk}} = \frac{N_{Conf}}{N_{Bulk}} \tag{2.3}$$

Where N_{Conf} and N_{Bulk} are the number of molecules inside and outside of the nanopore respectively. For the bulk fluid, the number of molecules is proportional to a product of the volume (V_{Bulk}) and density (d_{Bulk}). For the confined fluid, the volume of nanopore is given by ΦV_{Matrix}, where V_{Matrix} is the volume of the matrix and Φ is the volume fraction of nanopore (porosity). The mean density, d_{Conf}, in the nanopore can be simply estimated from the experimental I_{Conf}/I_{Bulk} by the following equation:

$$d_{Conf} = \frac{1}{\Phi}\frac{V_{Bulk}}{V_{Matrix}}\frac{I_{Conf}}{I_{Bulk}}d_{Bulk} \tag{2.4}$$

Where V_{Bulk}/V_{Matrix} is determined from the sample geometry.

Using this method, the calculated confined SF_6 density can be compared with the bulk density. In the gas phase, the density of the confined SF_6 increases sharply with the density of the bulk, this is ascribed to adsorption of SF_6 molecules to the wall of the Vycor Glass. At high bulk densities, the gradient of the increasing confined density becomes small and its value approaches that of the bulk in the liquid state. Above the critical temperature, a large difference is observed at 0.5 g·cm^{-3} which the authors state is in good agreement with a maximum excess adsorption observed for SF_6 on graphite by Thommes *et al* due the preference of SF_6 surface sorption.[153]

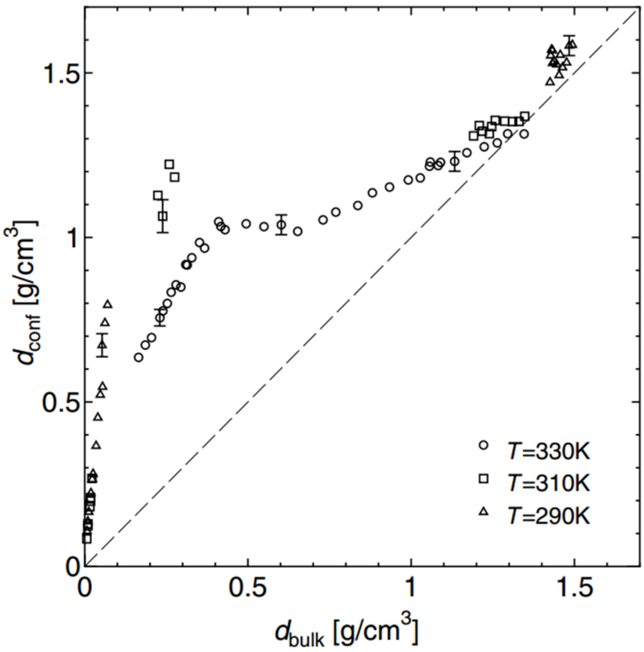

FIGURE 2.8: Mean density in nanopore as a function of bulk density for SF_6. The dashed line indicates $d_{Conf}=d_{Bulk}$. Reproduced from reference 151.

Pulsed field gradient (PFG) NMR spectroscopy has also been used to explore the behaviour of molecules in nanopores.[79] The fluid density and diffusivity of n-pentane has been measured in two porous glass materials, Vycor particles with a mean pore size of 6 nm, and ERM-FD121 with a mean pore size of 15 nm. From the diffusion spin-echo functions obtained at different temperatures using PFG-NMR, the authors were able to determine the change in the diffusivity of confined and bulk n-pentane, from which the critical temperature could be deduced. An anomalous increase in diffusivity indicted that the fluid's T_c had been reached, with a shift in T_c observed in both materials. In each case, the T_{cp} occurred at a lower temperature than for bulk n-pentane (T_c=470 K), showing that the interaction of the fluid with the pores causes criticality to occur at lower temperatures (438 K in Vycor and 458 K in ERM-FD121).

2.1.3 Gas Sorption Isotherm Studies

Gas sorption is the most widely used experimental technique to study phase behaviour in pores.[72,73,75,77,154–157] In contrast to NMR spectroscopy, gas sorption requires simpler apparatus and is not limited to compounds that have nuclear spin. However no chemical or structural information can be directly determined using this approach. Adsorption isotherms monitor both the uptake of a species into pores and its phase transition within the pore. This has allowed the thermodynamic properties of pore confined species to be more thoroughly understood.[75,154,155]

An example of a phenomenon observed through gas sorption is hysteresis (a difference in adsorption and desorption pressure). It was suspected that variations in diameter along a pore length and connectivity between different pore sizes in a material may lead to pore blocking effects and also cause hysteresis. This can be explained by the ink-bottle pore model, where the wide inner portion of the pore is filled at high relative pressures during adsorption but cannot empty during desorption due to the narrow “neck” of the pore.[158] However, hysteresis can also be observed in unconnected uniform arrays of pores where pore blocking should not be a factor and there are a number of explanations why this is the case. The independent pore model proposes that the change in shape of the pore fluid meniscus during condensation and evaporation leads to a pressure difference during the pore filling compared to the pore emptying process.[99] The meniscus takes a cylindrical shape during condensation and conversely during pore evaporation it is hemispherical, leading to a pressure difference in the phase transition during adsorption and desorption. According to the Kelvin equation this gives differing condensation and evaporation pressures because of the change in meniscus radius.

A more recent theory that has been developed to explain hysteresis is the existence of metastable fluid states within the pore.[98,100,101] During adsorption the fluid in the centre of the pore remains in the gas-like state with metastable fluid films partially wetting the walls of the pore. When the pore is sufficiently filled the metastable fluid reaches the limit of its stability and then spontaneously condenses, delaying the pore condensation during filling leading to hysteresis. The disappearance of this phenomena at a temperature significantly below the bulk fluid critical temperature has been attributed to disappearance of the difference in free energies between the gas-like state and fully condensed state of the pore confined fluid, leading to the conclusion that pore fluid is in a homogeneous phase and is therefore above the pore critical temperature. Morishige *et al.* studied the temperature dependence of the adsorption isotherms for argon, nitrogen, oxygen, ethylene, and carbon dioxide in MCM-41 with a number of different pore sizes.[72,156] This was in order to determine the critical temperature of the confined species and study any related phenomena. This work determined the temperature at which hysteresis disappeared for these species, referred to as the hysteresis critical temperature (T_{ch}), and again this was found to occur far below the bulk critical temperature (Figure 2.9).[72]

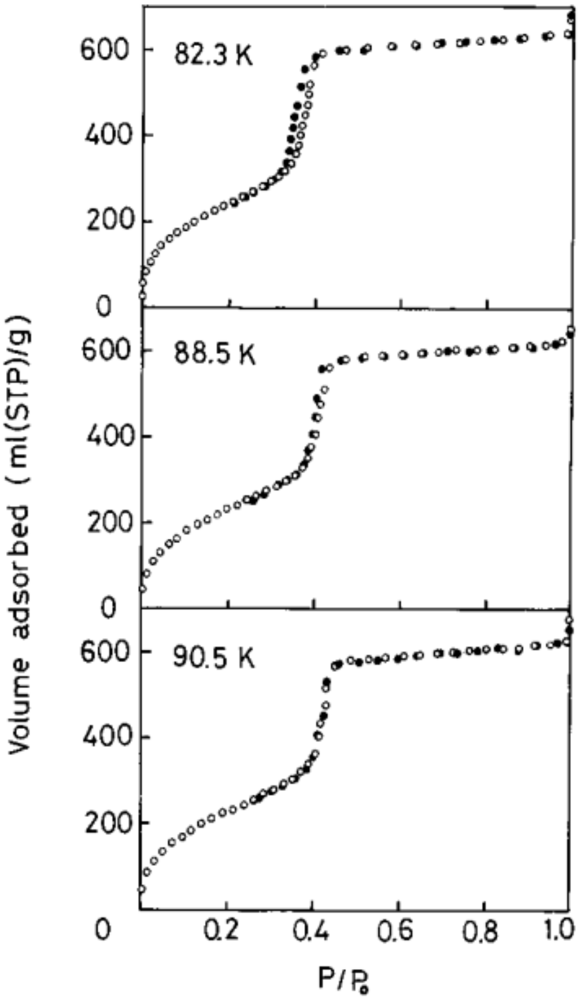

FIGURE 2.9: Sorption isotherms of oxygen in MCM-41 with an average pore size of 1.8 nm. Open circles denote adsorption. Solid circles denote desorption. Note the disappearance of the pressure difference in adsorption and desorption as the system approaches the hysteresis critical temperature. Reproduced from reference 72.

The actual T_{cp} was determined in other studies.[73,74] The T_{cp} is defined as the disappearance of the vertical jump in adsorption when monitored with pressure associated with pore condensation and therefore, the disappearance of the first order phase transition of the confined species (see Figure 2.10). This is supported by theoretical studies which show that the T_{ch} and the T_{cp} are not the same.[96]

Although T$_{ch}$ was wrongly thought to be the pore critical temperature for some time, it has been shown to be an artefact of the pore confined metastable states disappearing. Also at the T$_{ch}$ the pore fluid does not exhibit the other properties of criticality, such as a continuous phase transition. Hysteresis can therefore disappear at temperatures below T$_{cp}$, as the thermal energy required for the local minimum of free energy of the metastable state would be smaller than that required for all of the pore fluid to be above its critical temperature. The T$_{cp}$ is therefore the temperature at which the pore confined species undergoes a continuous second order phase transition, resulting in a non vertical increase in the order parameter, which in this case is the amount of species adsorbed into the pore.[73,74]

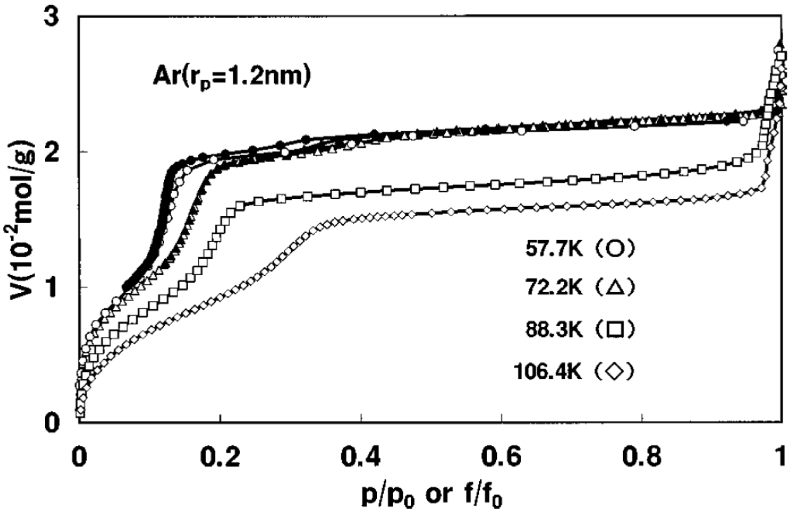

FIGURE 2.10: Temperature dependence of Ar adsorption isotherms in MCM-41 with a mean pore diameter of 1.2 nm. The isotherms at 57.7 and 72.2 K are plotted against relative pressure (p/p$_o$) while those at 88.3 and 106.4 K are plotted against relative fugacity (f/f$_o$). Desorption points are expressed by closed symbols. Reproduced from reference 73.

In order to determine the pore critical temperature, the authors studied the inverse of the gradient of the pore condensation with temperature. A steep change in this value indicates the point where the majority of the pores within the sample are above their critical temperature for a given fluid. This allowed for the determination of the temperature at which the first order gas to liquid phase transition becomes a second order gas to supercritical fluid phase transition within the pore, as shown in Figure 2.11.

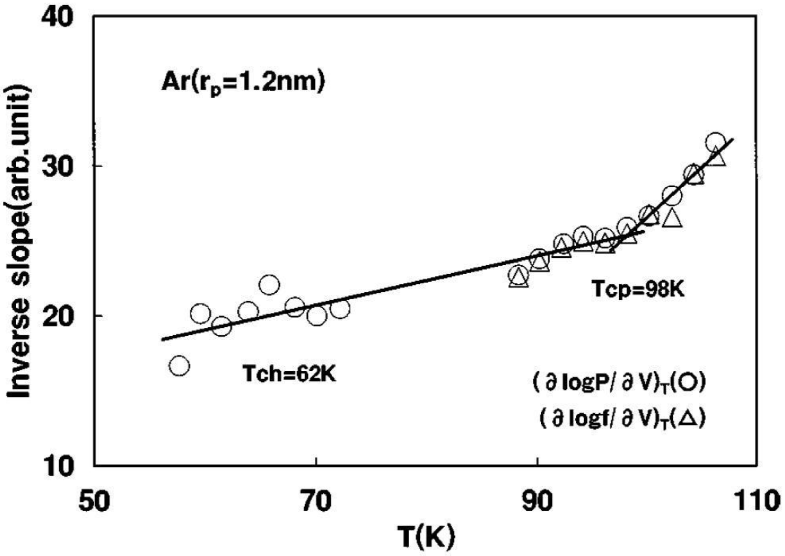

FIGURE 2.11: Temperature dependence of the inverse slope of the argon adsorption jump associated with capillary condensation, within MCM-41 with a mean pore diameter of 2.4 nm. Reproduced from reference 73.

Hexafluoroethane adsorption isotherms have been studied in MCM-41 silica with a mean radius of 2.6 nm (5.2 nm diameter) by Manchin.[157] Again it was observed that capillary condensation resembles a first order process below the pore critical temperature, which proceeds to a second order transition at temperatures above the pore critical temperature. Importantly the magnitude of the pore condensation step (phase transition) was found to decrease above the pore critical temperature resulting in a smaller density value. The critical temperature of hexafluoroethane in MCM-41 was shown to be 255 K, a depression of *ca.* 38 Kelvin compared to the bulk value.

Another example of gas sorption studies being used to determine critical parameters is the isochoric (constant volume) desorption of SF_6 measured in silica pores by Thommes *et al.*[77] SF_6 was removed from the pore with increasing temperature, resulting in a sharp decrease in desorption, a process which is first order in nature as capillary evaporation occurs. This shows that the desorption was taking place in a temperature range below the T_{cp}. It was found that the capillary evaporation takes a continuous second order form above the pore critical temperature. This process exhibits a large decrease in density below the pore critical temperature, with a smaller decrease found above the critical temperature.

The gas sorption studies that have investigated T_{cp} and T_{ch} as a function of pore diameter have suggested that the relationship between the change in critical temperature of a pore confined fluid (T_c-T_{cp}) is linear with respect to the inverse of the pore diameter.[72,73,77,156] These results are in line with previous predictions that are derived from from a simple slab approximation and scaling theory.[85,139–141] However only a small range of fluids have been studied in these experiments. Also as previously mentioned the mathematical predictions rely on simplified models or approximations. An example of which is the assumption that the pore wall adsorbed liquid slab and its bulk counterpart are analogous.[102,142]

2.1.4 Densimetry

Another simple approach of examining phase behaviour of confined fluids is through the use of vibrating tube densimetry (VTD). Gruszkiewicz and co-workers used this technique to study the density of both subcritical and supercritical propane and CO_2 in silica aerogels.[159] The principle of VTD is the linear dependence between the square of a cantilever vibration period and the density of the sample attached, which can be calibrated. Therefore this principle makes the interpretation of the data very simple. This study provides experimental evidence that the average density of the confined liquid-like phase can exceed the density of normal bulk liquid significantly, even if fluid-solid interactions are relatively weak within the pores. An estimated 1.7 K depression in the T_c of the confined C_3H_8 relative to the bulk was reported. The adsorption isotherm showed an enhanced density compared to the bulk under equivalent conditions calculated from the equation of state, as shown in Figure 2.12. The isotherm shape also allowed for the prediction of the confined C_3H_8 T_{cp}, becoming smooth and continuous as the critical temperature was approached.

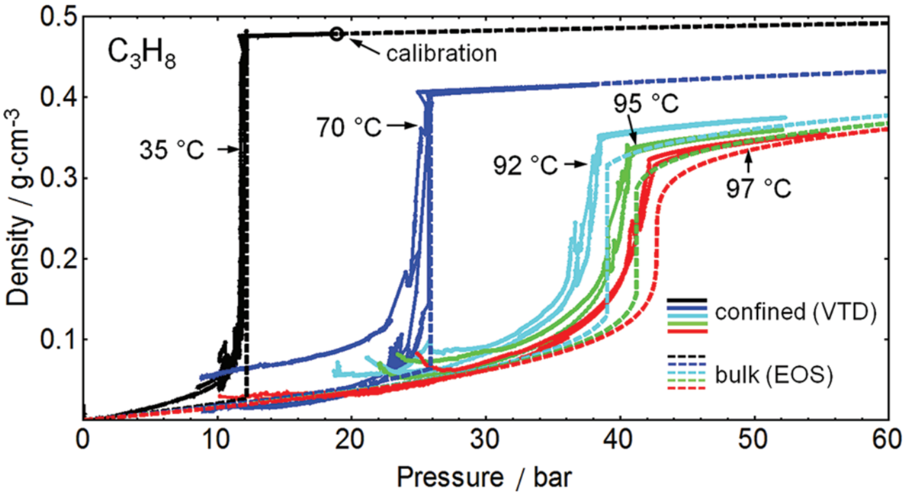

FIGURE 2.12: Subcritical (35, 70, 92, and 95 °C) and supercritical (97 °C) isotherms of confined fluid density for propane in silica aerogel compared to the bulk C_3H_8 equation of state (EOS). Reproduced from reference 159.

As with gas sorption, there are limitations when using VTD to study confined fluids. This technique provides no chemical or structural information relating to the pore confined fluid, therefore insight into the fundamental behaviour of the pore fluid molecules cannot be elucidated using this methodology.

2.1.5 Infrared Spectroscopic Studies

Infrared spectroscopic measurements of fluids in pores have also been attempted.[115,160,161] These measurements provide a quick methodology to assess the phase characteristics of a confined fluid and are not only sensitive to the chemical environment of a pore, but also relatively simple to carry out experimentally. Despite these benefits, as measurements are preformed with highly absorbing solid state porous templates and dense confined fluids, it can be difficult to conduct infrared transmission studies. Therefore attenuated total reflectance Fourier transform infrared spectroscopy (ATR-FTIR) is a more convenient method to study confined fluids. This is because the technique does not rely on the transmission of light and the penetration of the radiation into the sample is small, lowering the overall absorbance from the sample. However, because of this ATR-FTIR is not as sensitive as infrared transmission spectroscopy. ATR-FTIR has been utilised by Baiker and co-workers to investigate the adsorption and phase behaviour of CO_2 in mesoporous silica in a range pore of diameters.[115] These measurements used the single-beam-sample-reference (SBSR) technique to subtract interfering signals of the bulk phase, allowing the observed signals to be attributed either to the pore fluid or the bulk phase. The authors first measured the relationship between the bulk fluid density and the peak shift of the $\nu 2$ vibrational band of CO_2 ($\sim$ 665 cm^{-1}), as shown in Figure 2.13. The change in peak position which occurs with increasing pressure (and density) can be used to estimate the fluid density inside the pores.

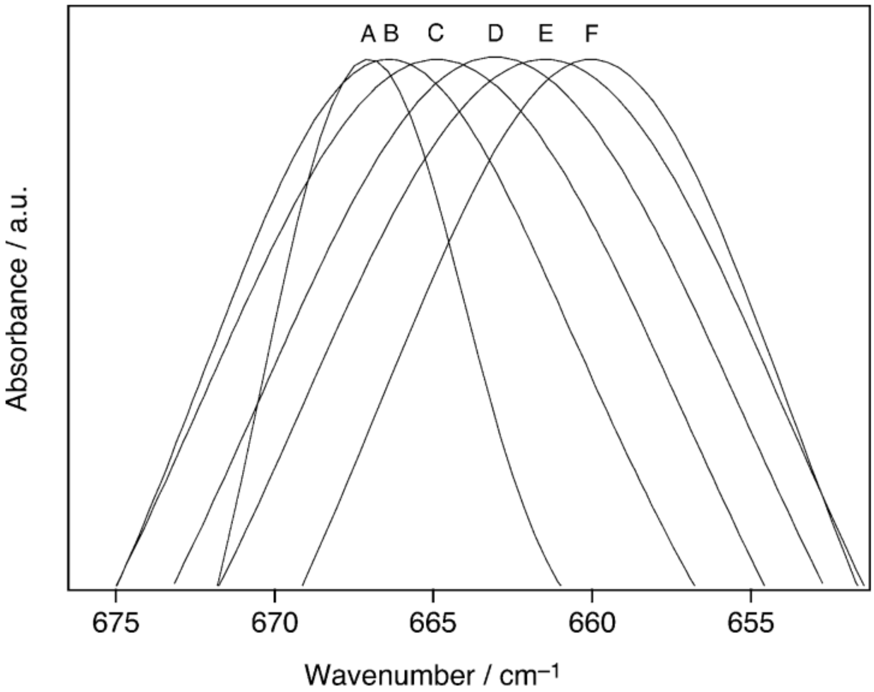

FIGURE 2.13: Shift of the normalised $\nu2$ band maximum of carbon dioxide with at the following density:(A) 37, (B) 142, (C) 208, (D) 526, (E) 588, and (F) 775 kg m^{-3}. Reproduced from reference 115.

The conclusion of this study is that at all temperatures and pressures investigated, even under bulk supercritical conditions, the pore fluid density was higher than in the bulk. By subtracting bulk reference spectra and studying the absorbance of the confined CO_2 $\nu2$ vibrational band, absorption isotherms could be constructed (see Figure 2.14). The shape of the isotherm displayed a smoother transition for the confined CO_2 suggesting that the confined fluid behaved as a supercritical fluid under bulk subcritical conditions. In the case of SI1402 type silica, the pore diameter distribution ranged from 4 to 12 nm, with a mean pore size of 10 nm. The pore T_c was determined to lie between 294 and 298 K. The large pore size distribution was reflected in the shape of the isotherms, showing a smoother phase transition when compared to the other materials with small pore size distributions.

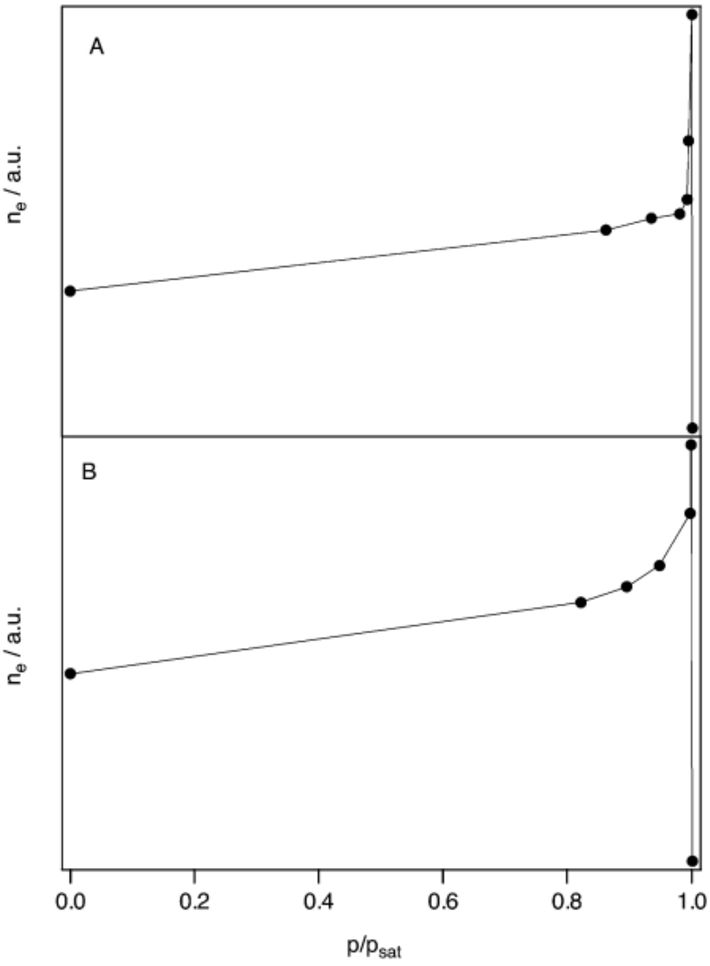

Figure 2.14: Adsorption isotherms of carbon dioxide in mesoporous silica with pore diameters of (A) 2 nm and (B) 14.5 nm, calculated from the integration of the difference bands at 660 cm^{-1}. Measured at 294 and 298 K respectively. The lines are to guide the eye. Reproduced from reference 115.

2.1.6 Summary

The extent of the critical temperature shift of a pore confined fluid depends on a number of factors. The primary factor is the pore size, with the smallest of pore sizes having the greatest effect on T_c as predicted by Fisher and Nakanishi (see Table 2.1).[85,139] No experimental studies have thoroughly investigated the influence of pore-fluid interaction strength and the part that this plays in the extent of the T_c depression. However it is clear from the theoretical studies that this plays a significant role. The pore-fluid interaction strength will depend on the adsorbent, pore wall structure and its chemical composition, as well as the adsorbate.

TABLE 2.1: A summary of observed critical temperature for confined fluids, relative to the bulk critical temperature.

Pore Size (nm)	Pore Type	Fluid	Δ T_c (K)	Method	Ref
2.4	MCM-41	CO_2	-91.2	Isothermal	73
		N_2	-39.2	Isothermal	73
		O_2	-52.8	Isothermal	73
		Ar	-52.7	Isothermal	73
		C_2H_4	-98.3	Isothermal	73
4	Vycor Glass	CO_2	-45	Isothermal	75
5.2	MCM-41	C_2F_6	-38	Isothermal	157
6	Silica Gel	*n*-pentane	-32	PFG–NMR	79
10	Borosilicate Glass	O_2	-5.3	Isothermal	76
		Xe	-12.7	Isothermal	76
		SF_6	-13.7	Isothermal	76
15	Silica Gel	*n*-pentane	-12	PFG–NMR	79
24		SF_6	-1.3	Isothermal	77
31	Sodium Borosilicate Glass	SF_6	-0.9	Isothermal	77

2.1.7 Aims

The aim of the work described in this Chapter is to use near-infrared spectroscopy to examine the critical temperature of fluids such as carbon dioxide and difluoromethane confined in porous ordered materials, with mean pore diameters ranging from 3.2–100 nm. This is in order to ascertain the relationship between pore size and critical temperature, and the effect of the pore adsorbed fluid on this relationship. This will lead to a firmer understanding of this behaviour for the confined fluids that are commonly used in supercritical fluid electrodeposition,[33,34] gas storage,[67]and extraction processes,[69] in this case carbon dioxide and difluoromethane. Finally this Chapter seeks to gain an understanding of the importance of the fluid-wall potential in the suppression of a confined fluid's critical temperature. This will be achieved *via* the analysis of pore confined ethane and the extent of the depression in its critical temperature. Ethane is a non-polar molecule and has a low dielectric constant,[10,162] suggesting the coulombic interaction strength with the pore walls will be weak, or the interactions with their functional groups may be unfavourable.

2.2 Results and discussion

2.2.1 Near-Infrared Spectrocopic Study of Phase Transitions to Determine Critical Temperature

The near-infrared (NIR) absorbance of a pure substance is proportional to its density and follows the Beer-Lambert law.[163] The assessment of a substances density using NIR absorption bands has been explored in the literature,[111,123,164] with only slight deviations from a linear relationship between density and absorbance at very dense and hot states. This deviation occurs because of repulsion between molecules and the occurrence of hidden or overlapping hot bands that need to be accounted for at high temperatures. The absorbance versus pressure plot adopts a characteristic shape depending on whether the substance is undergoing a phase transition from gas to liquid, where it displays a sharp increase in density and therefore absorbance (Figure 2.15 **Top**), or gas to supercritical fluid, displaying a smoother increase in density, and therefore absorbance (Figure 2.15 **Bottom**). At lower densities of the substance, rotational envelopes can be observed (Blue, Figure 2.15), for example, the prominent R and P branches of the gas phase CO_2 which are clearly visible.[165] These envelopes coalesce at higher densities when the substance has undergone a phase transition (Red). This is due to hindered rotation of the molecules.[111]

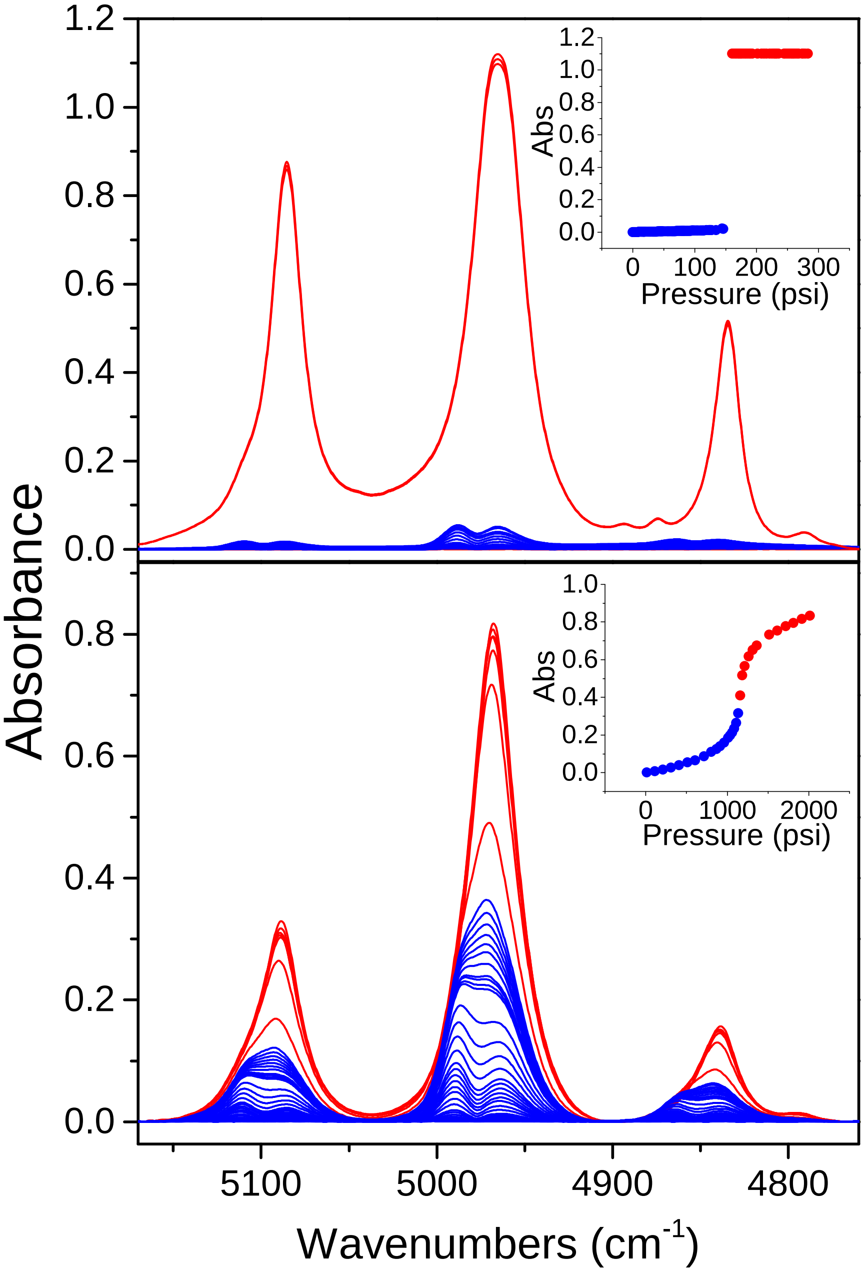

FIGURE 2.15: Near-infrared FTIR spectra of CO_2 recorded using the high-pressure-low-temperature (HPLT) cell, at increasing pressures, displaying the three absorbances of the Fermi triad centred at *ca.* 5000 cm^{-1},[111] below its T_c at 253 K **(Top)** and above its T_c at 305 K **(Bottom)**. The **Inset** demonstrates how the absorbance of the central $\nu_1 + 2\nu_2 + \nu_3$ band changes with pressure and during the phase transition.

This relationship means the phase transition and phase behaviour of CO_2 can be monitored by studying its NIR absorbance as a function of pressure at a set temperature (Figure 2.16). This provides a good indication as to whether a substance is above or below its critical temperature and demonstrates the move from a first order discontinuous to a second order continuous phase transition as the critical boundary is crossed.[9]

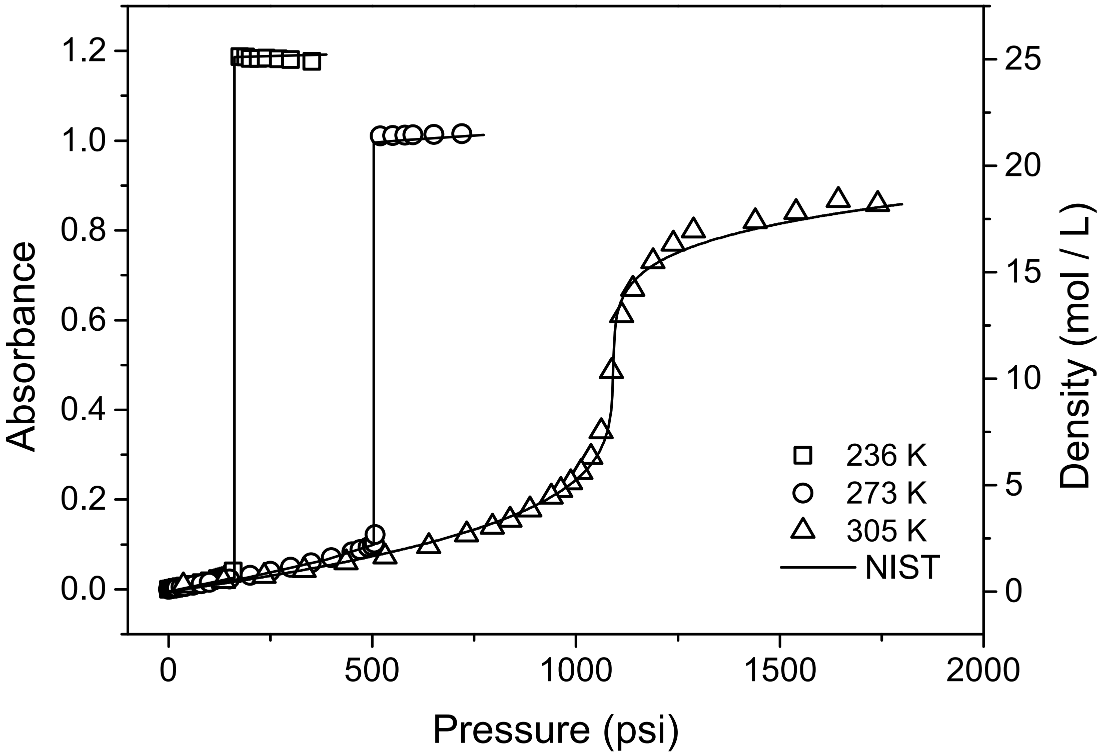

FIGURE 2.16: Near-infrared absorbance of CO_2 Fermi triad central $\nu_1 + 2\nu_2 + \nu_3$ band,[111] as a function of pressure below its T_c at 236 and 273 K or above its T_c at 305 K. This data is compared to the change in density of CO_2 with pressure taken from NIST database.[10]

2.2.2 Studying the Phase Behaviour of a Confined Substance Using Near-Infrared Spectroscopy

In order to examine the phase behaviour of substances in pores the following approach is taken. The porous material is placed into the HPLT (high-pressure-low-temperature) cell, described in Chapter 6 and the thickness of the material is measured (see Figure 2.17).

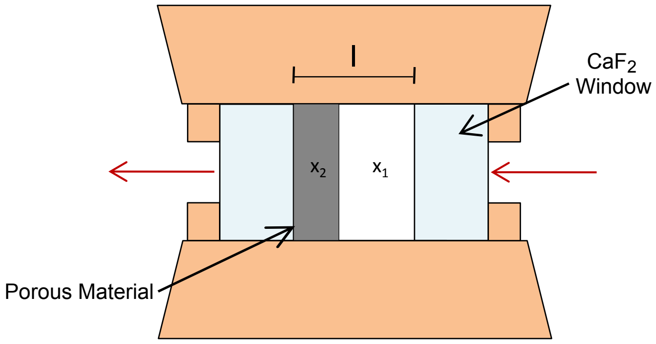

FIGURE 2.17: A diagram of the path taken by the NIR beam through the HPLT cell, where x_1 is the path length of the cell that remains empty, x_2 represents the thickness of the porous material layer in the cell and l is the overall path length of the cell.

The NIR absorbance versus pressure relationship in the presence of the porous material is expected to differ greatly from the measurements taken of the pure substance. The plot would contain both confined and bulk substance information, due to the fact that the bulk substance will be present in the space not occupied by the porous material in the cell. A plot of absorbance against pressure demonstrates how both the confined and bulk substances' absorbance changes with pressure, as shown in Figure 2.18. There are three important features demonstrated in such a plot. Firstly, in the presence of the porous material there is a linear increase in absorbance with a greater magnitude than that of the bulk at low pressures, indicating initial CO_2 adsorption into the pore. Secondly, there is a large increase in absorbance with pressure indicating a phase transition is taking place within the pores (Figure 2.18 *ca.* 200 psi). This is clearly observed as the magnitude of the absorbance and therefore density of the confined fluid is many times greater than the corresponding bulk gas phase, at equivalent pressures. Thirdly, the bulk phase transition can be observed at a higher pressure showing the distinctive sharp gas to liquid increase in absorbance (and therefore density), as shown in Figure 2.18) at *ca.* 380 psi. This is to be expected as at these relatively low temperatures (*e.g.* 260 K) the bulk CO_2 would be far below its critical temperature.

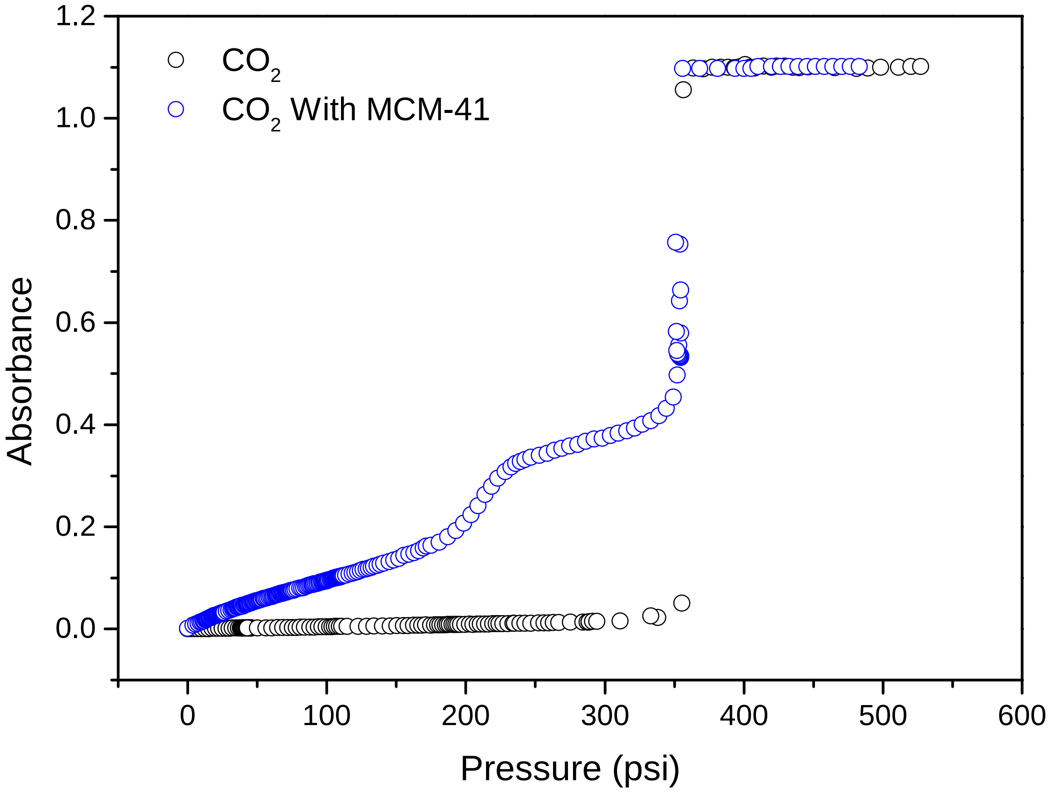

FIGURE 2.18: A plot constructed from the near-infrared absorbance of CO_2 as a function of pressure (Black) and in the presence of 3.2 nm pore size MCM-41 silica (Blue), both at 260 K.

In order to confirm that this is the observation of the confined fluid's behaviour, the proportion of absorbance contributed by the bulk is then subtracted from the spectra in the presence of the porous material, leaving the absorbance of the confined substance. The thickness of the porous material layer is known (x_2) along with the cell path length (l), therefore the proportion of the absorbance contributed by the bulk (x_1) can be accurately subtracted (Figure 2.17).

x_1 is given by:

$$x_1 = l - x_2 \tag{2.5}$$

and the absorbance of the confined fluid is given by:

$$abs_{Confined} = abs_{(x_1+x_2)} - x_1 \times (abs_{Bulk}) \tag{2.6}$$

The subtraction is performed on spectra taken at equivalent pressures of the bulk substance alone, as shown in Figure 2.20.

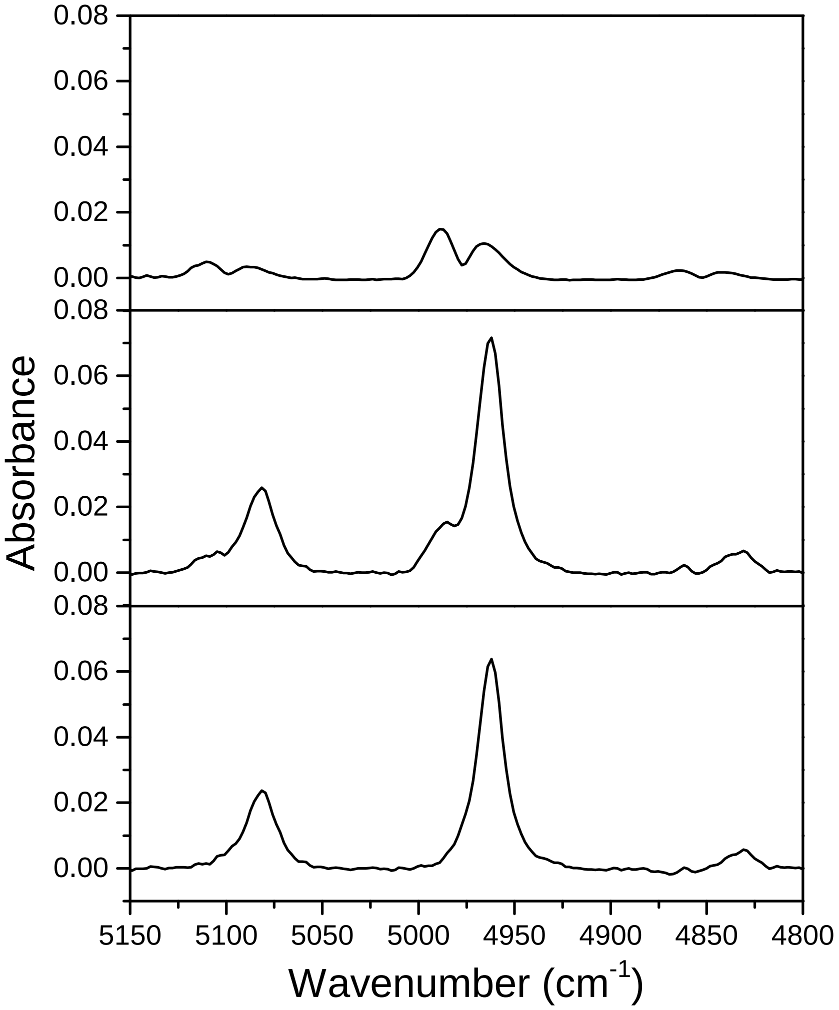

FIGURE 2.19: **(Top)** Near-infrared absorbance of bulk CO_2 at 100 psi at 260 K. **(Middle)** The near-infrared absorbance of CO_2 and MCM-41 (3.2 nm pore diameter) under the same conditions. **(Bottom)** The resulting spectrum of CO_2 confined in the MCM-41 after subtracting the bulk contribution.

Marked differences can be seen when compared with spectra of the pure CO_2. Even under bulk subcritical conditions the gas phase rotational envelopes, that are usually observed at the lower pressures of CO_2, are coalesced. This suggests the confined CO_2 is rotationally hindered and adsorbed. By preforming the subtraction described previously and plotting the confined fluid absorbance against pressure, the phase transition of the confined substance is confirmed. The bulk phase transition in this plot is subtracted and the pressure region of the plot where this was observed previously remains at a constant absorbance, similar to the condensed pore fluid. This shows that this behaviour is due to the confined substance and its phase behaviour, therefore the information observed is akin to that of an adsorption isotherm measured spectroscopically, as shown in Figure 2.20. This demonstrates that the isotherms obtained can then be examined to determine the species critical temperature in a particular pore diameter.

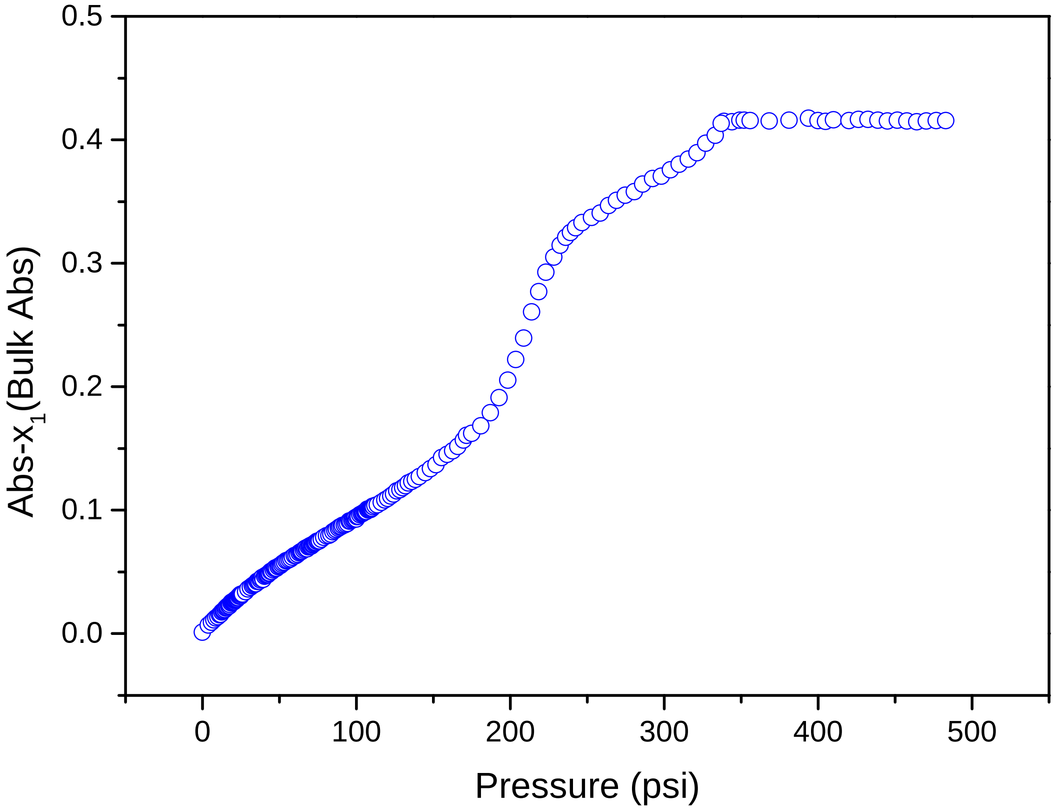

FIGURE 2.20: A plot constructed by subtracting the bulk near-infrared absorbance of CO_2 from those in the presence of 3.2 nm silica at 260 K. The confined species absorbance is plotted to produce an adsorption isotherm. This required multiple experimental runs to obtain enough spectra of the bulk and the confined fluid at equivalent pressures.

Both carbon dioxide and difluoromethane were chosen to investigate the effect of confinement on their critical temperature and how this changes with pore size. They were selected because they are both important and are used in current confined fluid applications.[33,34,67,69] As previously stated in Chapter 1, CO_2 storage in porous geological structures is a growing method of carbon capture and storage, but CO_2 has also been used together with an acetonitrile co-solvent in supercritical fluid electrodeposition, as has CH_2F_2. The two molecules also differ greatly in their physical properties, with differences in shape, size, relative permittivity and polarity. They also have vastly different thermophysical properties with a large difference in T_c, P_c, and condensation pressure.[10] By studying the critical parameters of these fluids in confinement, we aim to establish a greater insight into their phase behaviour under the conditions present during supercritical fluid electrodeoposition, gas storage and confined catalysis.

To directly compare the confined fluid density at different temperatures, the ratio of the CO_2 absorbance at 4950 cm^{-1} or the CH_2F_2 absorbance at *ca.* 4500 cm^{-1}, to the silica band (2νOH) at *ca.* 7300 cm^{-1} (Absorbance **(B)** Figure 2.21), are plotted against pressure for experiments carried out at a number of different temperatures. This allows the silica band at *ca.* 7320 cm^{-1} to be used as an internal standard to rule out any effect on the NIR absorbance of the CO_2 or CH_2F_2 band caused by inconsistent amounts of the silica sample present in different experiments, allowing the confined fluid absorbance to be studied at a range of temperatures to determine the T_{cp}. These bands were selected due to their high relative intensities and low degree of overlap with other bands from the species or from the other compounds present.

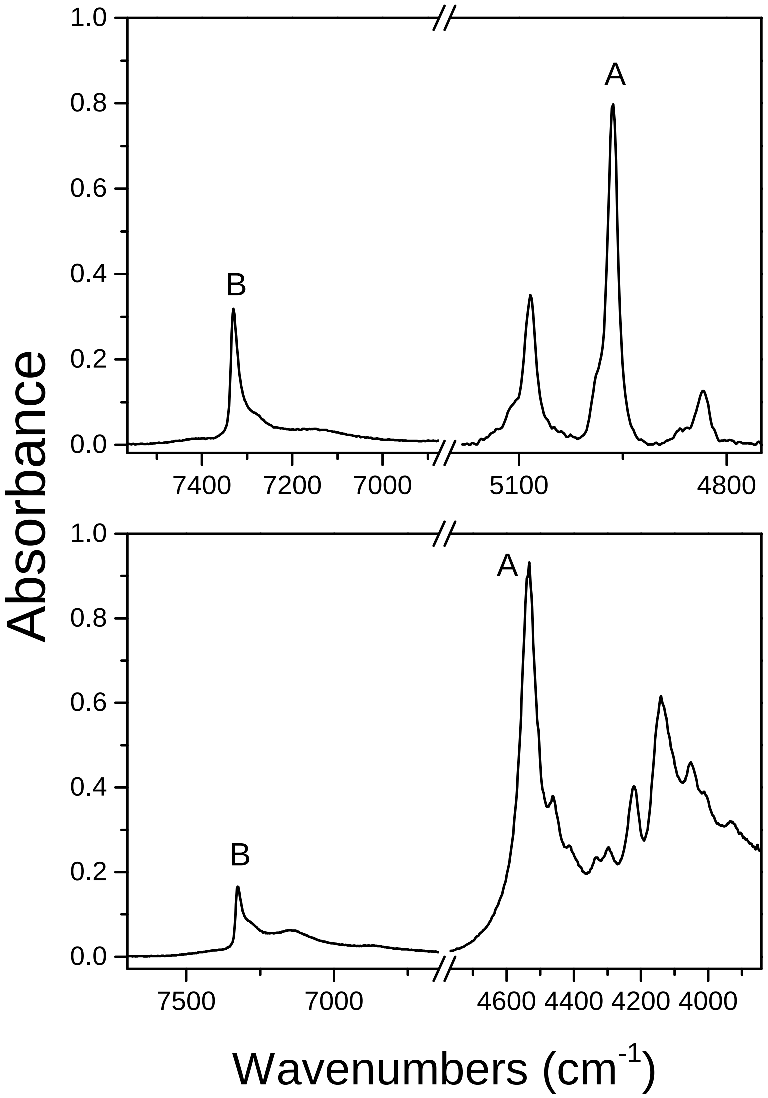

FIGURE 2.21: **(Top)** NIR spectrum showing **(A)** the $\nu_1 + 2\nu_2 + \nu_3$ CO_2 combination band[111] and **(B)** the Silanol (Si–OH) 2ν stretching overtone of the silica[166] that the absorbance is scaled to. **(Bottom)** NIR spectrum showing **(A)** CH_2F_2 ν_2+ν_6 combination band[167] and **(B)** the 2ν stretching overtone of the silica that the absorbance is scaled to.

The plots of Abs_{Fluid} / $\text{Abs}_{Material}$ as a function of pressure have the same characteristics as described before for the pure fluid, showing a sharp phase transition from gas to liquid at low temperatures and a smooth transition from gas to supercritical fluid at higher temperatures (Figure 2.22 **(1)**). In order to determine the critical temperature of the confined fluid, the Abs_{Fluid} / $\text{Abs}_{Material}$ value after the phase transition (Starred Point, Figure 2.22 **(1)**), was plotted against the temperature to generate Figure 2.22 **(2)**. The density of the condensed fluid goes through a rapid decrease near T_{cp}, as indicated by the sharp decrease in the Abs_{Fluid} / $\text{Abs}_{Material}$ value (*ca.* 213 K in Figure 2.22 **(2)**), this is due to the disappearance of true capillary condensation.[157] By inverting the ratio and calculating the first derivative of the sigmoidal fit of the data, the temperature where there is the fastest change in density and therefore the mean critical temperature of the confined CO_2 in MCM-41 (3.5 nm) was determined as 213 K, which is the maximum of the distribution obtained, as shown in Figure 2.22 **(4)**.

All the materials used have an intrinsic distribution of pore sizes, resulting in a range of pore critical parameters *e.g.* T_{cp} and pore critical pressure (P_{cp}). Pores of different sizes depress the fluid's T_c point to different extents when the fluid is confined in these materials. Therefore the T_{cp} point will be extended to a T_{cp} range. This range is affected by the pore size distribution in the materials and is indicated by the full width at half maximum (FWHM) of the distribution calculated from the first derivative of the fitted $\text{Abs}_{Material}$ / Abs_{Fluid} against temperature plot. The wider the derivative band, the broader range of T_{cp}, which indicates a wider pore size distribution of the material.

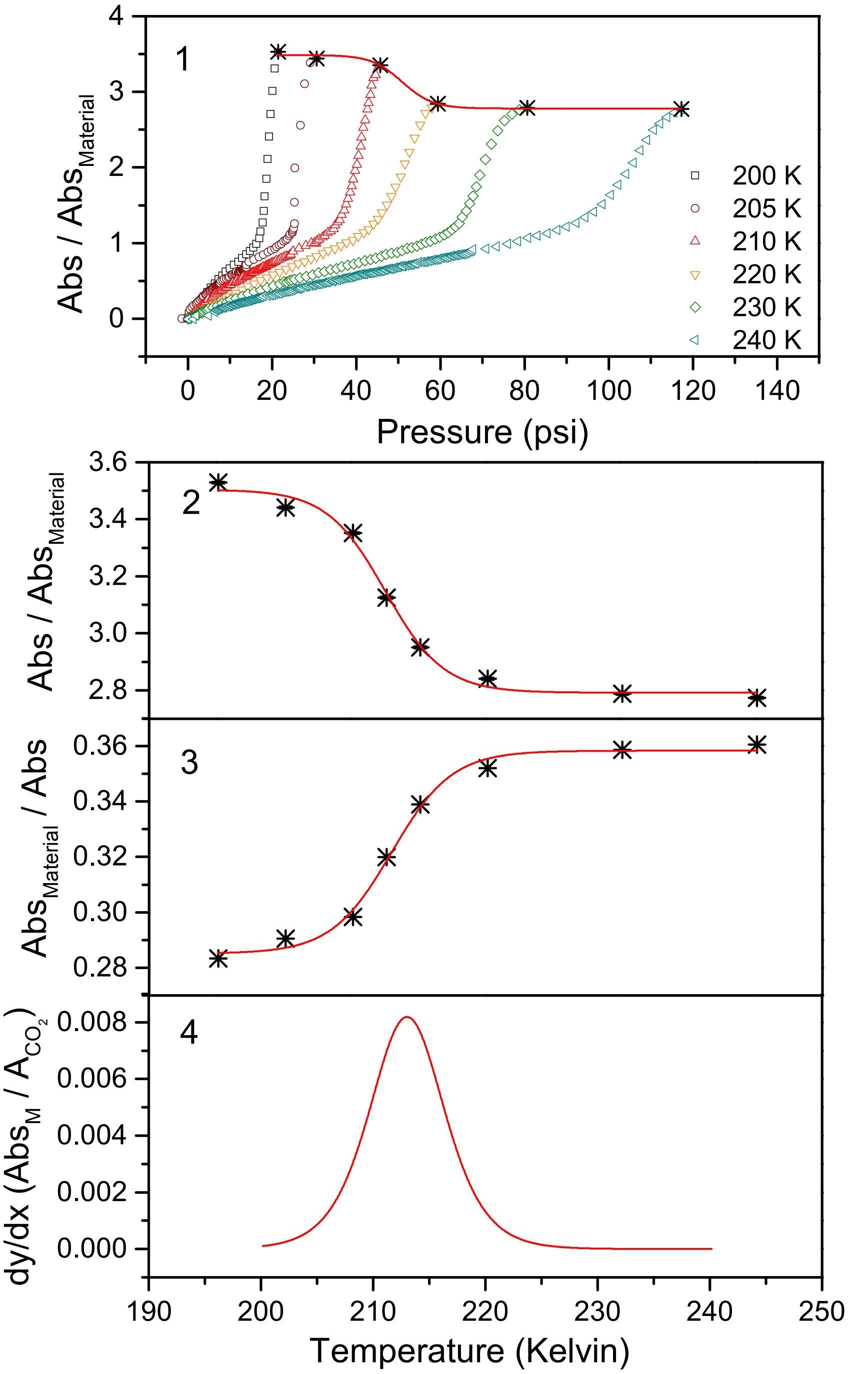

FIGURE 2.22: **(1):** A plot of the ratio between the CO_2 $\nu_1+2\nu_2+\nu_3$ absorbance and 3.5 nm MCM-41 silica 2νOH absorbance against pressure at different temperatures. Some plots are not shown for clarity. The starred point is the ratio of the absorbance after the confined CO_2 has undergone its phase transition. **(2):** The ratio of CO_2 $\nu_1+2\nu_2+\nu_3$ absorbance and 3.5 nm MCM-41 silica 2νOH absorbance against pressure at different temperatures fitted with a sigmoidal growth curve. **(3):** The inverse of **(2)** allowing it to be fitted with a positive sigmoidal growth curve **(4):** The first derivative of the positive sigmoidal curve fit of graph 3, the maximum position shows the mean T_{cp} of the fluid confined in the material.

2.2.3 The Pore Critical Temperature of Carbon Dioxide and Difluoromethane Confined in Mesoporous Silica

Figure 2.23 displays NIR spectra of CO_2 at 220 K with increasing pressure in the presence of 3.5 nm pore diameter MCM-41. The silica surface hydroxyl absorbance is visible in the near-infrared region. This is assigned as the second overtone of the O–H stretch (2νOH) at *ca.* 7300 cm^{-1} (Figure 2.23 **B**).[166] The O–H stretch at *ca.* 7300 cm^{-1} shifts to *ca.* 7125 cm^{-1} and broadens in appearance upon the addition of CO_2. This is due to CO_2 binding to the surface of the silica (**C** Figure 2.23).[160]

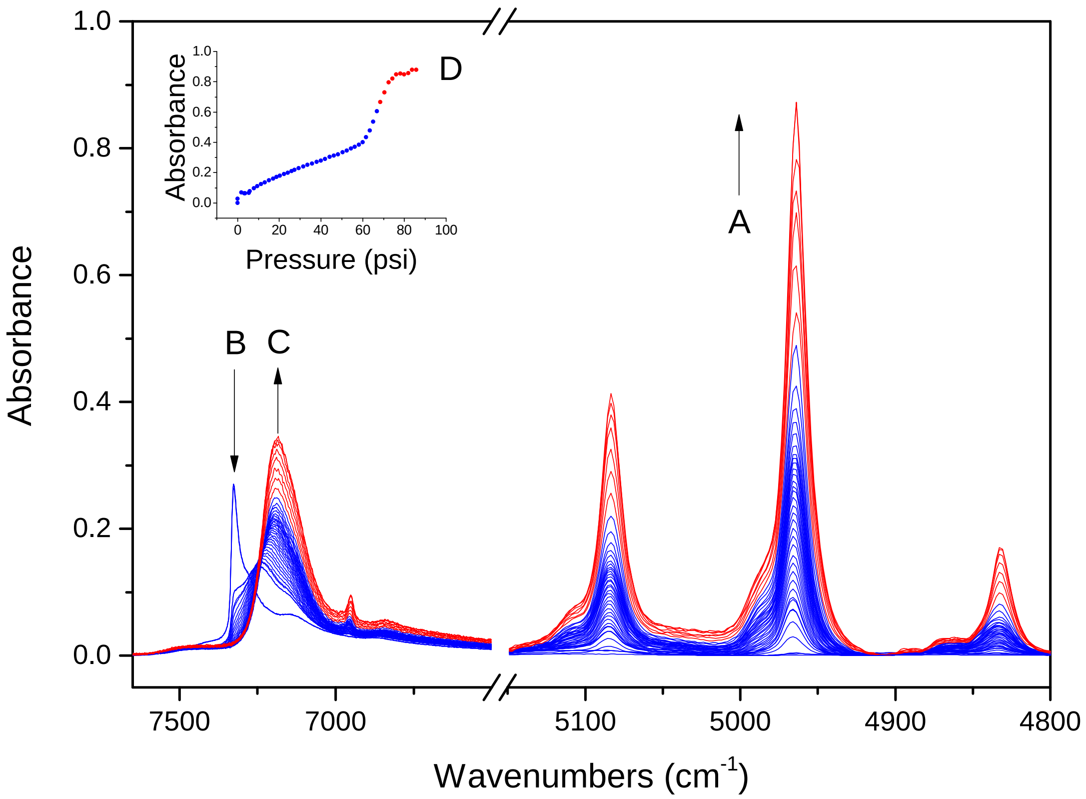

FIGURE 2.23: Examples of CO_2 spectra in the presence of 3.5 nm MCM-41, at 220 K. These spectra are taken at increasing intervals of pressure and show the Fermi triad[111] **(A)**, the silica hydroxyl overtone bands **(B)** and the broadened hydroxyl absorbance due to interactions with the CO_2 **(C)**. **Inset**: A plot showing the change of absorbance of the central $\nu_1 + 2\nu_2 + \nu_3$ band of the Fermi triad with pressure, **(D)** shows the confined fluid's absorbance after it has undergone a phase transition in the pores.

Figure 2.24 displays the NIR spectra of CH_2F_2 confined in 3.5 nm pore diameter MCM-41, with increasing intervals of CH_2F_2 pressure at a temperature of 220 K. Again there are differences when compared to spectra of the bulk CH_2F_2. The spectral features are coalesced compared to their bulk counterparts suggesting the confined CH_2F_2 is rotationally hindered. The silica hydroxyl band is again observed at *ca.* 7300 cm^{-1} and is seen to broaden and shift with the addition of CH_2F_2 pressure.

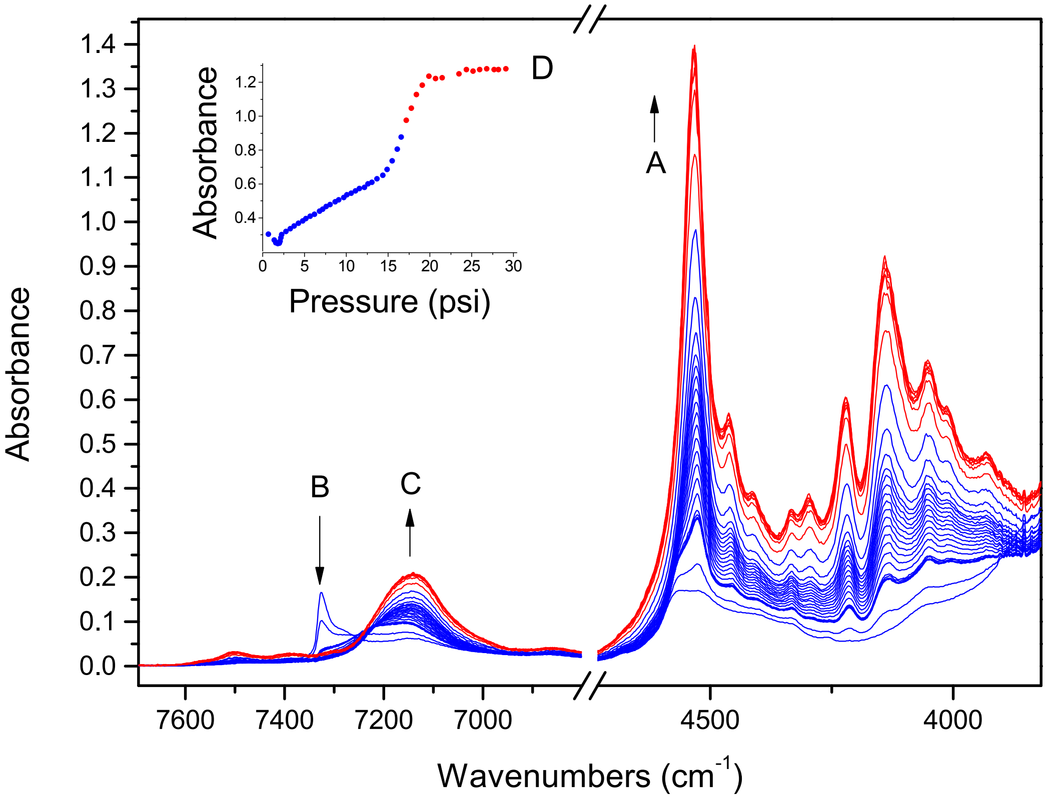

FIGURE 2.24: Examples of CH_2F_2 spectra in the presence of 3.5 nm MCM-41, at 220 K. These spectra are taken at increasing intervals of pressure, showing the CH_2F_2 combination bands **(A)**, the silica hydroxly overtone bands **(B)** and the broadened hydroxyl absorbance due to interactions with the CO_2 **(C)**. **Inset**: A plot showing the change of absorbance of the $\nu_2+\nu_6$ [167] combination band **(A)** of CH_2F_2 with pressure, **(D)** shows the confined fluid's absorbance after it has undergone a phase transition in the pores.

As discussed in the previous section, the change in absorbance measured as a function of pressure allows the observation of the phase transition within the silica templates. The characteristic gas to liquid phase transition is observed at lower temperatures within the pores, becoming a gas to supercritical fluid phase transition as the temperature increases, for example between 200–210 K, for CO_2 confined in 3.2 nm MCM-41 (Figure 2.25 (**1**)) and 213–233 K for CH_2F_2 (Figure 2.26 **(1)**). Further studies were carried out on a range of silica templates with pore sizes between 3.2–8.3 nm, all of which exhibit similar phenomena. The adsorption and pore confined condensation of the CO_2 and CH_2F_2 in the MCM-41 type silica resembles that of a type IV adsorption isotherm defined by IUPAC, which has characteristic features of condensation taking place in mesopores.[97] The initial large increase in adsorption of the Type IV isotherm is attributed to monolayer-multilayer adsorption into the pore. It is akin to adsorption on a non-porous surface. This is then followed by a large adsorption step due to pore condensation at a pressure significantly below the bulk condensation pressure.

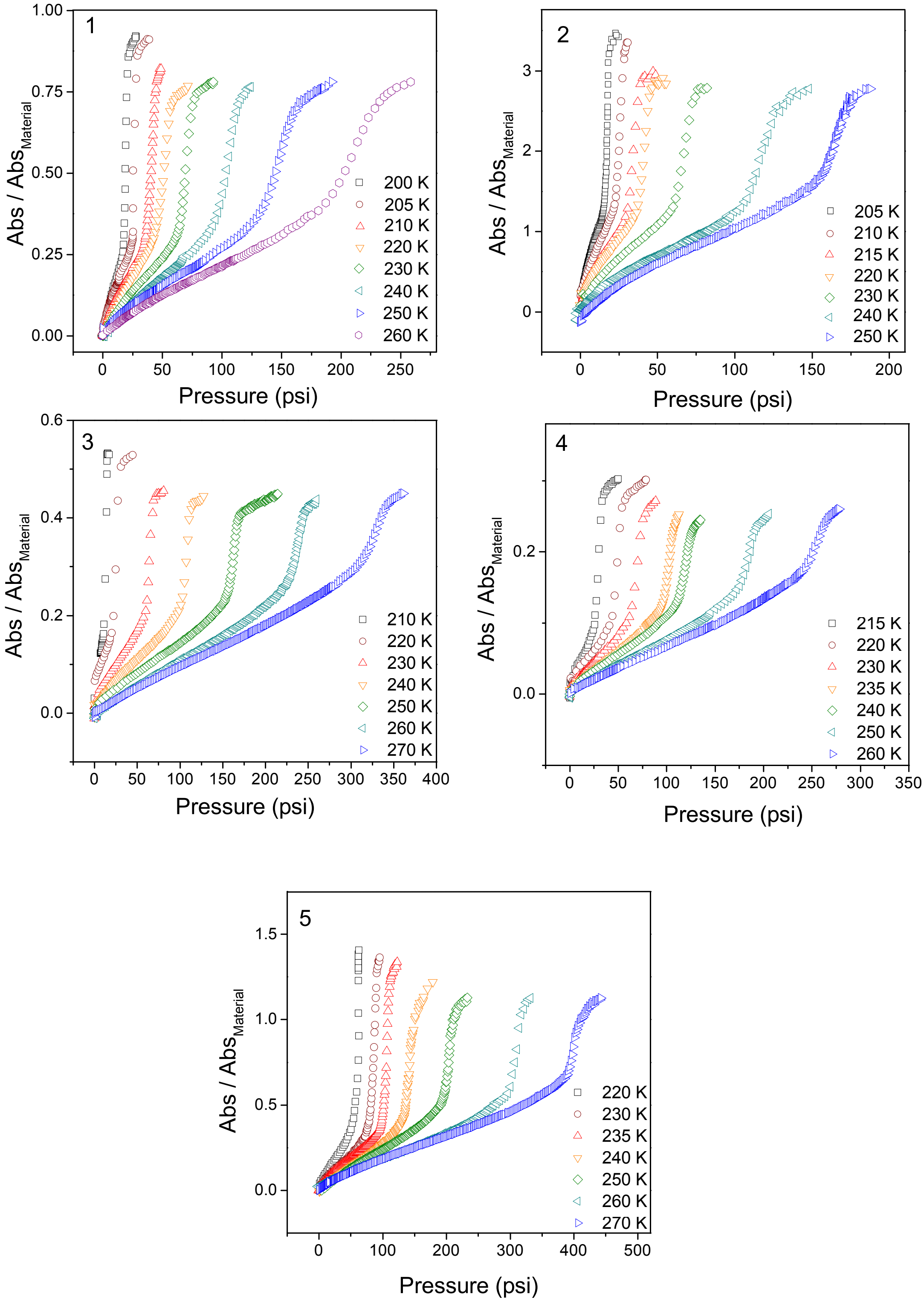

FIGURE 2.25: Adsorption isotherm curves of confined CO_2 in 3.2 nm **(1)**, 3.5 nm **(2)**, 4.0 nm **(3)** , 4.5 nm **(4)** MCM-41, and 8.3 nm MSU-H **(5)**.

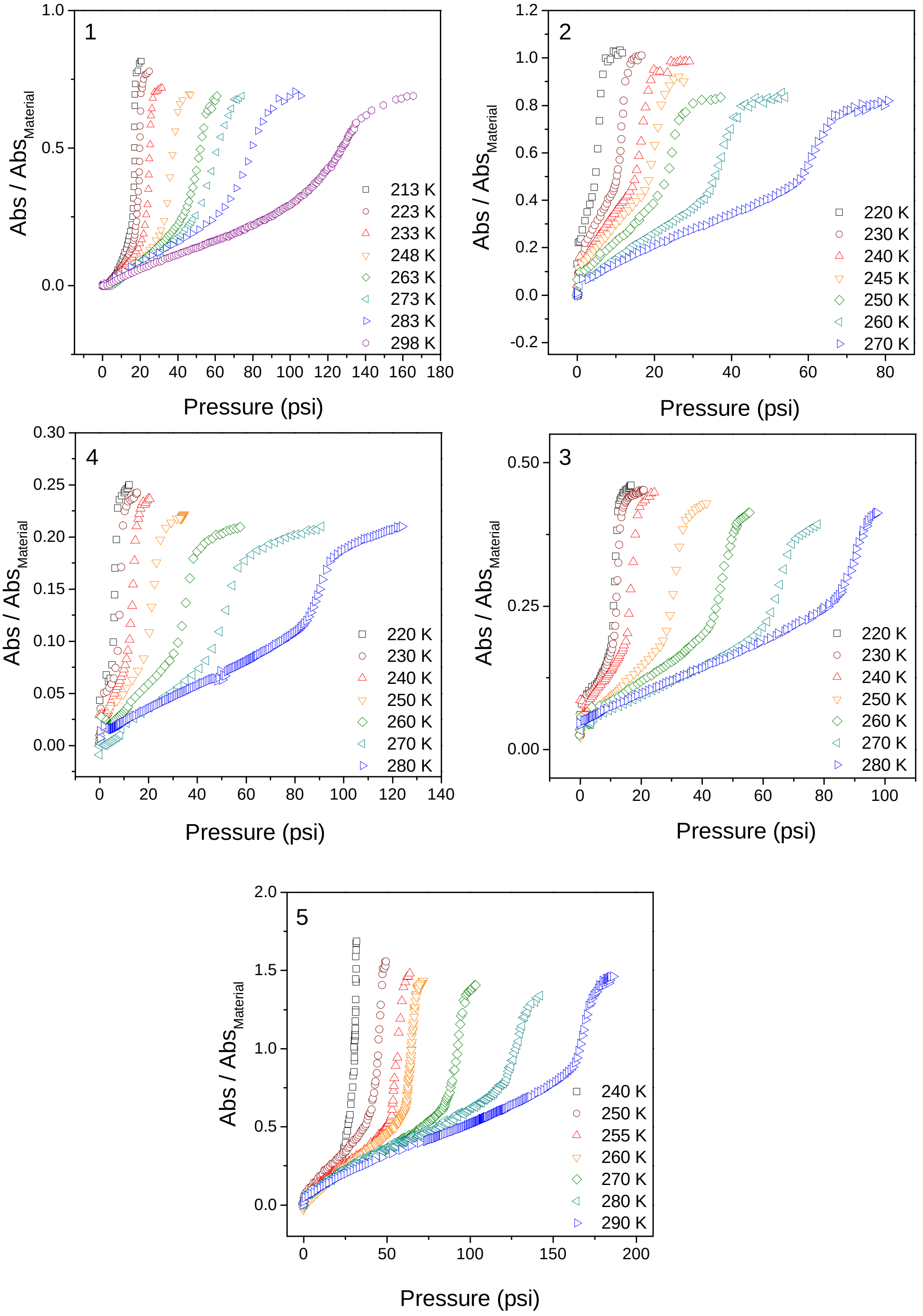

FIGURE 2.26: Adsorption isotherm curves of confined CH_2F_2 in 3.2 nm **(1)**, 3.5 nm **(2)**, 4.0 nm **(3)**, 4.5 nm **(4)** MCM-41, and 8.3 nm MSU-H **(5)**.

The mean T_{cp} value of CO_2 and CH_2F_2 confined in the silica samples were deduced by differentiating the sigmoidal fit of the scaled confined fluid absorbance ($Abs_{Material}$ / Abs_{Fluid}) with temperature. The maximum of the differential provides the mean T_{cp} value and the FWHM indicates the T_{cp} distribution within the material. It was determined that there was a relatively small distribution in critical temperatures (*ca.* 10–15 K) due to the small distribution of pores sizes in the samples, with only a wider distribution present in the 8.3 nm MSU-H silica (*ca.* 25 K), as shown in Figures 2.27 and 2.28). This can be attributed to the larger pore size distribution of MSU-H, as observed in the gas sorption measurements of the material displayed in Chapter 6.

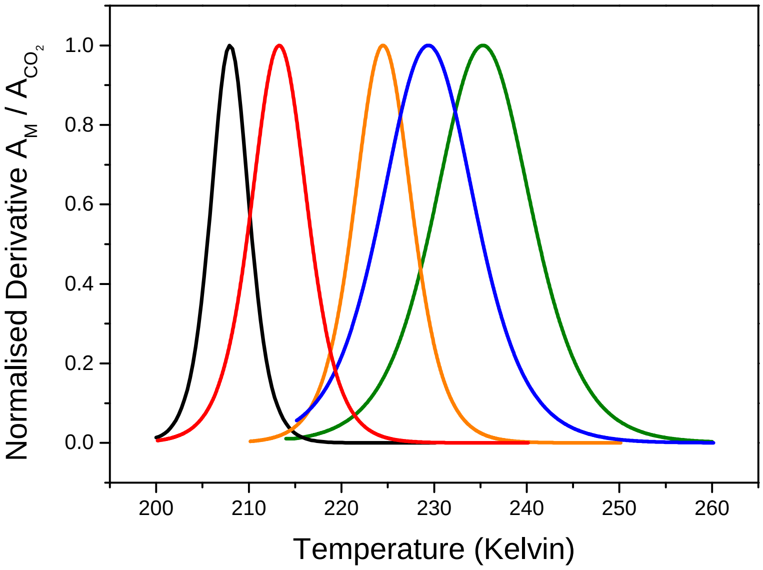

FIGURE 2.27: The range of critical temperatures for CO_2 present in 3.2 nm **(black)**, 3.5 nm **(red)**, 4.0 nm **(orange)**, 4.5 nm **(blue)** MCM-41 and 8.3 nm MSU-H **(green)** silica determined from the $Abs_{Material}$ / Abs_{Fluid} vs temperature differential.

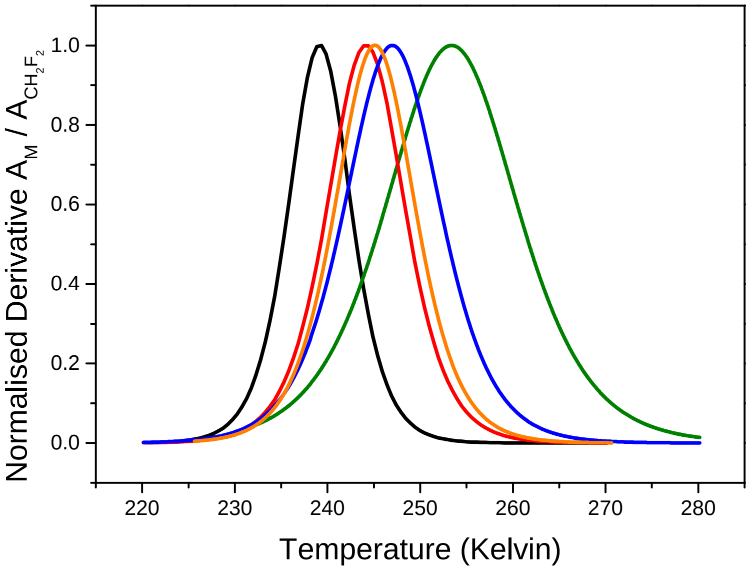

FIGURE 2.28: The range of critical temperatures of CH_2F_2 present in 3.2 nm **(black)**, 3.5 nm **(red)**, 4.0 nm **(orange)**, 4.5 nm **(blue)** MCM-41 and 8.3 nm MSU-H **(green)** silica determined from the $\text{Abs}_{Material}$ / Abs_{Fluid} vs temperature differential.

The mean T_{cp} values of both CO_2 and CH_2F_2 confined in these materials are summarised in Table 2.2 and demonstrate how the T_{cp} of these fluids change with pore diameter.

There is a significant depression in the critical temperature of CO_2 when confined in silica pores, in agreement with the literature.[73] These results show that at the smallest of pore diameters there is a very large depression in critical temperature of both fluids. There is a reduction of this effect with increasing pore size, causing a slower rate of T_{cp} increase with pore diameter. This results in a non-linear trend in mean T_{cp} with mean pore diameter as shown in Figure 2.29.

The large decrease in pore critical temperature at the smallest of pore sizes is less evident for CH_2F_2, which shows only a small sharp decrease in T_{cp} in the 3.2 nm pore size material. Unfortunately there are no literature studies of the pore critical temperature for CH_2F_2 in any pore type, so no comparisons can be made on the results obtained for this fluid.

TABLE 2.2: Summary of the critical temperatures (T_c) observed for CO_2 and CH_2F_2 confined in the silica materials.

		CO_2		**CH_2F_2**	
Material	Mean Pore Size (nm)	Mean T_{cp} (K)	T_{cp} Range (K)	Mean T_{cp} (K)	T_{cp} Range (K)
MCM-41 3.2	3.2	208	205 – 212	239	235 – 243
MCM-41 3.5	3.5	213	210 – 216	244	236 – 249
MCM-41 165	4.0	224	220 – 228	245	237 – 250
MCM-41 180	4.5	229	225 – 235	246	240 – 255
MSU-H	8.3	235	230 – 242	253	245 – 264
Bulk Fluid	–	304	–	352	–

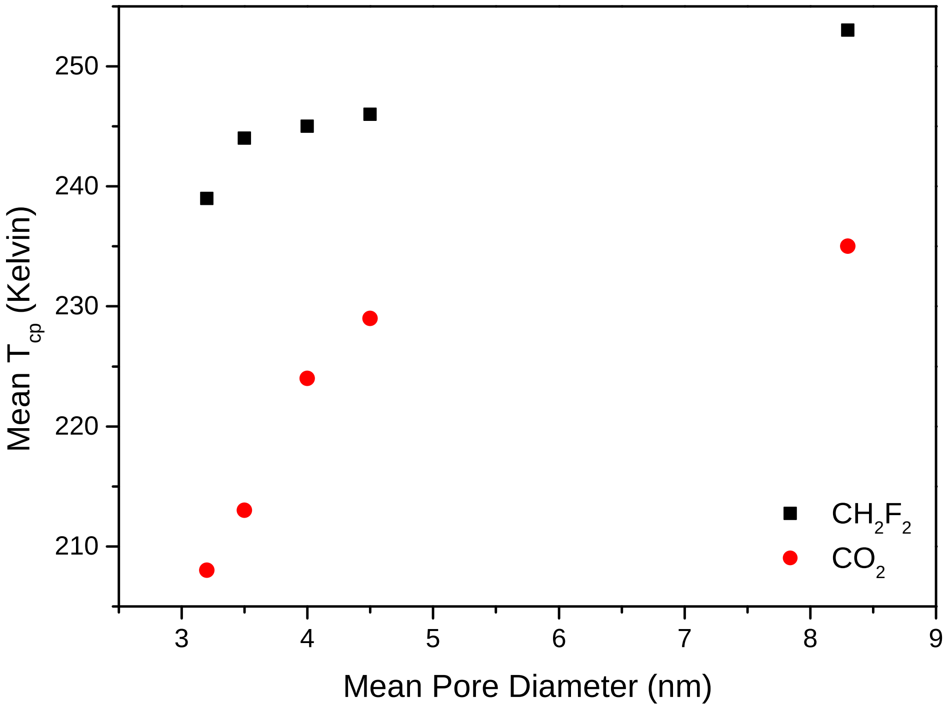

FIGURE 2.29: The mean pore critical temperature of CO_2 and CH_2F_2 in the porous silica templates ranging from 3.2–8.3 nm.

The T_{cp} of CO_2 in the 3.2 nm MCM-41 is 208 K which is comparable to that observed in the literature for smaller pore 2.4 nm MCM-41 by Morishige *et al.* of 213 K.[73] However the pore sizes in this study were measured by means of x-ray diffraction which does not provide a statistical mean pore diameter of the material and assumes all pores in the material are completely uniform. This method also makes assumptions for pore wall thickness.[96] The true mean pore size may actually be closer to that of the 3.2 nm MCM-41 used in this work if measured by gas sorption.

2.2.4 The Pore Critical Temperature of Carbon Dioxide and Difluoromethane Confined in Aluminosilicates

MCM-41 type silica pores are usually limited to relatively small pore diameters (*ca.* 2–5 nm). This is due to limitations in their synthetic procedure, which requires other molecules to be used as templates.[92,93] In order to determine the T_{cp} of larger pore sizes and pores with sizes between that of MCM-41 and MSU-H type silica, aluminosilicate templates were studied as larger pore sizes are usually easier to produce in these materials. The mean T_{cp} of CO_2 and CH_2F_2 confined in 6.7 and 12.2 nm aluminosilicates have also been investigated in this Chapter. In these cases the confined phase transition can be observed at a higher pressure due to the larger pore size of the material having less of an influence on capillary condensation, as shown in Figures 2.30 and 2.31. The adsorption and pore condensation of the CO_2 and CH_2F_2 in the aluminosilicates observed in these measurements resemble a type V adsorption isotherm. This is in contrast to the smaller pore MCM-41 type silica that was studied, which exhibited type IV isotherm behaviour, as described previously.[97] The characteristic adsorption behaviour of these aluminosilicates consists of a convex adsorption increase across most of the pressure range. Therefore these materials do not exhibit a large increase in adsorption at lower pressures, due to monolayer-multilayer adsorption. This is because the pore diameter is larger, meaning the pore wall interaction potential with the confined species has a smaller influence on the pore adsorption process, as the interaction range between the wall and the fluid in larger pores extends over a much smaller proportion of the pore volume. The larger pore diameter also increases the adsorbate condensation pressure due to these factors and the adsorbate is less spatially confined, making the environment of pore confined fluid more bulk-like in these materials.

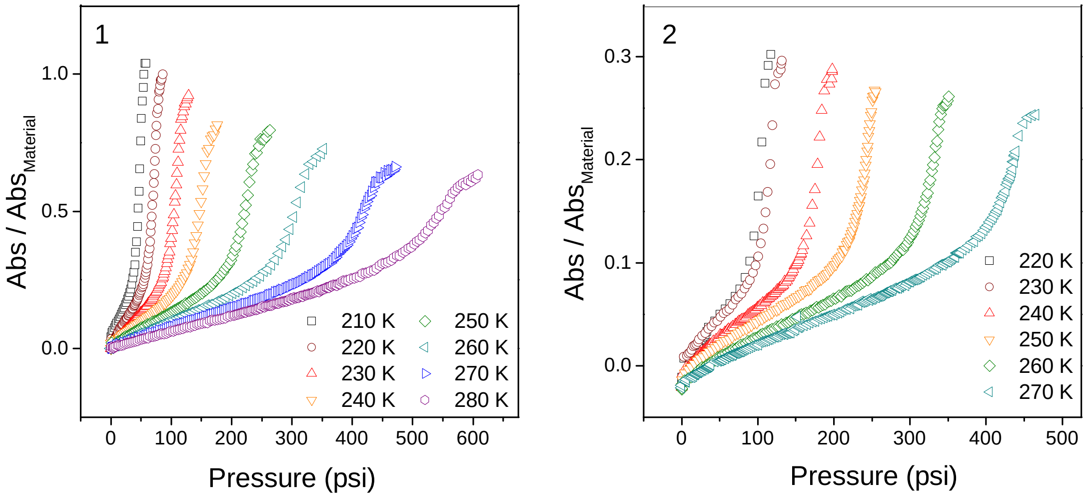

FIGURE 2.30: Adsorption isotherm curves of confined CO_2 in 6.7 nm **(1)** and 12.2 nm **(2)** pore diameter aluminosilicates.

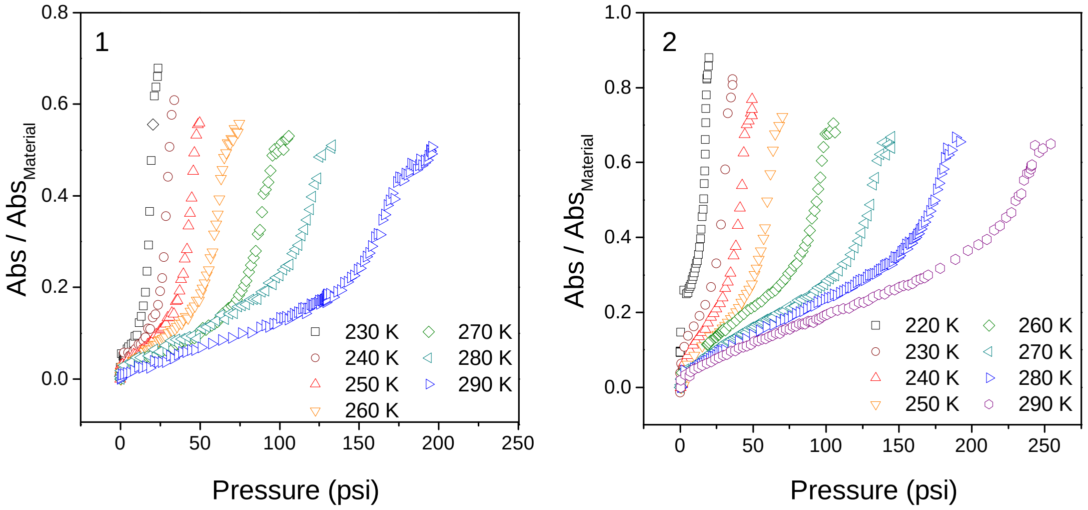

FIGURE 2.31: Adsorption isotherm curves of confined CH_2F_2 in 6.7 nm **(1)** and 12.2 nm **(2)** pore diameter aluminosilicates.

A large distribution in T_{cp} was deduced for both fluids from the $A_{Material}$ /

A_{Fluid} vs temperature differential (see Figures 2.32 and 2.33). This is due to the large distribution of pore sizes within the aluminosilicate samples, which has been established from the gas sorption measurements shown in Chapter 6.

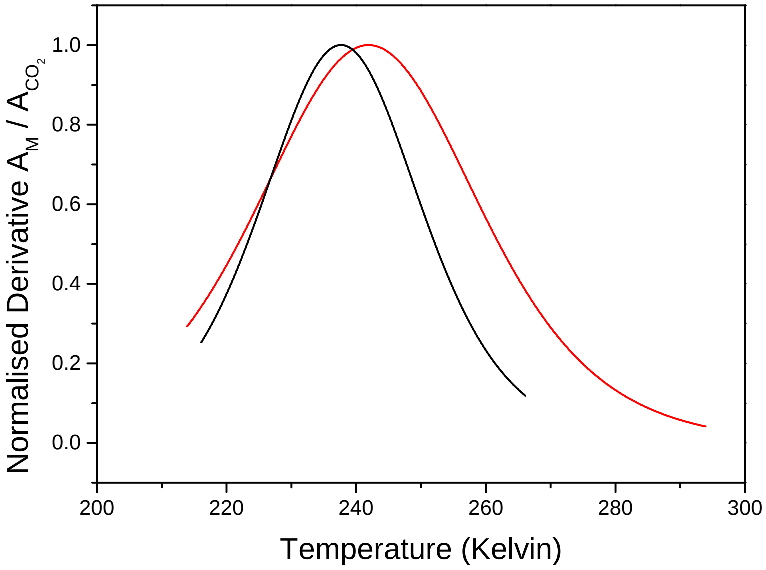

FIGURE 2.32: The range critical temperatures for CO_2 present in 6.7 nm aluminosilicate **(black)** and 12.2 nm aluminosilicate **(red)** determined from the $Abs_{Material}$ / Abs_{Fluid} vs temperature differential.

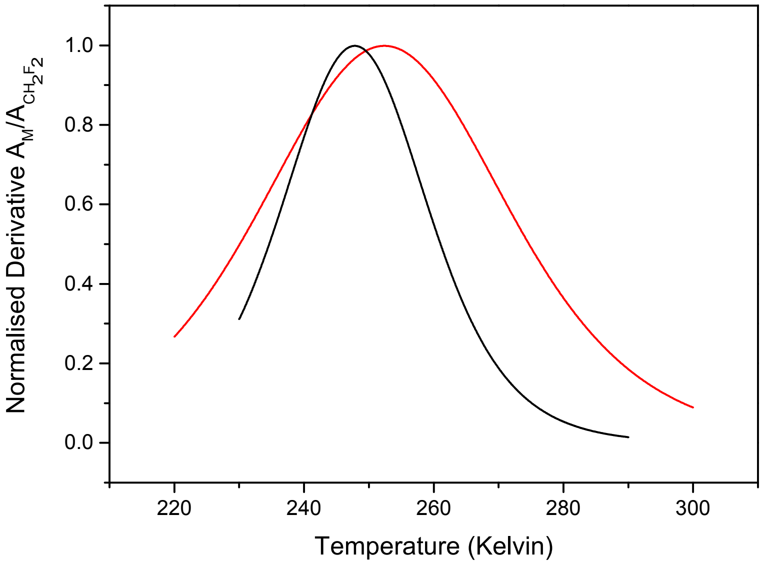

FIGURE 2.33: The range of critical temperatures of CH_2F_2 present in 6.7 nm **(black)** and 12.2 nm **(red)** aluminosilcates determined from the Abs$_{Material}$ / Abs$_{Fluid}$ vs temperature differential.

The mean T_{cp} values of both CO_2 and CH_2F_2 confined in the two aluminosilicate materials are summarised in Table 2.3 and demonstrate how the T_{cp} of these fluids change in their respective pore diameters. In the case of these materials there appears to be a relatively small change in T_{cp} in this pore size range for both fluids, although the T_{cp} still remains significantly below that of the bulk.

TABLE 2.3: Summary of the critical temperatures (T_c) observed for CO_2 and CH_2F_2 confined in the aluminosilicate materials.

		CO_2		**CH_2F_2**	
Material	Mean Pore Size (nm)	Mean T_{cp} (K)	T_{cp} Range (K)	Mean T_{cp} (K)	T_{cp} Range (K)
MZBN-100w3hd	6.7	237	222 – 251	249	238 – 260
MZBN-135w3h	12.2	241	220 – 260	255	230 – 278
Bulk Fluid	–	304	–	352	–

2.2.5 The Pore Critical Temperature of Carbon Dioxide and Difluoromethane Confined in Anodic Alumina Templates

Progressing the study to larger pore sized templates, the critical temperature of confined CO_2 and CH_2F_2 was studied in larger pore anodic alumina oxide (AAO). The AAO templates are in the form of a membrane consisting of a symmetrical porous structure with uniform cylindrical pores penetrating the entire thickness of the membrane.[168] They have a high degree of pore ordering and narrow pore size distribution,[169] with the supplier stating that there is a standard deviation as low as 5 %. As the templates are in the form of films with a known thickness, the use of a consistent number of templates in the cell for each experiment means there is no requirement to scale the absorbance. This is because the NIR beam will penetrate the same thickness of sample for each experiment. The adsorption plots for these materials are given in absolute absorbance units instead of an absorbance ratio seen previously. In order to determine the mean T_{cp}, the inverse absorbance was studied with temperature and the differential indicates the range of T_{cp} in the material. The pressure of pore condensation appears very close to the bulk condensation pressure, ranging between 5–20 psi lower. Some examples of these adsorption plots are given in Figure 2.34.

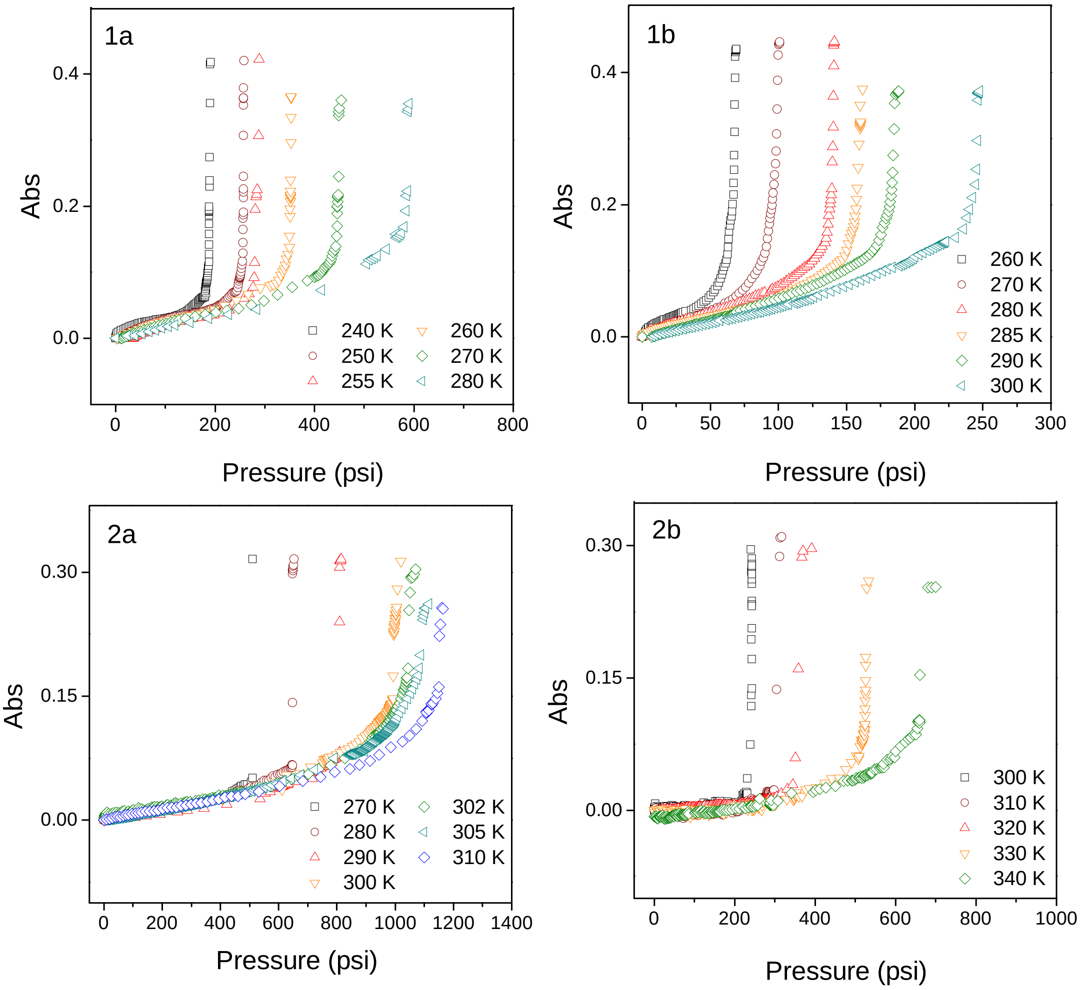

FIGURE 2.34: Adsorption isotherm curves of CO_2 confined in **(1a)** 18 nm and **(2a)** 55 nm pore diameter anodic alumina. With adsorption isotherm curves of CH_2F_2 confined in 18 nm **(1b)** and 35 nm **(2b)** pore diameter anodic alumina templates.

Although the materials exhibit pore condensation at larger diameters, they show no depression in the critical temperature of the fluid confined within them. In the case of carbon dioxide, although pore condensation can be observed in 80 nm pores there are no measured change in pore critical temperature and the isotherms progress with temperature in a the same manner as the bulk (see Figure 2.35).

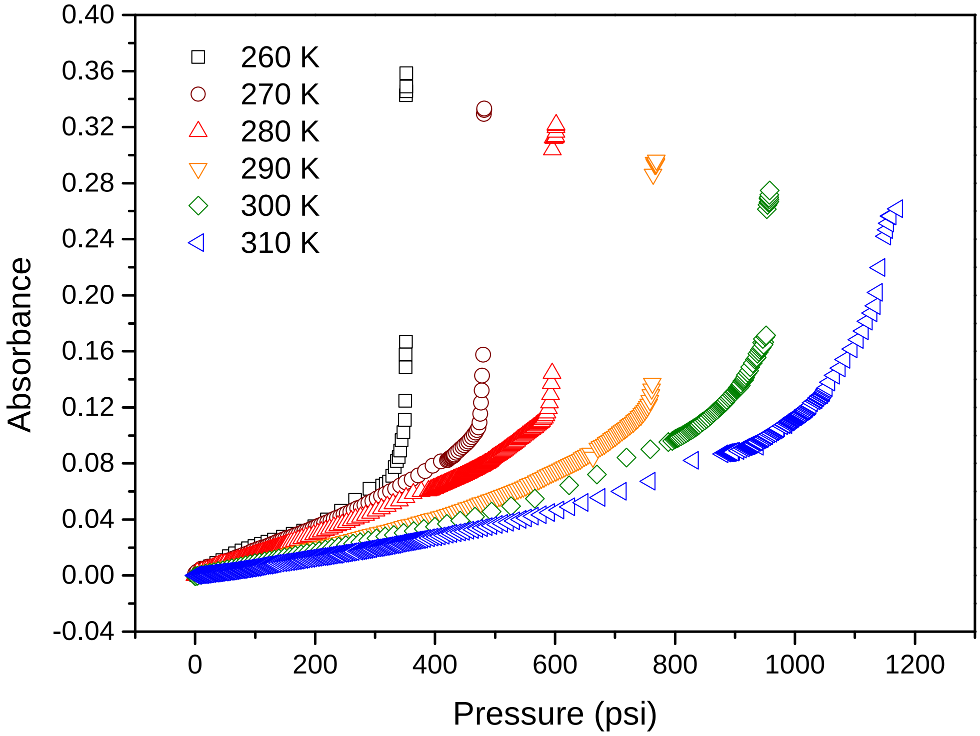

FIGURE 2.35: Adsorption isotherms of CO_2 in the 80 nm pore diameter anodic alumina displaying bulk like behaviour. This is evident as the isotherms simply progress to a more continuous phase transition with temperature, possessing a smaller adsorption step.

For difluoromethane, as is the case with CO_2, although the pore condensation can be observed in the 55 nm pores, the measured T_{cp} of CH_2F_2 is not significantly depressed from the bulk value, with a T_{cp} of 349 K compared to the bulk value of 352 K. At the pore sizes larger than those in which an effect on T_c is observed, the confined isotherm either progressed with temperature in the same manner as the bulk (Shown in Figure 2.35) or no pore condensation was seen to take place (*e.g.* in the 100 nm pores). This clearly indicted that the T_{cp} of the fluids in these very large pore sizes were close to or at the bulk value. This is to be expected as the T_{cp} of the fluids determined in the smaller anodic alumina templates are nearly or already coinciding with the bulk value.

The isotherms appeared to be convex and similar to the type III isotherm class, indicating the adsorbate-adsorbent interactions are weak and the pore size is large.[97] However these materials also display isotherm behaviour closely resembling the bulk fluid. The pore condensation step is closer to the bulk condensation pressure and the adsorption curve is less convex in nature across the entire pressure range before condensation. As expected, the width of the 1 / A_{Fluid} vs temperature differential observed for these pore types is very narrow in comparison to the mesoporus silica templates. This is due to the narrow pore size distribution within the anodic alumina templates (see Figures 2.36 and 2.37).

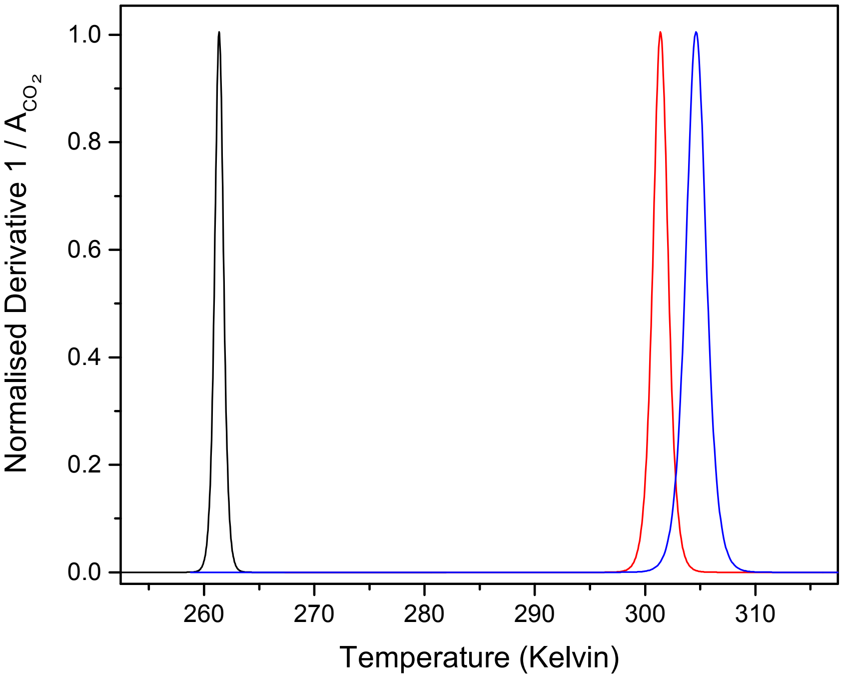

FIGURE 2.36: the range of critical temperatures of CO_2 present in 18 nm **(black)**, 35 nm **(red)** and 55 nm **(blue)** anodic alumina templates determined from the 1 / A_{Fluid} vs temperature differential.

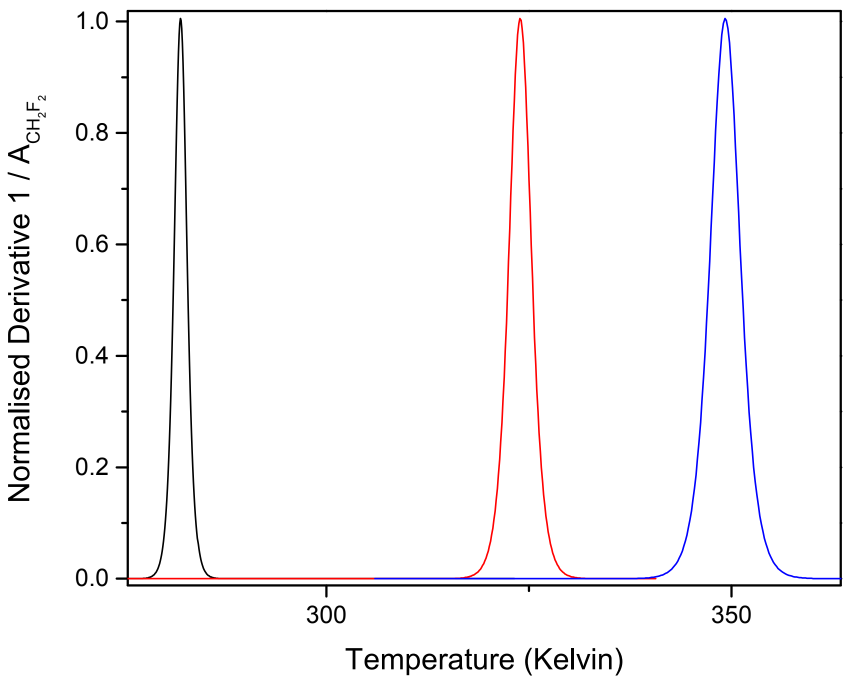

FIGURE 2.37: the range of critical temperatures of CH_2F_2 present in 18 nm **(black)**, 35 nm **(red)** and 55 nm **(blue)** anodic alumina templates determined from the 1 / A_{Fluid} vs temperature differential.

The mean T_{cp} values of both CO_2 and CH_2F_2 confined in the anodic alumina materials are summarised in Table 2.4. The values of T_{cp} versus increasing mean pore diameter for the anodic alumina materials show an almost linear dependency toward the bulk T_c for both fluids. It was observed that CH_2F_2 was required to be confined in larger pore diameters than that of CO_2 in order to reach its bulk T_c value. As the bulk T_c is reached for both fluids, the determined T_{cp} of the fluid remains constant as the pore size increases up to 100 nm (Figure 2.38). Although no literature studies of the phase behaviour of CO_2 in anodic alumina pores exist, SANS studies in large 200 nm coal pores show that properties of the confined CO_2 is comparable to the bulk.[62] It is therefore expected that at these larger pore sizes the effect of confinement on the T_{cp} of CO_2 is negligible.

Table 2.4: Summary of the critical temperatures (T_c) observed for CO_2 and CH_2F_2 confined in the anodic alumina materials.

		CO_2		**CH_2F_2**	
Material	Mean Pore Size (nm)	Mean T_{cp} (K)	T_{cp} Range (K)	Mean T_{cp} (K)	T_{cp} Range (K)
SM-18-100-13	18	261	260 – 262	282	280 – 284
SM-35-100-13	35	301	300 – 302	324	319 – 328
SM-55-100-13	55	304	303 – 307	349	336 – 352
SM-80-100-13	80	304	–	352	–
SM-100-100-13	100	304	–	352	–
Bulk Fluid	–	304	–	352	–

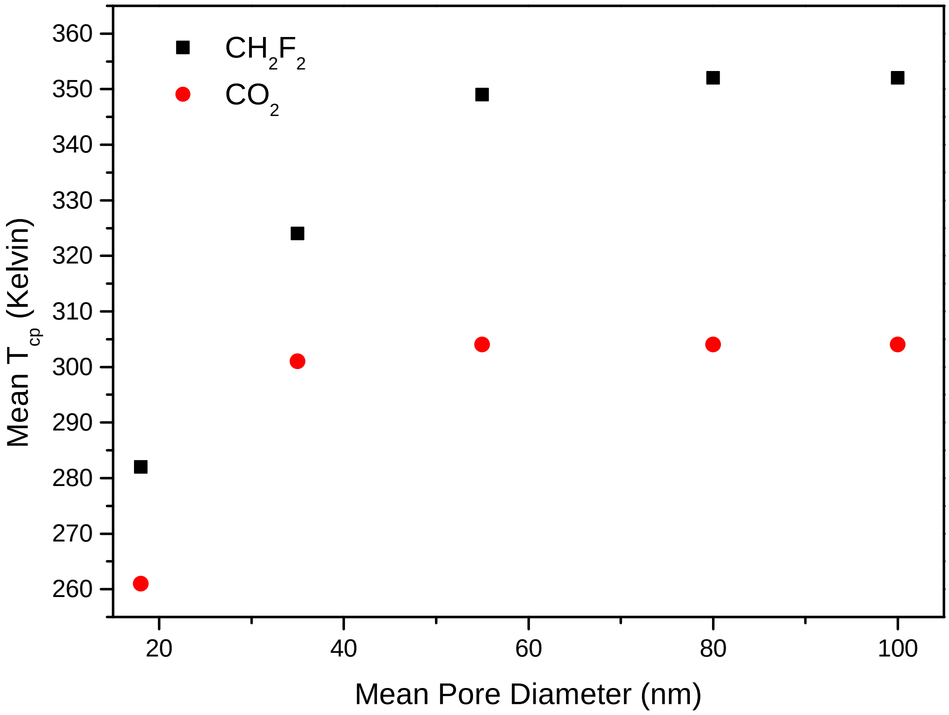

Figure 2.38: The mean pore critical temperature of CO_2 and CH_2F_2 in the anodic alumina templates ranging from 18–100 nm.

A summary of the measured pore critical temperatures of both CO_2 and CH_2F_2 confined in the twelve separate materials is given in Figure 2.39 and in Table 2.5.

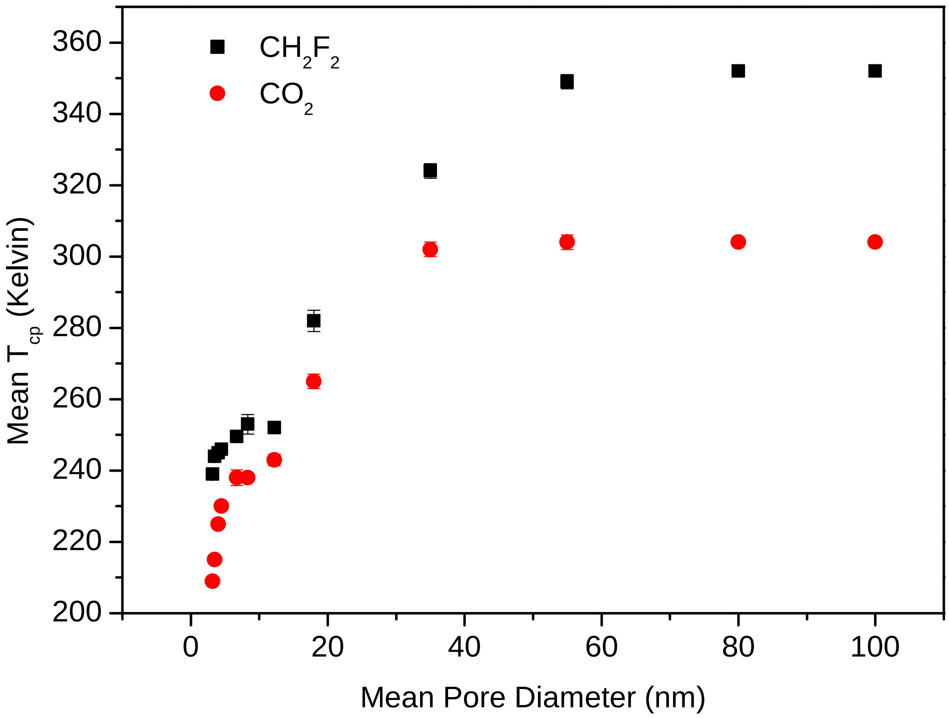

FIGURE 2.39: The mean pore critical temperature of CO_2 and CH_2F_2 in each of porous templates. The bulk critical temperature is 304 and 352 K for CO_2 and CH_2F_2 respectively

There is a profound depression of the critical temperature of both carbon dioxide and difluoromethane when confined in nanopores. In both cases, smaller pore sizes exhibit a larger depression in T_c.

TABLE 2.5: Summary of the critical temperatures (T_c) observed for CO_2 and CH_2F_2 confined in the twelve porous materials.

		CO_2			**CH_2F_2**		
Material	Mean Pore Size (nm)	Mean T_{cp} (K)	Depression (K)	T_{cp} Range (K)	Mean T_{cp} (K)	Depression (K)	T_{cp} Range (K)
MCM-41 3.2	3.2	208	96	205 – 212	239	112	235 – 243
MCM-41 3.5	3.5	213	91	210 – 216	244	107	236 – 249
MCM-41 165	4.0	224	80	220 – 228	245	106	237 – 250
MCM-41 180	4.5	229	74	225 – 235	246	105	240 – 255
MZBN-100w3hd	6.7	237	66	222 – 251	249	103	238 – 260
MSU-H	8.3	235	69	230 – 242	253	98	245 – 264
MZBN-135w3h	12.2	241	62	220 – 260	255	97	230 – 278
SM-18-100-13	18	261	42	260 – 262	282	70	280 – 284
SM-35-100-13	35	301	3	300 – 303	324	28	319 – 328
SM-55-100-13	55	304	0	303 – 307	349	3	336 – 352
SM-80-100-13	80	304	0	–	352	0	–
SM-100-100-13	100	304	0	–	352	0	–

In summary, the critical temperatures of CO_2 and CH_2F_2 are significantly depressed when confined in a range of pore sizes. The greatest effect occurs at the pore widths approaching the scale a few molecular widths of the adsorbate. For example, the 3.2 nm MCM-41 pores are approximately 10 CO_2 molecules in diameter.[170] This behaviour is predicted in theoretical studies and has been demonstrated for confined water which exhibits a non-linear decrease in pore T_c at the smallest of pore diameters (< 5 nm) due to the extreme confines of the small pores.[171] There appears to be a plateau of pore critical temperature between the pore diameters of 6.7–12.2 nm before approaching the bulk critical temperature at the larger pore sizes. For both fluids the trend observed in T_{cp} from the smallest to the largest pore sizes consists of three distinct regimes. Between 3.2–4.5 nm there is a steep increase in the pore critical temperature of both fluids, which is more evident with carbon dioxide. In the case of difluoromethane this steep increase seems to be mainly evident between the 3.2–3.5 nm pore sizes. Between 6.7–12.2 nm the T_{cp} of both fluids reaches a plateau where there is little change in the T_{cp} value as the pore size increases (see Figure 2.40).

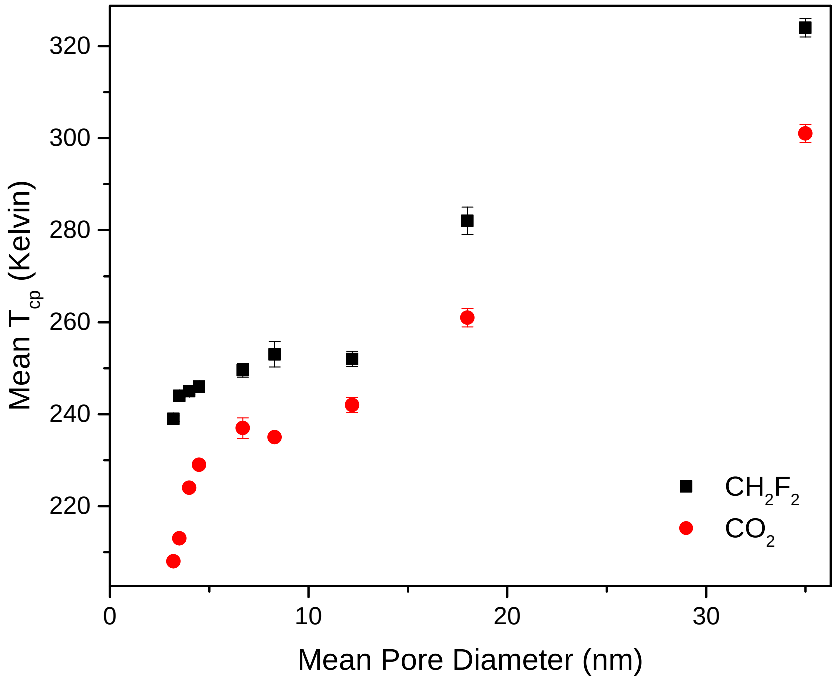

FIGURE 2.40: The mean pore critical temperature of CO_2 and CH_2F_2 in porous templates ranging from 3.2–35 nm.

The pore T_c of each fluid remains at a much lower value than the bulk T_c across this pore size range. Finally between 12.2–55 nm the T_{cp} progresses almost linearly up toward the bulk T_c value. Experimental studies conducted on confined fluids have concluded that there is a linear relationship between the change in critical temperature (T_c-T_{cp}) for a confined fluid with the inverse pore size, in agreement with the scaling theory of criticality.[73] However there is some theoretical evidence from previous studies that there may be a non-linear relationship between T_c-T_{cp} and inverse pore size as shown by Singh *et al.* using GC-TMMC (grand canonical-transition matrix Monte Carlo) simulations.[145] It was found in this study, in contrast to previous predictions, that the dependence of the shift in critical temperature versus the inverse slit width is not linear and is in fact made up of multiple linear regimes, becoming more prominent as the surface-fluid attraction increased. The study showed a large change in the pore critical temperature as the pore width increased for slit widths of only a few molecular diameters. This rate of increase was found to be much slower as the pore width increased from a quasi 2D to a 3D geometry. Importantly this non-linear behaviour was found to be dependant on the interaction energy between the fluid and the wall of the pore. As the interaction energy increases, the more the relationship between T_c-T_{cp} and inverse pore size deviates from a linear dependence. This would suggest that the attractive potential between the molecule and the walls of the pore is an important factor in the T_{cp} versus pore size relationship.

The experimental studies that predict a linear relationship have mainly studied the confined fluid T_c depression using non-polar molecules and noble gases. These are likely to interact with the wall of the pore *via* weak intermolecular forces such as van der Waals or dispersion interactions, as opposed to dipole-dipole interactions or hydrogen bonding. Conversely difluoromethane and carbon dioxide are more polar or posses higher dielectric constants making them more polarisable than most of the species studied in small pore silica materials in the literature.[172] These molecules are likely to interact more strongly with the pore wall as they reorientate or have their electron cloud distorted by any charges present on the pore surface, therefore they likely possess a greater interaction energy. They also offer sites of potential hydrogen bonding which again allows for a stronger interaction potential with the pore wall. It has been reported that the walls of silica and anodic alumina pores are not strictly neutrally charged non-interacting boundaries. This can be demonstrated by studies of fluid wetting and the enthalpies or heats of adsorption of pore confined species, which relate to the fluid-wall interaction energies.[173,174]

The geometry and orientation of atoms making up the pore wall means that there are dipole moments or moieties of high and low electron density pointing into the pore, which will attract polar molecules. For example, the alternating silicon-oxygen lattice in silica results in relatively positively charged silicon atoms and relatively negatively charged oxygen atoms making up the pore surface. The relative point charges on the silicon and oxygen atoms of the pore wall arise from the different electronegative properties of oxygen and silicon acting through the bonds between them,[175–177] and a similar effect can be expected of the lattice in the anodic alumina. There are also hydroxyl (–OH) groups present in these materials,[178,179] particularly on silica surfaces (silanol) which offer hydrogen bonding opportunities. The effect of these factors is evident as the pore critical temperature of difluoromethane, which is more polar than carbon dioxide (reflected in their respective dielectric constants and difluoromethane's dipole moment),[56,57,180] is lowered to a much larger proportion across the whole pore size range studied. This phenomenon can be observed if the shift in critical temperatures of the respective pore confined fluids are scaled to their bulk T_c values, revealing the extent of the depression in their critical temperature. This value, the decrease in reduced pore critical temperature ($\Delta\mathrm{T}_{rp}$), should have a linear dependence on the inverse pore size if scaling theory applies. ΔT_{rp} is given as:

$$\Delta T_{rp} = \frac{T_c - T_{cp}}{T_c} \tag{2.7}$$

The T_{cp} of difluoromethane also appears to remain below its bulk T_c when confined in pore diameters which have no effect on the T_{cp} of carbon dioxide, again demonstrating the greater effect pore confinement has on the T_{cp} of difluoromethane (Figure 2.41). In the case of both fluids the ΔT_{rp} as a function of inverse pore diameter deviates from a linear relationship, suggesting that the fluid-wall interaction potential is strong.

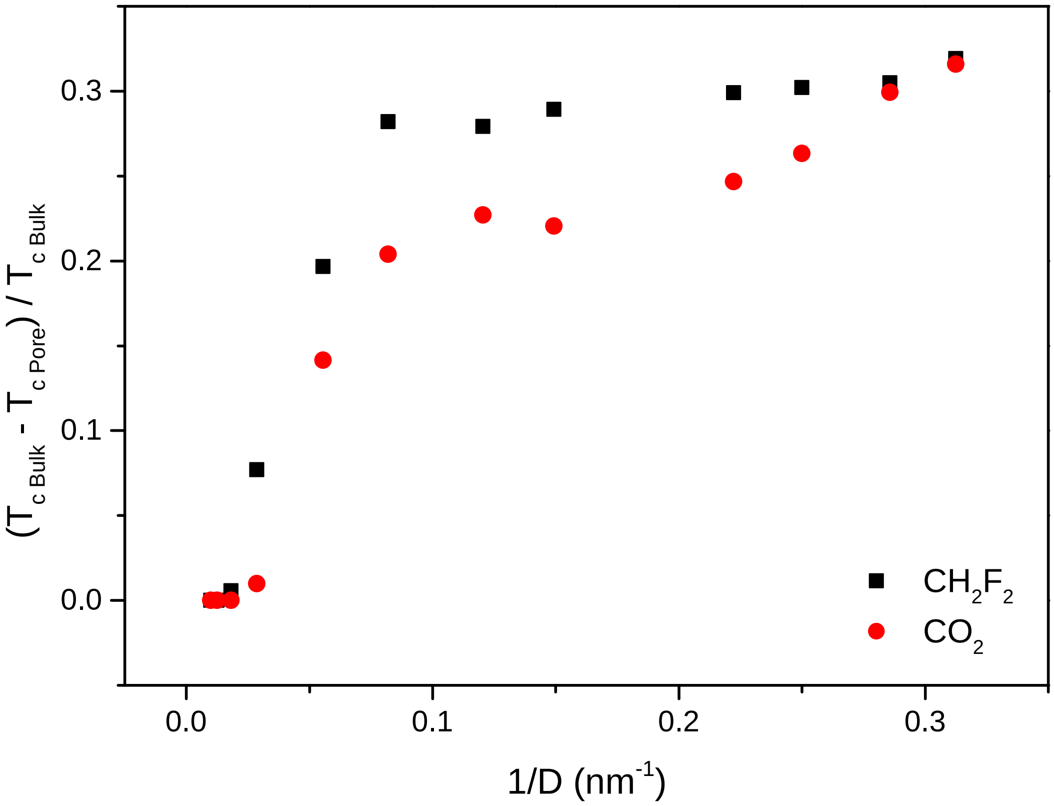

FIGURE 2.41: The decrease in reduced pore critical temperature (ΔT_{rp}) for CH_2F_2 and CO_2 as a function of the inverse pore diameter.

2.2.6 The Pore Critical Temperature of Ethane Confined in Silica, Aluminosilicate and Anodic Alumina Templates

To probe the relationship of fluid-wall interaction strength further, the T_{cp} of ethane was studied in a range of the porous materials. Ethane has been shown to be a weakly interacting adsorbate exhibiting a relatively low enthalpy of adsorption in microporous silica, with a value of -16 kJ mol^{-1}.[181] In contrast CO_2 has an enthalpy of adsorption of around -32 kJ mol^{-1} in a mesoporous silica pore.[182] Ethane is also non-polar as a molecule, hydrophobic and possesses low polarisability as fluid, which can be demonstrated by the low dielectric constant of saturated liquid ethane of 1.42 at 295 K and 1581 psi.[162] For comparison liquid CO_2 is 1.60 at 293 K and 735 psi[183] and liquid CH_2F_2 is 14.40 at 303 K and 1740 psi.[184] These factors all contribute to a weak interaction with the pore wall, making ethane an ideal fluid to probe the relationship between T_{cp} and fluid-pore interaction strength. To carry out this study, the $\nu_6 + \nu_{10}$ near-infrared band of ethane,[185] which is a combination of the C–H bend and C–C twist respectively, was studied as a function of pressure isothermally in silica, aluminosilicates and anodic alumina materials (see Figure 2.42).

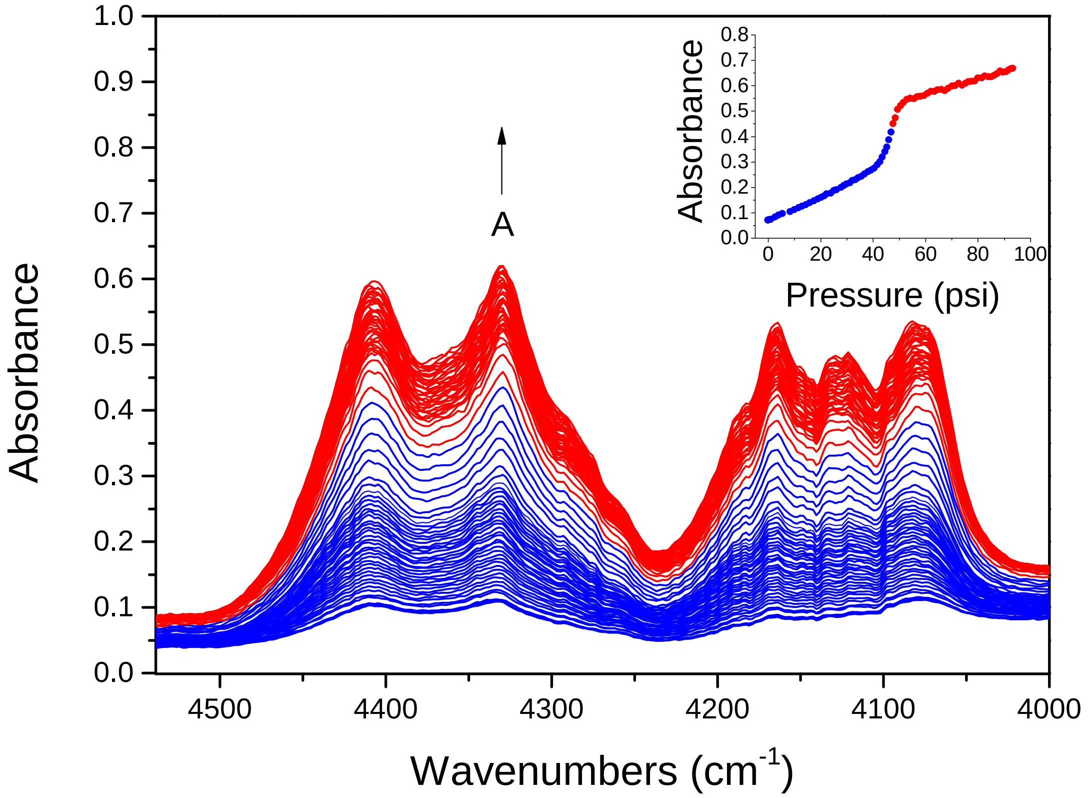

FIGURE 2.42: The $\nu_6 + \nu_{10}$ near-infrared combination band of ethane **(A)** confined in 4.5 nm MCM-41 180 at 230 K as a function of increasing pressure. This allows the pore phase transition to be observed **(Inset)**.

This again allowed for the observation of the phase transition of confined ethane by near-infrared spectroscopy and the progression from a low temperature gas–liquid to a higher temperature gas–supercritical phase transition taking place within the pores (see Figure 2.43). Although C_2H_6 condensation was observed in pore sizes above 35 nm it exhibited a normal progression of a steep gas to liquid phase transition becoming a gas to supercritical fluid phase transition with increased temperature, as observed with bulk substance. Therefore no indication of the distribution of T_{cp} values in the larger pore templates ($>$ 35 nm) were determined, with the ethane in these pores evidently possessing the bulk T_c. No ethane pore condensation was observed in the 100 nm pores.

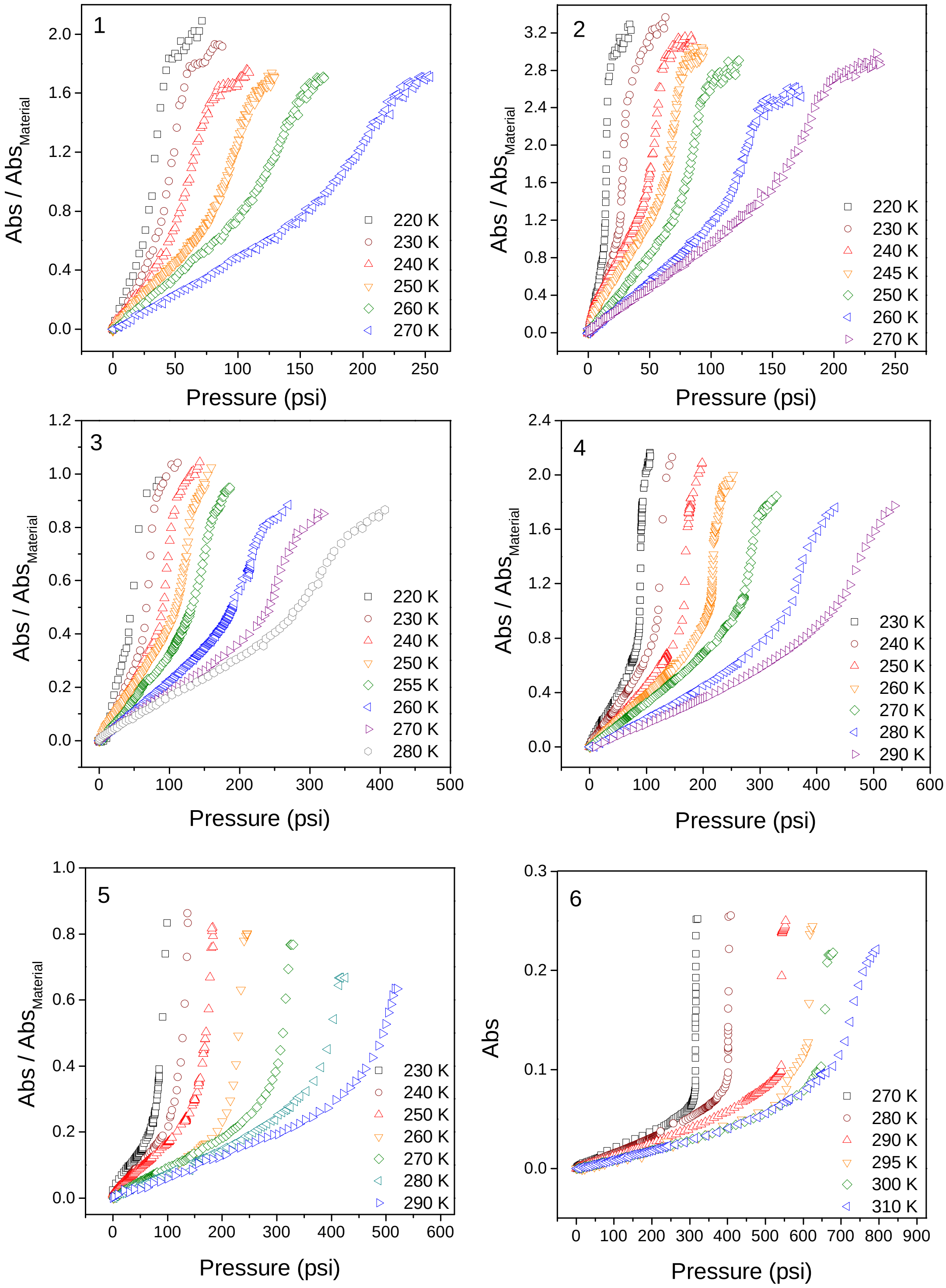

FIGURE 2.43: Adsorption isotherms, measured by near-infrared spectroscopy of C_2H_6 confined in 3.2 nm **(1)**, 4.0 nm **(2)** and 4.5 nm **(3)** MCM-41. Along with 8.3 nm **(4)** MSU-H silica, 12.2 nm aluminosilicate **(5)** and 18 nm anodic alumina **(6)**.

The lower ethane-silica interaction energy is evident from the adsorption isotherms obtained in these experiments. The isotherm resembles more of a type V isotherm, which indicates a smaller fluid-wall interaction potential.[97] There is a smaller increase in the amount adsorbed in the initial part of the isotherm due to less monolayer-multilayer adsorption when compared to a typical Type IV isotherm, demonstrated by CH_2F_2 in the 3.2 nm pore diameter MCM-41 at 230 K (Figure 2.44 **A**).

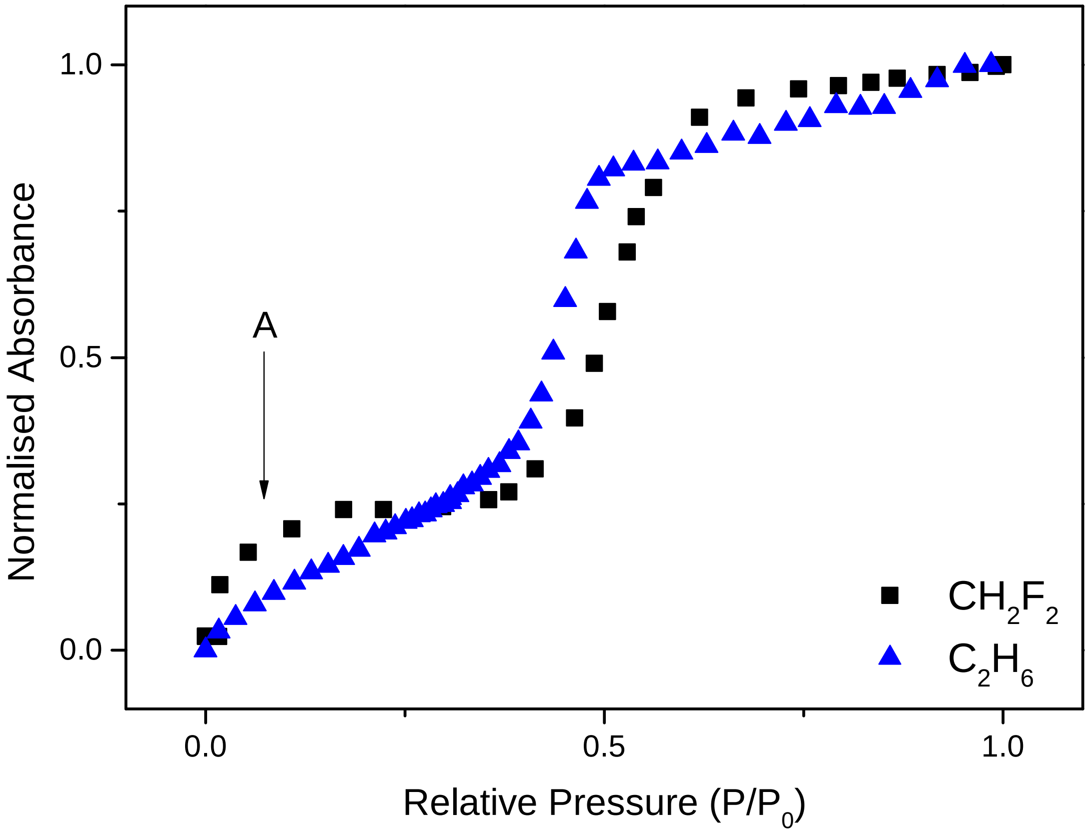

FIGURE 2.44: Adsorption isotherms measured by near-infrared spectroscopy, of CH_2F_2 and C_2H_6 confined in 4.5 nm MCM-41 180 at 220 K. The initial increase of pore uptake due to monolayer-multilayer adsorption with pressure is indicated by **A**.

An indicated range of ethane critical temperatures present in the materials were determined. As observed with both CO_2 and CH_2F_2, it is evident that the materials possessing a larger pore size distribution displayed a larger range of critical temperatures present, as shown in Figures 2.45 and 2.46.

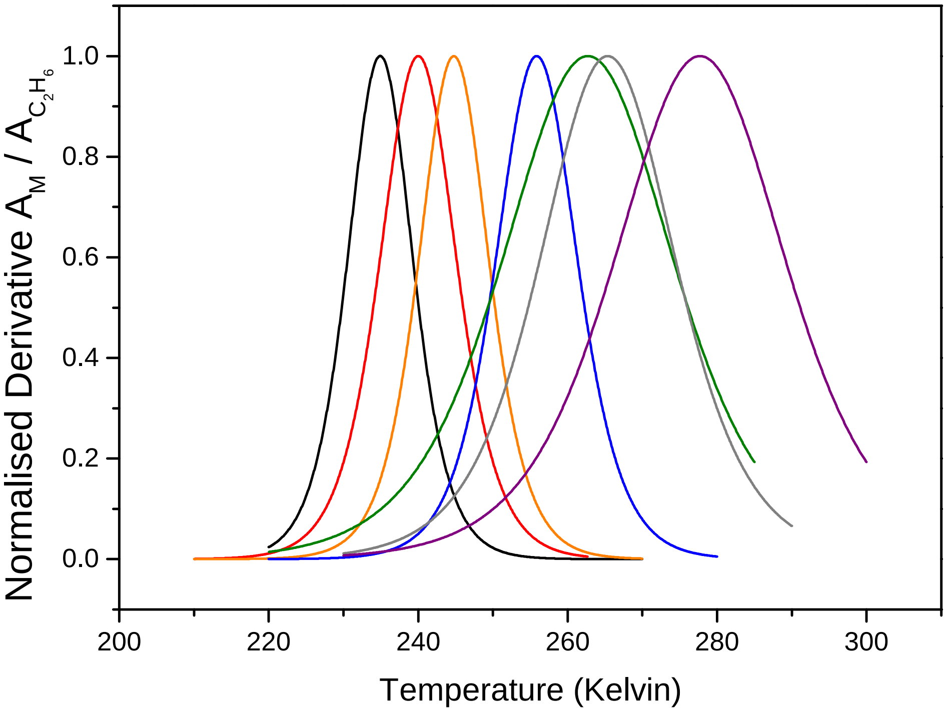

FIGURE 2.45: The range of critical temperatures of C_2H_6 present in 3.2 nm **(black)**, 3.5 nm **(red)**, 4.0 nm **(orange)**, 4.5 nm **(blue)** MCM-41, 8.3 nm MSU-H **(grey)** silica. Along with 6.7 nm **(green)** and 12.2 nm **(purple)** aluminosilicates determined from the $\text{Abs}_{Material}$ / Abs_{Fluid} vs temperature differential.

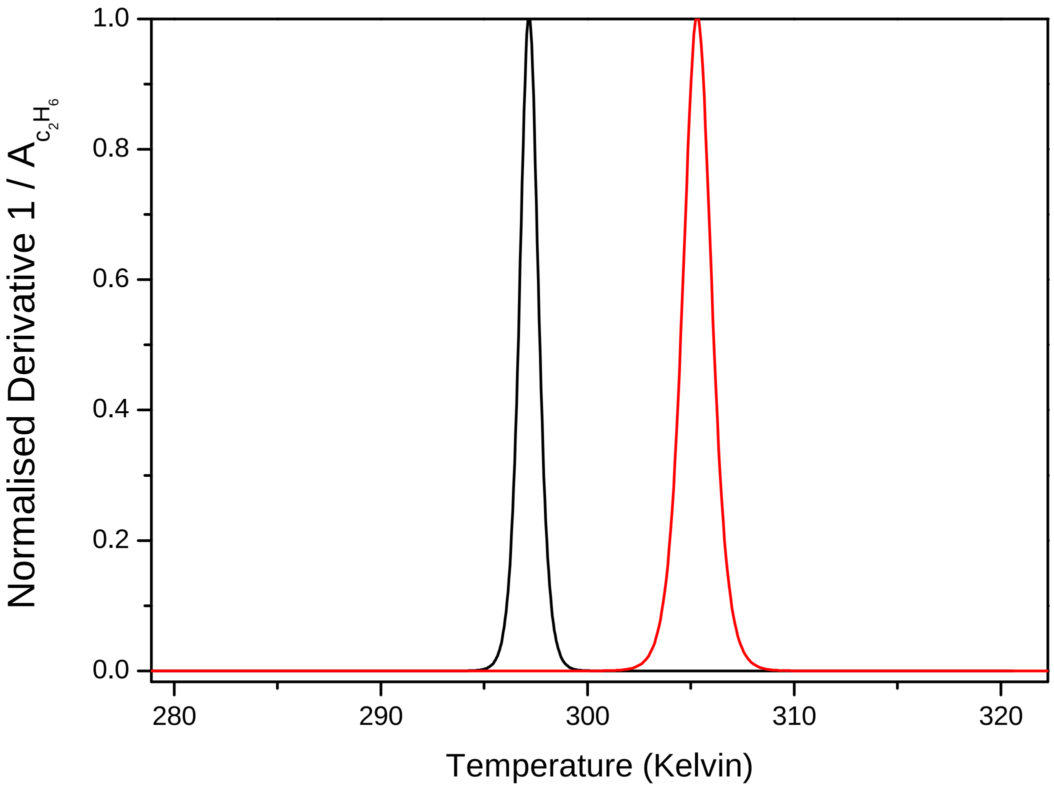

Figure 2.46: The range of critical temperatures of C_2H_6 present in 18 nm **(black)** and 35 nm **(red)** anodic alumina materials determined from the 1 / Abs_{Fluid} vs temperature differential.

The mean T_{cp} of ethane in pore sizes ranging from 3.2 to 100 nm, determined by near-infrared spectroscopy are displayed in Table 2.6.

Table 2.6: Summary of the pore critical temperatures (T_{cp}) observed for C_2H_6 confined in the silica, aluminosilicate, and anodic alumina materials.

Material	Mean Pore Size (nm)	Mean T_{cp} (K)	Depression (K)	T_{cp} Range (K)
MCM-41 3.2	3.2	234	71	230–240
MCM-41 3.5	3.5	240	65	234–246
MCM-41 165	4.0	244	61	235–250
MCM-41 180	4.5	255	50	249–262
MZBN-100w3hd	6.7	262	43	249–276
MSU-H	8.3	265	40	255–276
MZBN-135w3h	12.2	277	28	265–291
SM-18-100-13	18	297	8	296–298
SM-35-100-13	35	305	0	302–307
SM-55-100-13	55	305	0	–
SM-80-100-13	80	305	0	–
SM-100-100-13	100	305	0	–

The trend of C_2H_6 T_{cp} versus mean pore diameter exhibits different behaviour to that of both CO_2 and CH_2F_2. Between 3.2 and 4.5 nm there is a very steep increase of the mean T_{cp}, as observed with the other two fluids. However, after this initial rise, the value of the mean T_{cp} appears to increase almost linearly with mean pore diameter up to the bulk value, which is estimated to occur around the 20 nm pore diameter region, as shown in the inset of Figure 2.47. This is in contrast to results obtained for both CO_2 and CH_2F_2, which display a plateau of T_{cp} in the 6.7–12.2 nm pore diameter range before linearly increasing up to the bulk value in the pore sizes $\geq$ 18 nm. The measured critical temperatures of CO_2, CH_2F_2 and C_2H_6, confined in the twelve separate materials are summarised in Figure 2.47.

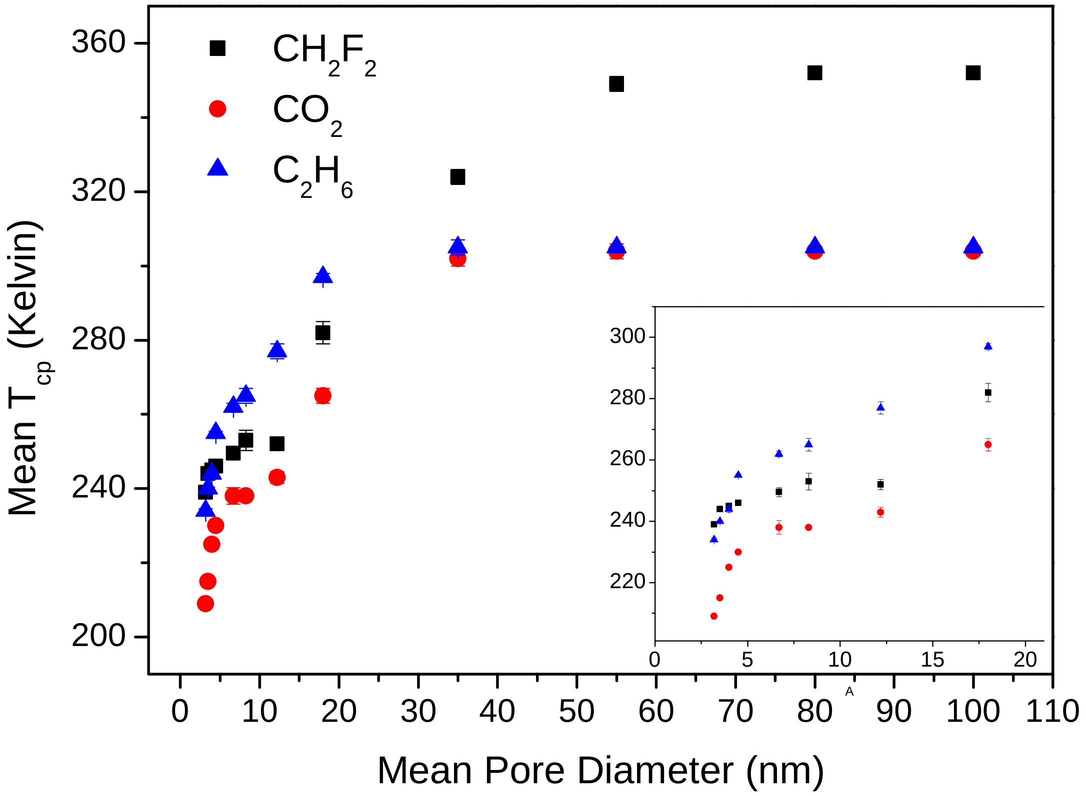

FIGURE 2.47: The mean pore critical temperature (T_{cp}) of CO_2, CH_2F_2 and C_2H_6 as a function of mean pore diameter determined by near-infrared spectroscopy. The **Inset** highlights the mean T_{cp} of the fluids confined in the smaller pore sizes ranging from 3.2–18 nm.

The decrease in reduced pore critical temperature (ΔT_{rp}) value as a function of the inverse pore diameter for ethane follows a more linear trend than that previously observed for CO_2 and CH_2F_2. This is in contrast to the trends observed the other two adsorbates which consist of a number of very distinct regimes that deviate from a linear relationship and are reminiscent to those predicted by Singh *et al.* for a strong fluid-wall interaction potential.[145] An interesting trend is observed when considering the ΔT_{rp} of each of the species across the pore size range, where CH_2F_2 consistently shows the most depressed T_{cp}, which is reflected in its higher ΔT_{rp} values, followed by the CO_2, and then finally the C_2H_6 (see Figure 2.48).

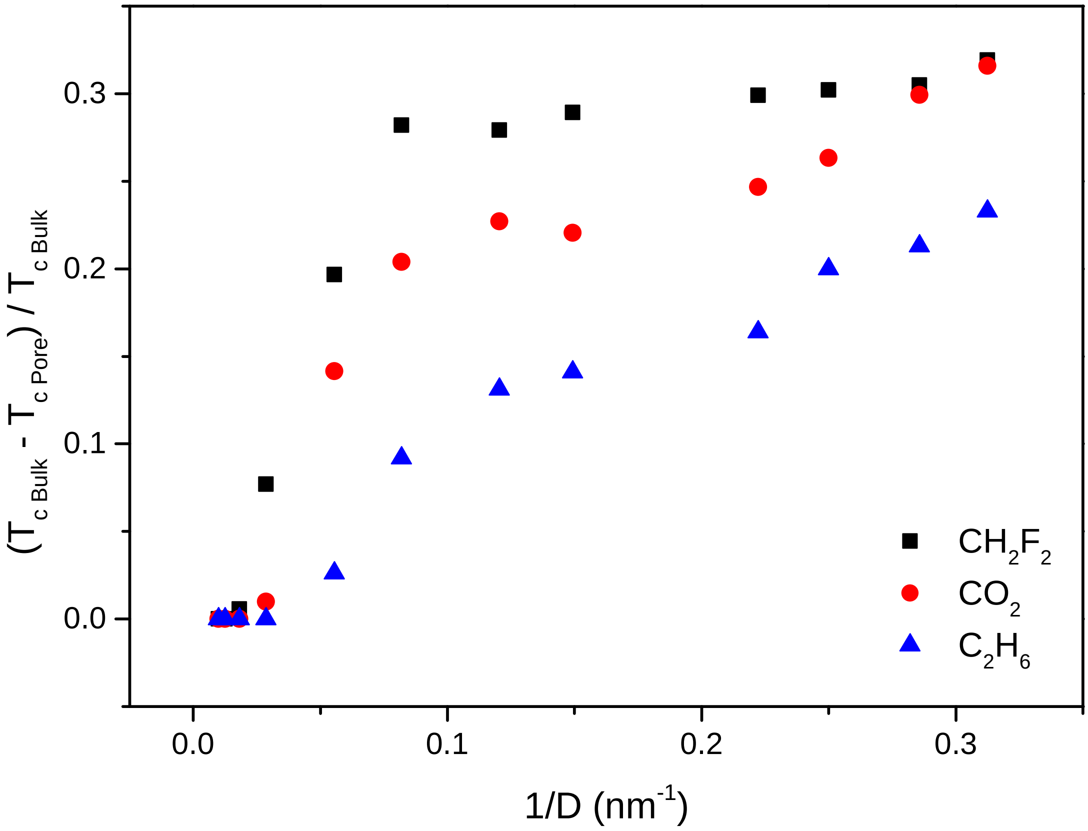

FIGURE 2.48: The decrease in reduced pore critical temperature (ΔT_{rp}) for CH_2F_2, CO_2, and C_2H_6 as a function of the inverse pore diameter.

This would indicate that polarity of the molecule or the ability of the molecule to be polarised is a paramount factor in this behaviour, as the dielectric constant of these fluids decreases from CH_2F_2 to CO_2 and finally C_2H_6. It would be expected that the polarity or the dielectric constant of the fluid would have a measurable effect on the fluid-pore wall interaction energy, with the most polar or polarisable fluid being able to interact with the wall surface charges with stronger dipole-dipole, dipole-induced dipole or hydrogen bonding interactions. As difluoromethane has a dipole moment without the presence of an electric field,[10] it would be expected to have the strongest interaction with the functional groups of the silica wall. The walls of a silica pore are known to be hydrophilic due to the presence of –SiOH surface groups,[186] these groups are also observed in anodic alumina templates,[179] so it would be expected that the hydrophobic C_2H_6 would only weakly interact with the pore wall in the vicinity of these groups, therefore lowering the fluid-pore potential. Although CO_2 and CH_2F_2 are not traditionally hydrophilic, they do possess oxygen or fluorine atoms that provide strong hydrogen bonding opportunities with the –SiOH surface groups or the -Si-O-Si- lattice. The deviation from linearity for the ΔT_{rp} value versus inverse pore diameter is observed to be dependant on the fluid-wall potential which is dependant on the polarity, dielectric or hydrophilic properties of the molecules, with the trend for C_2H_6 being the most linear and the trend for difluoromethane being the least (see Figure 2.48).

The effect of fluid-wall interaction energy on the depression of T_{cp} is rationalised in the following way by Fisher and Nakanishi in their scaling theory of criticality for fluids between plates.[85,139] The increase of interaction energy increases the likelihood of a film of adsorbate forming on the inside of the pore wall at pressures below the pore condensation pressure. This film of adsorbate will reduce the effective pore size for the molecules present in the core of the pore that undergo condensation. The stronger the interaction potential between the fluid and wall, the thicker this initial layer of adsorbate will be. This explains how the depression in the T_{cp} of CH_2F_2 is consistently the largest across all pore sizes. This also explains why even at very large pore widths that have no effect on the CO_2 or C_2H_6 T_{cp}, there is still a measured influence on the T_{cp} of CH_2F_2 as the effective pore width for this adsorbate would be smaller.

GC-TMMC studies estimating the density profiles of fluids in pores of varying widths suggest that the increase in fluid-wall interaction strength results in a smaller difference in density between coexisting vapour and liquid phases present in a pore.[144,145] This effect is due to the attractive wall potential not only facilitating the development of a dense adsorbate on the pore wall, but a gas phase in the core of the pore that possesses a highly enhanced density when compared to the bulk. The effect this has on the critical temperature can be rationalised the following way. The critical temperature of a fluid can be estimated from a least squares fit scaling law.[187,188] The T_c is proportional to the difference in densities in the two coexisting phases in a system and how this difference changes with temperature. Larger differences in coexisting densities result in higher values of T_c and smaller differences result in a lower T_c, as shown in Equation 2.8.

$$\rho_l - \rho_v = B\left(1 - \frac{T}{T_c}\right)^{\beta} \tag{2.8}$$

Where ρ_l and ρ_v are the densities of the coexisting liquid and gas phases respectively, B is a proportionality constant and β is the critical exponent which describes the power dependence the critical temperature takes relating to the order parameter, in this case density. As the difference in density between the two coexisting phases decreases, less thermal energy is required to drive molecules from the liquid phase to the gas phase in order to produce equivalent densities in both phases, removing the free energy barrier between the two. Therefore the critical point of the system is reached at a lower temperature value. At the smaller pore diameters the coexisting phases of the pore fluid were found to have a small difference in density, due to increased pore surface interaction, enhancing the density of both the gas and liquid phases, significantly lowering T_c. However in the larger pores, the density difference between phases was found to be greater, resulting in larger T_{cp} values.[144,145]

Singh *et al.* found a non-linear change in the density difference as the pore size increases, due to the crossover from a pseudo 2-3 dimensional geometry, creating a non-linear enhancement of the coexisting phase densities.[144,145] This occurs because the interaction potential in this model has a constant magnitude despite the pore diameter. At the smallest of pore sizes the wall potentials will overlap increasing their effect on the fluid. However, as the pore diameter increases this influence quickly decreases with fewer molecules in the centre of the pore being attracted to the pore wall. Finally, at the largest pore sizes only a small proportion of molecules in the pore which reside next to the pore wall will be attracted to this potential, leaving the majority of the pore substance uninfluenced by this potential. This results in a non-linear trend of ΔT_{rp} versus inverse slit width, with deviation from a linear relationship in agreement with the results in this work. This also explains why the deviation from the linear relationship is more apparent with the most polar or polarisable species and hence the strongest interacting fluid with the pore wall, as the magnitude of the fluid-wall interaction potential is larger, requiring a much larger pore size for the majority of the fluid to be out of the range of this potential. These factors also explain why even at very large pore widths that have no effect on the values of CO_2 or C_2H_6 T_{cp} there is still a measured influence on the CH_2F_2 T_{cp}. This is because the density difference of coexisting phases for this more strongly binding adsorbate, would be smaller even in the larger pore sizes, due the higher likelihood of the phases density being enhanced by pore wall potential, resulting in an overall lower T_{cp}.

2.3 Conclusions

Near-infrared spectroscopy has been used to probe the phase properties of carbon dioxide, difluoromethane and ethane confined in a range of porous silica, aluminosilicate and anodic alumina materials. It has been shown that there is a significant depression in the critical temperature of these confined substances when compared to the bulk counterpart and that the pore size has a measurable impact on the extent that the critical temperature is depressed. This is in agreement with the literature which shows that a confined fluid experiences a depression in T_c and this is dependent on pore size.[85,139–141] The range of pore sizes investigated in this study is also larger than any single experimental investigation in the literature, providing a more complete picture of the effect of pore size on a fluid's T_c. The results presented in this Chapter also suggest that the magnitude of the fluid-pore interaction potential plays a significant role in the extent of this depression. The depression in the critical temperature is most evident for difluoromethane, followed by carbon dioxide and finally ethane. This follows a trend ranging from the most polar and highest dielectric fluid difluoromethane, to the least polar and lowest dielectric fluid ethane, suggesting that the more polar and polarisable difluoromethane interacts strongly with the functional groups on the walls of the pore and is therefore depressed in its critical temperature the most. This again is also supported by theoretical investigations presented in previous literature studies.[85,139,145] The ΔT_{rp} versus inverse pore diameter value also exhibited a trend of difluorormethane being the least linear and ethane being the most, suggesting that the fluid-wall interaction potential determines the behaviour of the relationship between ΔT_{rp} versus inverse pore diameter, as predicted in the literature. The results obtained in this work therefore suggest that the predictions obtained from scaling theory and early empirical work, that the depression in critical temperature versus inverse pore diameter, may not apply to adsorbates that strongly interact with pore wall.

Chapter 3

Raman Spectroscopic and Theoretical Investigations of Confined Fluid Critical Temperature

3.1 Introduction

The investigation of the phase behaviour of fluids confined within nanopores utilising Raman spectroscopy is a relatively unexplored field. This Chapter will describe the use of Raman spectroscopy to investigate the depression in the critical temperature of carbon dioxide, difluoromethane and ethane when confined in the porous templates examined in the previous Chapter. The results determined by Raman spectroscopy will be compared to the NIR results obtained in the previous Chapter as a means of corroborating the findings. First an overview of literature Raman studies relating to this topic will be presented. This Chapter continues to focus on understanding the relationship between fluid-pore potential and the pore critical temperature. Therefore the primary means of studying both the critical and physical properties of pore confined fluids and their relationship to this interaction potential, which is through the use of theoretical studies, will also be discussed. Theoretical studies are often used because they provide a convenient approach to examine the thermophysical properties of pore confined fluids and how these properties relate to fluid-wall or fluid-fluid interaction parameters, which are applied in the simulation. This Chapter will then conclude with theoretical investigations which have been undertaken for this work to investigate confined fluid T_c and its relationship to the fluid-wall potential further.

3.1.1 Raman Spectroscopic Studies

Conventional Raman spectroscopy is rarely used in the literature for the purpose of studying the phase space relating to the critical parameters of a substance in a pore. However, fluid dynamics and interfacial phenomena within nanopores have been studied extensively through the use of CARS (coherent anti-Stokes Raman spectroscopy).[116,117,131] The CARS technique relies on two pump beams, the first beam excites the molecule to a virtual state, the second laser is tuned to the energy difference between the virtual state and an excited rotational-vibrational energy level. This second beam induces a transition of the molecule to a higher rotational-vibrational energy level, therefore, as the molecule scatters a second photon from the initial pump laser it undergoes a transition to an even higher energy virtual state and emits an anti-stokes photon to return to its ground state as shown in Figure 3.1.[189]

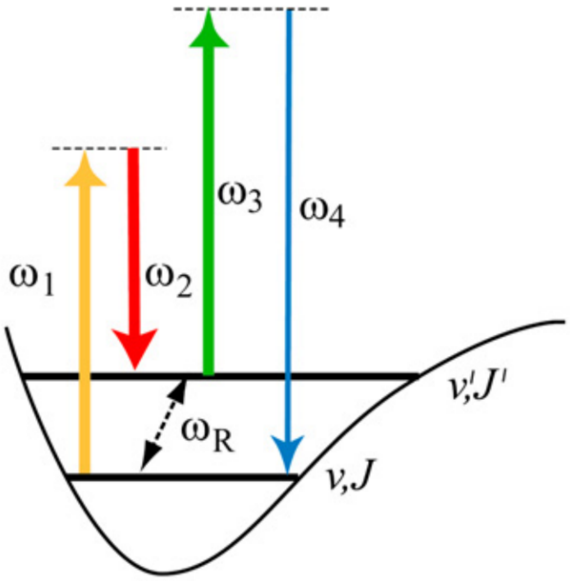

FIGURE 3.1: Schematic diagram of molecular states and the CARS signal generation process. The Raman transitions between ro-vibrational states ν, J and $\nu^{'}, J^{'}$ are probed with CARS spectroscopy where ω_1 is the pump beam frequency, ω_2 is the Stokes beam frequency, ω_3 is the probe beam frequency and ω_4 is the frequency of the CARS scattered photons. ω_R is the frequency of the Raman shift between the two probed ro-vibrational states. Taken and adapted from reference 190.

The benefits of CARS include a lack of fluorescence interference due to a blue shift of the detected signal relative to pump beam, good spatial resolution (200 nm in microscopy), good time resolution (*ca.* 100 fs) allowing for ultra fast spectroscopy and an increase in Raman scattering intensity compared to conventional Raman scattering.[189] An example of studying the behaviour of liquid subcritical CO_2 adsorbed in nanopores using Raman spectroscopy is reported by Arakcheev *et al.*,[116] where CARS was used to probe the inhomogeneity of the molecules in the pores. This inhomogeneity is reflected by the appearance of new bands in the Raman spectrum. Spectra were recorded of subcritical CO_2 at 303.7 K between 74–200 bar (1073–2901 psi) either as a bulk fluid or adsorbed in a nanoporous glass (NG) with a pore size of 4 nm. The measured Raman scattering linewidth in the experiments with the NG sample exceeds the measured linewidth from the bulk CO_2. This spectral broadening indicates the increased number of environments for the confined species. It is reasoned that there are two groups of molecules inside the pores, “core” molecules in the centre of the pore and molecules near surface layers that may be adsorbed onto the surface of the inside of the pore, or have a strong attraction to them.

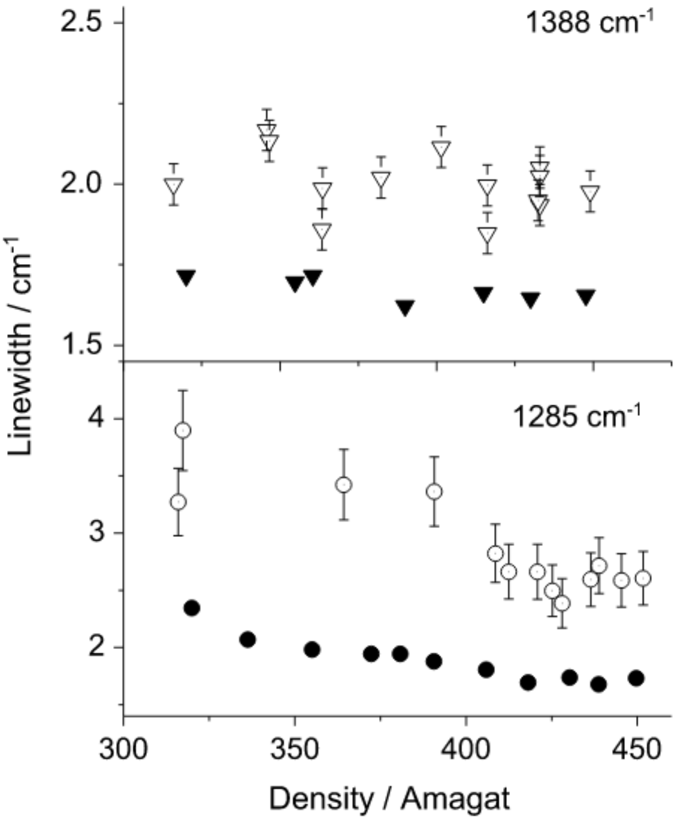

Figure 3.2: Density dependence of the Raman linewidth measured for both unconfined and nanoporous glass confined CO_2. The solid points are bulk CO_2 linewidths and the open points are those of confined CO_2. Density is given in amagat, where 1 amagat is the number of ideal gas molecules per unit volume at 1 atmosphere of pressure. Reproduced from reference 116.

Further studies with CARS looked more closely at the spectral contributions that lead to this broadening phenomenon and again showed that there was an increased Raman linewidth for CO_2 in the presence of a porous material.[117] The spectral features of CO_2 were fitted with a mathematical model that describes the interference of two closely lying resonant components in the spectrum and a non-resonant background, which accounts for the porous matrix. This allowed the determination of three Raman spectral features, which relate to three environments of the CO_2; the gas phase bulk, the pore condensed liquid-like molecules, and the interface liquid layer adsorbed to the pore wall (Figure 3.3).

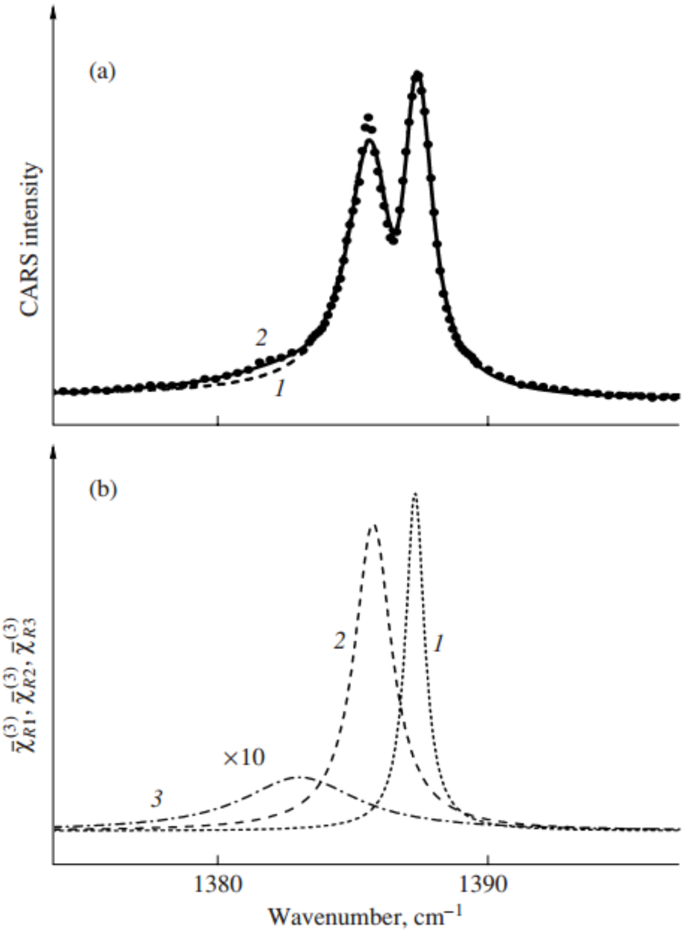

FIGURE 3.3: (a) Best-fit data obtained using a two-component model (1) with variable linewidths and positions, (2) best-fit data obtained using a three-component model. (b) The spectral contributions related to the (1) gas phase, (2) the liquid-like phase inside pores, and (3) the interface liquid layer inside the pores. Reproduced from reference 117.

In this case, the spectral linewidth and frequency of the contribution that corresponds to pore confined molecules at a subcritical temperature are comparable to those obtained for the bulk SCF. This indicates that the pore confined CO_2 is a supercritical fluid under bulk subcritical conditions. There was also no observed condensation within the pore at bulk supercritical conditions, suggesting that the confined CO_2 is already in a uniform supercritical state. Furthermore, Andreeva *et al.* used spectral fitting to isolate the contribution of the confined fluid and how this changed with pressure, allowing pore adsorption to be observed spectroscopically.[131] It was also determined, by studying peak linewidths, that pore condensation pressure depends on pore diameter, with the smaller pore size exhibiting a lower condensation pressure, as shown in Figure 3.4.

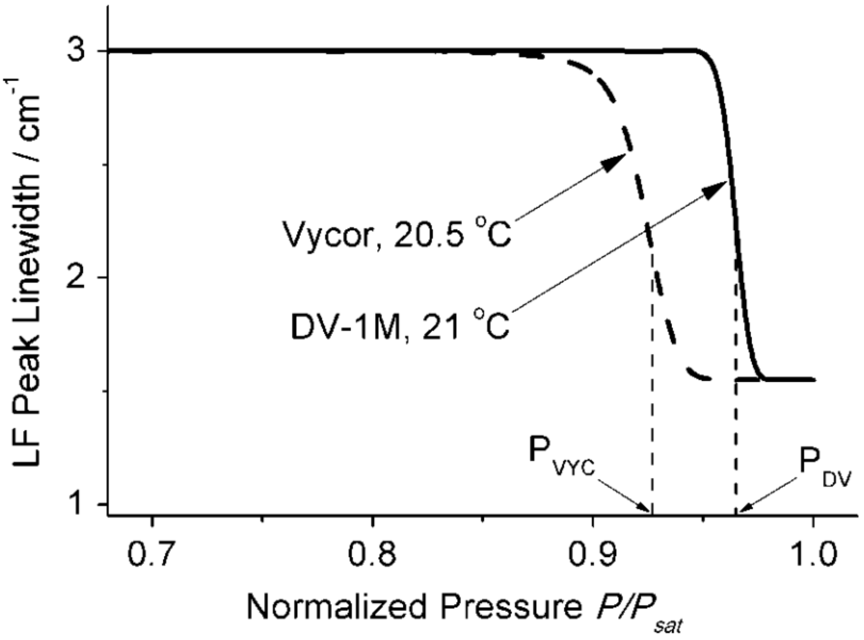

FIGURE 3.4: Change in Raman scattering linewidth fitted with a Lorentzian profile as a function of pressure, showing the pore condensation of CO_2. The smaller pore Vycor is shown to lower CO_2 condensation pressure than the larger pore DV-1M. Reproduced from reference 131.

An alternative approach was taken by Yi *et al.* to investigate confinement of benzene in nanoporous silica glasses with pore sizes ranging from 1.4–4 nm.[191] The polarised and de-polarised Raman spectra of the totally symmetric benzene-d6 (deuterated benzene) vibrations were studied at 295 K and atmospheric pressure. This allowed the vibrational relaxation rate (τvib^{-1}), the reorientational relaxation time (τ_{reo}), and the perpendicular diffusion constants (D$\perp$) to be obtained from the totally symmetric ν_2 band. The parallel diffusion constants (D$\|$) were obtained from the doubly degenerate ν_{16} band. The results of this study showed that all these parameters are significantly affected by the confinement of the molecules. As pore size decreases, τvib^{-1} decreases and τ_{reo} increases. The dependence of τvib^{-1} and τ_{reo} on the pore size is proportional to 1/R (R = pore radius), indicating a dominant surface interaction effect rather than just a spatial confinement effect. This is because the increased surface interactions in the smaller pores hinder molecular vibrations and reorientation, decreasing the τvib^{-1} and increasing τ_{reo}. Importantly the authors point out that in their previous NMR studies of confined polar liquids,[192] these surface interaction effects were observed to dominate the confined nuclear relaxation times in the same manner. This reinforces the point that polar fluids exhibit strong surface driven effects due to the large fluid-pore potential. Additionally D$\|$ and D$\perp$ decrease with pore size showing that diffusion is severely limited at the smallest of pore diameters.

Restricted geometry effects on p-azoxyanisole (PAA) liquid crystal phase transitions have also been studied using Raman spectroscopy.[193] The isotropic–nemetic and nemetic–solid phase transitions could be monitored spectroscopically, where the nemetic phase is a state of roughly aligned liquid crystal and the crystals in the isotropic phase have no alignment.[194] This was achieved by studying the Raman linewidth of the benzene ring stretch, band positions of the benzene-oxygen stretch, and intensity ratios of bands at 1244 and 1272 cm^{-1}, which are characteristic of the solid and nemetic phase respectively and how they change with temperature. In a similar manner to a fluid's critical temperature, the solid to nematic phase transition temperature of PAA within the pores was found to be depressed when compared to the bulk phase. For the pores with an average diameter of 8.9 nm the depression was found to be 33 K below the corresponding bulk phase transformation. It was shown that the depression in transition temperatures was linearly dependent on the reciprocal of the pore diameter. The phase transition temperatures were also found to extend over a wide temperature range, attributed to the fact there is a distribution of pore diameters, as shown in Figure 3.5. As expected, the phase transition takes place at higher temperatures in larger pores and lower temperatures in in smaller pores, which results in a broad temperature distribution. In the bulk phase the transitions of PAA are first order in nature exhibiting a sharp discontinuous change in alignment, as indicated by the abrupt changes in order parameters, Raman band intensity ratio, linewidth, and band maximum position. In the pores, the transitions occurred over a wide temperature range and resembled continuous phase transitions, confirming a range of critical temperatures.

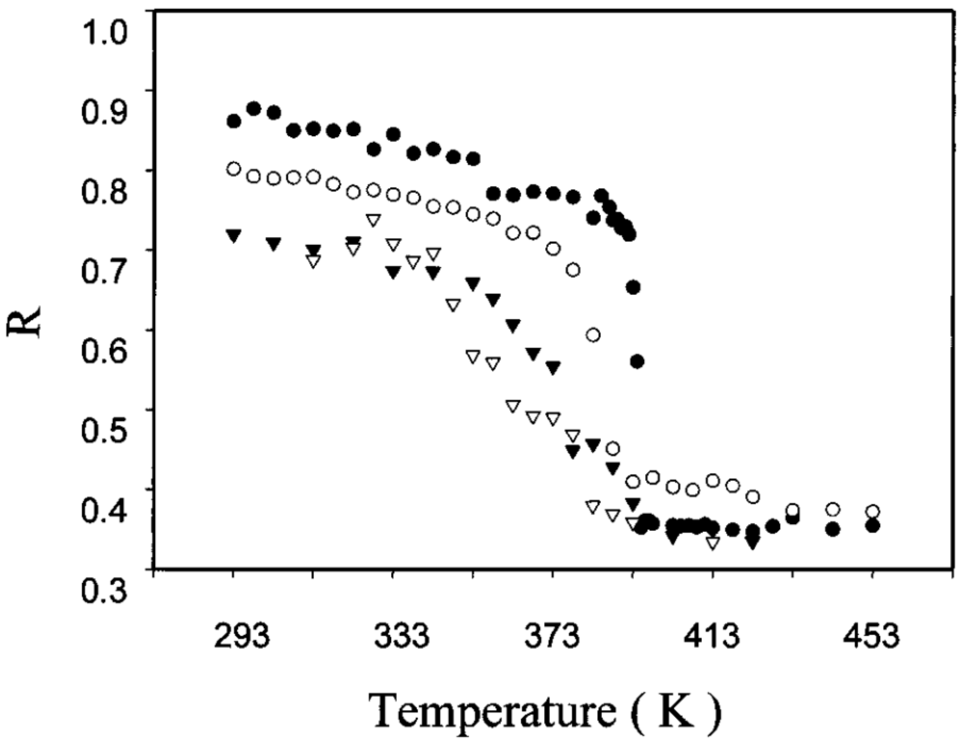

FIGURE 3.5: Peak intensity ratio (R) of characteristic bands relating to the PAA phases in pores of different sizes. The high and low R values correspond to the solid phase and nemetic phases respectively. The solid circles are bulk PAA, open circles are PAA in 20 nm pores, solid triangles are PAA in 16 nm pores and the open triangles are PAA in 8.9 nm pores. Reproduced from reference 193.

Raman spectroscopy however can require complex interpretation of spectra to determine confined fluid properties and does not provide direct snapshots of the fluid's behaviour within the pores. However a move to theoretical studies allows for a more thorough examination of fluid inhomogeneity in pores.

3.1.2 Theoretical Studies

As this Chapter presents theoretical work to support the findings obtained from experiment, a background of literature computational work undertaken in this area is given in this section. Theoretical investigations offer a convenient way of studying the phase properties of confined fluids. They allow for the calculation of the pore confined properties of a substance such as critical pressure and density, which are difficult to measure experimentally as usually only external parameters such as temperature and pressure can be measured directly in an empirical setting. The simplest theoretical approach using a scaling theory with an Ising model fluid confined between parallel plates, shows a depression in the critical temperature upon confinement.[85] This model consists of a three dimensional lattice with a spacing, consisting of layers of sites populated by Ising spins ($S_i = \pm 1$) which correspond to a lattice site either filled or left vacant by molecules, interacting *via* nearest neighbour couplings. This theory relies on macroscopic thermodynamic assumptions such as the surface tension and density of the fluid, so it may not provide the most accurate picture. In order to fully investigate the critical behaviour of pore confined fluids, molecular simulations are required. An overview of the simulations attempted in the literature will be presented.

3.1.2.1 Density Functional Theory

Density functional theory (DFT) calculations offer a more fundamental approach to study the phase properties of confined fluids without making assumptions based on the macroscopic properties of fluids. The use of DFT methods have allowed for the calculation of vapour-liquid interfaces,[195] adsorption,[96,106] and a material's pore size distribution from experimental isotherms.[196] This demonstrates that a DFT approach is a powerful tool to investigate the properties of confined fluids. DFT calculations preformed on a Lennard-Jones fluid, which is a fluid consisting of spheres interacting *via* a Lennard-Jones potential, in slit-like pores have been carried out by Peng *et al.*[197] This method has been used to investigate the calculated density profiles, adsorption isotherms, pressures, and fluid phase transitions for various slit widths and fluid-solid interaction potentials. This approach also makes use of a mean field weight function (MFWF) along with DFT. This makes the procedure more computationally efficient when compared to conventional DFT, as a mean field approach treats the interaction of a single body with others in the system as an averaged field. It was found that when the fluid was confined in a slit-like pore, the critical temperature was depressed further as the pore size decreased and as the fluid-wall interaction energy increased. The increasing fluid-wall interaction energy for the smaller pore diameters shifted the critical density to higher values than observed for both the bulk simulation and the larger pores, in which the critical density values were comparable (see Figure 3.6). The results are shown to reproduce the vapour-liquid coexistance and critical temperatures of confined methane predicted by Monte Carlo simulations and also predict layering and capillary transitions that statistical methods may not be sensitive to.

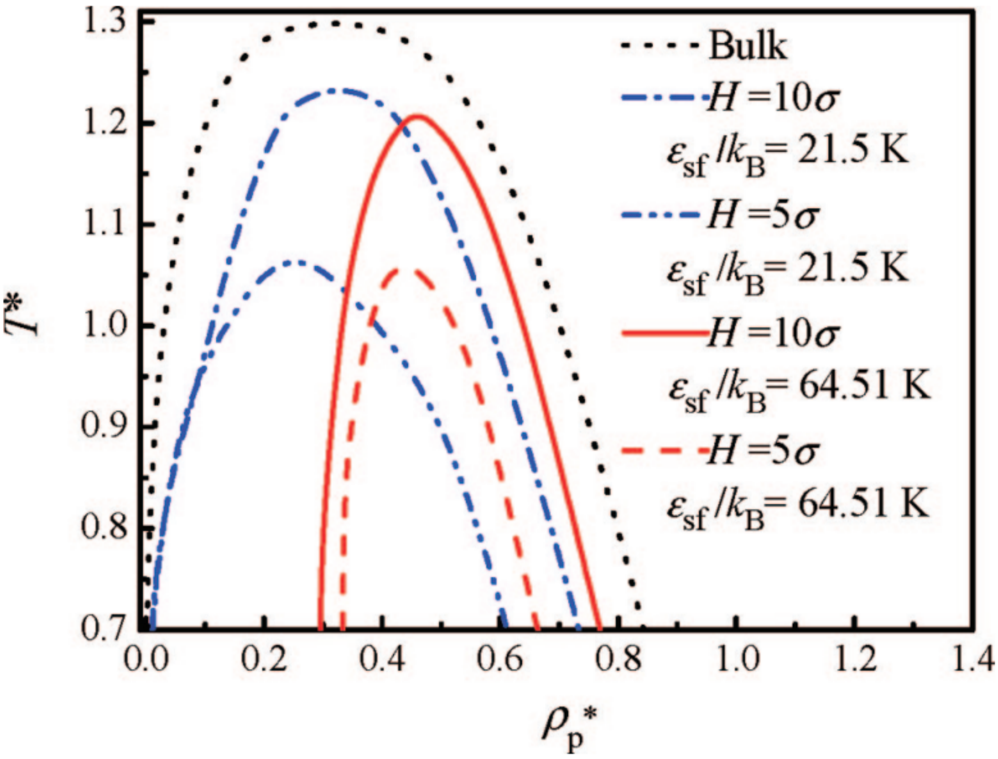

FIGURE 3.6: Predicted vapour-liquid coexistence diagrams of the Lennard-Jones fluid confined in the slit-like pores with different pore widths (H) and wall-fluid interaction strengths (ε_{sf}/k_B). Reproduced from reference 197.

3.1.2.2 Monte Carlo Methods

Statistical methods have also extensively employed to model the properties of confined fluids. Monte Carlo (MC) simulations preformed by Binder and Landau investigated a three dimensional lattice gas model with nearest-neighbour attractive interactions, confined in a slit-like pore.[198] This study varied chemical potential, temperature, and short range interaction strength between the walls and the gas to determine their effect on the phase behaviour in the pore. A distortion of the gas-fluid coexistence curve due to the attractive walls was also calculated, with a lowering of the liquid phase density and an increase of the gas phase density in the pore.

Other simulations studying the transitions of a fluid in a disordered porous material show that the fluid phase diagram changes vastly in appearance in the porous material, displaying a narrowed vapour-liquid coexistence curve.[199] As expected, the critical temperature is lower than that of the bulk. The critical density and width of the vapour-liquid coexistence region depend upon the relative strength of fluid-solid interactions, with a high interaction energy promoting a dense vapour phase and high fluid density near the solid matrix. The vapour-liquid coexistence was also found to be narrowed by the introduction of solid matrix disorder, a result of inhomogeneity of the adsorbed liquid phase. The study also provides evidence of an additional phase transition at lower temperatures, associated with wetting or drying behaviour of the fluid in the smaller confines of the disordered matrix.

Grand canonical Monte Carlo (GCMC) has also been used to study sorption phenomena.[200] Simulation of adsorption and desorption behaviour of molecules into pores allowed for the study of hysteresis loops and the reason for their occurrence. The results of this study indicates that the hysteresis loops are indeed due to metastable states of the adsorbed molecules, including metastable vapour and liquid phases. It was also found that by varying the strength of the solid-fluid potential adsorption isotherms and hysteresis loops that closely resemble those seen in experiments could be obtained with hysteresis branches in the adsorption/desorption isotherm (see Figure 3.7).

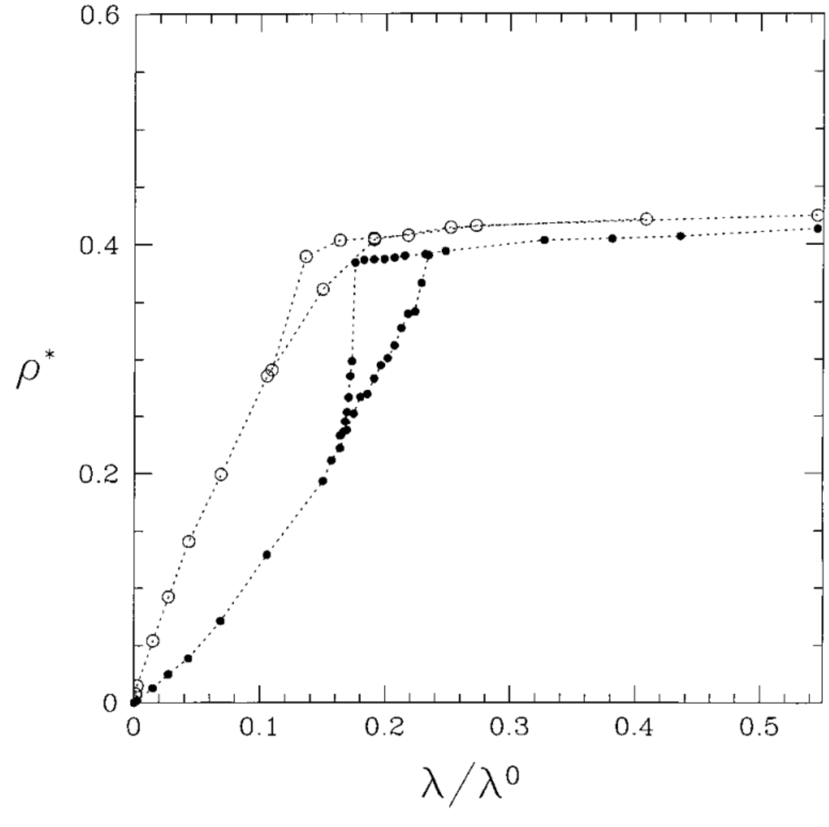

FIGURE 3.7: Adsorption/desorption isotherms of density versus relative activity (λ/λ_0), where λ_0 is the activity at the bulk vapour pressure. Activity is an exponential function of the difference between the chemical potential and the ideal chemical potential of the substance as a ratio to the ideal gas constant and temperature. The substance is confined in disordered adsorbent with 1.5 α, a high fluid-solid interaction (filled circles) and 1.8 α (open circles), a low fluid-solid interaction. Where α is a ratio of the solid fluid potential well depth to the fluid-fluid potential well depth. Reproduced from reference 200.

GCMC simulations have been used to model supercritical methane adsorption at 273 K on an open graphite surface and in slit-like micropores of different sizes.[201] The effect of the pore size on the maximum surface excess and isosteric (fixed surface coverage) enthalpy of adsorption for methane on these surfaces was studied, with methane storage applications in mind. A detailed microscopic picture of methane densification near the homogeneous graphite wall in the slit-like pores was visualised with calculated local density profiles and snapshots. This method also allowed for the determination of reliable pore size distributions, which could be obtained for the two microporous activated carbon fibres modelled in this study. The pore size distribution information was calculated from the adsorption isotherms obtained *via* the GCMC simulation.

Further studies of the phase coexistence of methane in slit-like graphite pores, using a simple lattice model, found that the critical temperature will be lower in narrower pores and a strong adsorption field.[202] A linear dependence of the critical temperature on the pore width was determined. By extrapolating the linear trend to wider pores, it was estimated that in graphite pores with a diameter of 10–15 nm, the critical temperature will still be substantially (several degrees) lower than that in the bulk phase. This is despite the fact that the state of methane in the core of the pore is analogous to equilibrium bulk phase state. However, for a weak adsorption field, the critical temperature approaches that of the bulk system in pore diameters as small as 8–10 nm. The critical density in the pores stays higher than that of the bulk in relatively small pores, but decreases toward the bulk value as pore width increases.

Grand canonical-transition matrix Monte Carlo (GC-TMMC) simulations have been used to model vapour-liquid equilibria of square-well fluids and alkanes,[138,143–145,203] along with surface tension and contact angle (wetting). These simulations where carried out in a range of slit-like pore sizes with various fluid-wall interaction strengths. Square-well fluids are a convenient way of simulating a pore confined fluid, as they provide a simple way of modelling fluid-fluid and fluid-wall interactions as hard spheres with attractive short range interactions and repulsive interactions if the molecules are too closely packed.[204] Rosch *et al.* have used this technique to produce confined phase diagrams.[138] The calculations indicate that the pore critical temperature is dependant on both the strength of the pore-fluid and fluid-fluid interactions, both of which are shown to have an influence on the wetting contact angle of the pore confined fluid. The calculations also indicate that the substrate conditions that produce maxima in pore critical temperature represent a balance between the strength of pore-fluid and fluid-fluid interactions, with this balance is quantitatively linked to the contact angle that the fluid exhibits in a particular pore. Low pore-fluid and high fluid-fluid interaction strengths increase the contact angle of the fluid with the pore, decreasing the wetting of the pore wall. This increases the pore critical temperature as the pore fluid is more bulk-like in its behaviour and requires higher thermal energy to reach a supercritical state. GC-TMMC is therefore shown to be an excellent method of calculating the critical and physical properties of a confined fluid.

Singh and coworkers have also investigated the critical properties of simple model fluids in pores using GC-TMMC.[144,145,203] The properties of methane, butane and octane have been calculated in slit-like models for graphite and mica pores.[144] By examining the trend of the critical temperature shift against the inverse of the slit width, it is observed that the rate of the critical temperature shift increases with decreasing slit width, until a limit of the T_c shift is reached.

The change in pore critical temperature with inverse slit width is found to vary in a non-linear fashion at a fixed fluid-wall potential. The presence of two regimes in this relationship is due to the fact that the pore geometry crosses from pseudo one dimensional to three dimensional, with the density enhancement of the pore adsorbed species becoming less prominent at the large pore widths of more than a few molecular diameters, due to the fixed fluid-wall potential (Figure 3.8). This indicates that the difference between the density of coexisting phases has an influence on the pore T_c value.

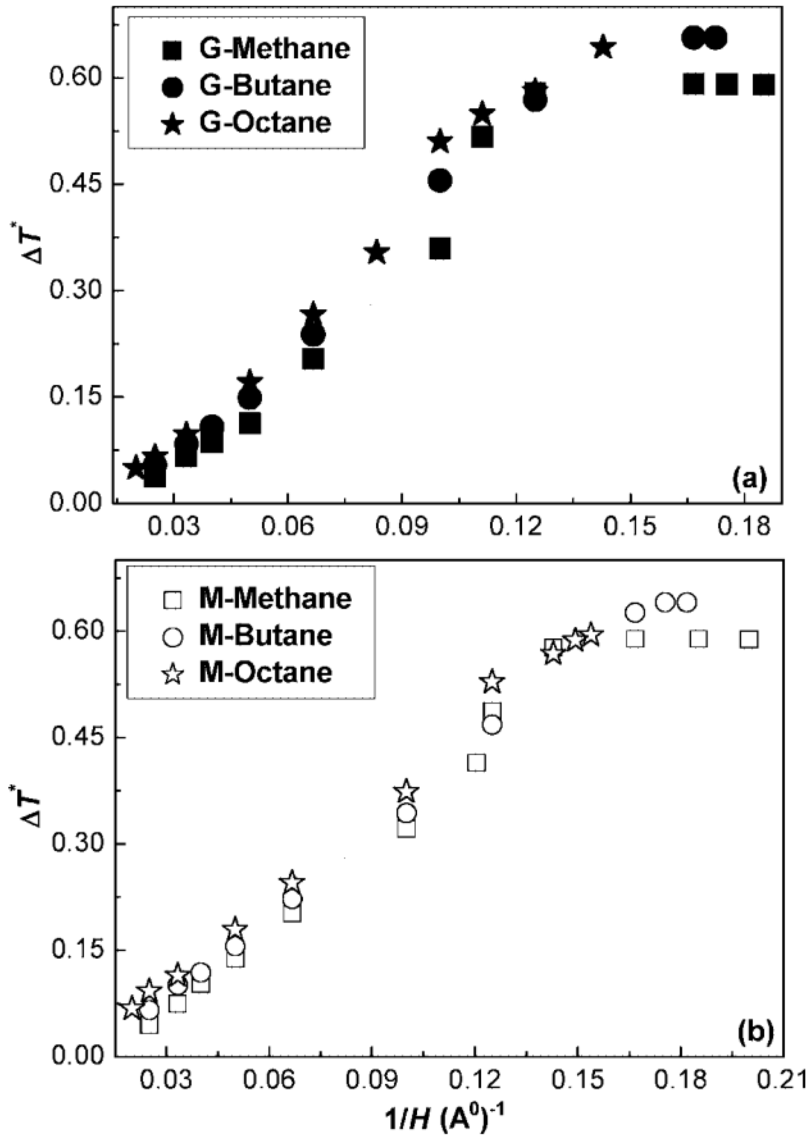

FIGURE 3.8: Shift in the critical temperature vs inverse of the slit width (H) for n-alkanes in (a) graphite and (b) mica slit pores. Reproduced from reference 144.

In other work, the influence of pore size on the shift in the critical temperature of square well fluids, with varying fluid-fluid interaction energies was studied in slit widths ranging from 12 to 1 molecular diameters.[143] The dependence of the shift in T_c versus inverse slit width for the fluid confined in a repulsive pore was found to follow two linear regimes and was therefore non-linear, as shown in Figure 3.9. The first linear regime, with a large change in the pore critical temperature shift with pore diameter, continued down to 2.5 molecular diameters (1/H=0.4). This even occurred for fluids with relatively small fluid-fluid interaction potential. This behaviour was even seen in slightly smaller pores for the fluids with a higher fluid-fluid potential, where the first linear regime ends at a slit width slightly higher than 2 molecular diameters (1/H=0.5). The second linear regime at the smallest of pore sizes consists of of a constant shift in critical temperature with decreasing pore size, where the effect of confinement on the pore fluid critical temperature reached a limit. This non-linear behaviour is explained by the change in fluid-fluid interaction range due to a change in constraint with pore size, despite a constant fluid-fluid potential magnitude. The two distinct regimes are therefore accentuated by the increase in fluid-fluid interaction potential. Surface tensions at all the fluid-fluid interaction ranges were found to be lower than their corresponding bulk value. However the linear relationship between surface tension and temperature remained, even under confinement. All except the smallest of the fluid-fluid potentials modelled displayed this behaviour, as it was found to be difficult to locate the vapour-liquid coexistence in pores with a slit width less than 2.5 molecular diameters (1/H=0.4) for the least attractive fluid (λ=1.25).

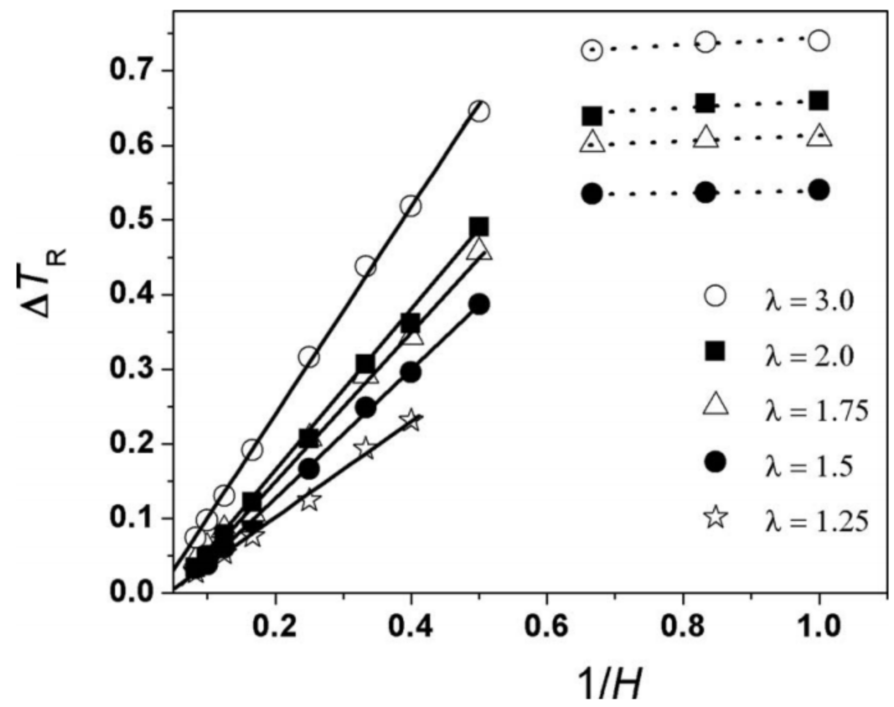

FIGURE 3.9: Shift in the critical temperature (ΔT_R) vs inverse of the slit width (1/H) for different fluid-fluid potential well extents(λ). Reproduced from reference 143.

The determination of critical parameters using least squares fitting with scaling laws, on GC-TMMC calculated coexistence data has been used to study the influence of pore size on the phase coexistence envelope and various critical properties.[145] The calculations were preformed in slit-pores with sizes ranging from 40 to 1 molecular diameters, for a model fluid under a range of fluid-pore interaction energies. It was found that the dependence of critical temperature shift versus inverse of the slit width is not linear and is in fact made up of multiple linear regimes. These distinct linear regimes become more prominent as the surface-fluid attraction strength is increased, as shown in Figure 3.10. There is a large change in the pore critical temperature as the pore width increases in the range of slit widths that are only a few molecular diameters wide (*ca.* 0.6–0.4 1/H).

This rate of change is much slower as the pore width increases from quasi 2D to 3D geometry. The non-linear dependence of critical temperature shift versus inverse of the slit width, relates to the non-linear change in the difference between the pore liquid and vapour phases as the pore changes from pseudo 1D to 3D geometry, with a fixed magnitude of the fluid-pore potential.

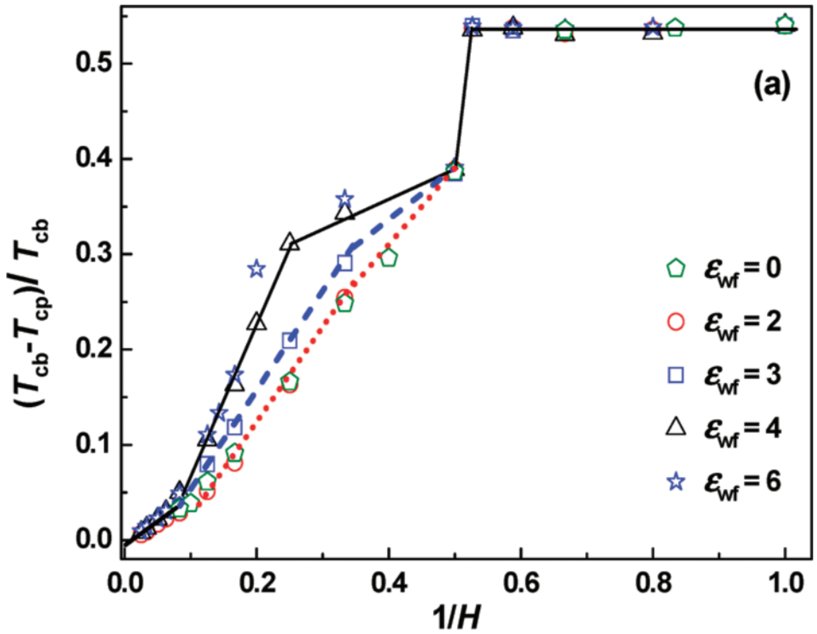

FIGURE 3.10: Shift in the pore critical temperature vs inverse slit width (1/H) for different wall-fluid interactions (ε_{wf}). Adapted from reference 145.

3.1.3 Aims

The aim of this Chapter is to present a unique approach to measure the critical temperature of a fluid confined in a pore, using Raman spectroscopy. This approach will ascertain the relationship between pore size and the critical temperature of confined carbon dioxide, difluoromethane and ethane in a range of porous templates. The methodology will then be used to corroborate the results obtained by NIR spectroscopy in the previous Chapter. The validity of both the NIR and Raman spectroscopic methods will then be evaluated and finally the results will then be compared to a theoretical study carried out using grand canonical Monte Carlo simulations. These simulations will help to provide some insight into the relationship between pore critical temperature, pore size, and the fluid-pore interaction potential.

3.2 Results and Discussion

3.2.1 Raman Spectroscopic Study of Phase Transitions to Determine Critical Temperature

The Raman intensity for a given vibrational mode of a pure substance is directly proportional to its density or concentration,[205] given by the following equation:

$$I_R = \sigma L C I_0 K \tag{3.1}$$

Where I_R is the observed Raman intensity, σ is the apparent Raman scattering efficiency, L is the interrogated volume of the sample and C is the species concentration or density, I_0 is the incident intensity, and K is the instrumental throughput. Assuming σ, L, I_0, and K are constant, this equation simplifies as:

$$I_R = mC \tag{3.2}$$

Where m is the gradient of intensity change when the concentration or density changes, which can be determined experimentally. This relationship allows the characteristic phase transition of CO_2 to be observed by plotting the intensity of the ν_1 Fermi diad intensity against pressure at a set temperature. As observed with the near-infrared measurements, these isotherms adopt characteristic shapes depending on if the substance is undergoing a phase transition from gas to liquid, where it displays a sharp increase in density and therefore intensity (Figure 3.11 **Top**), or from gas to supercritical fluid displaying a smoother increase in density, and therefore intensity (Figure 3.11 **Bottom**). This indicates whether a substance is above or below its critical temperature. At lower densities of the substance, the Fermi diad of CO_2 has a relatively small intensity, which then increases and red-shifts by *ca.* 4 cm^{-1} toward higher densities approaching and beyond the phase transition.

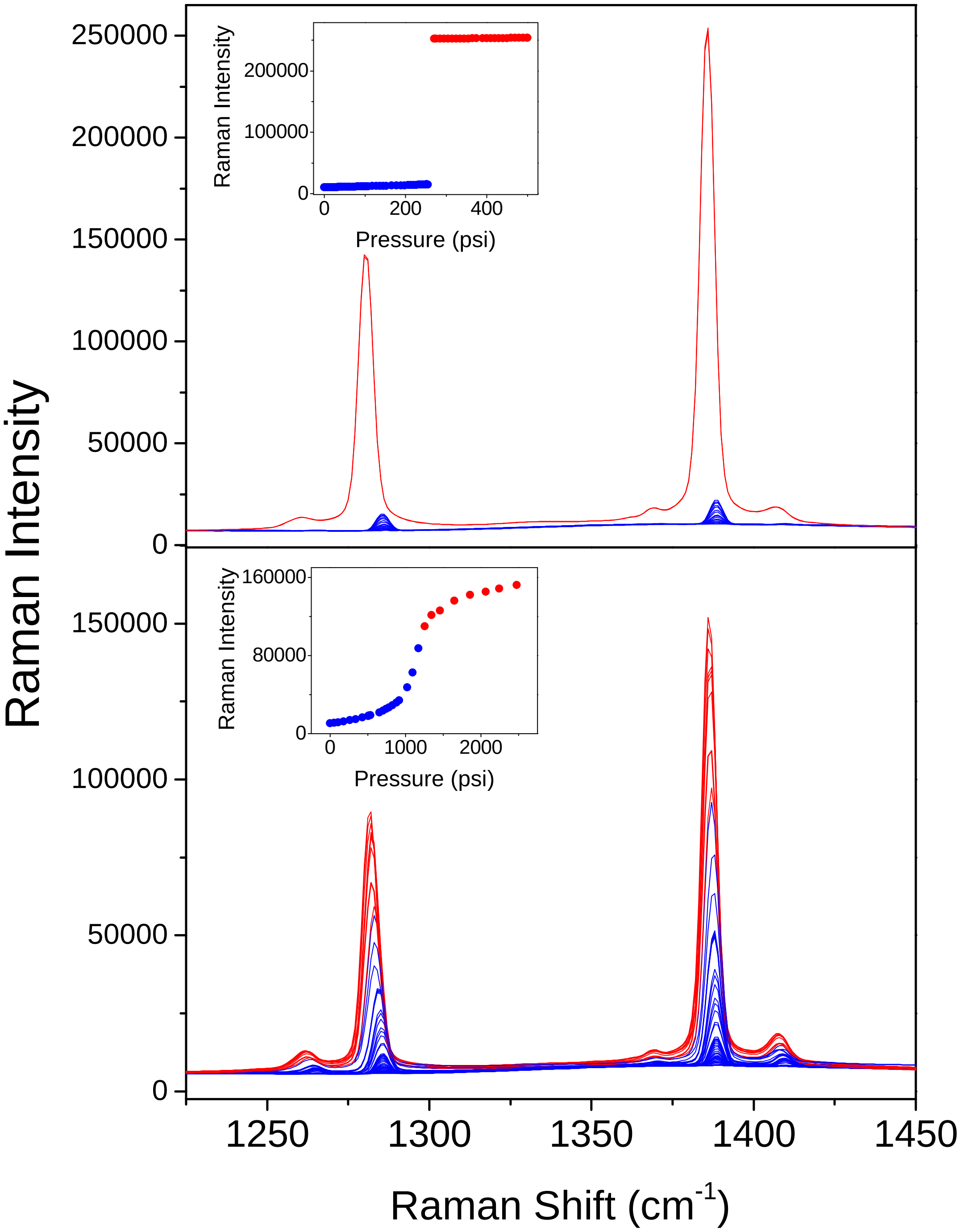

FIGURE 3.11: Raman spectra of the CO_2 Fermi diad centred at 1325 cm^{-1},[206] recorded using the high-pressure-low-temperature (HPLT) cell with increasing pressure, below its T_c at 253 K **(Top)** and above its T_c at 308 K **(Bottom)**. The **(Inset)** demonstrates how the intensity of the higher energy ν_1 band changes with pressure and during the phase transition. The spectra and points at pressures representing the gas phase are shown in blue and those after condensation to a liquid or supercritical fluid are shown in red.

The observed phase transition from the Raman spectroscopic measurements again correlate well to change in density of CO_2 predicted from the NIST database,[10] as shown in Figure 3.12.

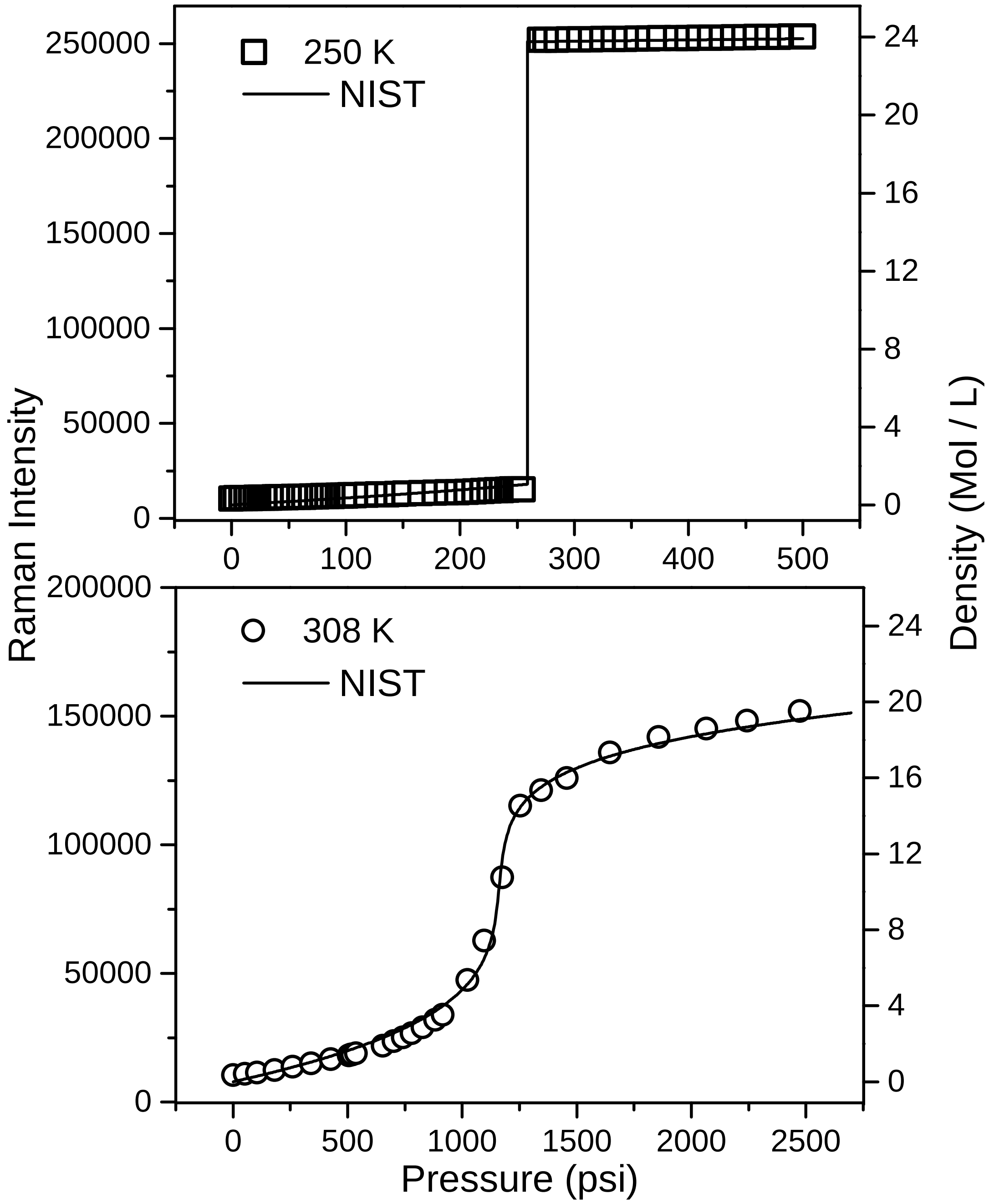

FIGURE 3.12: Raman intensity of CO_2 Fermi diad ν_1 band (open symbols) as a function of pressure below its T_c at 250 K **(Top)** and above its T_c 308 K **(Bottom)**. This data is compared to the change in density of CO_2 with pressure taken from the NIST database (black line).[10]

3.2.2 Studying the Phase Behaviour of a Confined Substance Using Raman Spectroscopy

In order to determine the critical temperature of a confined substance utilising Raman spectroscopy the following approach is taken. The porous material was loaded into the HPLT cell (see Chapter 5 for a description of the cell), filling its entire path length. The Raman laser was then focussed through the surrounding vacuum shroud and the front quartz window of the cell approximately into the centre of the porous material layer as shown in Figure 3.13. The opaque material allowed for the focal point of the Raman laser to be observed on its outer surface. The probe could then be moved toward the material moving the laser focal point into the centre of the porous material.

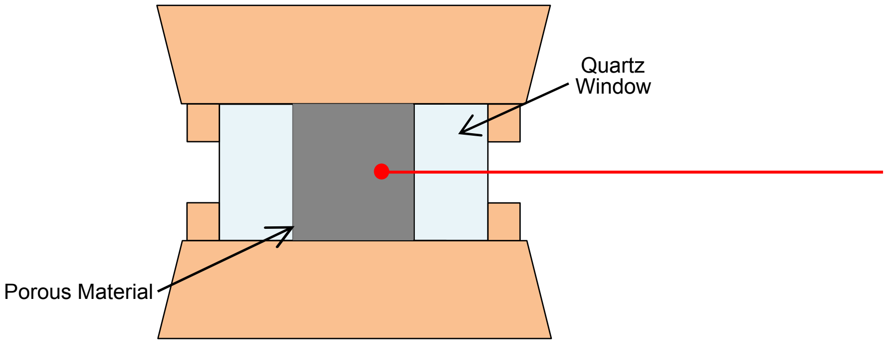

FIGURE 3.13: A diagram of the Raman laser (red) focussed into the porous material within the HPLT cell.

The pressure of the adsorbate is increased slowly as Raman spectra are collected. If the Raman band intensity is plotted against pressure, both the adsorption isotherm consisting of initial adsorption and the confined fluid phase transition can be observed (Figure 3.14). The bulk phase transition, as seen previously with NIR is also evident. This shows that Raman spectroscopy can be used to measure adsorption isotherms and allows the study of confined phase behaviour in a simple way not previously used in the literature. The majority of the cell is filled with the porous material, therefore there is very little contribution of the bulk fluid to the Raman spectrum, with only the small space between the particles or films of the porous material where the bulk phase can exist. This is evident as the bulk phase transition, which is observed after the confined phase transition, is relatively small in magnitude compared to that which is observed in the NIR experiments where a portion of the path length is unoccupied by the porous material.

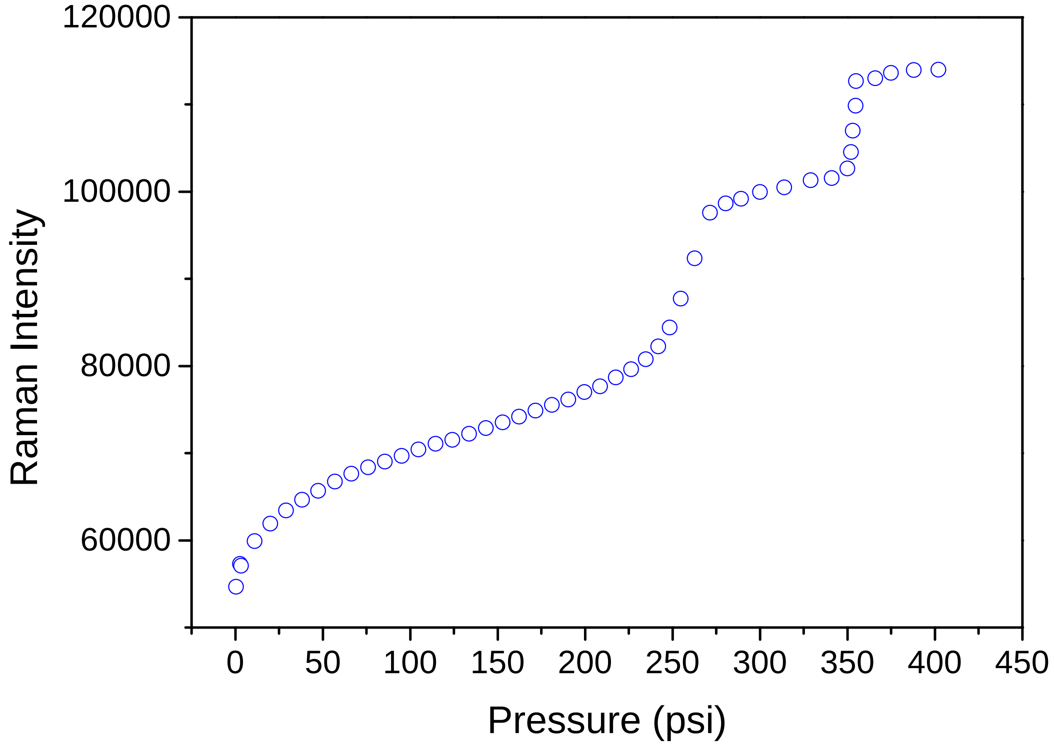

Figure 3.14: A plot constructed from the ν_1 Raman intensity of CO_2 as a function of pressure in the presence of 4.0 nm pore size MCM-41 silica at 260 K.

A different approach to the NIR studies was taken in order to deterimine the pore critical tempreture. This was due to the lack of a viable internal standard present in the Raman spectra belonging to the porous material. The porous silica bands are hidden by the quartz window Raman bands and any anodic alumina bands are particularly weak, even with long collection and exposure times to the Raman laser. Morishige *et al.* determined the critical temperature of a substance by studying its adsorption isotherm as a function of temperature.[73,74] In this approach, the inverse slope of the confined substance's phase transition (step in adsorption), measured from the adsorption isotherm is tracked with temperature. This allows the point at which the steep discontinuous first order phase transition (gas–liquid) in the pore progresses to a smoother continuous phase transition (gas–supercritical fluid), and therefore the pore fluid's critical temperature could be determined.[207] Using Raman spectroscopy to measure the absorption isotherms of the adsorbate into each of the templates, this method could be replicated (see Figure 3.15).

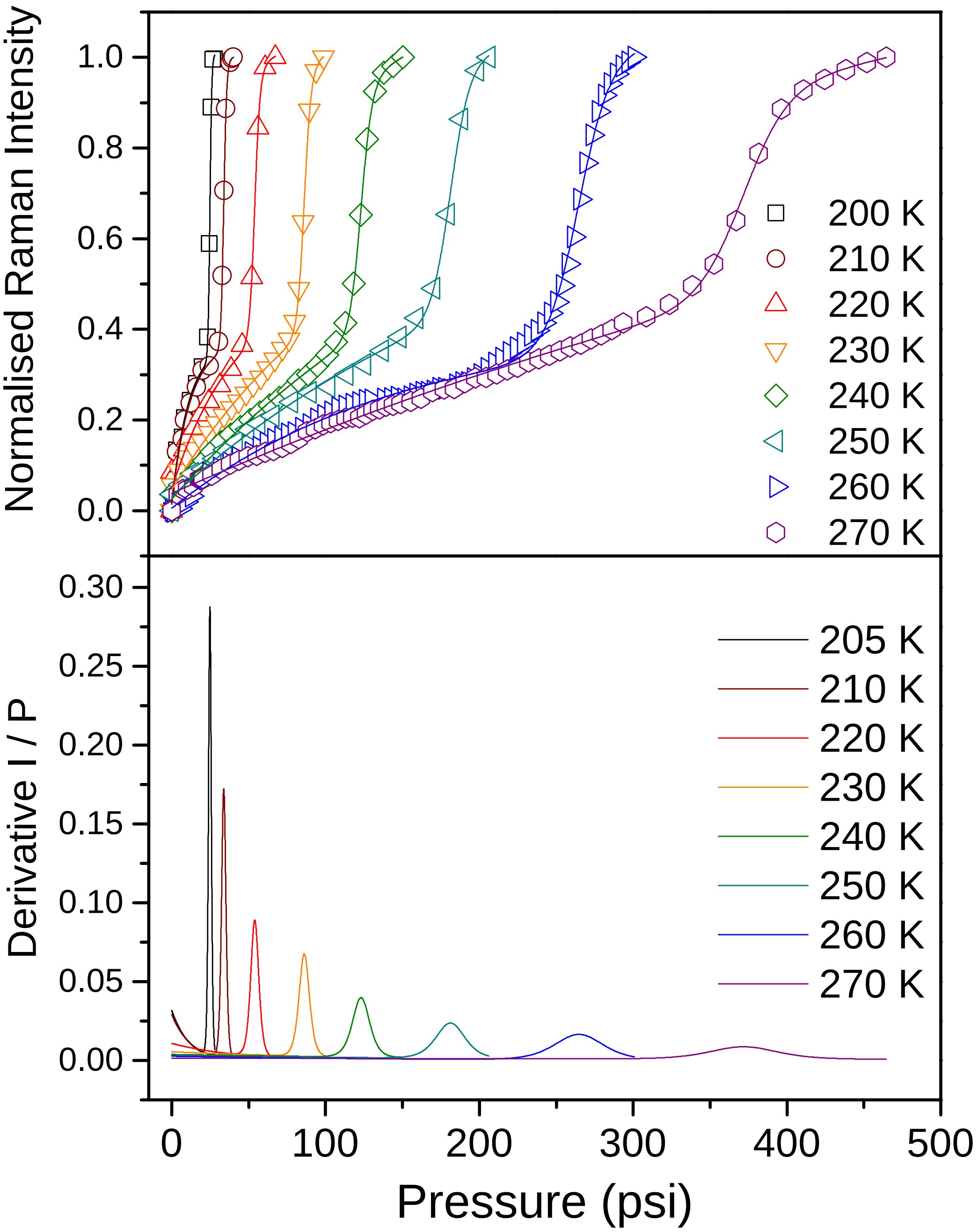

FIGURE 3.15: **(Top)** CO_2 at a range of temperatures undergoing a phase transition confined in MCM-41 with a mean pore size of 4.5 nm. The data is fitted with a bi-dose response function. **(Bottom)** The first differential of the fitted isotherms obtained from CO_2 undergoing its phase transition within 4.5 nm diameter MCM-41.

The obtained isotherms, where possible, are fitted with a bi-dose response function. This allows the gradient of the pore fluid phase transition to be determined with greater confidence as gradient values obtained with fewer points have to be interpolated.

The inverse slope value of the steps in the adsorption isotherm rises slowly with temperature, as the phase transition is not fully discontinuous below the mean critical temperature within the material. This is due to a number of factors. Firstly, there is a pore size distribution within the sample leading to a lowering of the transition slope, as a small number of pores will be above their critical point leading to non-discontinuity in their phase transition.[73] Secondly, the smallest of pores are pseudo one-dimensional with enough space for only a few adjacent molecules. This introduces finite size effects which leads to multilayer adsorption behaviour dominating. This means a pressure range is required in order for the pore to be filled in this manner and then for a transition to take place.[77] Finally, any temperature gradient through the sample will lead to the pores experiencing a range of temperatures, this would destroy the first-order transition and result in non-verticality of the capillary condensation.[73] The initial behaviour of the inverse slope value is then followed by a large increase in inverse slope value with temperature as the majority of the pores within the sample are above their critical temperature, reducing the pore transition gradient and making the transition continuous in nature (gas–supercritical fluid). The point at which these two gradients intersect, given by the linear fitted lines, is therefore proposed to be the mean critical temperature within the porous material for a particular substance, as shown in Figure 3.16.

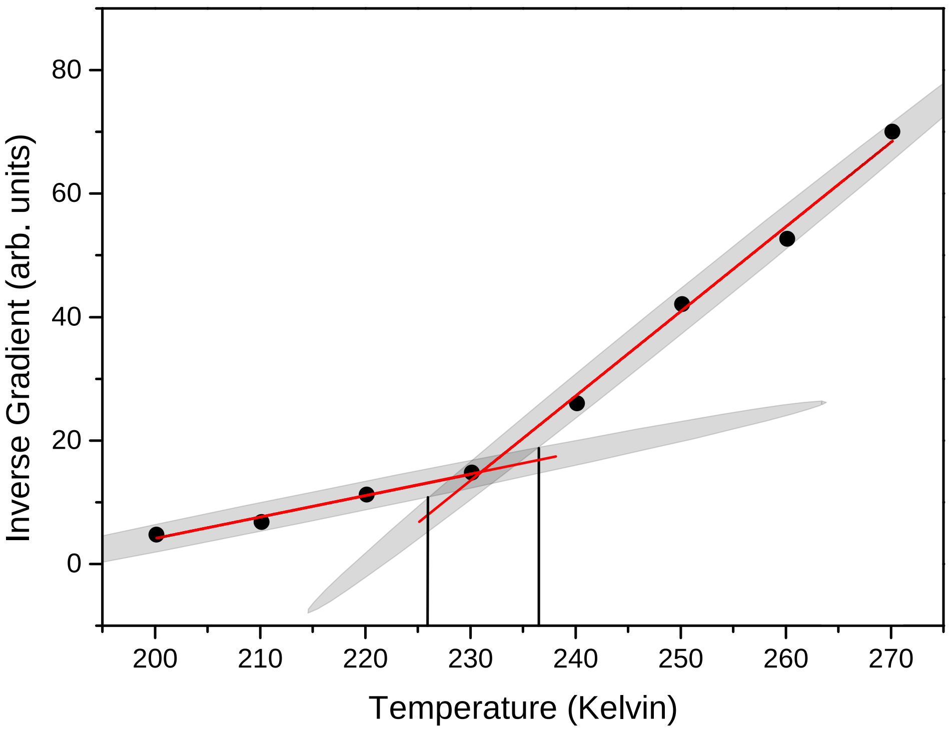

Figure 3.16: Temperature dependence of the inverse slope of the adsorption jump associated with capillary condensation and therefore phase transition of CO_2 within MCM-41 with a mean pore size of 4.5 nm. The shaded areas represent the standard deviation from the linear fit with 95% confidence and the black vertical lines represent the possible extremes of the pore critical temperature.

The inverse slope versus temperature plot consists of two regimes. The slope of the initial flatter portion of the plot is dependant on the pore size distribution, with a larger pore size distribution resulting in a greater change in inverse slope value with temperature. This is because there will be smaller pores within the material that will be above their critical temperature, increasing the inverse slope value. The steeper part of the plot is also affected by this phenomeona as it requires a larger temperature range for all pore sizes to be above their critical temperature, resulting in a smaller increases of the inverse slope value with temperature for this section. In a system where there is only one true critical point the plot would consist of regime with a low and constant inverse slope value, followed by a very steep upward change in inverse slope. The influence of the pore size distribution on this behaviour is demonstrated in Figure 3.17.

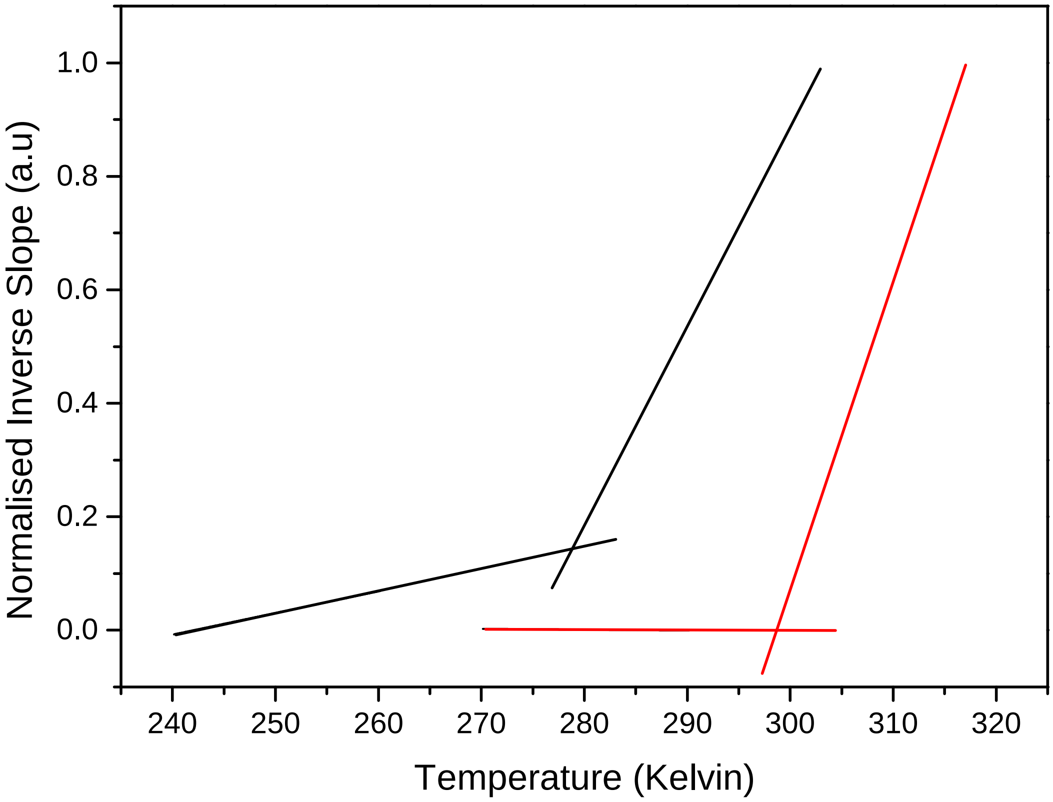

Figure 3.17: A comparison of the inverse slope value fit-lines obtained from ethane absorption isotherms in (black) a wide pore size distribution material (12.2 nm aluminosilicate) and (red) a narrow pore size distribution material (18 nm anodic alumina).

3.2.3 The Pore Critical Temperature of Carbon Dioxide, Difluoromethane and Ethane Confined in Silica, Aluminosilicate and Anodic Alumina Templates

As shown in Figure 3.18, the adsorption isotherms and therefore phase transitions of both carbon dioxide and difluoromethane could be observed within pores. This is in a similar manner to that previously seen in the near-infrared measurements.

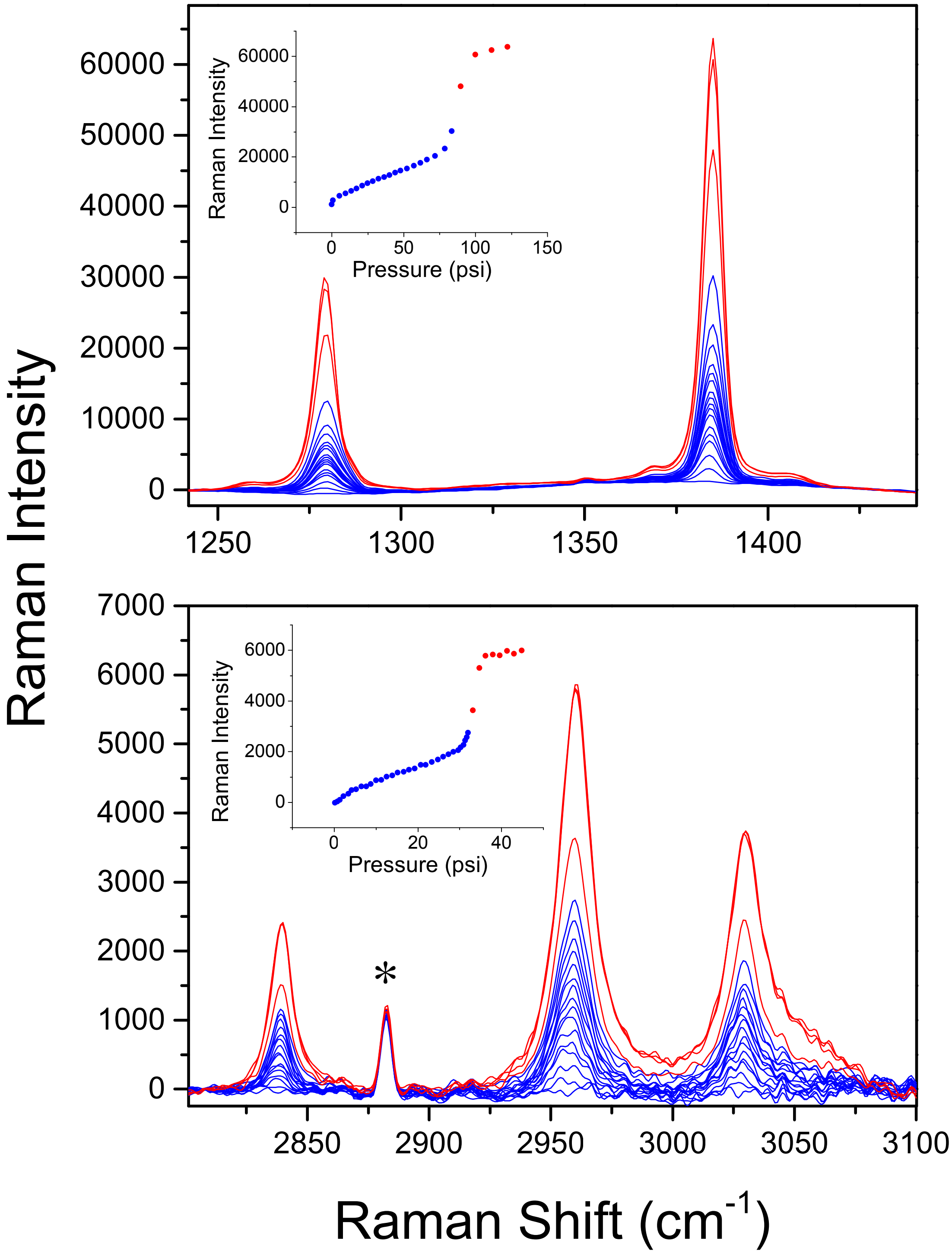

FIGURE 3.18: Absorption isotherms **(Inset)**, for CO_2 **(Top)**, and CH_2F_2 **(Bottom)** in 3.2 nm MCM-41, measured using Raman spectroscopy at 230 and 260 K, respectively. The isotherms are obtained by measuring the intensity of the CO_2 ν_1 symmetric stretching vibration of the Fermi diad at *ca.* 1370 cm^{-1} and the CH_2F_2 ν_1 C–H symmetric stretch intensity at *ca.* 2955 cm^{-1}.[208] The starred point indicates detected stray light.

Examples of isotherms obtained for both adsorbates are shown in Figure 3.19. In the small pore MCM-41 type silica (3.2–4.5 nm), typical type IV isotherms were observed again as described in Chapter 1.[97] In the larger pore aluminosilicates and anodic alumina samples both type V and III isotherm behaviour was exhibited, although in the case of anodic alumina it closely resembled that of bulk fluid condensation.[97] The pore condensation step in the anodic alumina materials was again observed close to the bulk condensation pressure and the adsorption curve is less convex in nature compared to the other material types across the entire pressure range before condensation. Because of this, these larger pore anodic alumina template isotherms could not be fitted with a function, therefore derivatives of the raw data were used to obtain the inverse slope value of the phase transition. Again no condensation was observed in the 100 nm pore diameters.

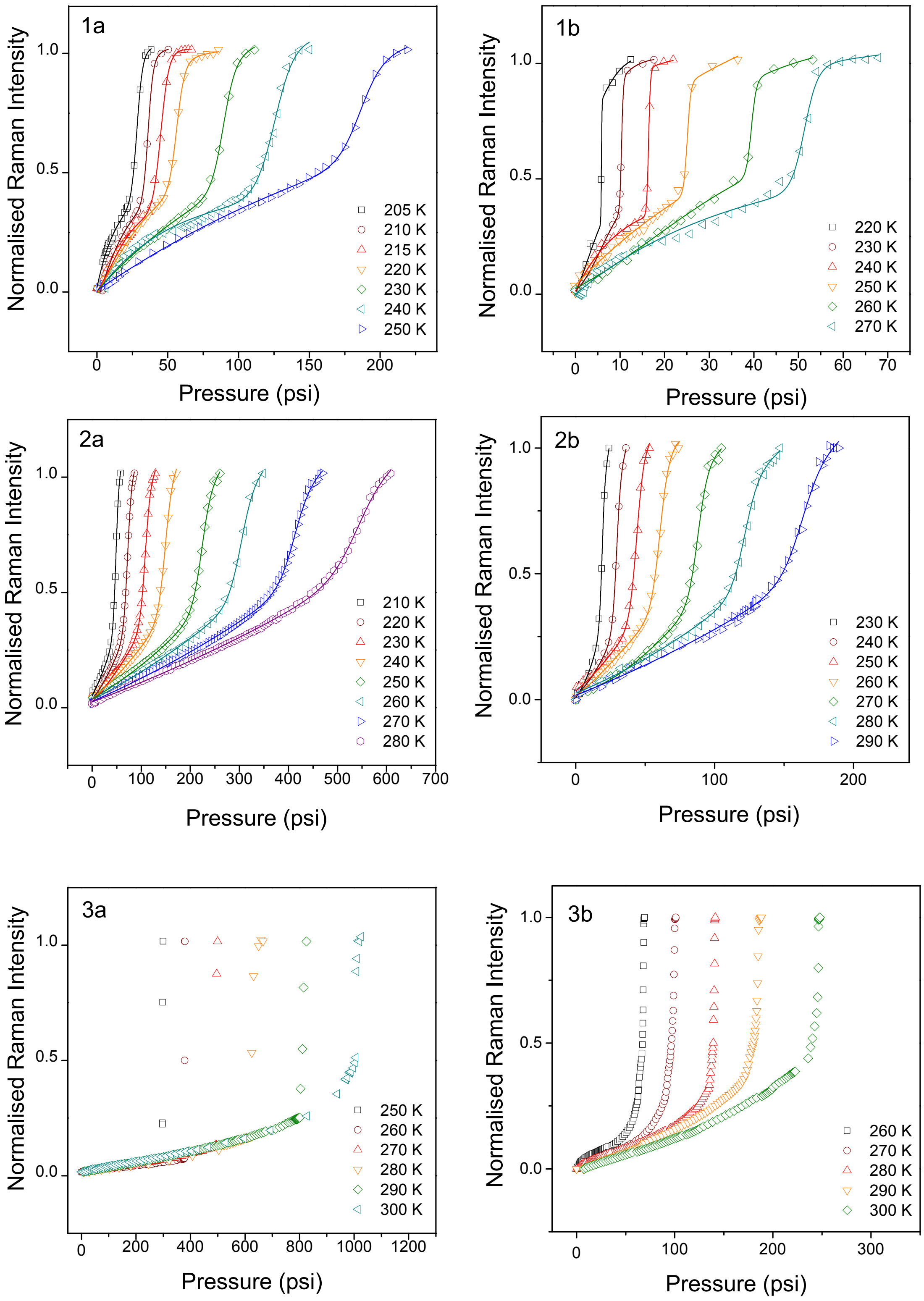

FIGURE 3.19: Adsorption isotherms, measured by Raman spectroscopy of CO_2 confined in 3.2 nm MCM-41 **(1a)**, 6.7 nm aluminosilicate **(2a)** and 18 nm anodic alumina **(3a)**. With adsorption isotherms of CH_2F_2 in 3.2 nm MCM-41 **(1b)**, 6.7 nm aluminosilicate **(2b)** and 18 nm anodic alumina **(3b)**.

The adsorption of ethane was again studied in the wide range of available porous materials using Raman spectroscopy. To carry out this study, the ν_3 Raman band of ethane,[209,210] which is assigned as the C–C symmetric stretch, was studied as a function of pressure isothermally in silica, aluminosilicates and anodic alumina materials (see Figure 3.20).

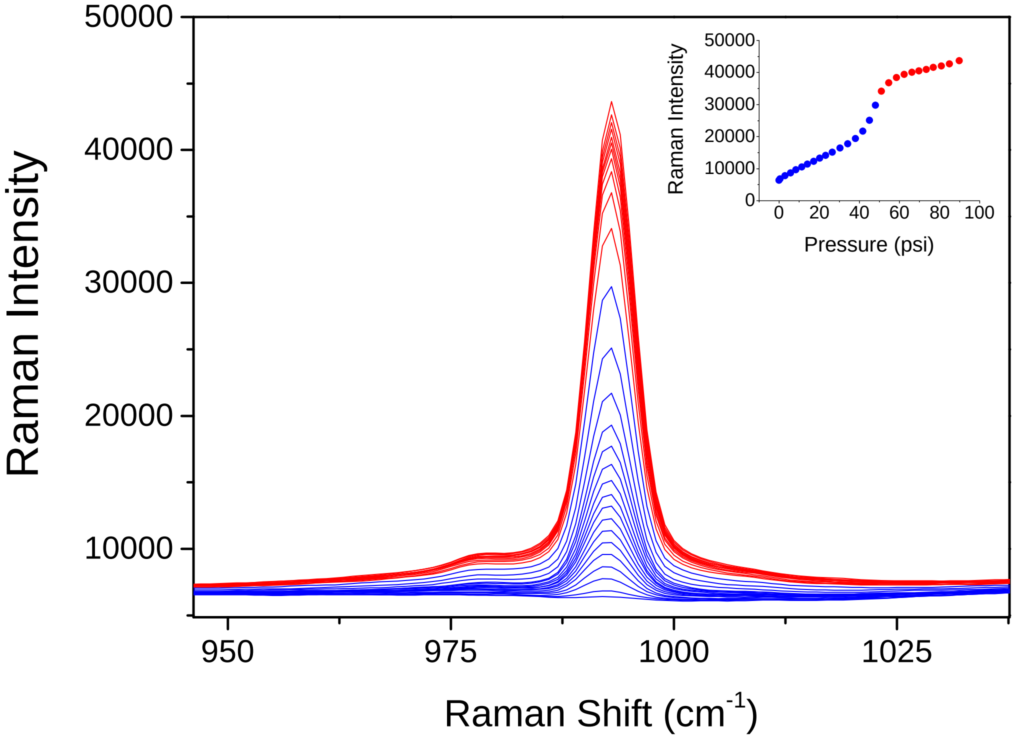

FIGURE 3.20: The ν_3 Raman band of ethane assigned as the C–C symmetric stretch,[209,210] confined in 3.2 nm MCM-41 at 230 K as a function of increasing ethane pressure. This allows the pore phase transition to be observed.

This allowed for the observation of the phase transition of confined ethane by Raman spectroscopy and the progression from a low temperature gas–liquid phase transition, to a higher temperature gas–supercritical phase transition taking place within the pores. Examples of this behaviour is displayed in Figure

3.21.

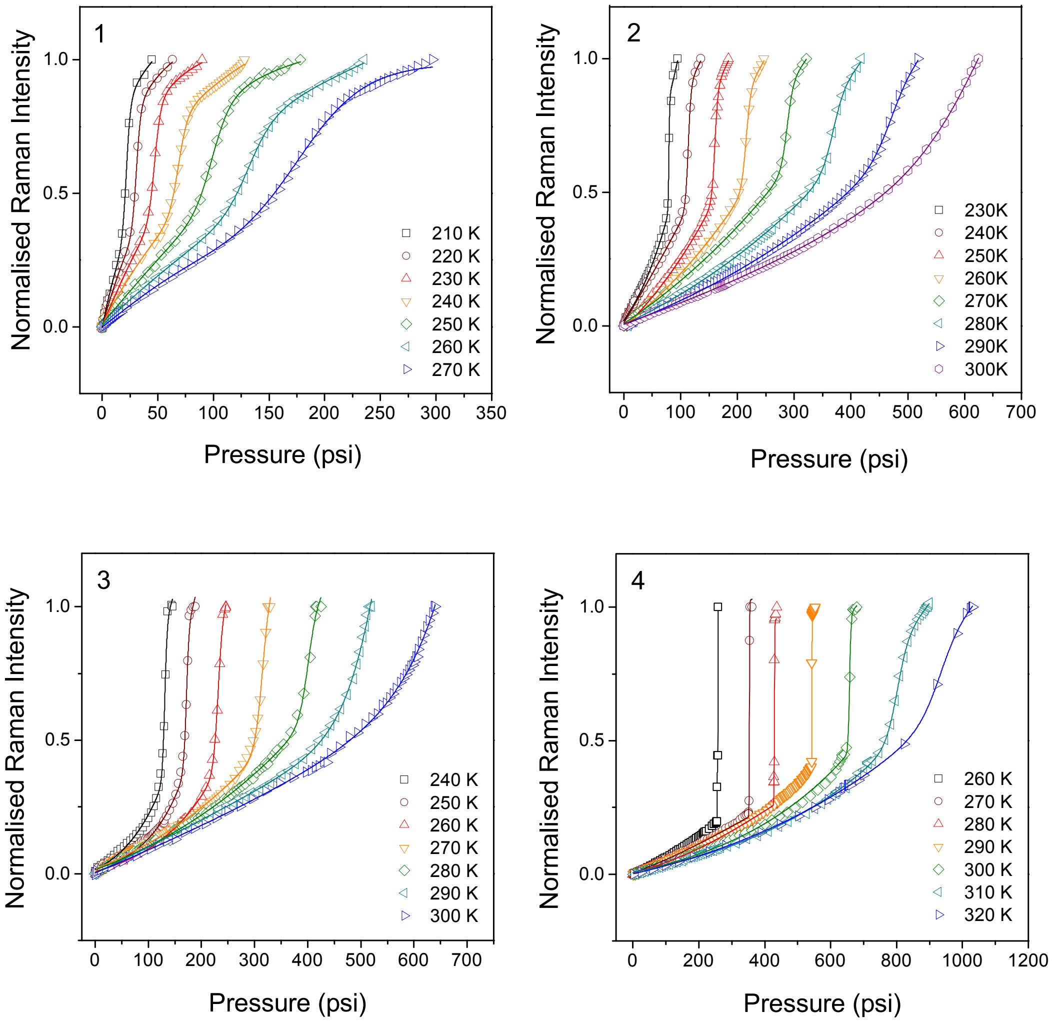

FIGURE 3.21: Adsorption isotherms, measured by Raman spectroscopy of C_2H_6 confined in 3.2 nm **(1)** MCM-41, 8.3 nm **(2)** MSU-H silica, 12.2 nm aluminosilicate **(3)** and 18 nm anodic alumina **(4)**.

The critical temperatures of CO_2, CH_2F_2 and C_2H_6 confined in the twelve separate materials and measured by Raman spectroscopy, using the previously described methodology are summarised in Figure 3.22 and in Table 3.1.

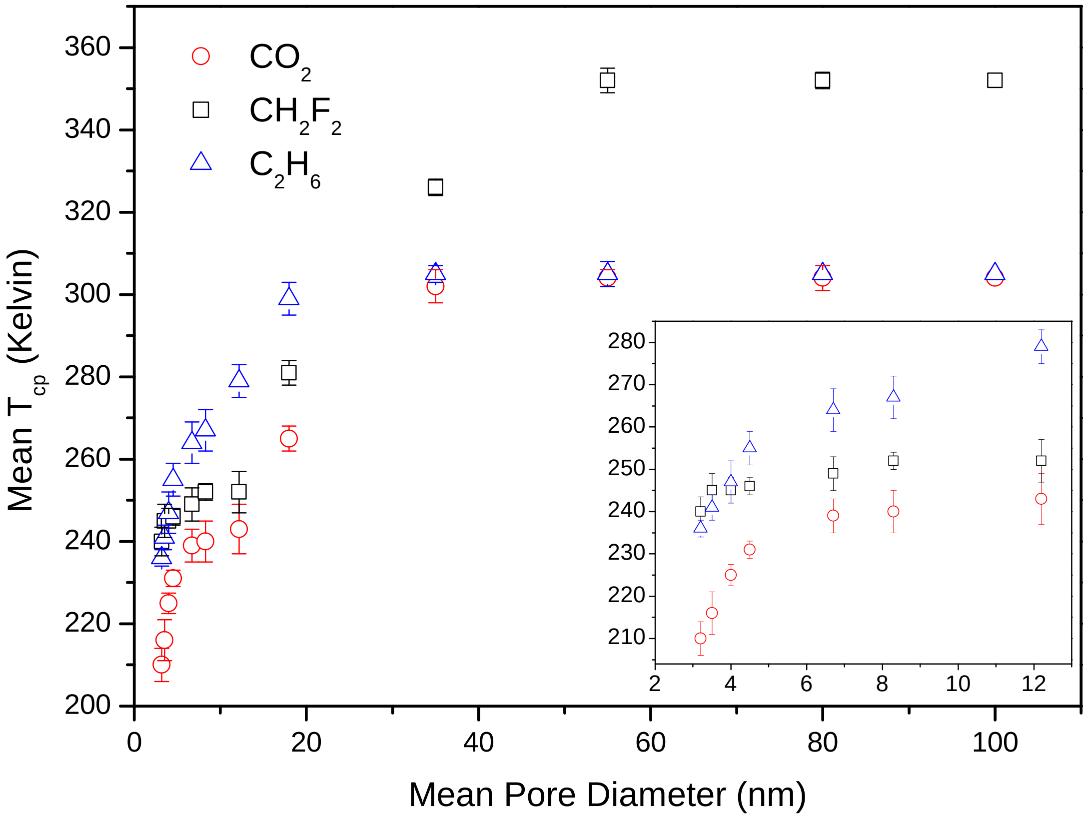

FIGURE 3.22: The mean pore critical temperature (T_{cp}) of CO_2, CH_2F_2 and C_2H_6 as a function of mean pore diameter determined by Raman spectroscopy. The **Inset** highlights the mean T_{cp} of the fluids confined in the smaller pore sizes ranging from 3.2–12.2 nm

TABLE 3.1: Summary of the critical temperatures (T_c) observed for CO_2, CH_2F_2, and C_2H_6 confined in the twelve porous materials rounded to the nearest kelvin.

		CO_2		**CH_2F_2**		**C_2H_6**	
Material	Mean Pore Size (nm)	Mean T_{cp} (K)	Depression (K)	Mean T_{cp} (K)	Depression (K)	Mean T_{cp} (K)	Depression (K)
MCM-41 3.2	3.2	209	95	240	112	236	69
MCM-41 3.5	3.5	215	89	245	107	241	61
MCM-41 165	4.0	225	79	245	107	247	58
MCM-41 180	4.5	230	74	246	106	255	50
MZBN-100w3hd	6.7	238	66	249	103	264	41
MSU-H	8.3	238	66	252	100	267	38
MZBN-135w3h	12.2	243	61	252	100	279	26
SM-18-100-13	18	265	39	281	71	299	6
SM-35-100-13	35	302	2	326	26	305	0
SM-55-100-13	55	304	0	352	0	305	0
SM-80-100-13	80	304	0	352	0	305	0
SM-100-100-13	100	304	0	352	0	305	0

3.2.4 Comparison of Raman and Near-Infrared (NIR) Spectroscopic Methods to Determine Pore Critical Temperature

To check the validity of the Raman spectroscopic method, the results can be compared to those previouly obtained from the near-infrared measurements. The NIR method relies on the change in the adsorbed fluid density or volume adsorbed, as observed in previous literature,[77,157] leading to a change in the absorbance as it approaches and continues above its critical temperature. The Raman spectroscopic method however, is used to ascertain the temperature at which the confined substance phase transition becomes second order in nature and continuous. It should be noted that due to finite size effects and a distribution of pore sizes in the material studied, the confined substance phase transition is never truly first order (fully discontinuous with a large gradient). There is however a temperature where the phase transition becomes fully second order and continuous in nature (the pore critical temperature). When compared, the results of the NIR and Raman spectroscopic methods show a good agreement in the determined pore critical temperature of all three fluids (see Figure 5.1). This lends confidence to the fact that the true pore critical temperature is being measured by both methods. As observed with the NIR studies, the trend of mean T_{cp} for both CO_2 and CH_2F_2 as a function of mean pore diameter resembles three distinct regimes. The lowest measured T_{cp} is at the smallest of pore diameters, with a steep rise in T_{cp} value as the mean pore diameter increases over a small range between *ca.* 3–8 nm. This is again followed by a plateau, where there is little change in T_{cp} between the *ca.* 8–12 nm pore diameter, which progresses to an almost linear increase in T_{cp} between *ca.* 12–60 nm pore diameters. Ethane on the other hand again shows a more linear progression of T_{cp} with mean pore diameter possibly due to the lower fluid-pore interaction energy.

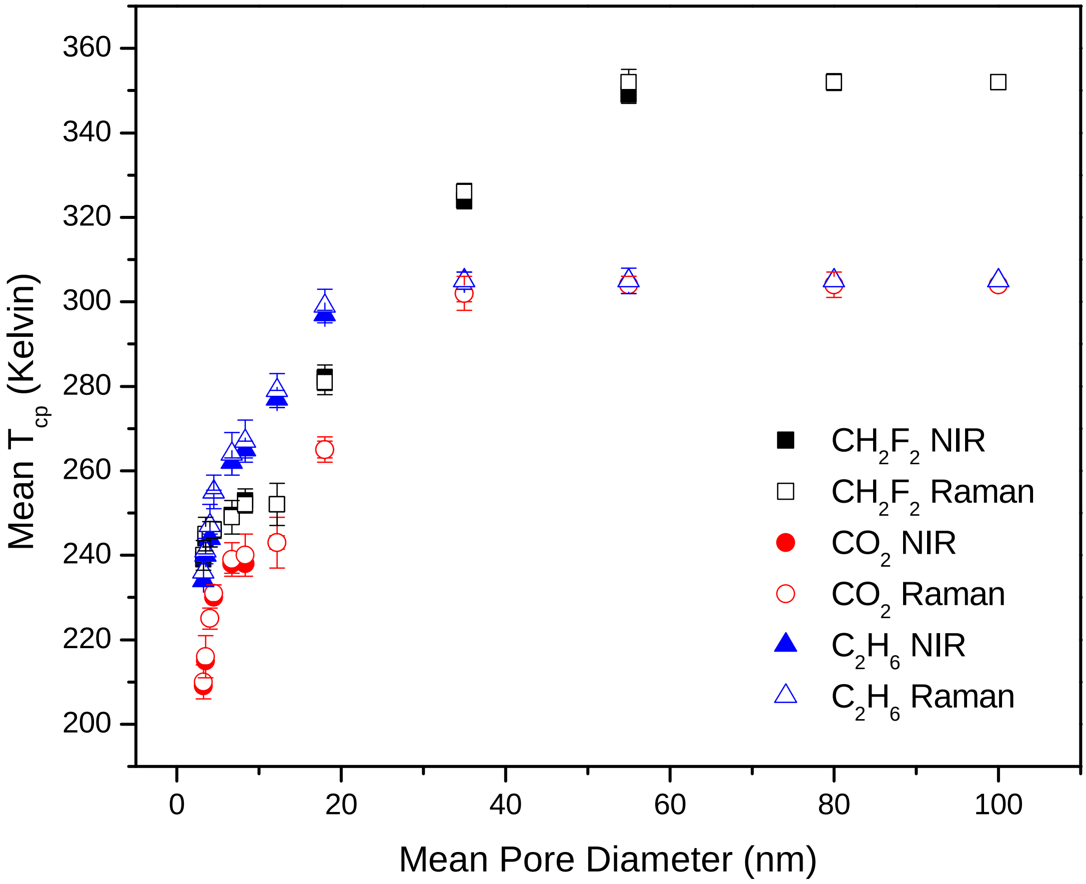

FIGURE 3.23: The mean pore critical temperature (T_{cp}) of CO_2, CH_2F_2 and C_2H_6 as a function of mean pore diameter, determined by both NIR and Raman spectroscopy.

The trend of ΔT_{rp} as a function of inverse pore diameter (1/D) values determined by Raman spectroscopy also agree strongly with those that were obtained with the use of NIR spectroscopy, as shown in Figure 5.1. This confirms that the more polar or polarisable fluids are depressed to a greater extent in their critical temperature, in pore sizes across most of the range studied. This is again possibly due to the increased fluid-pore interaction strength because of these properties. These results also corroborate the previous findings that the trend of ΔT_{rp} as a function of inverse pore diameter deviates further from a linear relationship into distinct linear regimes as the dielectric constant, polarisability or polarity of the fluid and therefore the fluid-pore interaction strength increases.[144,145]

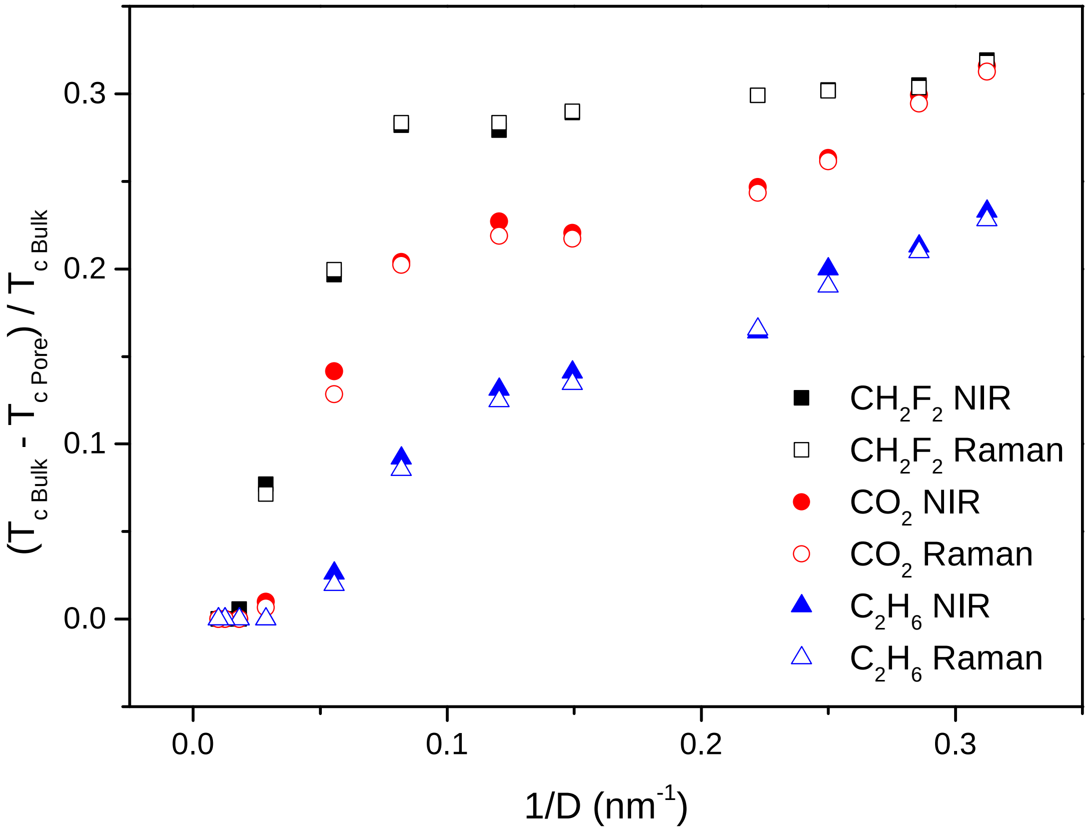

FIGURE 3.24: The decrease in reduced pore critical temperature (ΔT_{rp}) for CH_2F_2, CO_2, and C_2H_6 as a function of the inverse pore diameter, determined by both NIR and Raman spectroscopy.

The Raman spectroscopic methodology provides a more direct approach to study this behaviour, without the need to scale the spectroscopically obtained isotherm to account for the differing amounts of porous material loaded in the cell. Also since there is no need for light to be transmitted through the sample to obtain an absorbance spectrum, the full path length of the cell could be filled with the porous material. Therefore there is very little spectral contribution of the bulk fluid, making the interpretation of the spectrum a more straightforward process for Raman spectroscopy when compared NIR. However the Raman spectroscopic measurements unlike those of the near-infrared, do no provide the clear indication of the range of T_{cp} present in the porous templates due to their inherent pore size distribution.

3.2.5 Theoretical Study of Confined Fluid Critical Temperature through the use of a Grand Canonical Monte Carlo Method

To gain further insight into the critical behaviour of fluids relevant to this study GCMC simulations of CO_2 have been carried out in a range of modelled pore sizes. The pore models in this study have been constructed hexagonally with lattice spacings between the silicon and oxygen atoms of 0.162 nm, an average of the bond lengths previously reported for silica.[211,212] CO_2 was selected in this study as the work carried out in this Thesis has shown that CO_2 exhibits interesting behaviour with respect to its pore critical temperature versus pore size relationship, showing large increase in T_{cp} between 3–5 nm. Also the T_{cp} value between the pore diameters of *ca.* 5–12 nm was determined to show very little change. This plateau has not been previously predicted in theoretical studies regarding CO_2 and has only been shown to occur for simple square well fluids modelled in the literature.[145] Another reason CO_2 was selected is the fact that a good theoretical description of the CO_2 molecule and its associated force field is already in existence. These models have previously been successful in predicting the critical properties and phase behaviour of CO_2. To carry out this study the elementary physical model 2 (EMP2) description of CO_2 was used, as first described by Harris and Yung.[213] Although this model overestimates the critical temperature of bulk CO_2 by *ca.* 10 kelvin, predicting a T_c of 314 K, it does provide a simple and computationally efficient description of the molecule with reasonable accuracy of the phase properties, when compared with other models. Finally the interaction energy between the CO_2 and the walls of the pore was simulated by applying a potential to the pore walls. A value of -32 kJ mol^{-1} was selected for the CO_2 pore wall interaction strength. This value has been determined experimentally in the literature as the heat of adsorption of CO_2 into a MCM-41 type silica pore.[182] This potential takes the form of a Bessel function which allows a wave to be modelled in cylindrical coordinates.[214] The Bessel function in this case is periodic with respect to the pore lattice in the radial orientation and is modulated longitudinally by a sine function down the vertical pore axis, which is again periodic. The silicon atoms in the lattice are positively charged sites and the oxygen atoms are negatively charged, in order to simulate the pairwise atomic interactions between the CO_2 and the relative charges of the pore lattice. This allows the interaction between the fluid and the whole pore to be simulated. The GCMC program along with its pore model was written by Dr. Richard Wheatley and all calculations were preformed by Dr. Hainam Do.

In order to examine the phase properties of CO_2 in pores, a range of chemical potentials were selected at a given temperature and the volume number density of the system was left to equilibrate using the GCMC algorithm. The volume number density (n) is given as:

$$n = \frac{N}{V} \tag{3.3}$$

Where N is the number of molecules and V is the volume. This produces an isotherm showing the phase transition taking place within the pore, starting from a low chemical potential and volume number density in the gas phase, progressing to a high chemical potential and volume number density in the liquid phase. A sharp increase in volume number density can be observed with a relatively small increment in chemical potential as the system undergoes a gas to liquid phase transition. This behaviour is shown in Figure 3.25.

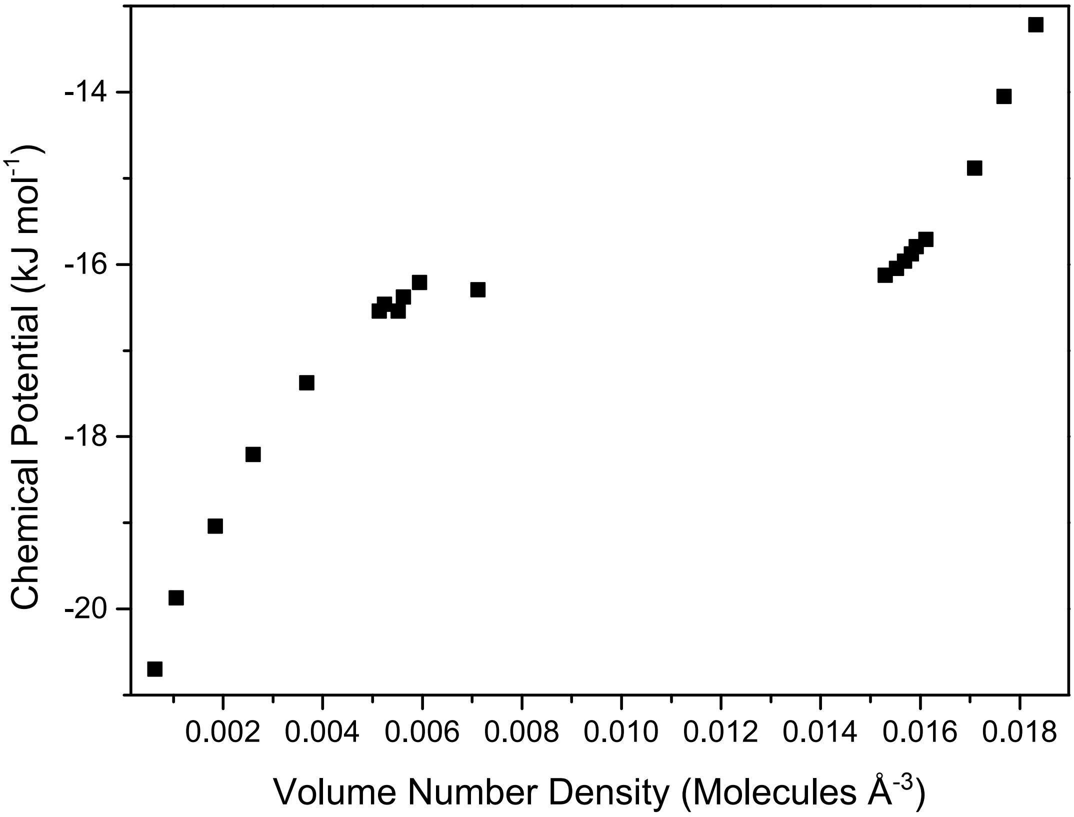

FIGURE 3.25: The chemical potential of CO_2 as a function of volume number density in 3 nm diameter pores at 240 K. The large increase in volume number density around -16 kJ mol^{-1} indicates that a gas to liquid phase transition is taking place in the pore.

The critical temperature of the modelled pore confined CO_2 was determined by studying the isothermal behaviour of the phase transition with temperature. As the T_{cp} is approached the sharp increase in volume number density with chemical potential becomes a smooth and continuous. This is due to the change from a first order gas to liquid phase transition to a continuous gas to supercritical fluid phase transition, as shown in Figure 3.26.

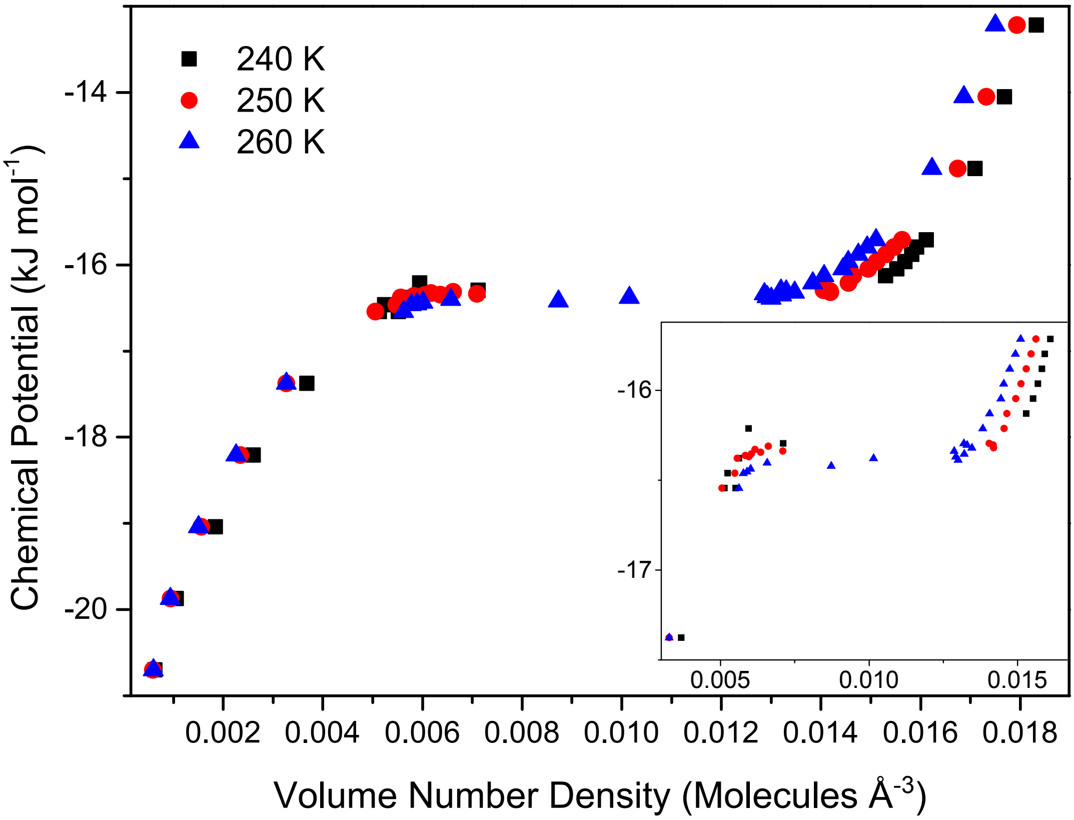

FIGURE 3.26: The chemical potential of CO_2 as a function of volume number density in 3.5 nm diameter pores at 240, 250 and 260 K. The sharp increase in volume number density around -16 kJ mol^{-1} at 240 and 250 K indicates a gas to liquid phase transition. The smooth increase in volume number density at 260 K shows a continuous gas to supercritical fluid phase transition taking place, indicating that the system is above T_{cp}. The **Inset** highlights the temperature at which the phase transition becomes continuous at 260 K, demonstrated by the fact points appear between the gas and supercritical fluid branches of the isotherm.

The T_{cp} of CO_2 was determined using this method in pores ranging from 3–8 nm in diameter as shown in Figure 3.27. The trend of calculated T_{cp} with pore diameter shows a large significant depression in T_{cp} at the smaller pore diameters that increases steeply with pore size. This increase then diminishes as the larger pore diameters are approached until the pores with a diameter of 7 and 8 nm is reached, where no difference in T_{cp} between these two pore sizes was calculated.

This behaviour is in agreement with that which has been observed in experiments in this Thesis.

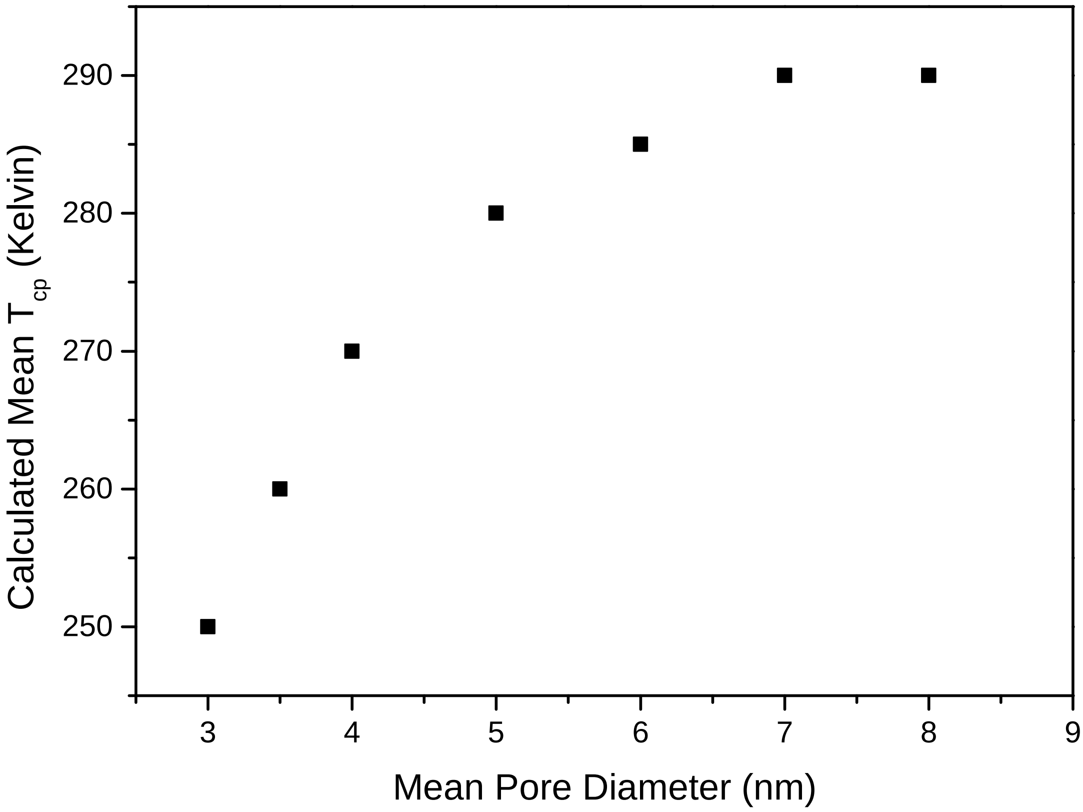

FIGURE 3.27: The calculated critical temperature of CO_2 confined in pores ranging in diameter from 3–8 nm.

Although the simulations demonstrate similar behaviour to that which has been observed by the spectroscopic measurements obtained in this work, the absolute values obtained from the calculations are much higher, even if the 10 K difference in T_c between the model and the actual fluid is taken into account, as shown in Figure 3.28.

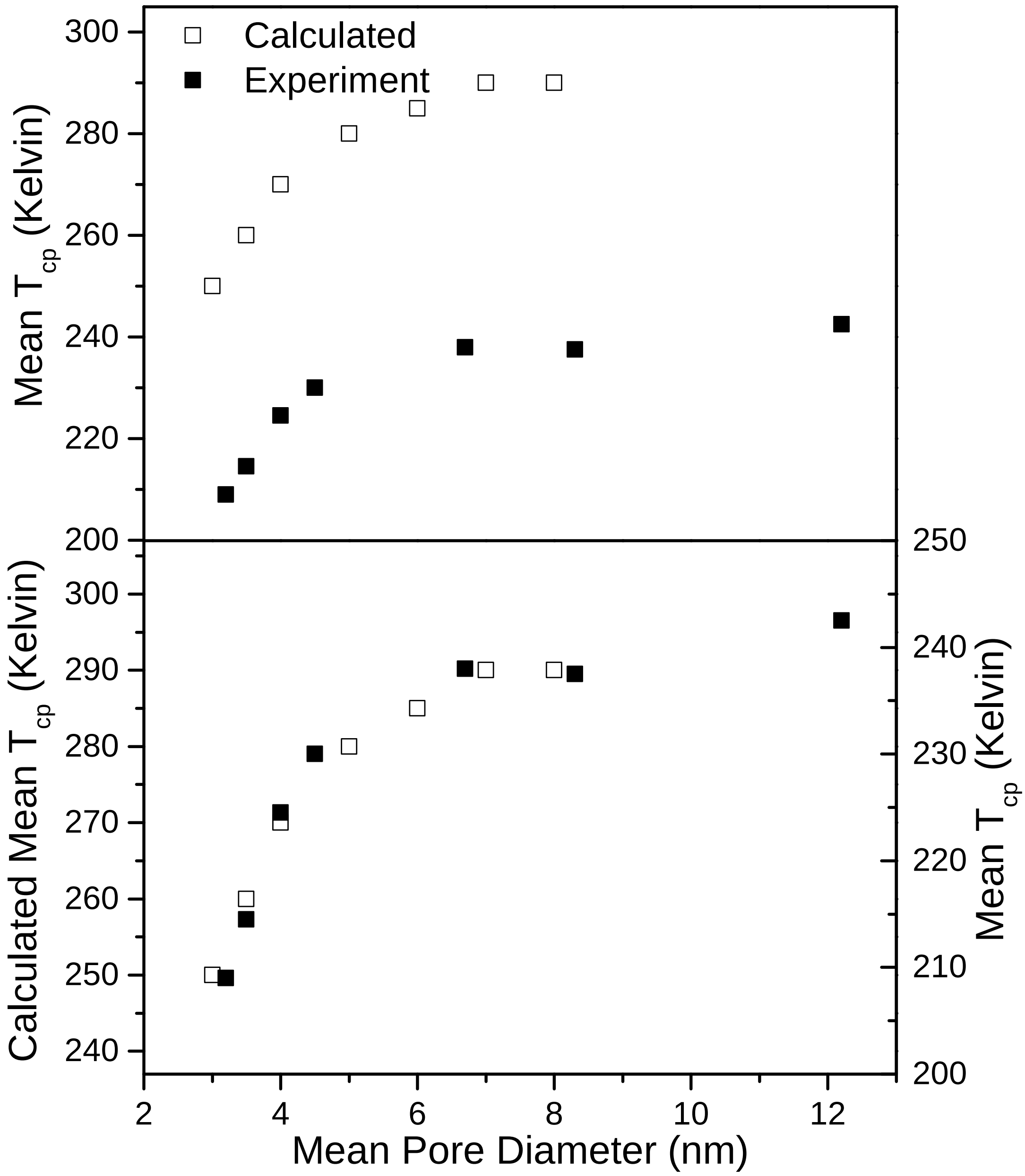

FIGURE 3.28: **(Top)** A comparison of the absolute calculated critical temperature of CO_2 confined in pores ranging in diameter from 3–8 nm and the values determined from Raman spectroscopy. **(Bottom)** A comparison of the calculated critical temperature values and those determined from Raman spectroscopy with an adjusted scale, highlighting the similarity of their trends.

The change in T_{cp} value with pore diameter in the smaller pore region appears to increase at a smaller rate before the plateau is reached. There could be a number of explanations as to why this is the case. Firstly the fluid-wall interaction potential may not have been modelled precisely in terms of the functions used to describe the interaction, or the magnitude of the interaction potential may not be correct. Secondly the EPM2 of CO_2 may not be replicating the force field of CO_2 molecules confined in the silica pore accurately, therefore raising the calculated pore critical temperature of the fluid and changing the relationship between pore diameter and the pore critical temperature. Lastly the simplified pore wall structure may not provide an accurate enough description of the pore lattice and missing functional groups such as the silanol groups present in silica that have not been included may have an influence on the critical temperature value. However it is clear that these simulations are replicating the general behaviour of CO_2 determined from the spectroscopic measurements used in this work.

To probe the influence of the fluid-wall potential further on confined CO_2, GCMC calculations where preformed in pores without a fluid-wall interaction potential. Therefore these simulations allowed the influence of just the confines of the pore without an attractive component could be investigated (see Figure 3.29).

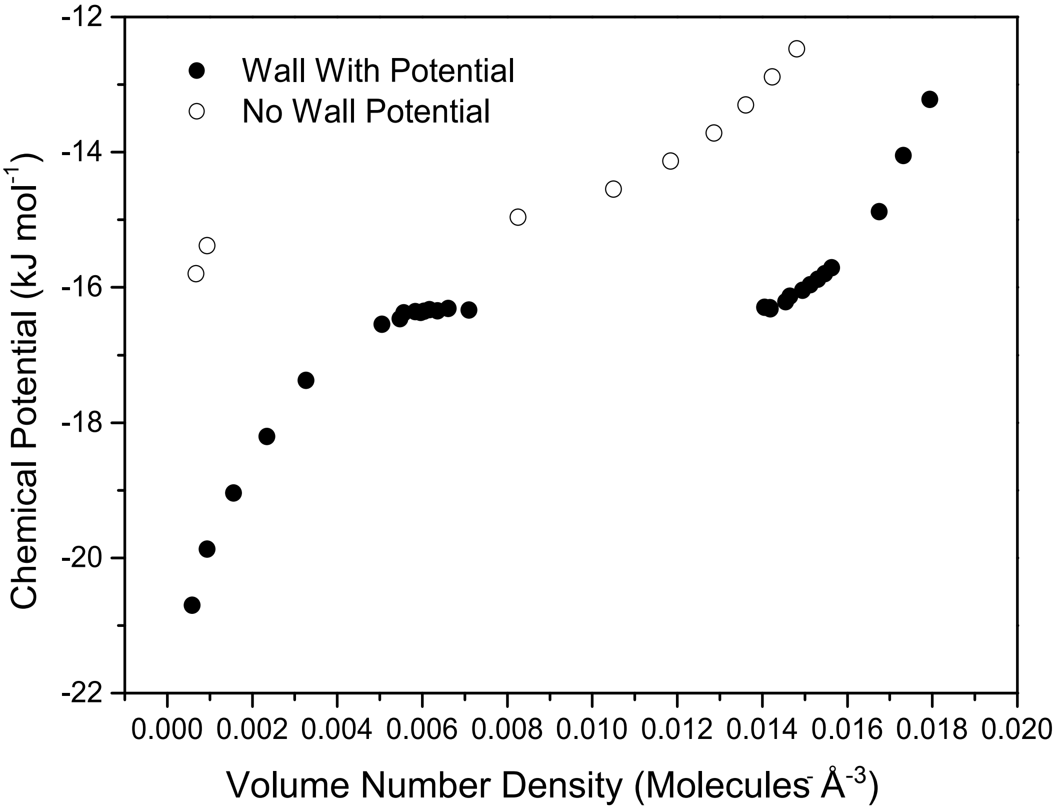

FIGURE 3.29: The chemical potential of CO_2 as a function of volume number density at 250 K in 3 nm diameter pores, with and without a potential on the wall of the pore.

The removal of the wall potential exhibits two significant effects on the confined CO_2. Firstly, the isotherm of CO_2 confined in a pore with no wall potential shows a shift to a higher chemical potential in both the liquid and gas phases. This indicates that the pore wall potential stabilises the molecules present in their phases. This is to be expected as the wall interaction would increase the energy required for the molecules to escape their respective phases or states, due to binding to or near the wall. Secondly both the gas and liquid phase branches of the isotherm shift to a lower volume number density, therefore they contain a smaller amount of molecules and exhibit a lower density. This confirms that the potential on the pore wall densifies the confined substance and therefore indicates that this shift in the coexistence envelope may influence the critical temperature, as predicted by Singh *et al.*[144,145]

The pore critical temperature of CO_2 was calculated in pores ranging from 3–7 nm in diameter. These values are shown and contrasted to the values obtained from a pore with a potential in Figure 3.30.

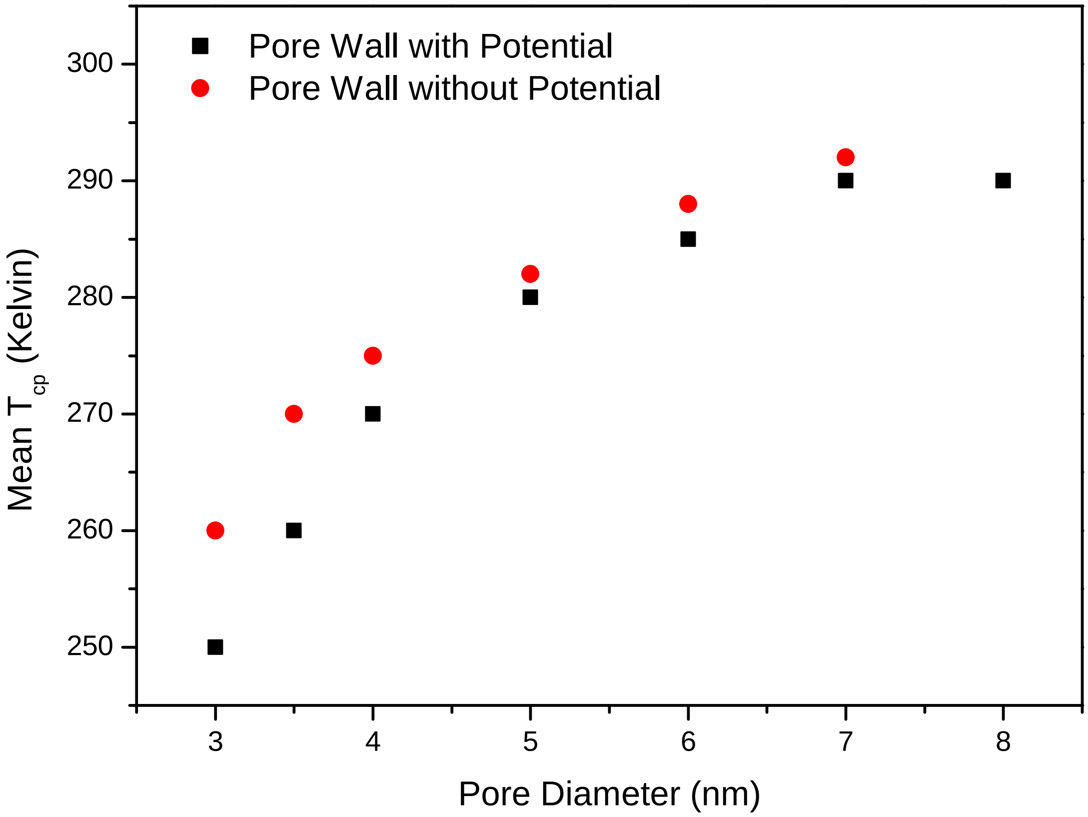

FIGURE 3.30: The calculated critical temperature of CO_2 confined in pores ranging in diameter from 3–8 nm in pore with and without an attractive potential.

The calculated pore critical temperature of CO_2 in the pores without a fluid-wall potential exhibit a higher critical temperature across the entire range of pore sizes calculated (3–7 nm), when compared to those in a pore with a fluid-wall attraction. This demonstrates that the attraction of the fluid to the pore wall is an important factor that influences that confined fluid's T$_c$. In agreement with the literature, it does appear that the attractive influence of the pore wall on the fluid, will lower the fluid's pore critical temperature value. As suggested previously, this may be due to the fact the wall potential changes the coexisting phases density, as shown isothermally in these simulations (Figure 3.29) and as predicted by Singh *et al.*[144,145]

The trend of T$_{cp}$ with pore diameter in the pores without an attractive potential exhibits a more linear relationship compared to those with the potential. This trend is more reminiscent of the results obtained for ethane in this Thesis, which is predicted to be a weakly interacting adsorbate and approaches the bulk T$_c$ with increasing pore size in a more linear fashion. This supports the idea that the shape and behaviour of the T$_{cp}$ versus pore diameter trend depends on the magnitude of the fluid-pore interaction potential. The gradient of the change in T$_{cp}$ with pore diameter is also lower between 3–5 nm, indicating that the very steep drop in T$_{cp}$ as the pore size decreases may be driven primarily by pore surface interaction effects. This is to be expected as the fluid-pore potential would extend over a larger proportion of volume in the smaller pores, exerting a greater effect on the fluid. However, it is still unclear from these calculation results whether or not the lack of fluid-pore potential has an effect on the plateau in T$_{cp}$ above 7 nm. As this effect is thought to be due to the attraction between the pore and fluid, it is expected that this phenomenon will not be as evident for the neutrally charged pores. Therefore more calculations at larger pore diameters are needed to confirm if this is the case.

3.3 Conclusions

Raman spectroscopy has been used to further probe the critical temperature of carbon dioxide and difluoromethane, confined in a range of porous silica, aluminosilicate, and anodic alumina materials. The results obtained were compared to those determined by near-infrared spectroscopy. There was good agreement between the two methods both in absolute critical temperature values and the trend of how the pore critical temperature of these fluid is affected by the pore diameter of the template they are confined in. Again it was found that ethane, a non-polar low dielectric and therefore less strongly interacting adsorbate was significantly less depressed in its T_{cp} across the pore size range. Also ethane approached the value of its bulk T_c in pores which still had an effect on the other two adsorbate molecules studied. For ethane the ΔT_{rp} versus inverse pore diameter trend also exhibited a more linear dependence, suggesting a weaker fluid-wall interaction potential, as predicted in the literature.

The T_{cp} of CO_2 has also been investigated in a range of pore diameters with the use of grand canonical Monte Carlo simulations. It was confirmed that the T_c of CO_2 is significantly lowered when confined in nanopores. The theoretical results also support the experimental findings in this Thesis, indicating that there is a steep increase in T_{cp} value with pore size in the 3–5 nm range followed by a plateau in T_{cp} between *ca.* 5–12 nm. This effect is thought to be due to the diminishing influence of the fluid-wall potential as the pores cross from pseudo 1D to 3D geometry.

Calculations of the pore critical temperature of CO_2 confined in pores with no fluid-wall potential were also preformed. The pore critical temperature was found to shift to a higher value showing that the interaction potential plays a significant role in the extent a fluid's T_c is depressed in a pore. This is evident as the pores exhibited a higher CO_2 T_{cp} when compared to equally sized attractive pores across the range studied (3–7 nm). The phase behaviour was also found to change when the fluid-pore potential was removed. Both the coexisting liquid and the gas phases shifted to a lower density and a higher chemical potential. This confirms that the formation of densified pore phases may be responsible for the increased depression in critical temperature for fluids that strongly interact with the pore walls. The trend of CO_2 T_{cp} vs pore diameter for the neutrally charged pores was more linear when compared to those with a potential. This indicates that the trend of T_{cp} with pore size is dependant on the magnitude of the pore-fluid interaction potential. The lack of a pronounced depression in T_{cp} which is evident between 3–4 nm for the charged pores also suggest that at the smallest of pores sizes, surface interaction effects are the dominant factor that determines the relationship between T_{cp} and pore diameter.

Chapter 4

Spectroscopic Studies of Confined Binary Mixture Composition

4.1 Introduction

The previous Chapters have focussed on the phase characteristics of pure fluids confined in pores. This Chapter will examine how the properties of a pore confined mixture deviates from its bulk counterpart, specifically relating to the composition of a mixture. One application of this knowledge is in the supercritical fluid electrodeposition process, which makes use of a supercritical mixture inside the nanopores in order to deposit metallic structures. This is because electrodeposition, above or below the critical point, requires a mixture of substances to take place. Therefore, understanding the fundamental changes confinement exerts on a mixture and its composition is key to fine tuning this process, allowing deposition to take place optimally within a pore. Since the composition of a mixture affects its properties (*e.g.* surface tension, diffusivity and conductivity),[60,61] studying the difference between bulk composition and confined composition is an important avenue of research, allowing the conditions used to be tailored for pore deposition. Changes in mixture composition in pores also has implications in gas storage and confined catalysis. This is because the selectivity of a pore will influence storage efficiency or the preference of reactants to be consumed during a reaction, possibly affecting product formation.

Theory has shown that confined mixture composition will not only be affected by confinement in nanoscopic dimensions,[215,216] but also by the interaction preference of the confinement medium for molecules of one of the mixture components.[217] This selectivity causes an enrichment of the preferred component in proximity to the pore walls. The adsorption of mixtures into a pore differs from that onto a single flat surface. A flat surface is characterised by a composition profile, which decays to the bulk composition within some length (ξ) with an adsorption volume $V_a = \xi A_s$, where A_s is the surface area. However, when the liquid is confined by two surfaces separated by less than 2ξ, the composition profiles starting from the two opposite surfaces of the pore walls will overlap,[218] leading to a greater enhancement of the adsorbed amount of the preferred component compared to a single free surface of equal A_s, whenever the pore volume confined by this given surface area is less than the respective adsorption volume for the single flat surface.[15] Unfavourable interactions between differing molecules of each mixture component, when compared to favourable interactions between the pairs of like molecules, will also cause enhanced absorption of the preferred mixture component.[219] For larger pores the concentration profile decay length of a component corresponds to the correlation length of concentration fluctuations, where the correlation length fluctuations are the size of the composition domains in the system.[220] In narrow pores however, the mean pore width is typically less than the correlation length and concentration profiles which are at maximum near the pore walls overlap, causing enhanced adsorption.

Since the correlation length increases as the critical point is approached, which is a characteristic of criticality in a physical system, enhanced adsorption also occurs in the core of the pore in the near-critical region of the phase diagram for the mixture.[15,218] In this case the near-critical region of the phase diagram is in the vicinity of the mixture critical temperature and critical composition. Under two-phase subcritical conditions of a mixture, the pore walls are wetted either partially or completely by the phase in which the preferred component is the major component. This pre-wetting allows the build up of an interfacial film, leading to an enhancement on the pore surface of the preferred component. An overview of the techniques previously used to investigate the effect of confinement on mixture composition will follow.

4.1.1 Non-linear Dielectric Effect and Light Transmission Measurements

The behaviour of nitrobenzene/n-hexane mixtures has been studied by Gubbins and co-workers, in 100 nm pore size Bio-Glas, using the non-linear dielectric effect (NDE) and light transmission measurements.[217] Measurements taken using both methods were made at a constant bulk composition whilst varying the temperature, starting at a temperature in the single phase region above liquid-liquid coexistence. The temperature was then reduced until the phase transition was observed. This was then repeated at different bulk compositions to produce the liquid-liquid coexistence curve (T vs x_N), where x_N is nitrobenzene mole fraction, as shown in Figure 4.1.

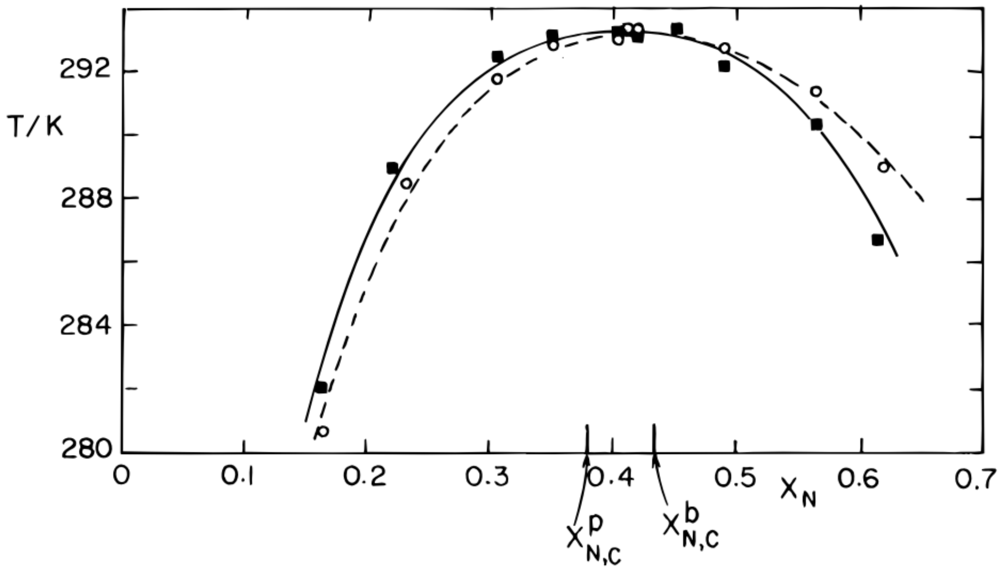

FIGURE 4.1: Liquid-liquid coexistence curves for nitrobenzene/n-hexane mixtures for the bulk mixture (○) and for the mixtures in Bio-Glas, with pores of of 100 nm (■). x_N is the mole fraction of nitrobenzene in the (coexisting) bulk fluid. $x^P_{N,c}$ and $x^B_{N,c}$ are the critical concentrations of the mixture in the pore and in the bulk respectively. Reproduced from reference 217.

The NDE is defined as the change in the medium permittivity (ε) in a strong external electric field (E), as shown in Equation 4.1.

$$\frac{\Delta\varepsilon}{E^2} = \frac{\varepsilon^E - \varepsilon^0}{E^2} \tag{4.1}$$

Where ε^E is the permittivity of the medium in the electric field E and ε^0 is the permittivity of the mixture in the absence of the field. The NDE is advantageous as it is very sensitive to the fluid inhomogeneities in the vicinity of the critical point, which is exhibited as an anomalous increase in $\Delta\varepsilon$.[221] The increase in $\Delta\varepsilon$ is related to the density fluctuations in the mixture due to fluctuating correlation lengths as the system approaches criticality.[222,223] This method can also determine mixture composition as the value of $\frac{\Delta\varepsilon}{E^2}$ depends on component concentration.[221] The permittivity of the mixture is measured via a capacitor in the apparatus. Light transmission measurements were conducted using a photodiode, with the detected voltage proportional to the amount of light transmitted. This was used to determine the temperature of the phase separation in the mixtures, *i.e.* the temperature at which a strong haze (turbidity) of the system is observed due to near-critical concentration fluctuations. This makes light transmission an ideal technique to determine the phase coexistence properties of mixtures.

The study demonstrated that the liquid-liquid phase coexistence curve of the confined mixture was shifted toward the hexane-rich side of the coexistence phase diagram, suggesting that the hexane is more strongly attracted to the walls than nitrobenzene. The critical concentration decreased by a mole fraction of 0.04, while the critical temperature was found to be slightly lowered by 0.05 K. In the bulk mixtures the correlation length and NDE both tend to infinity as the temperature tends toward the critical temperature at the critical composition. In contrast, for the mixture in the porous matrix the NDE tends to a finite value at the critical pore composition, an artefact of the limitation placed on the increase in the correlation length due to pore size. In the case of larger pore diameter materials (100 nm), the maximum correlation length is comparable to the wavelength of light, leading to turbidity at the pore critical point.

4.1.2 Differential Refractometry

Differential refractometry (DR) measurements of binary mixtures in pores offers another experimental approach to study the effect of pore size and adsorbent on mixture component uptake selectivity. DR is based on the precise determination of laser beam deflection on passing through a measurement cell. The deflection of the laser beam is proportional to the refractive index difference between the liquids present in the sample compared to a reference, usually pure liquid water. This means the composition of the liquid sample can be determined *via* a calibration as described by Grüll and Woermann.[186,224] Therefore DR allows for relatively direct and simple determination of mixture composition.

The temperature and composition dependence of preferential water adsorption on a pore surface from 2-butoxyethanol/water mixtures were studied using this method.[186] Experiments were carried out close to liquid-liquid coexistence conditions in the vicinity of the critical point of the system, in controlled glass pore (CPG) silica with a mean pore size of 94.4 nm. Plots of temperature versus composition in adsorption equilibrium with the porous glass exhibit a distortion when compared to the bulk. This distortion reflects the preferential adsorption of water especially near the mixture critical point, which the authors reason is due to the fluctuation of correlation lengths as the critical point is neared. This temperature driven effect can be observed in Figure 4.2, which shows an enhancement in the surface water as the proportion of water in the mixture increases. This effect was determined by taking into account the mass of the adsorbent, its surface area and the change in mixture composition. This temperature effect occurs because the droplet phase becomes more water rich, leading to water rich fluctuations in the near-critical, region enhancing water uptake. These water rich fluctuations increase water uptake as they take place throughout the whole volume of the pore, allowing more water to be pulled into the pore, as it can favourably interact with like molecules throughout the entire pore space and is not just localised near the pore walls. The preferential adsorption of water was found to also depend on the composition of the bulk mixture. This second effect was proposed to be caused by the presence of –SiOH and $–SiO^-$ groups at the hydrophilic surface of the adsorbent, along with the H^+_{aq} counter ions. On the surface of the hydrophilic porous glass the –SiOH and $–SiO^-$ groups are assumed to be hydrated. However, a fraction of the –SiOH groups will exist in the ionized form $–SiO^-_{aq} + H^+_{aq}$. In narrow pores the H^+_{aq} counter ions form a constant charge density over the cross section of the pores caused by the thermal motion of the counter ions and they preferentially bind to water.

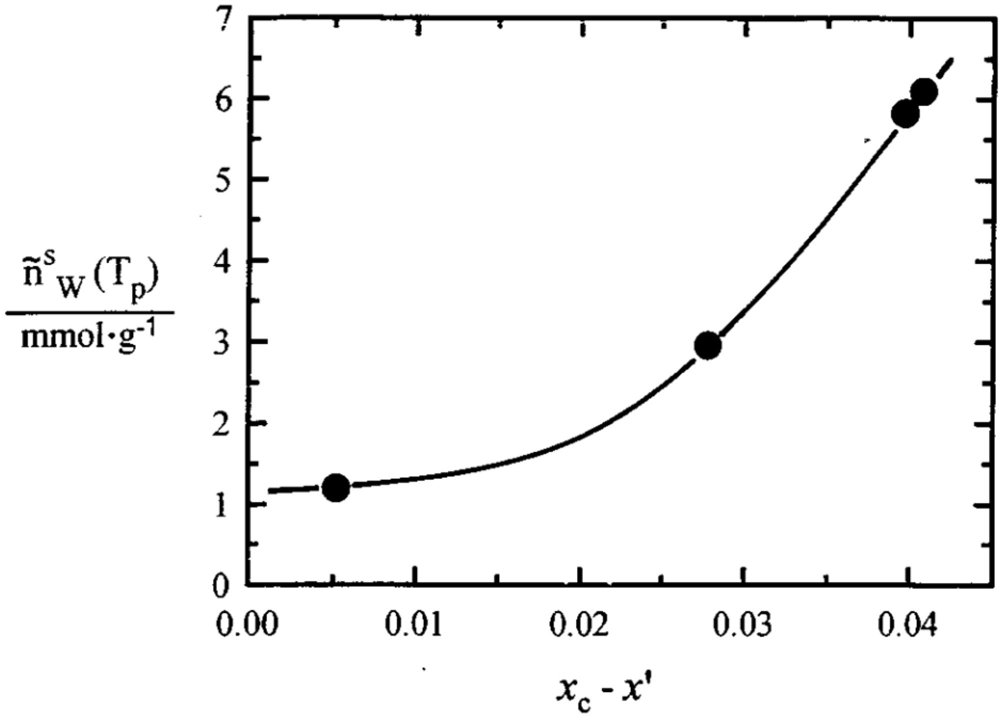

Figure 4.2: Composition dependence of the adsorbed water per unit mass of the hydrophobic porous glass as a function of the difference in mole fraction of 2-butoxyethanol to the critical composition ($x_c - x^{'}$), at phase separation temperature (T$_p$). Reproduced from reference 186.

Work following on from this investigated the extent of the preferential adsorption with the same binary system in porous glass modified with hydrophobic –SiO–C_8H_{17} groups.[224] This is in contrast to the hydrophilic –SiOH groups examined in the previous study. When the mixture is above its critical composition ($x > x_c$), there are composition fluctuations in the system that are water rich due to a water rich droplet phase. The water rich droplet phase is the minor component and coexists with a major phase rich in 2-butoxyethanol. The water rich composition fluctuations which are assumed to determine the adsorptive properties of the hydrophilic –SiOH containing adsorbent, lead to an overall increase in the amount of water absorbed into the pore (Figure 4.3 **(a)**). The presence of the hydrophobic –SiO—C_8H_{17} groups causes the amount of water absorbed in the hydrophobic glass pore to be lower than that of the unmodified hydrophilic glass. This is due to unfavourable interactions with the pore surface, meaning the water rich concentration fluctuations with their short correlation lengths lose their dominating influence on the preferential adsorption of water at the modified surface. This takes place at a certain temperature difference along the coexistence curve, away from the critical temperature (*ca.* 10 K) as shown in Figure 4.3 **(b)**.

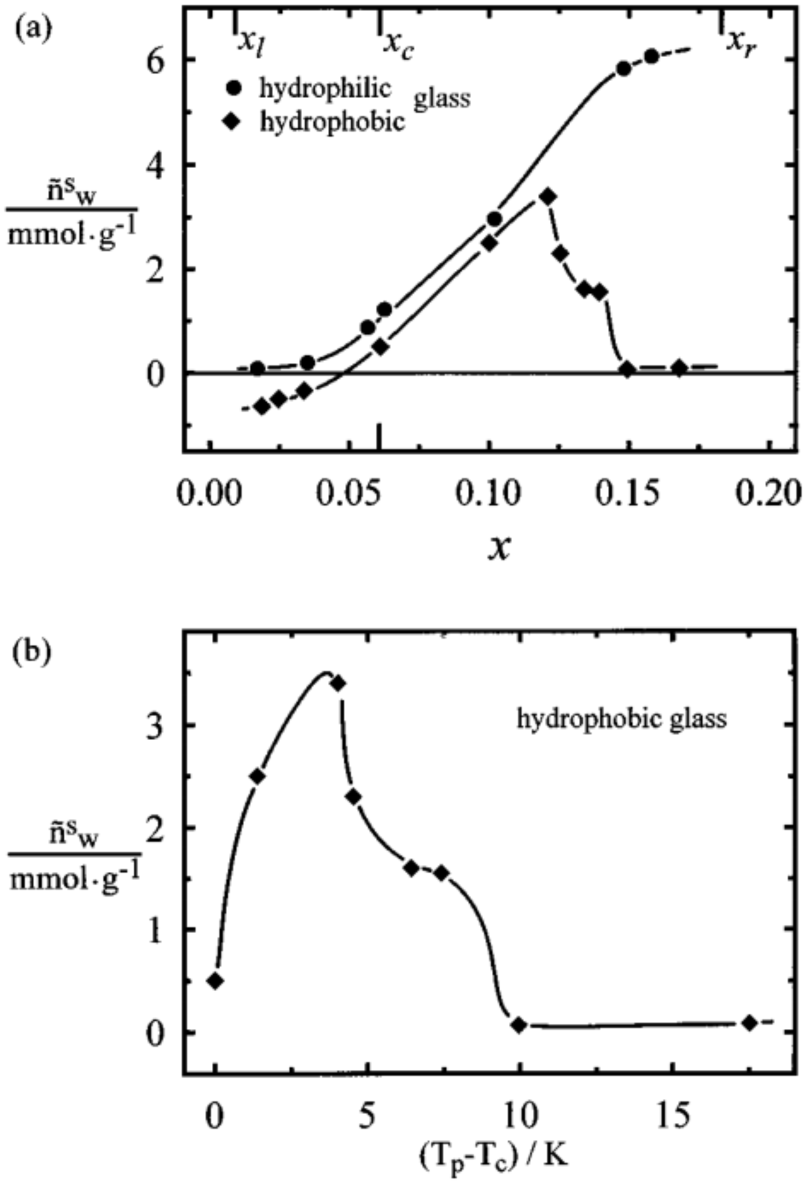

FIGURE 4.3: Composition dependence of the adsorbed amount of water per unit mass of the hydrophobic porous glass as a function of 2-butoxyethanol mole fraction x **(a)** and proximity to the mixture critical temperature (T$_p$-T$_c$) for a composition of x= 0.110 **(b)**. Reproduced from reference 224.

Findenegg and coworkers have also utilised this method to look at a the preferential adsorption of 2-butoxyethanol/water mixtures at the inner surfaces of mesoporous silica glasses,[15] in a wide range of compositions at temperatures close to liquid-liquid phase separation. Butoxyethanol is an amphiphile, possessing both hydrophilic and lipophilic properties.

The confinement effects on the adsorbed binary mixture was investigated using three controlled-pore glass materials, with mean pore sizes of approximately 75, 240, and 500 nm. Preferential adsorption from binary amphiphile/water mixtures (A/W) into the porous glass was determined by the mass of the mixture (m^0), taking into account the known initial composition (w^0), mass of adsorbent (m_s) with its specific surface area (a_s), and the equilibrium composition (w) after equilibration with the adsorbent. Preferential adsorption of the amphiphile can then be expressed as reduced surface excess ($\Gamma_A^{(m)}$).

$$\Gamma_A^{(m)} = \frac{m^0(w^0 - w)}{M_A m_s a_s} \tag{4.2}$$

where w^0 and w denote the mass fractions of the amphiphile in its respective solutions, and M_A is the molar mass of the amphiphile 2-butoxyethanol. Measurements of the pore composition were made by means of DR, which again can be determined from a calibration curve allowing the $\Gamma_A^{(m)}$ to be calculated making the assumption that the adsorbed layer consists only of water.

For all three CPG materials, the deviation from the bulk composition by water adsorption onto the wall is very small in the water-rich regime ($w \leqq 0.2$, Figure 4.4, where w is the mass fraction of the amphiphile). This deviation then increased strongly with rising mass fractions of amphiphile, in the amphiphile-rich regime. The extent of this increase is most pronounced for the material with the widest average pore size and least pronounced for the material with the smallest pore size. At the highest experimental amphiphile mass fraction (w =0.53), the amount of adsorbed water is *ca.* 100 μmol.m^2 at the pore walls of CPG-75, and nearly 300 μmol.m^2 at the pore walls of CPG-500.

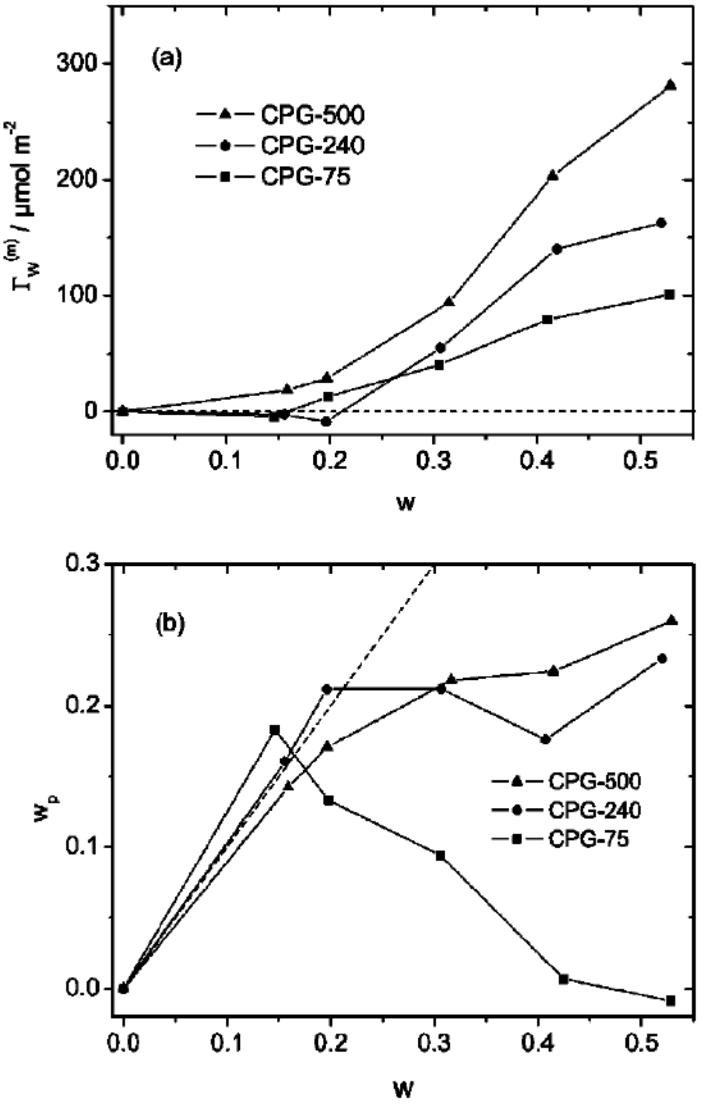

FIGURE 4.4: Dependence of preferential adsorption at 0.1 K below the mixture critical temperature, on the bulk composition w, which is the mass fraction of the amphiphile, of **(a)** the mass-reduced surface excess concentration of water, $(\Gamma_w^{(m)})$ and **(b)** the mean composition of the pore liquid (w$_p$). Reproduced from reference 15.

At low bulk concentrations of amphiphile, a weak positive adsorption of the amphiphile is found in CPG-75 and CPG-240. In the regime of high amphiphile concentrations, which are above or equal to the critical composition and near the mixture critical temperature, the proportion of the amphiphile becomes much smaller than the respective bulk and exhibits a pronounced dependence on the pore width. For CPG-500, the mass fraction of amphiphile in the pore space remains weakly increasing as the mass fraction in the bulk rises. For the material with the narrowest pores, such as CPG-75, the proportion of amphiphile is an inverse function of the mass fraction of amphiphile in the bulk phase, leading to a complete depletion of amphiphile in the pore. In this strong adsorption regime, the area related surface excess amount of adsorbed water decreases with decreasing pore width (Figure 4.4 **(a)**), while the shift in the pore volume related mean composition of water shows an opposite trend (Figure 4.4 **(b)**), *i.e.* greatest deviation from bulk composition occurs in the most narrow pores. The authors rationalise this behaviour by suggesting that the preferred adsorption of water is switching from a pore surface driven effect, to the whole volume of the pore due to the mixture being near the critical point.

4.1.3 Neutron Scattering

As in the case of pure fluids, neutron scattering has also been shown to be a useful technique in probing confined mixture properties. Its excellent spatial resolution allows the distribution, arrangement and unique confined behaviour of mixture components to be studied, for example the wetting of specific components on the pore wall.[146] It also provides a means of measuring the critical point of mixtures, as neutron scattering is sensitive to fluctuations in the mixture's correlation length (concentration domains), which approach a maximum near the critical point.[225,226]

Isobutyric acid/heavy water (iBA/D_2O) binary mixtures, confined in CPG silica with a mean pore width of *ca.* 10 nm have been studied by SANS.[226] This system was studied at off-critical compositions (*i.e.* compositions above and below the critical composition), in a temperature range above and below the mixture T_c. The study suggests the existence of a water-rich adsorbed film at the pore wall in the high-temperature single phase region. This is accompanied by a transformation to a tube-like structure of the pore liquid in the phase separated state below the mixture T_c. The transition temperature to a single phase was also found to be lowered by *ca.* 10 K in the pores relative to the bulk system. Figure 4.5 shows the reduced surface excess of water ($\Gamma_W^{(m)}$) as a function of temperature, for mixtures of three different initial mass fractions of iBA. In the water-rich regime up to the critical composition, the surface excess of water was nearly independent of temperature. However, a pronounced temperature dependence of the surface excess of water is found in the iBA-rich regime w =0.54, where w is the mass fraction of iBA. This is characteristic behaviour of incipient wetting of the pore wall by a water-rich phase, as the phase separation temperature is approached, demonstrating the affinity of the water component to the pore wall.

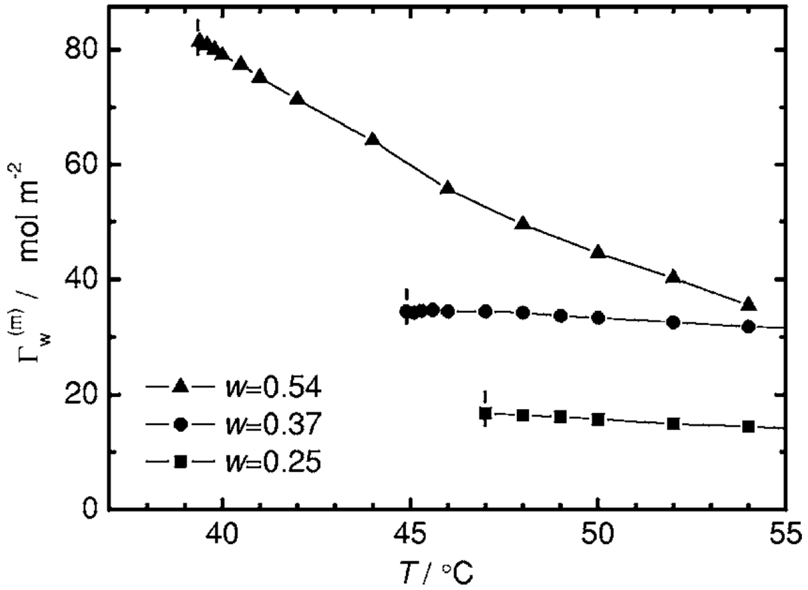

FIGURE 4.5: Adsorption behaviour of iBA/D_2O mixtures in CPG-10, showing the temperature dependence of the surface excess concentration of water ($\Gamma_W^{(m)}$), at three bulk compositions of the iBA mass fraction (w). The curves for w=0.37 and w=0.54 terminate at the respective phase-separation temperature of the mixtures. Reproduced from reference 226.

4.1.4 Theoretical Studies

The phase behaviour of mixtures in pores and the pore selectivity of mixture components can also be investigated through the use of theoretical models. One example is the use of computational models building on the previously discussed SANS data.[218] This study allowed the analysis of the phase behaviour of a binary liquid amphiphile/water mixture, confined between two planar homogeneous surfaces in a slit pore to be calculated. Molecules of water were found to interact preferentially with the solid walls of the pore *via* a long-range potential. A mean lattice gas model was used to analyse the experimental SANS data and examine the microscopic structure of the binary iBA/D_2O system, inside a CPG substrate, with a 10 nm mean pore diameter. The model parameters were adjusted, allowing the theoretical liquid-liquid coexistence curve in the bulk to match its experimental counterpart. Appropriate values of the pore width and the attraction strength between the pore allowed for the estimation of the effect of confinement on the phase behaviour. A shift in the critical point on the mixture phase diagram and the appearance of two more coexistence curves within the pore, exhibiting very low critical temperatures were observed. These additional coexistence curves are due to the existence of water rich films, of one or two layers of molecules near the wall of the pore, due to the pore selectivity. Overall this behaviour shifts the confined coexistence to a more water rich composition and depresses the liquid-liquid critical point as shown in Figure 4.6. It was also shown that composition of the first layer adsorbed at the walls is unchanged in all phases in the temperature range studied. Therefore, the theoretical predictions are consistent with results of the previous SANS study and support the interpretation that the surface concentration of water is almost independent of temperature and mixture composition. This again points to incipient wetting behaviour of water on the pore wall.

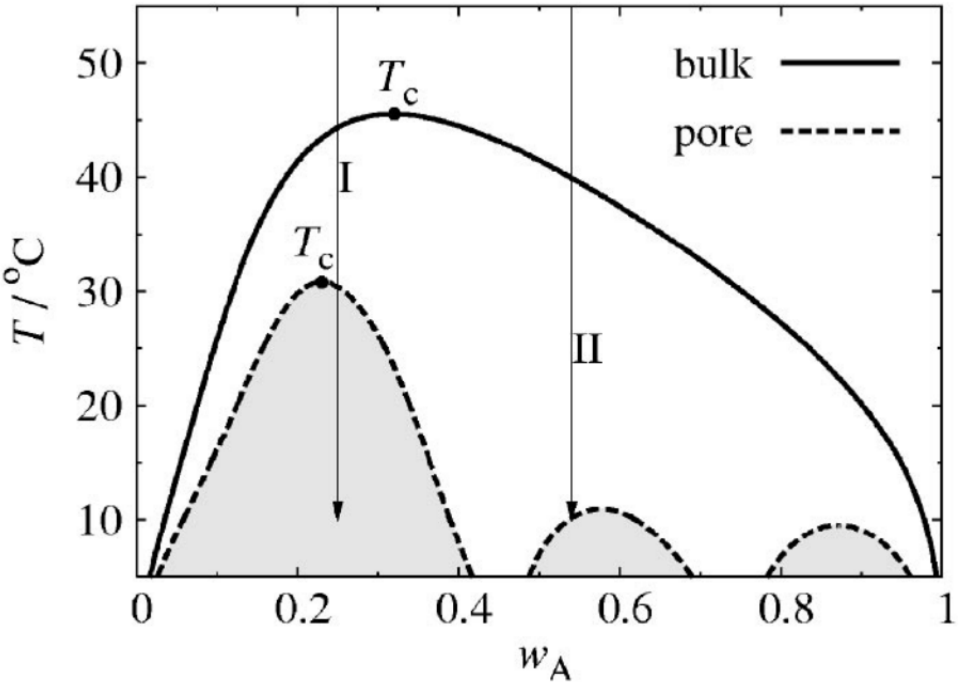

FIGURE 4.6: Phase diagram of the simulated mixture in the temperature (T) vs amphiphile fraction (w_A) projection for the bulk system (line) and confined in the slit pore (dotted line). Shaded regions are phase coexistences of the confined system. Dots indicate critical points. Reproduced from reference 218.

Density functional theory calculations carried out by Gubbins and coworkers,[217] in tandem with their experimental NDE and light transmission study, have shown that when the fluid-wall attraction is greater for one component, the coexistence curve shifts toward the attractive component rich side of the diagram (see Figure 4.7). The calculations indicate an overall lowering of the mixture critical temperature as the fluid-wall interaction strength is increased. The solubility of the less attractive component, in the more attractive component rich phase is reduced, while the favoured component in the less attractive rich phase is increased. The change in solubility is large, especially at the lower temperatures. These effects are enhanced when the pore size is reduced and when the difference in attractive fluid-wall forces for the two components is increased. This effect occurs due to the increase in the relative pore volume occupied by the preferred wall bound component, reducing the solubility of the second component in the pore confined fluid.

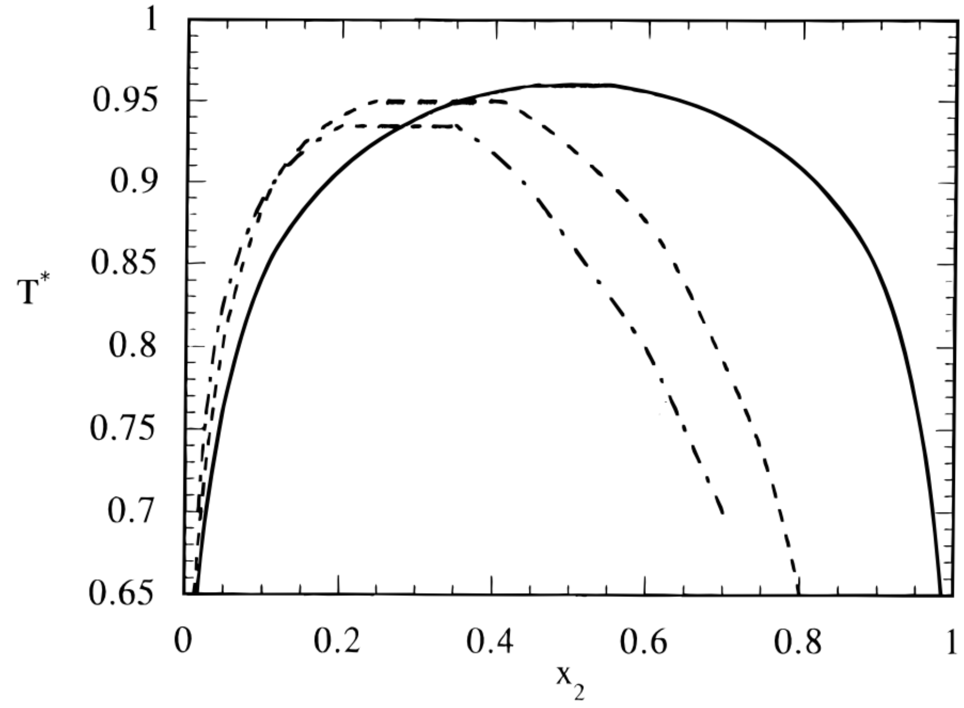

FIGURE 4.7: Liquid-liquid phase diagrams for the bulk (solid line) and confined Lennard-Jones mixture in two pore widths (H/σ). Where σ is the fluid-fluid interaction parameter, for 10.0 H/σ (dotted-dashed line) and 20.558 H/σ (dashed line). Reproduced from reference 217.

Simulated pores approximated from pseudoatoms have been used to study the selective adsorption of carbon dioxide in mixtures with methane in a grand canoncial ensemble.[227] The pseudoatom model allowed the comparison between different pore geometries and the influence of adsorption energy on absorption selectivity, due to the simplicity of the model. The selectivity of a binary mixture (S) can be expressed as:

$$S = \left(\frac{ax_1}{ax_2}\right)\left(\frac{bx_1}{bx_2}\right) \tag{4.3}$$

where x_1 and x_2 are the mole fractions of each component and the a and b refer to the respective values in the adsorbed and bulk phase.

The slit pore and cylindrical pore models studied show a number of differences that have been attributed to geometric effects. These arise from the greater constraint on the freedom of rotation for the CO_2 molecule in the cylindrical geometry, resulting in a reduced uptake of CO_2 compared to that in a slit pore, as its pressure increases. This study also suggests that energetic effects play a major role in determining selectivity. The importance of energetic effects was supported by tailoring the adsorbent selectivity to range from four to one in favour of CO_2, to four to one in favour of methane, in the models used. This is illustrated in Figure 4.8.

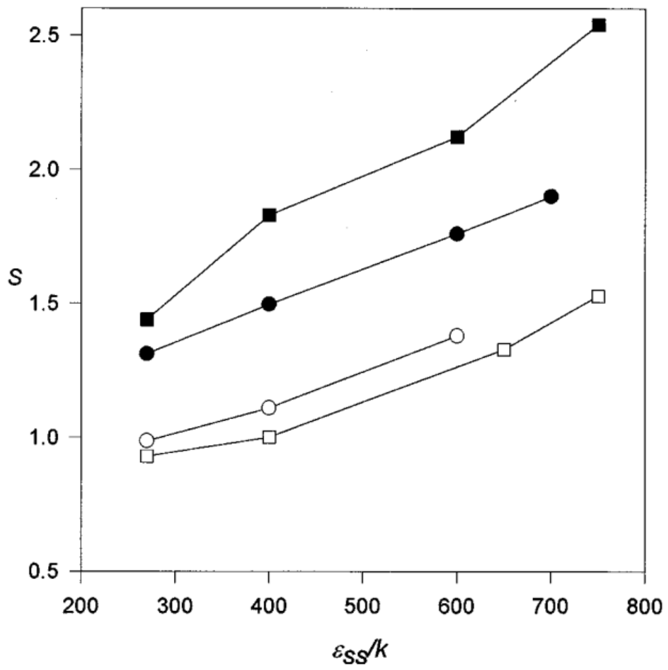

FIGURE 4.8: Variation of carbon dioxide selectivity at 298 K, with a bulk mole fraction of 0.5, for cylindrical pores (circles) of radius 0.915 nm, and slit pores (squares) of width 1.0 nm, at different surface energies. The filled points are at a fugacity of 24 bar, and the open points are at a fugacity of 2.5 bar. Fugacity is the pressure of an ideal gas that has the same chemical potential of its real counterpart. Reproduced from reference 227.

GCMC simulations of water-methanol mixtures have been carried out in activated slit carbon and graphite pores with a 2 nm diameter, at 298 K.[228] The adsorption of the mixtures were found to commence at lower pressures for the activated carbon pore than for the graphite equivalent. The activated carbon pore has an abundance of carboxylic acid groups (–COOH) leading to different wall-fluid binding selectivity. Also a cooperative bonding mechanism between water molecules leads to enhanced hydrogen bond formation with the –COOH groups, resulting in the continuous filling of activated carbon pores with pressure, compared to a sharp capillary condensation seen in the graphite pores. Water from the mixtures was found to be preferentially adsorbed in the activated carbon pores, over a wide range of pressures, due to these stronger hydrogen bonding interactions. However, at the lowest of pressures, methanol is the major component in the pore due to its stronger dispersion interactions. Water in the activated carbon pore mixtures, exhibits bulk-like behaviour over the entire pore, in terms of the number of formed hydrogen bonds between water molecules, unlike its adsorption in the graphite pore. The complexation of both water and methanol molecules with the –COOH active sites, result in a preferred orientation near the wall. Water molecules were found to form two different complexes with the active sites, in comparison to one by methanol, as shown in Figure 4.9. The average number of hydrogen bonds per molecule for both water and methanol were close to their bulk values. Negative values of solvation force obtained for the mixture, reflect the hydrophilic interactions of the mixtures with activated carbon pores, in contrast to the positive values obtained in graphite pores.

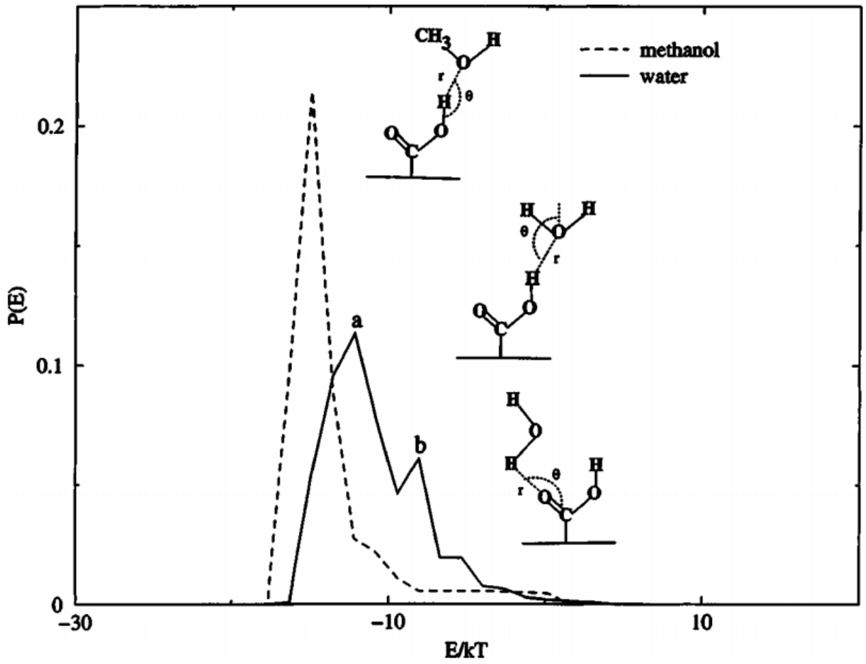

FIGURE 4.9: Probability distributions of fluid–COOH pair interaction energy due to coulombic and dispersion interactions, for a water-methanol mixture ($x_{bulk,m}$ = 0.5) in a slit activated carbon pore of width 2 nm at 298 K and a relative pressure (P/P_0)=0.15. The geometric arrangements of the molecular complexes are also shown. Configurations **a** and **b** represent the probability of the water forming hydrogen bonds through the hydroxyl or carbonyl portions of the carboxylic acid. The favourable interaction energy of the methanol probability distribution is due to the molecule's favourable dispersion interactions in this low pressure environment. Reproduced from reference 228.

GCMC simulations have also been used to study the pore selectivity of small sulfur containing molecules from a simple binary gas mixture.[216] In this study the pore size, mixture composition, temperature, and pore functional groups have all been investigated to optimise the uptake of both hydrogen sulfide (H_2S) and sulfur dioxide (SO_2), in single wall nanotubes (SWNTS). A pronounced maximum was observed to appear in selectivity at a particular diameter, as shown in Figure 4.10. This maximum is explained as the synergistic effect between the competitive adsorption of the two components and the steric effect of a pore. For very small pores no molecules can be adsorbed in the pores, resulting in a low selectivity. In a large pore, the fluid-solid interaction lengths no longer dominate the volume of the pore, since they rapidly decay with distance. This leads to a reduction in selectivity. For H_2S/CH_4, H_2S/CO_2, and SO_2/N_2 mixtures, the greatest selectivity is obtained at a pore diameter of 0.81 nm because the pore can accommodate one layer of H_2S or SO_2 molecules. However, for the SO_2/CO_2 mixture, the optimal pore diameter shifts to a higher diameter of 1.09 nm due to a synergistic effect between the competitive adsorption of the components and the steric effect of a pore. The composition, pressure, temperature, and competitive adsorption were all shown to affect the optimal pore size of the adsorbent.

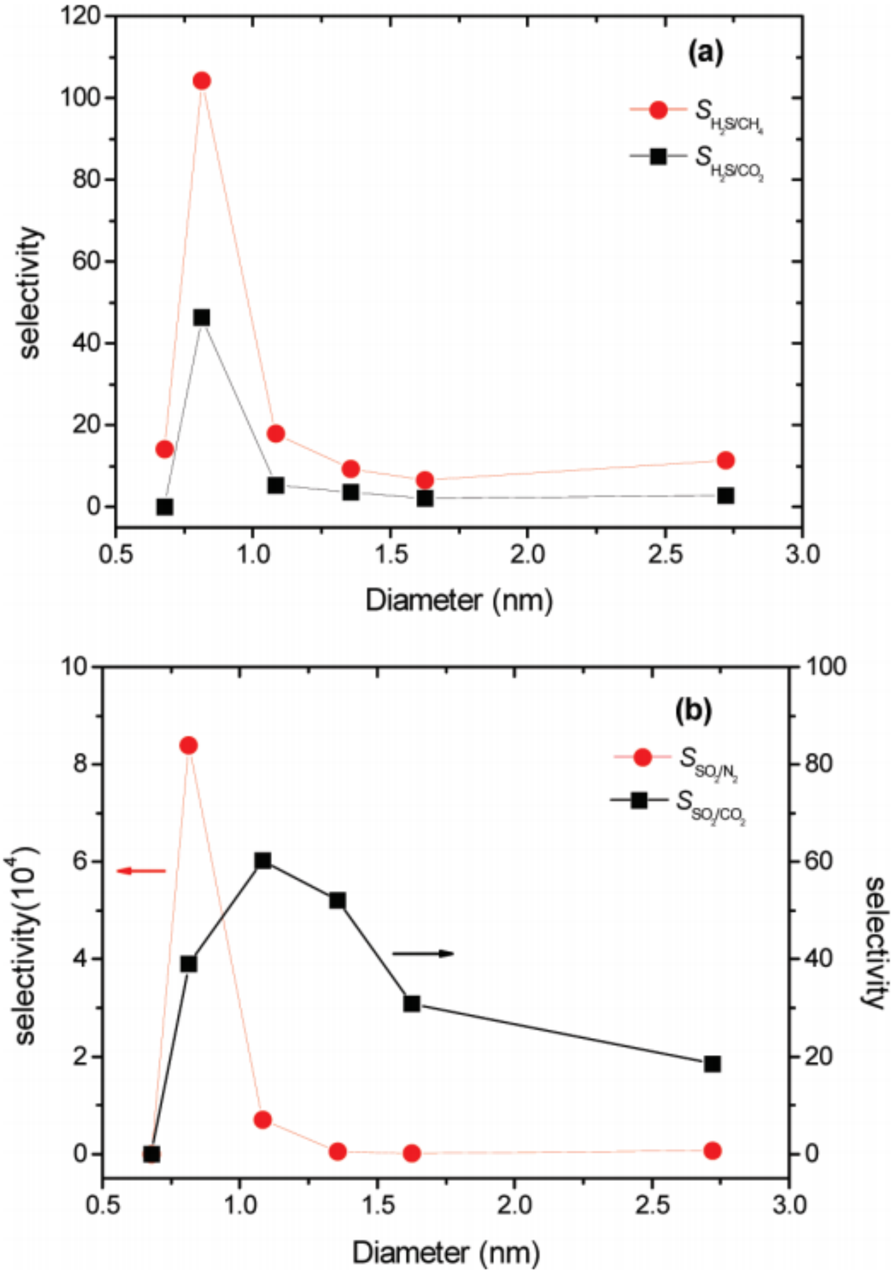

FIGURE 4.10: Selectivity of **(a)** H_2S/CH_4 (xH_2S = 0.00333) and H_2S/CO_2 (xH_2S = 0.005), also **(b)** SO_2/N_2 (xSO_2 = 0.00556) and SO_2/CO_2 (xSO_2 = 0.04762) at various diameters of the SWNTs at 303 K and 100 kPa (14.5 psi). Reproduced from reference 216.

The effect of temperature on the selectivity of the sulfur containing compounds, at the previously established optimal pore size was also examined in this study.

For all the binary mixtures, increasing the temperature reduces the selectivity, with the selectivity of the SO_2/N_2 mixture influenced the most by the temperature. However, beyond the T_c of the N_2 it remained constant, as the supercritical N_2 does not adsorb easily onto SWNT walls. As SO_2 under these conditions is a subcritical gas, it exhibits preferential adsorption. This is because the SO_2 is liquefied at the pore wall due to the temperature and potential energy of the pore surface, causing a drastic decrease of the selectivity of the N_2 in the SO_2/N_2 mixture.

The influence of pore wall functional groups was also examined by this study. Randomly distributed carbonyl groups on the surface of the SWNTs, with different site densities were used to determine this effect. It was found that the selectivities of H_2S or SO_2 in the H_2S/CO_2 and SO_2/CO_2 mixtures respectively, are not influenced by the site density of the carbonyl groups. By contrast the increase of site density can improve the selectivity of H_2S in the H_2S/CH_4 mixture. This is because the CH_4 is non-polar and the polar carbonyl functional group unfavourably interacts with CH_4. However these groups do favourably interact with the more polar H_2S species, leading to an increase in the selectivity of the H_2S in the SWNTs. Out of the three mixtures the carbonyl groups have the most distinct effect on the adsorption of SO_2 for the SO_2/CO_2 mixture. At low pressures only a few molecules are adsorbed, most of which are SO_2 molecules. These molecules assemble near the two positions of the nanotube interstice and carbonyl groups. In case of the interstice, the adsorption arises from the overlap of the solid-fluid potential of adjacent nanotubes, while the latter is due to the existence of carbonyl groups that contribute to the adsorption of the fluid molecules.

The behaviour of benzene/water mixtures in graphitic slit pores have also been studied with Monte Carlo simulations.[229] It was shown that the adsorption of the mixture starts with the adsorption of benzene molecules on the graphite surface, and they act as binding sites for water molecules to adsorb onto, as shown in Figure 4.11.

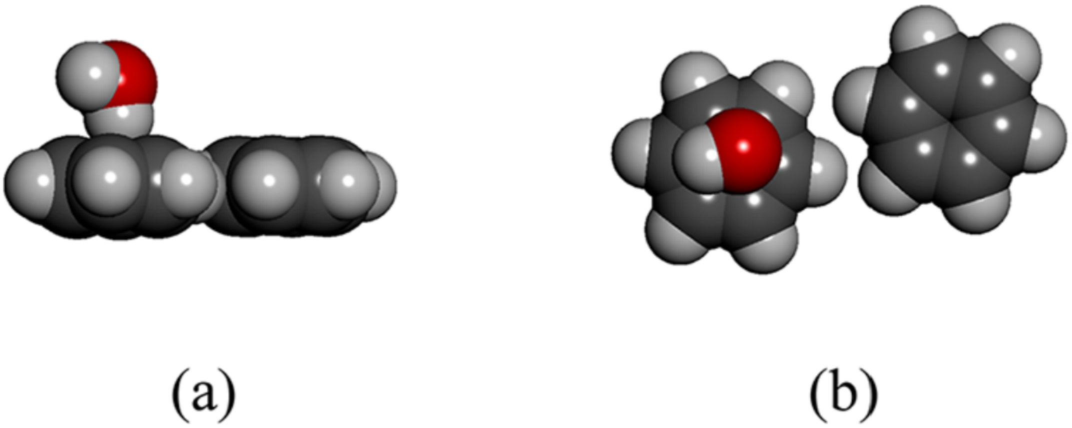

Figure 4.11: Anchoring effect of benzene on water (a) front view and (b) top view. Black sphere: carbon (C), red sphere: oxygen (O), and white sphere: hydrogen (H). Reproduced from reference 229.

High loadings of water in a slit-pore significantly affect the arrangement and orientation of benzene molecules. In the absence of water the benzene molecules stay parallel and close to the pore surface, maximising their interaction with the graphite surface even at loadings below monolayer coverage. When water molecules are introduced into the pore, they form clusters that attach to benzene molecules through electrostatic interactions and span across the pore. As the water density is increased further these clusters grow until the pore is completely filled. This growth of water clusters did not affect the benzene distribution on the surface or its orientation. When the pore is completely filled, some benzene molecules are displaced from the pore walls and the parallel orientation of benzene is compromised to facilitate their hydrogen bonding with the water molecules. When the water density in the pore approaches its bulk liquid density, the water molecules displace some benzene molecules from the surface and the benzene sorption process switches from an adsorption to absorption mechanism, where adsorption is the condensation of the molecules primarily near the walls and absorption is condensation of the fluid into whole pore volume. The authors also studied the influence of the external vapour composition on the adsorption isotherms of benzene and water. It is observed that a high concentration of benzene in the vapour phase facilitates the adsorption of both benzene and water, in such a manner that the condensation pressure of benzene and the pressure of water adsorption shift to lower values. Again at high pressures, the adsorption of water is dominant at the expense of benzene adsorption. When the molar fraction of water in the vapour phase is higher than 0.5, there is a competition between benzene and water after the condensation of benzene. Due to its smaller molecular size and the stronger fluid-fluid interactions, adsorption of water becomes dominant, resulting in the desorption of some benzene molecules from the pore.

4.2 Aims

The aims of this Chapter are to describe the use of vibrational spectroscopy to investigate the change in pore adsorbed mixture composition, for carbon dioxide/acetonitrile (CO_2/CH_3CN) and difluoromethane/tetrabutylammonium tetrafluoroborate (CH_2F_2/TBA.BF_4) binary mixtures, neither of which have been previously studied in the literature. Although many studies have investigated the mixture composition of pore confined fluids, no research has been undertaken with supercritical fluid electrodeposition relevant systems. The binary mixtures selected for this study are of particular interest for supercritical fluid electrodeposition,[34,45,230] as the CO_2 and CH_2F_2 components provide a supercritical solvent from which deposition takes place, with the CH_3CN and TBA.BF_4 enhancing conductivity and solubility of the dissolved ions. A greater understanding of how pore sorption changes the mixture composition will allow changes in composition to then be taken into account, providing the ability to tune the electrodeposition process from the single phase, into the porous templates.

4.3 Results and Discussion

4.3.1 Near-Infrared and Raman Spectroscopic Measurements of Carbon Dioxide and Acetonitrile Mixtures

Near-infrared spectra of a range of CO_2/CH_3CN mixtures of known compositions were recorded, allowing the absorbance ratio of each component to be calibrated to mixture composition. The spectra were simple, mainly consisting of non-overlapping bands relating to each species. In the case of CO_2 this consisted of the three combination bands in Fermi resonance known as the Fermi triad, centred at *ca.* 5000 cm^{-1}, assigned as $4\nu_2 + \nu_3$, $\nu_1 + 2\nu_2 + \nu_3$ and $2\nu_2 + \nu_3$ combination bands, from lowest to highest energy.[111] Acetonitrile has lower energy bands in close proximity to the CO_2 Fermi triad in the 4300-4500 cm^{-1} range, and these can be assigned as the $\nu_1 + \nu_3$, $\nu_1 + \nu_6$, $\nu_3 + \nu_5$ and $\nu_5 + \nu_6$ bands,[231] from lowest to highest energy (see Figure 4.12).

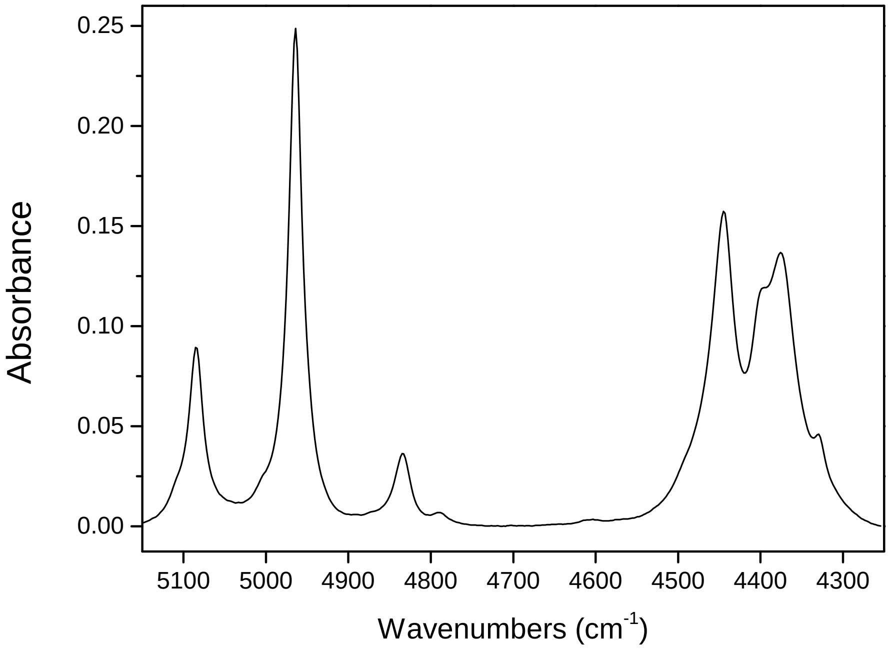

FIGURE 4.12: Near-infrared spectrum of a 5.6 molar ratio (CO_2/CH_3CN) mixture clearly showing the carbon dioxide Fermi triad centred at *ca.* 5000 cm^{-1} and acetonitrile peaks at *ca.* 4410 cm^{-1} .

The composition of a mixture can also be determined using Raman spectroscopy after calibration. Again, the Raman measurements exhibited simple spectra, consisting of bands from each species. In the case of CO_2, the Fermi diad centred at *ca.* 1300 cm^{-1}.[232] These bands are assigned as the ν_1 vibration at lower energy and the $2\nu_2$ vibration at higher energy.[206] Acetonitrile has two higher energy bands in the Raman spectrum, assigned as the ν_2 C≡N stretch at *ca.* 2250 cm^{-1} and ν_1 symmetric C–H stretch at *ca.* 2950 cm^{-1} (see Figure 4.13).[233]

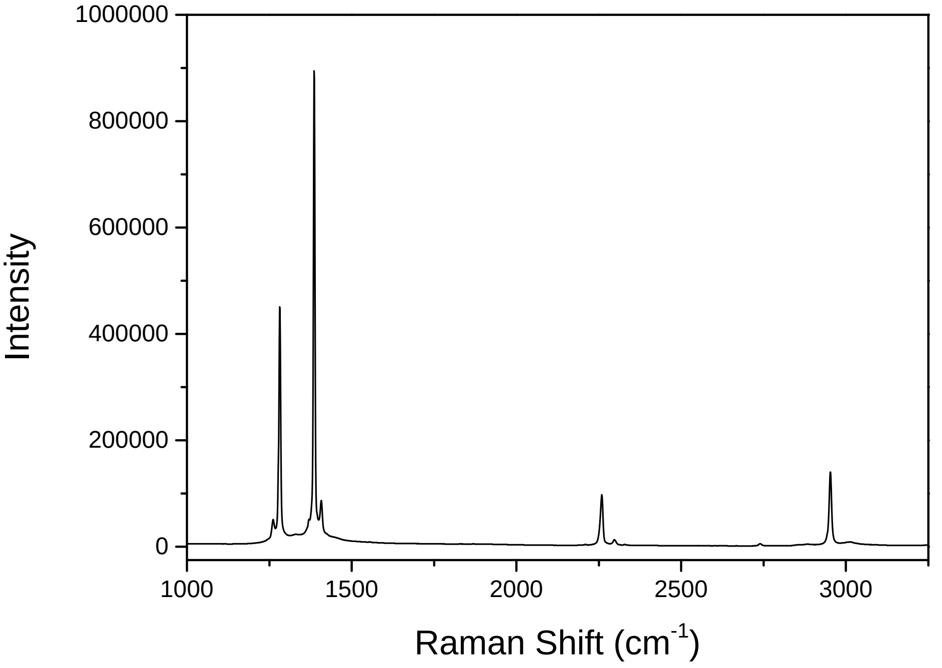

FIGURE 4.13: Raman spectrum of a 5.7 molar ratio (CO_2/CH_3CN) mixture clearly showing the carbon dioxide Fermi diad centred at *ca.* 1300 cm^{-1} and acetonitrile peaks at *ca.* 2250 and 2950 cm^{-1} .

The mixtures were prepared by weight in a variable volume view cell, then heated and pressurised into the single phase region of the binary mixture.[234] The mixture was left to stir to ensure homogeneity, and flowed from the view cell into the preheated spectroscopy cell by opening the view cell's outlet valve. The mixture was pumped using the rear hydraulic ram in the view cell, reducing the volume and flowing the mixture through the system. The system was kept at a constant pressure in the one phase region for the mixture, by means of venting through a back pressure regulator (BPR). Bulk mixture composition could be checked spectroscopically by collecting Raman spectra through the front window of the view cell, or allowing the mixture to be flowed through the infrared cell, allowing it to equilibrate, and then collecting near-infrared spectra. This enabled the bulk mixture composition to be monitored throughout the experiment, ensuring that the composition introduced into the pores did not change and allowing calibration to take place. Finally as the mixture was flowed through the porous material, spectroscopic measurements were taken and the CO_2/CH_3CN band ratios were monitored as a function of time, ensuring the pore confined mixture composition had equilibrated. This was indicated by a stabilisation of the band ratio with time, as shown in Figure 4.14).

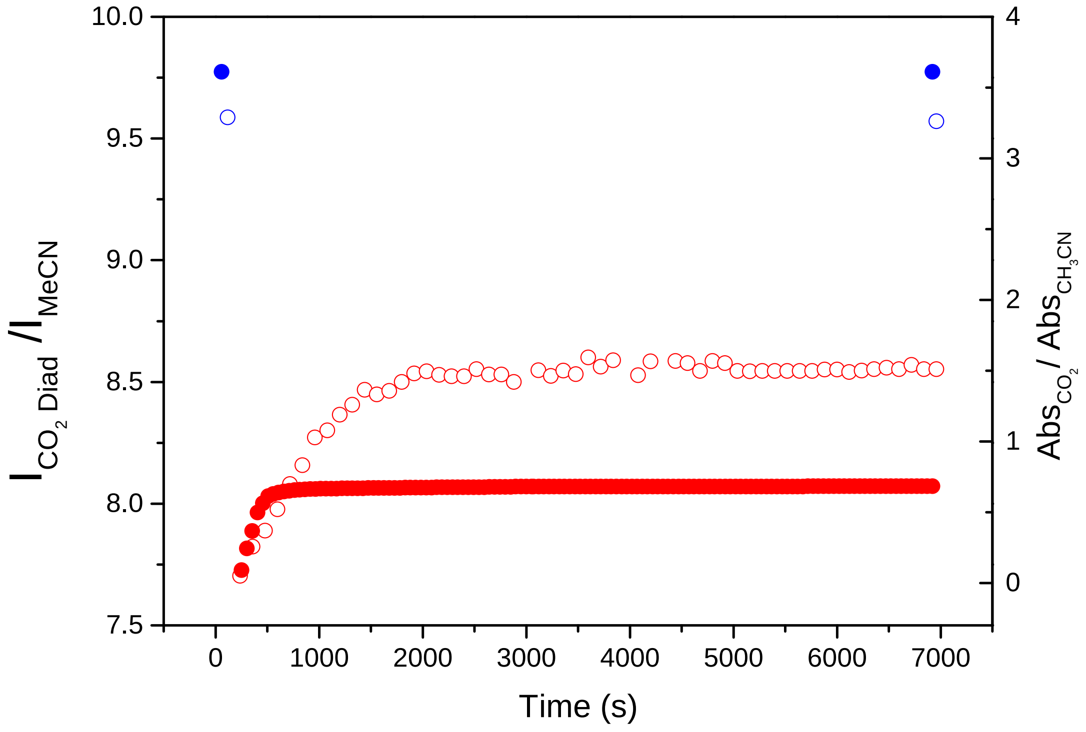

FIGURE 4.14: Examples of Raman (open symbols) and NIR (closed symbols) band ratios for CO_2 and CH_3CN plotted as a function of time with bulk mixtures with a molar ratio (CO_2/CH_3CN) of 5.69 and 17.40 respectively. The red points are the pore confined band ratios and blue are the bulk at the start and end of the experiment.

4.3.2 Calibration of Carbon Dioxide and Acetonitrile Mixture Composition by Near-Infrared and Raman Spectroscopy

Near-infrared and Raman spectroscopy preformed on a range of CO_2/CH_3CN mixtures of varying molar ratio results in a change in the relative peak intensities. Molar ratio can be defined as the number of moles of the first component (x_1) as a ratio of the second component (x_2) as shown in Equation 4.4.

$$MolarRatio = \frac{x_1}{x_2} \tag{4.4}$$

The variance in the peak intensity ratio with mixture composition can be clearly seen, with the intensities of the CH_3CN bands at *ca.* 4400 cm^{-1} (NIR) and 2950 cm^{-1} (Raman) becoming weaker at higher molar ratios of CO_2 (see Figures 4.15 and 4.16).

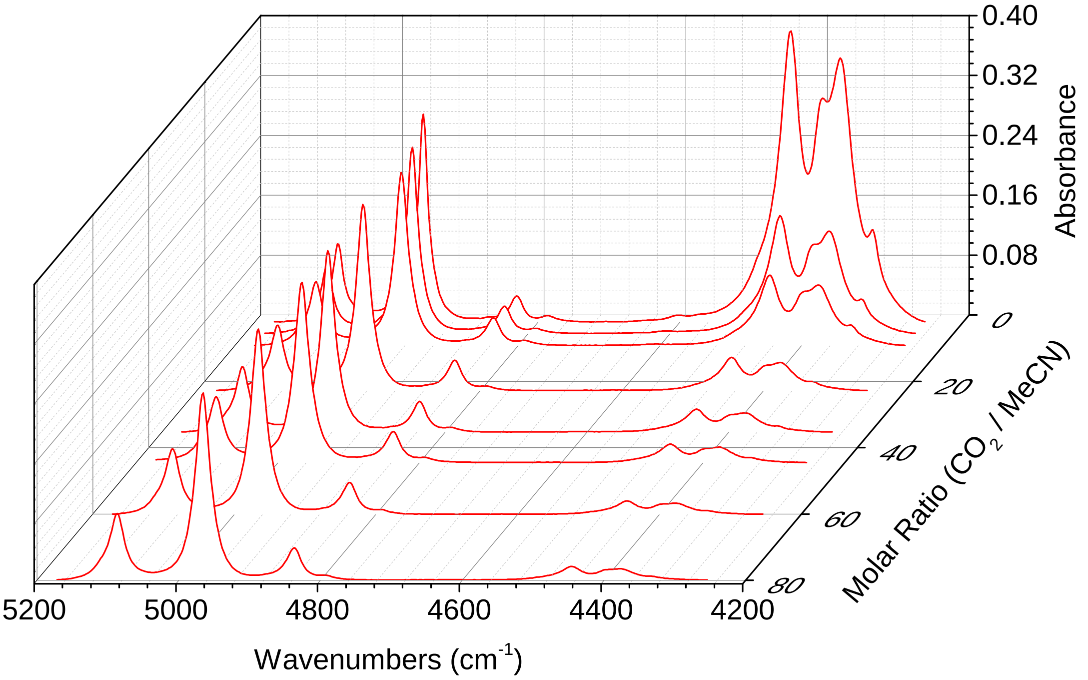

FIGURE 4.15: A waterfall plot of near-infrared spectra of CO_2 and CH_3CN mixtures at a range of molar ratios clearly displaying the changes in ratio of the carbon dioxide Fermi triad centred at *ca.* 5000 cm^{-1} and acetonitrile absorbances at *ca.* 4410 cm^{-1}.

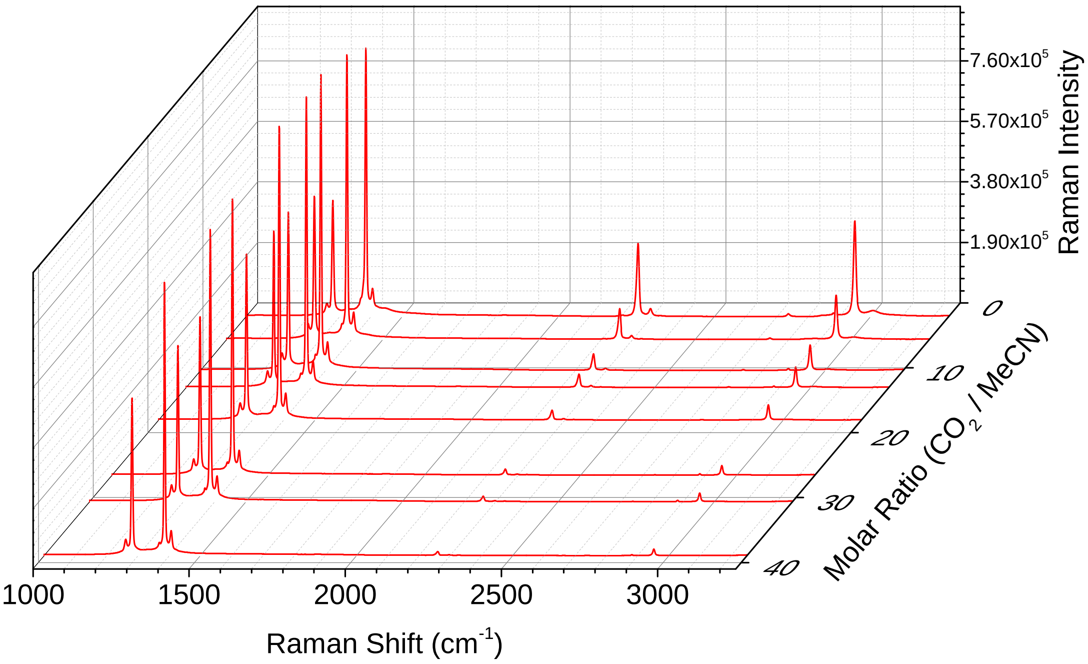

FIGURE 4.16: A waterfall plot of Raman spectra gathered from a number of CO_2 and CH_3CN mixtures displaying how the intensities of the spectral bands vary with molar ratio. The CO_2 Fermi diad is centred at *ca.* 1300 cm^{-1} and the Raman bands for CH_3CN appear above 2200 cm^{-1} .

The ratio of the central $\nu_1 + 2\nu_2 + \nu_3$ NIR absorbance of the CO_2 Fermi triad at *ca.* 5000 cm^{-1} to the higher energy $\nu_5 + \nu_6$ CH_3CN band at *ca.* 4450 cm^{-1} was studied as a function of the mixture molar ratio, allowing a linear calibration plot to be constructed. Furthermore, the ratio of the Raman peak intensities of the higher energy CO_2 ν_1 peak belonging to the Fermi diad, and the CH_3CN ν_1 symmetric C–H Stretch at *ca.* 2950 cm^{-1} was also determined. Plotting the absorbance or Raman intensity ratio as a function of molar ratio also allowed for a linear regression of the data, giving a mathematical equation to deduce molar ratio (CO_2/CH_3CN) solely from the absorbance or Raman intensity ratio (see Figure 4.17).

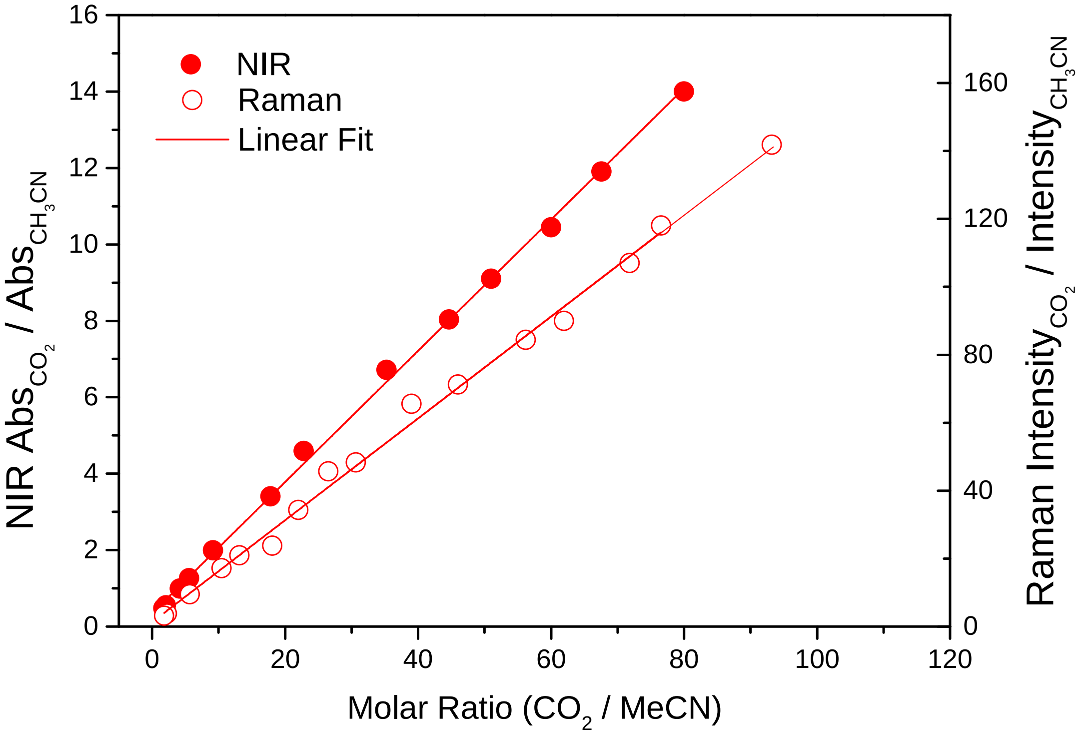

FIGURE 4.17: Calibration plot of the NIR CO_2/CH_3CN absorbance or Raman intensity as a function of molar ratio. The standard errors of the NIR and Raman spectroscopic calibrations are 1 and 2 % respectively

4.3.3 Composition of Carbon Dioxide and Acetonitrile Mixtures in Silica and Anodic Alumna Templates, Determined by Near-Infrared Spectroscopy

The established relationship between the relative vibrational band intensities of each mixture component allowed the study to progress, probing the change in mixture composition when confined in a pore. Using the calibration of band intensities obtained from the bulk mixtures, the composition of the pore mixture could be calculated from the spectroscopic band intensity ratios and compared to that of the bulk mixture. It can be seen that there is a profound deviation in composition from the bulk mixture, with an enhancement of the CH_3CN component, resulting in a significantly lower pore molar ratio value, as shown in Figure 4.18. This deviation appears to be much greater at lower concentrations of CH_3CN.

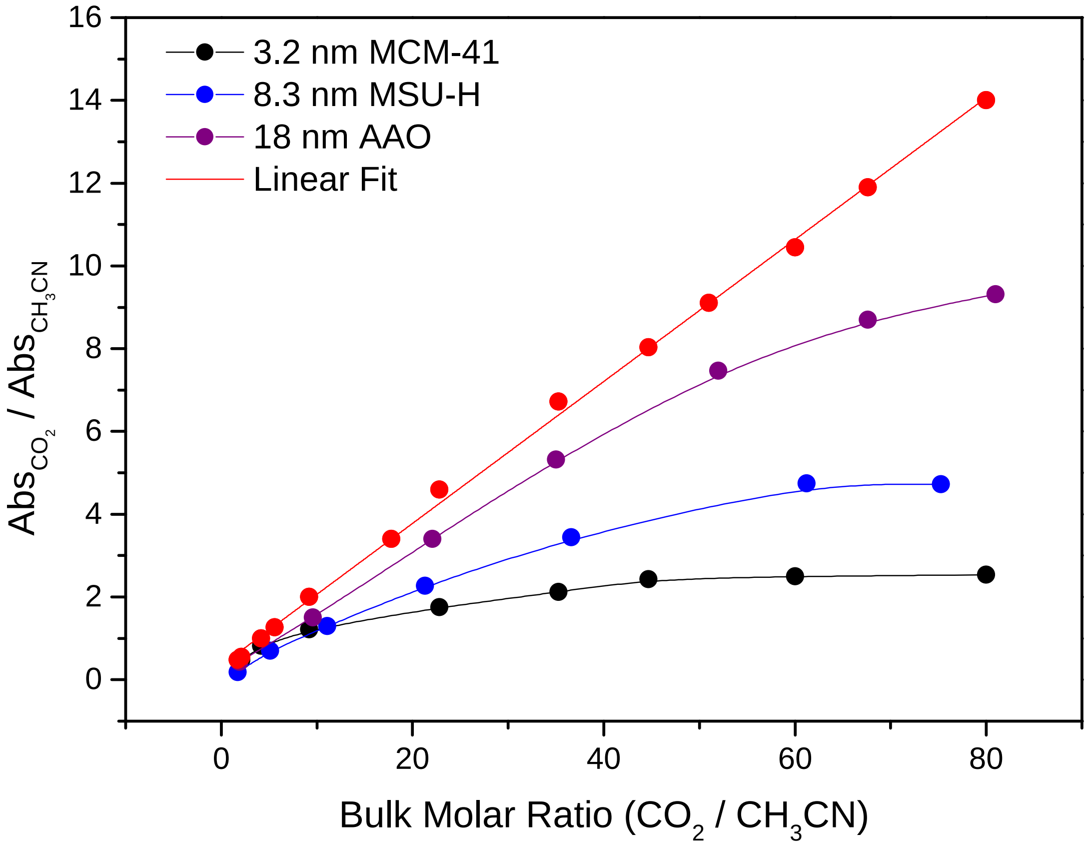

FIGURE 4.18: The ratio of the CO_2/CH_3CN absorbances as a function of the bulk mixture molar ratio.

In order to equate these results to the application of supercritical fluid electrodeposition, it is appropriate to relate this change in composition to a mole fraction value (see Equation 4.5). In the literature, this process takes place in a mixture of CO_2/CH_3CN with an approximate mole fraction of CH_3CN between 0.12–0.13 in the mixture.[34,45]

$$Mole\ Fraction = \frac{x_1}{x_1 + x_2} \tag{4.5}$$

Where the moles of CH_3CN is x_1 and the moles of CO_2 is x_2.

Figure 4.19 clearly demonstrates that there is a large impact on the pore confined fluid CH_3CN mole fraction, across the entire range of mixture compositions studied. The deviation increases if the pore diameter of the material decreases. There is also proportionally a greater increase of CH_3CN mole fraction in the pores containing mixtures with a lower proportion of CH_3CN.

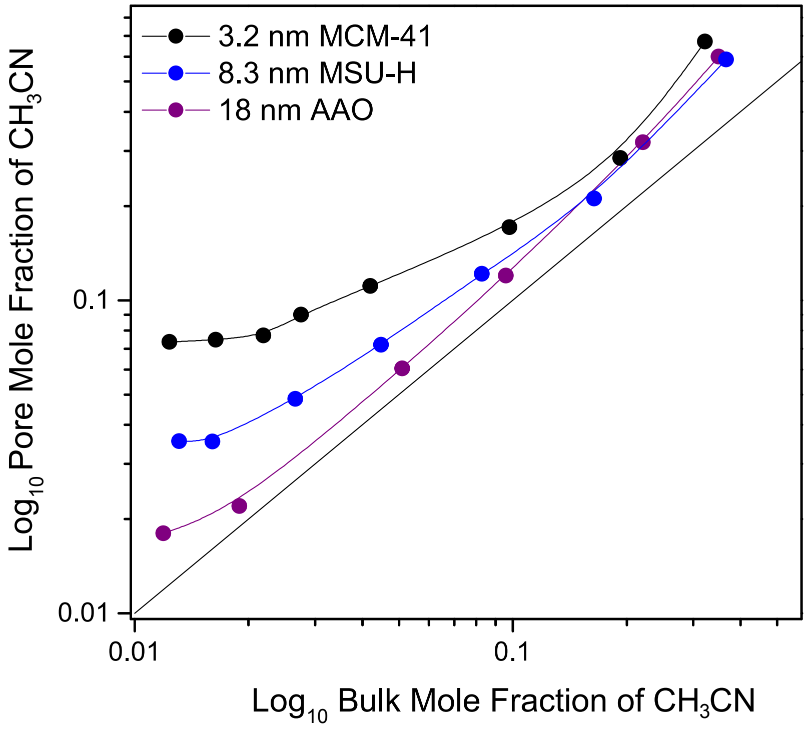

FIGURE 4.19: The pore confined mole fraction of CH_3CN as a function of bulk CH_3CN mole fraction determined by NIR. The black line indicates the mole fraction value if the bulk and the confined mixtures are of an equivalent composition and the curved coloured lines serve as guides to for eye.

4.3.4 Composition of Carbon Dioxide and Acetonitrile Mixtures in Silica and Anodic Alumna Templates Determined by Raman Spectroscopy

Raman spectroscopic measurements taken of the mixture within MCM-41 (3.2 nm pore size) again display the largest enhancement of the proportion of CH_3CN within the pore mixture, when compared to the bulk. Again this difference is observed to be greatest at the bulk mixtures containing the lowest proportion of CH_3CN (see Figures 4.20 and 4.21).

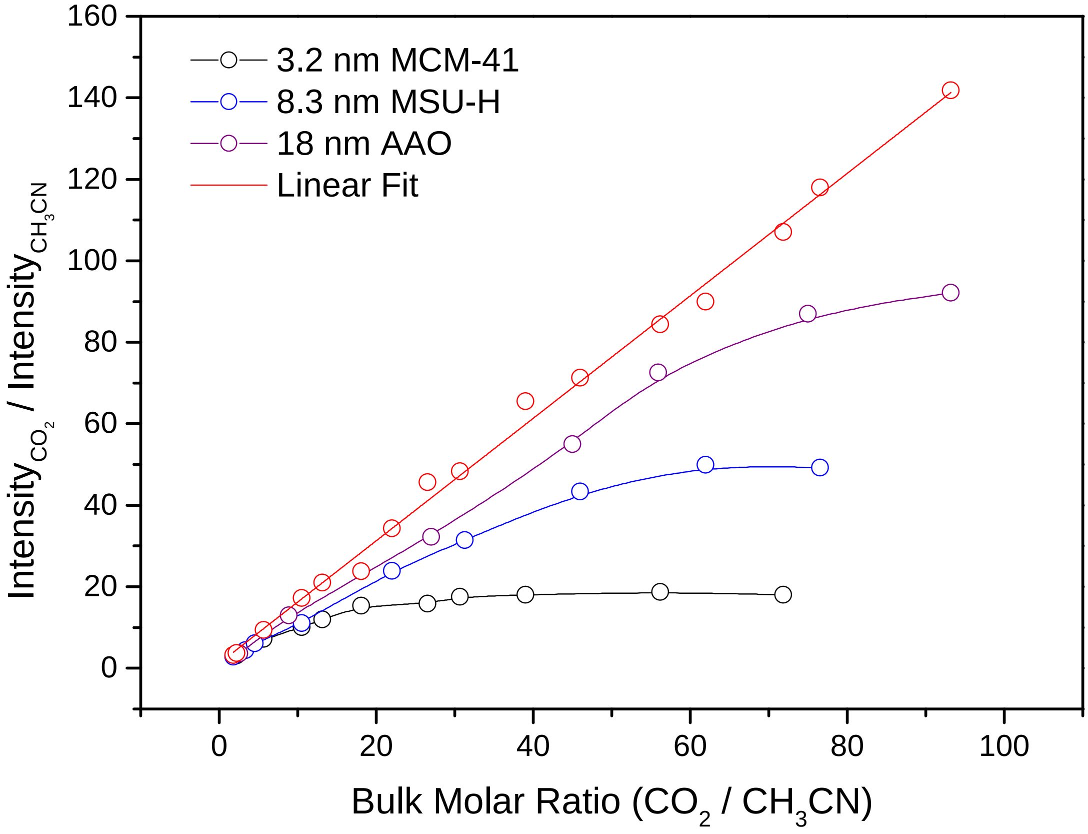

FIGURE 4.20: The ratio of the CO_2/CH_3CN Raman intensities as a function of the bulk mixture molar ratio.

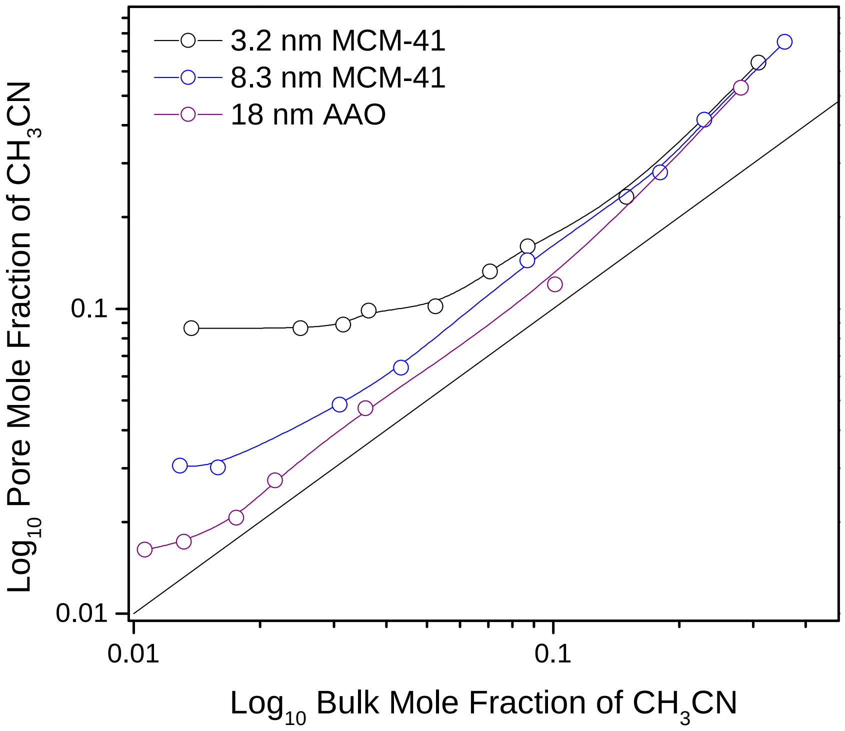

Figure 4.21: The pore confined mole fraction of CH_3CN as a function of bulk CH_3CN mole fraction determined by Raman spectroscopy. The black line indicates the mole fraction value if the bulk and the confined mixtures are of an equivalent composition and the curved coloured lines serve as guides to for eye.

4.3.5 Comparison of Near-Infrared and Raman Spectroscopic Measurements of Carbon Dioxide and Acetonitrile Mixture Composition in Nanopores

The comparison of the NIR and Raman results shows that there is good agreement between the pore compositions determined. Figure 5.3 shows both methods exhibit a comparable trend, with the deviation from the bulk composition greatest in the smallest pore sized material, becoming smaller as the mean pore diameter of the material increases. Both methods also appear to show that the greatest deviation from the bulk composition in the pore occurs in mixtures with the lowest mole fraction values of CH_3CN studied. Data from the NIR and Raman spectroscopic measurements appear to fall close to each other although they do show some variation. This may be due to the error present in determining the bulk mole fraction of CH_3CN. This error can arise due to the complicated mixture preparation process, which has to be achieved volumetrically and by weight. Other errors may be introduced into this value by factors such as dead volume in the apparatus. Although Raman spectroscopy provides a more convenient approach to collect spectra, as the apparatus does not require to be mounted in an FTIR spectrometer, it does exhibit a higher signal to noise ratio.

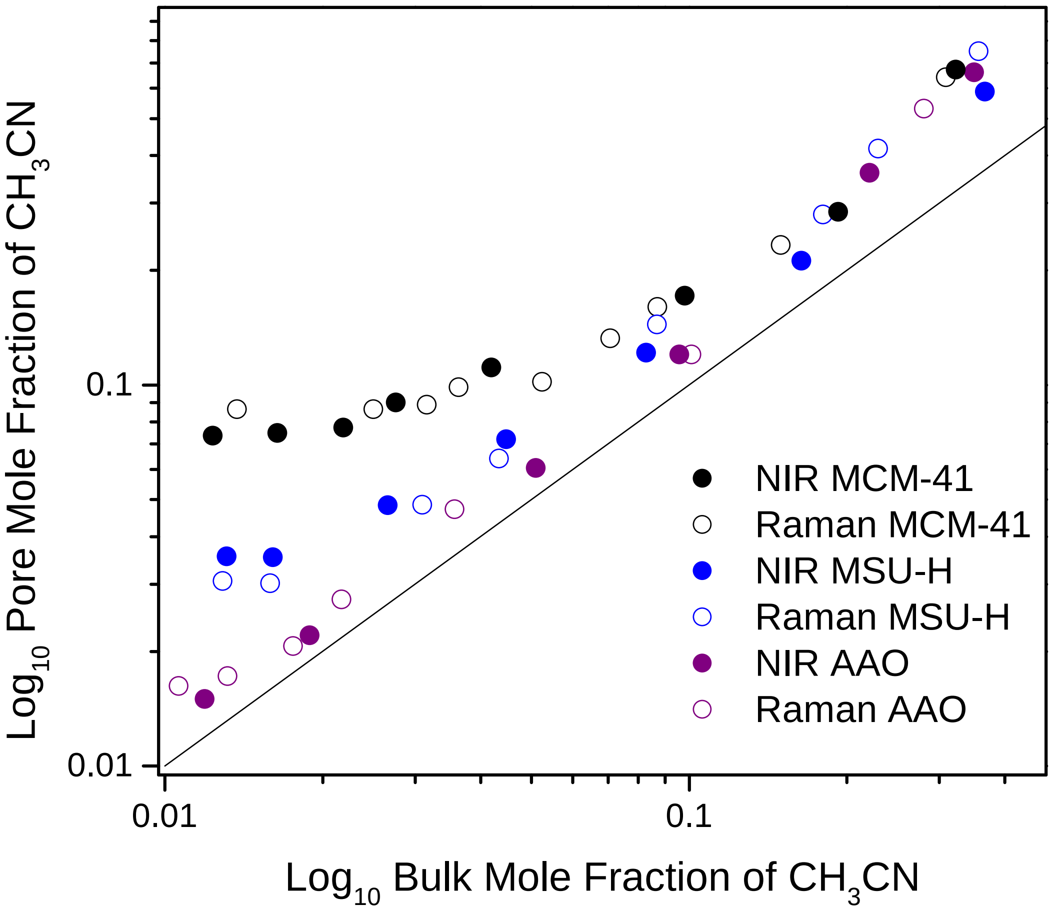

FIGURE 4.22: The pore mole fraction of CH_3CN confined in 3.2, 8.3 and 18 nm pores, as a function of bulk CH_3CN mole fraction determined by NIR and Raman. The black line indicates the mole fraction value if the bulk and the confined mixtures are of an equivalent composition.

4.3.6 Raman Spectroscopic Measurements of Difluoromethane and Tetrabutylammonium Tetrafluoroborate Mixture Composition in Silica and Anodic Alumina Templates

The composition of a second binary mixture has been studied in nanopores. CH_2F_2/TBA.BF_4 mixtures, which have applications in supercritical fluid electrodeposition due to their conductivity and ion solubility have been probed by Raman spectroscopy in the three porous templates. Due to the relatively low solubility of TBA.BF_4 in supercritical CH_2F_2, and therefore its low concentration, along with the overlapping of absorbance bands for both components in the NIR spectrum, NIR is not a suitable technique to determine the composition of CH_2F_2/TBA.BF_4 mixtures in pores. The low concentration of TBA.BF_4 in the mixtures however are relevant, with small proportions of electrolytes being used in solutions to electrodeposit from.[45] So another approach is needed in order to determine the change in confined CH_2F_2/TBA.BF_4 mixture composition. As demonstrated previously in this Chapter, Raman spectroscopy has proved to be a reliable and comparable method to NIR in order to determine pore mixture composition and in this case offers a superior detection limit. Raman spectra collected of the CH_2F_2/TBA.BF_4 mixtures exhibit bands belonging to each of the species present. CH_2F_2 displays relatively strong higher energy Raman bands in the *ca.* 2800–3100 cm^{-1} region. The spectral signature of TBA.BF_4 largely overlaps with that of CH_2F_2 in the Raman spectrum, particularly between 1000–1500, 2800–3200 and around 600cm^{-1},[235–237] as shown in Figure 4.23. This issue is compounded due to the low concentrations of TBA.BF_4 examined in this study.

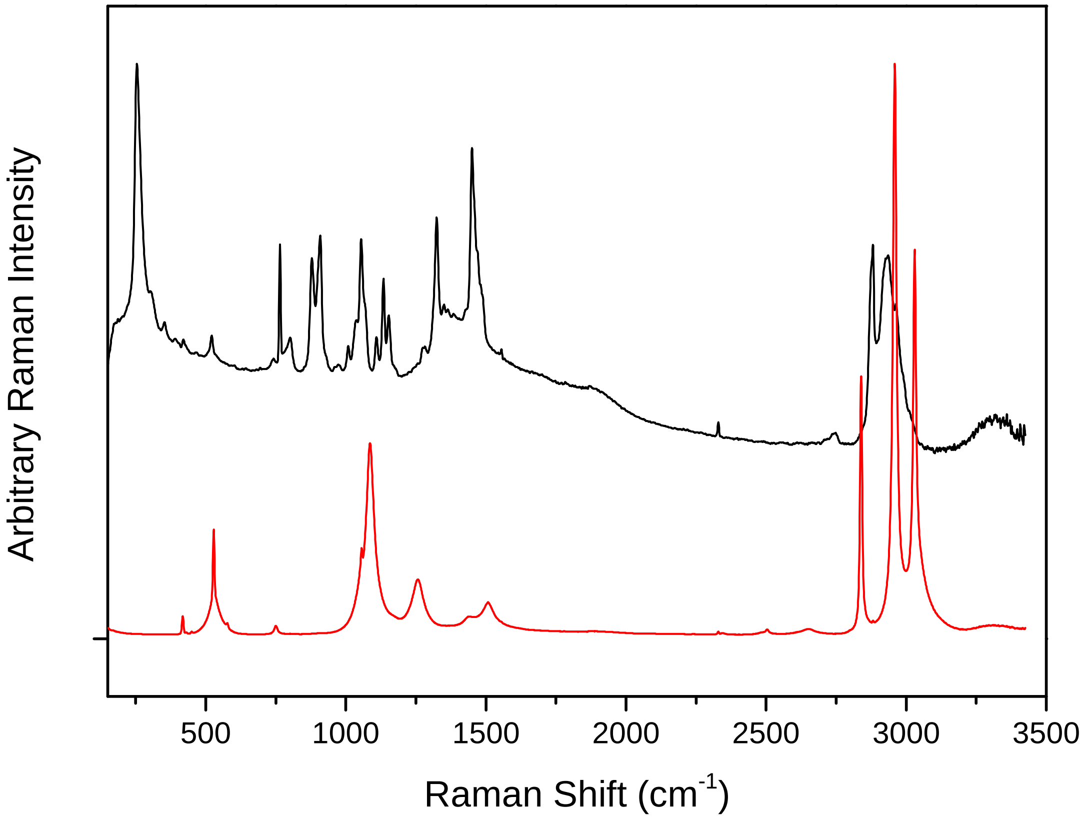

FIGURE 4.23: Raman Spectrum of 400 psi liquid CH_2F_2 at 308 K (red) and TBA.BF_4 (black) in the solid state.

There is a collection of lower energy bands in the *ca.* 850–940 cm^{-1} region of the Raman spectrum that can be used to determine the composition of this binary mixture. This is demonstrated in Figure 4.24.

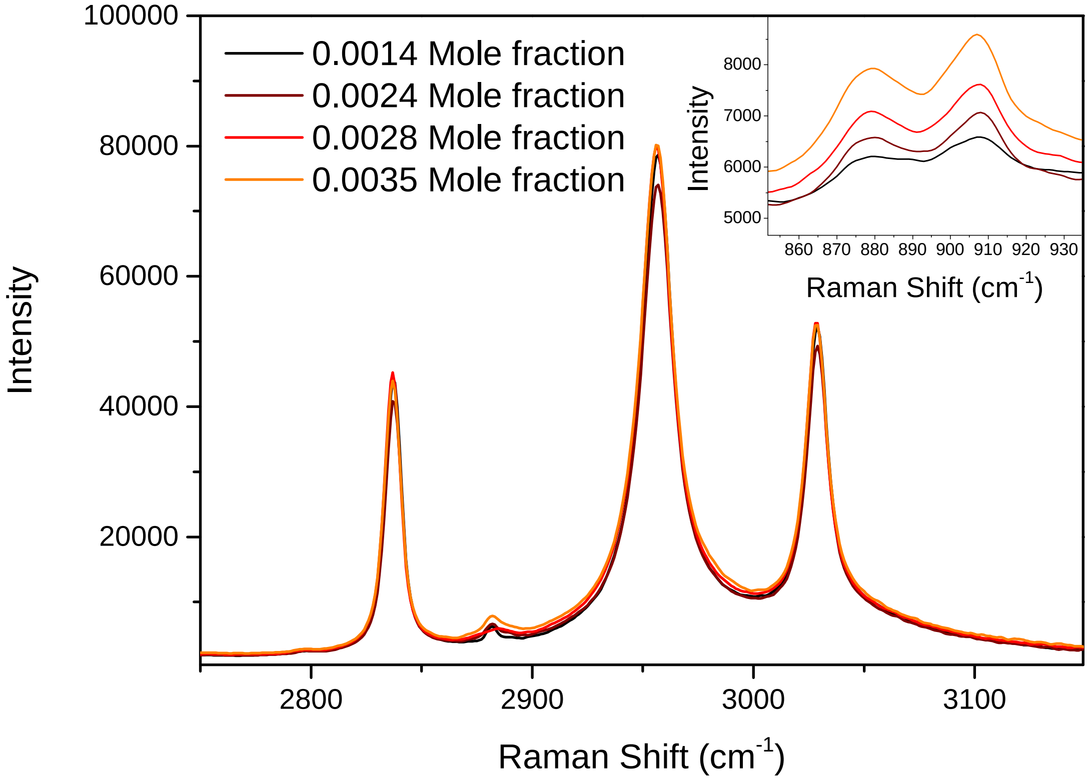

FIGURE 4.24: Raman Spectrum of CH_2F_2/TBA.BF_4 at a number of TBA.BF_4 mole fraction ranging from the detection limit of the Raman spectrometer to the solubility limit in the supercritical CH_2F_2.

All measurements were carried out in a single supercritical phase of the mixture at 363 K and *ca.* 2000 psi. These conditions also present good conductivity of this mixture when an approximate mole fraction between 0.0013–0.0014 of TBA.BF_4 is present.[36] The ratio of the peak intensities for the central C–H symmetric stretch ν_1 peak belonging to CH_2F_2 in the 2800–3100 cm^{-1} region,[236,237] and the TBA.BF_4 can be measured. The composition of the mixture can be linearly calibrated as the intensity fraction of the Raman bands versus mole fraction of TBA.BF_4 (see Equation 4.6).

$$Intensity\ Fraction = \frac{Intensity\ TBA.BF_4}{Intensity\ TBA.BF_4 + Intensity\ CH_2F_2} \tag{4.6}$$

This results in a linear trend, with linear regression used to deduce the mole fraction of TBA.BF_4, from the intensity fraction (see Figure 4.25).

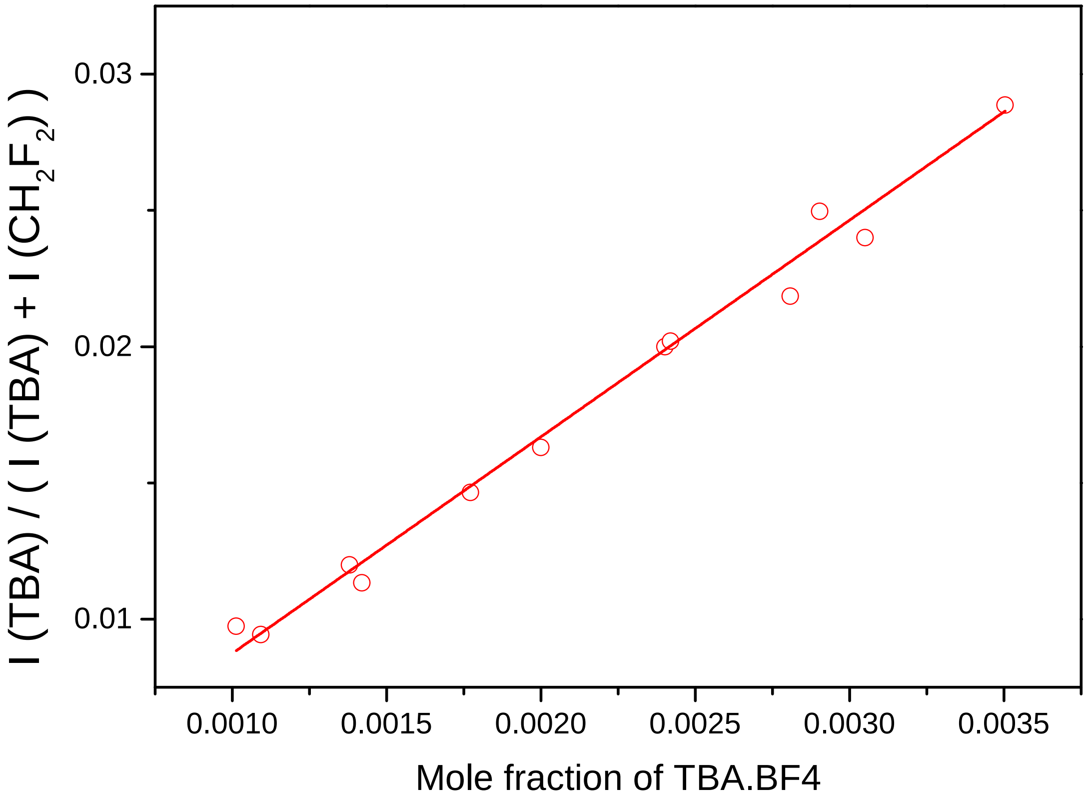

FIGURE 4.25: A calibration plot of the Raman intensity fraction of the CH_2F_2/TBA.BF_4 mixture as a function of TBA.BF_4 mole fraction, with a fit error of 3.2 %.

The pore mole fraction values of TBA.BF_4, determined in the three pore types show a very large enhancement of the TBA.BF_4 component in this CH_2F_2/TBA.BF_4 binary mixture (see Figure 5.4). This appears to be enhanced by a much greater proportion than CH_3CN in the CO_2/CH_3CN mixture. The pore mole fraction values of TBA.BF_4 were determined for mixtures ranging from the detection limit of the Raman instrument to the solubility limit of the TBA.BF_4 in supercritical the CH_2F_2.

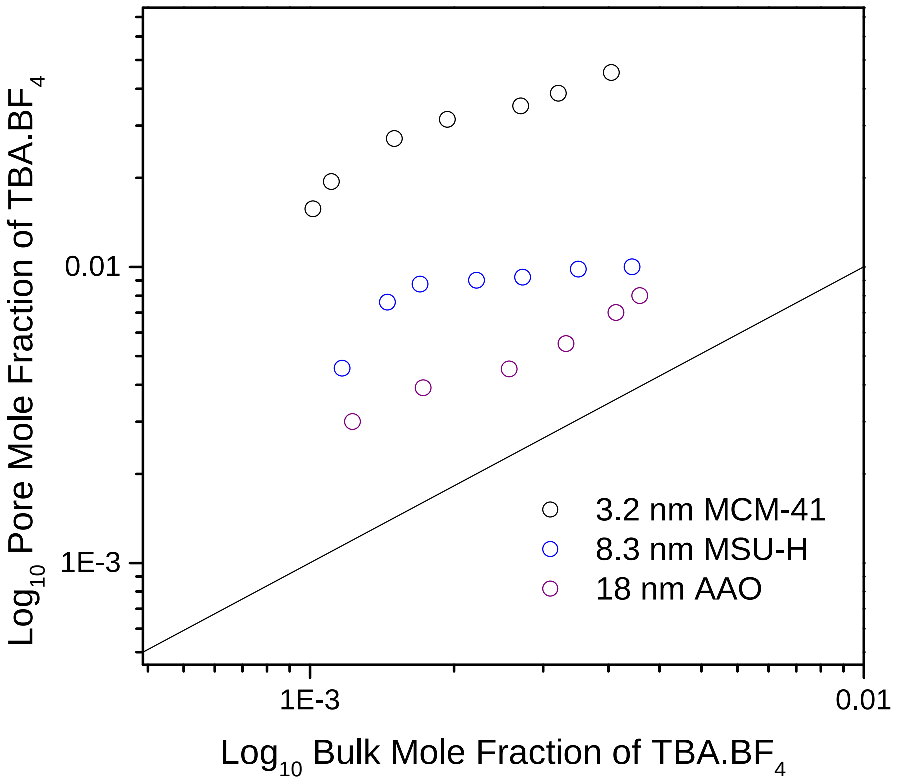

FIGURE 4.26: The pore confined mole fraction of TBA.BF$_4$ as a function of bulk TBA.BF$_4$ mole fraction determined by Raman spectroscopy. The black line indicates the mole fraction value if the bulk and the confined mixtures are of an equivalent composition.

The proportion of change in the minor component of each mixture can be studied as a function of its mole fraction, giving a clearer picture of the behaviour of the mixture composition when introduced into pores.

The proportion change in composition is given as:

$$Proportion\ Change = \frac{MoleFraction_{Pore} - MoleFraction_{Bulk}}{MoleFraction_{Bulk}} \tag{4.7}$$

If this relationship is studied for the CO_2/CH_3CN binary mixture, a number of things become clear. Firstly, as stated previously, there appears to be a large enhancement in pore CH_3CN for the bulk mixtures containing the lowest mole fraction of CH_3CN in all pore sizes studied (see Figure 4.27). The enhancment is evident at the mole fraction values used in the supercritical fluid electrodeposisition process (*ca.* 0.12–0.13). This increased uptake can be explained by the formation of a strongly bound layer of CH_3CN forming on the pore wall regardless of the concentration. There also appears to be a second enhancement at higher mole fraction values of CH_3CN. This second effect may arise due to the influence of the bulk mixture composition facilitating the uptake of like molecules into the pore.[219] The favourable interactions between CH_3CN molecules at higher concentrations may dominate, filling the pore space with interacting CH_3CN molecules, resulting in a further decreased uptake of CO_2. This is an effect that has been observed in the literature with MC simulations of benzene/water mixtures in graphitic slit pores.[229]

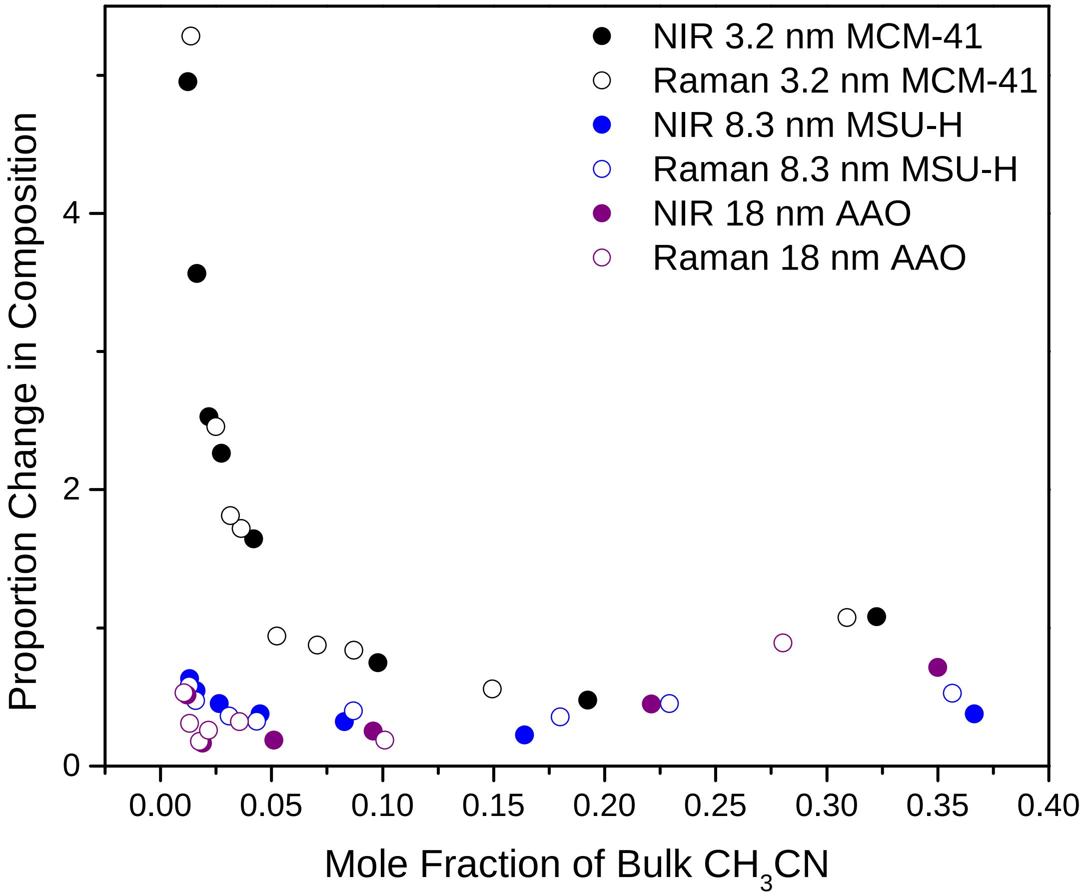

FIGURE 4.27: Proportion change in the CH_3CN component as a function of bulk CH_3CN mole fraction.

It is also clear that the pore uptake in CH_3CN increases, as the mean pore diameter of the material decreases. This can be rationalised the following way. The concentration profiles of the preferred adsorbate, which are at maximum near the pore walls due to their interaction potential, will overlap more in the pores with smaller diameters, causing an enhanced adsorption in the pore space.[15] This effect decreases with larger pore sizes, as less of the pore volume is taken up by the range of this potential and therefore the CH_3CN concentration profile.[218] This leads to a proportionally lower uptake of the preferred component.

Acetonitrile molecules have been previously found to exist in two kinds of state when absorbed into the mesopores of MCM-41 silica.[160] The literature shows that there is a monolayer of molecules that are anchored strongly to surface hydroxyls by hydrogen bonding, explaining the greatly increased preference of the silica pores for CH_3CN. The second state consists of capillary condensed molecules in the core of the pore, which exists as a fluid.

This hydrogen bonded state explains the initial selectivity of the CH_3CN component in the MCM-41 silica, especially seen at the lower concentrations of CH_3CN studied. These surface groups may still exist in the MSU-H silica in the form of surface hydroxyls,[238] therefore allowing for this behaviour to occur. There is also evidence of hydroxyls being formed on anodic alumina surfaces,[179] again possibly contributing to CH_3CN selectivity, although perhaps this influence has less of an effect due to the larger pore size or a possible lower incidence of these groups. The overall greater selectivity for CH_3CN in the pores can be attributed to the stronger interaction preference of CH_3CN with the pore walls. This arises due to the dielectric properties of the molecule, as it possesses a dipole moment and relatively high dielectric constant (ε_r=36.64) when compared to $scCO_2$ (ε_r=1.5),[56,183,239] making it susceptible to any charges present on the pore wall. These factors will allow it to interact strongly with the relatively negative oxygen and the relatively positive silicon present in the silica lattice in comparison to CO_2.[175–177] A similar effect may also occur for the oxygen-aluminium lattice present in the anodic alumina.

The CH_2F_2/TBA.BF_4 binary mixture displays a much greater enhancement of the preferred component (TBA.BF_4), than previously seen with the CH_3CN in the CO_2/CH_3CN mixture across all pore sizes studied in the mole fraction range applicable to high pressure supercritical fluid electrodeposition (*ca.* 0.0013–0.0014), as shown in Figure 4.28.

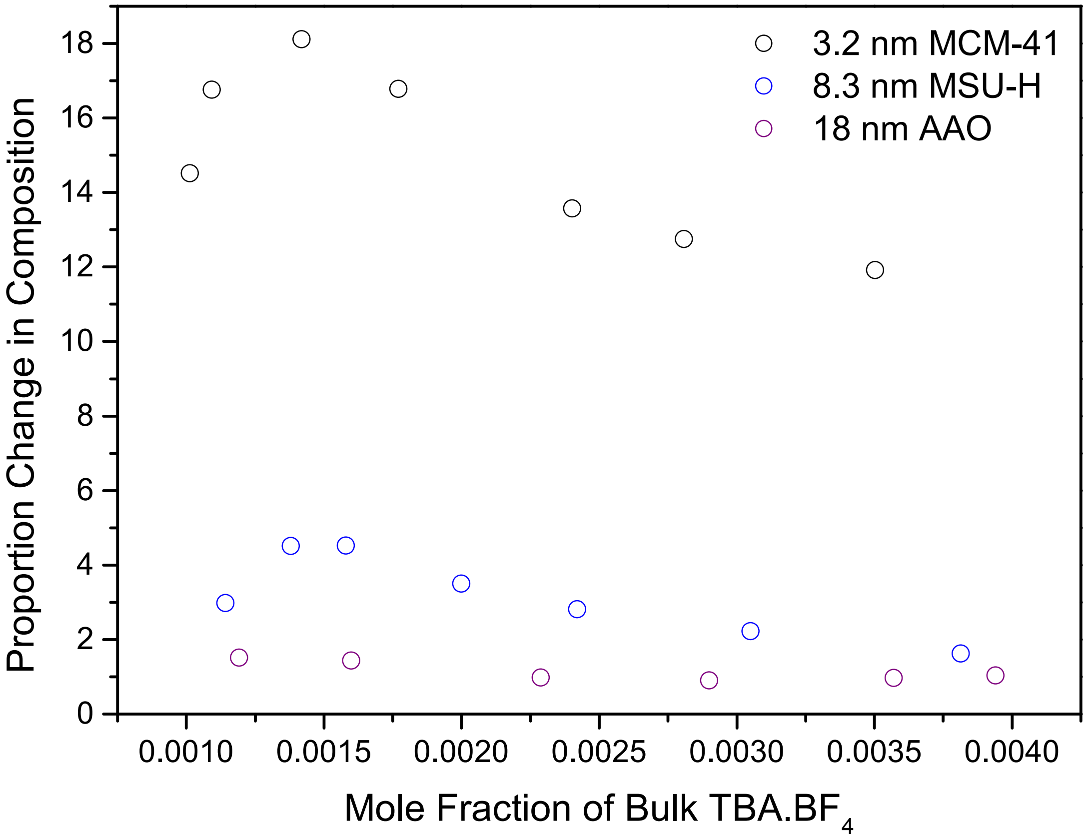

FIGURE 4.28: Proportion change in the TBA.BF_4 component as a function of bulk TBA.BF_4 mole fraction.

The increase in TBA.BF_4 selectivity in the pores for this binary mixture is again possibly due to the walls of the capillary interacting more favourably with the salt, as opposed to the CH_3CN in the CO_2/CH_3CN binary mixture. The TBA.BF_4 could bind strongly with the alternating silicon-oxygen lattice of the pore wall, with the positive TBA^+ attracted to the relatively negative oxygen and the BF_4^- attracted to the relatively positive silicon.[175–177] As before this behaviour would also be likely to occur in the anodic alumina pores. The salt also offers stronger hydrogen bonding opportunities, with either the surface silanol groups or the silicon-oxygen/aluminium-oxygen lattice of the pore wall. These factors would lead to an increased uptake of $TBA.BF_4$ as the higher wall potential with the salt would extend the concentration profile of the $TBA.BF_4$ in the pore. As stated previously for the CO_2/CH_3CN mixture, favourable interaction between like molecules by layering after this initial wall adsorption would pull more $TBA.BF_4$ into the pore, further increasing selectivity. The proportion of pore $TBA.BF_4$ again increases as the pore diameter decreases, as expected due to the wall selectivity increasing its influence on the pore volume.[218] The amount of $TBA.BF_4$ in the pore appears to increase relative to the bulk composition as the mole fraction of the bulk solution increases. This reaches a maximum, and then decreases whilst still remaining above the concentration of the $TBA.BF_4$ in the bulk.

This uptake maximum at low mole fraction values was not observed for CH_3CN in the CO_2/CH_3CN mixture, where only a large enhancement that decreases with bulk concentration was observed. One possible explanation is that this is an artefact of pre-wetting phenomena and at the lowest concentrations there is not enough $TBA.BF_4$ to sufficiently wet or bind to the walls of the pore. This would lead to a lowered uptake. As the concentration in the bulk increases the wall can be fully wet with $TBA.BF_4$ which in turn pulls in more $TBA.BF_4$, leading to the uptake maximum. As the bulk concentration of TBA.BF$_4$ is increased to a mole fraction of *ca.* 0.0025, the resulting fully wetted pore wall, no longer offers the same interaction preference. The loss of interaction preference at higher mole fraction values may be due to the fact that the fluid-wall potential cannot extend past a few layers of interacting molecules, leaving any additional enhancement effects due to like molecules favourably interacting. Another possibility is that an incipient wetting phase of CH$_2$F$_2$ is also formed at the lowest concentrations of TBA.BF$_4$ due to the low availability of TBA.BF$_4$ molecules to wet the walls. This fills the pore space, leading to very little TBA.BF$_4$ adsorbed as its interaction preference would be with more CH$_2$F$_2$ molecules, an effect observed in water/amphiphile mixtures.[15] This effect then diminishes at higher concentrations of TBA.BF$_4$, leading to an increased uptake as there is less chance of this layer forming, creating the perceived maximum.

This effect may not have been observed with the CO$_2$/CH$_3$CN mixture as the concentration range studied for this second binary mixture is both smaller and at lower mole fraction values of the minor component, meaning it may have been apparent at very low mole fractions of CH$_3$CN, where there is not enough CH$_3$CN present in the mixture to fully wet walls with this component. Another explanation for the lack of this behaviour in the CO$_2$/CH$_3$CN mixture is that the CO$_2$ does not have a high enough interaction preference to fully wet the pore at low concentrations of CH$_3$CN and prevent the uptake of CH$_3$CN. This is due to its dielectric properties, resulting in a low interaction potential, unlike CH$_2$F$_2$ which may possess a large enough interaction potential to wet the wall at low concentrations of TBA.BF_4 due to its polarisability. Therefore the pore space and its mixture component selectivity is not dominated by CO_2 layering in the same way it might with CH_2F_2.

These low concentration measurements are ambiguous however due to the relatively low intensity of the TBA.BF_4 band in the Raman spectrum, so caution must be taken before drawing any conclusions about the behaviour described previously. Despite this, the information obtained from these studies again show a clear trend of the greatest enhancement of TBA.BF_4 concentration in the smallest pores, with the effect decreasing as the pore size increases across all concentrations studied. This enhancement of the preferred component is again probably due to the overlapping component-wall potentials dominating the small pore volume, leading to increased uptake.[218]

In both mixtures, the more polar higher dielectric component is preferentially taken into the pore, suggesting that the fluid-wall potential (which can be influenced by polarity or dielectric properties, and therefore coulombic interaction strength) is paramount in determining the mixture component uptake into a pore, as suggested in the literature.[216–218,228]

4.4 Conclusions

Vibrational spectroscopy has allowed for the study of two pore confined binary mixtures, relevant to supercritical fluid electrodeposition. Both NIR and Raman spectroscopy provide a simple approach to study confined mixture composition, with the potential to yield more chemically sensitive information compared to other previously used techniques such as DR and NDE.

These spectroscopic studies have demonstrated how the mixture composition of a binary mixture is affected when confined in a pore. The ratio of the characteristic spectroscopic bands associated with CO_2 and CH_3CN have been used to establish a spectroscopic method, relating the near-infrared absorbance and Raman intensity of these species to bulk mixture composition, exhibiting a linear dependence. This has permitted the use of vibrational spectroscopy to determine the composition of a pore confined CO_2/CH_3CN, in a range of different pore sizes (3.2–18 nm), in silica and anodic alumina materials. It was found that there was a significant enhancement of the CH_3CN component across all bulk compositions and all pore sizes and types studied. This enhancement was found to be greatest in the mixtures containing the lowest concentrations of CH_3CN and in the smaller of the pores studied. The extent of the enhancement was found to decrease with increasing pore size, suggesting the constant magnitude of the component-pore potential loses its dominating influence over the whole pore volume in the larger pores. The results obtained by both the near-infrared and Raman spectroscopy were also in good agreement.

A second binary mixture consisting of CH_2F_2/TBA.BF_4 was also examined, with the use of Raman spectroscopy. The previously discussed porous materials were studied and a very large enhancement of the TBA.BF_4 component in the pore was observed. This enhancement was exhibited across all pore sizes and bulk mixture compositions, with the greatest enhancement again observed in the smallest pores.

A preferential uptake for the more polar/high dielectric component of both binary systems was observed. This indicates that the pore wall surface chemistry, due to its functional groups and their favourable interaction potential with the more polar/polarisable component of the mixture, plays an important part in determining the pore mixture composition.

Chapter 5

Conclusions and Future Outlook

5.1 Introduction

This Thesis presents a wide ranging study on the critical behaviour of confined fluids and the compositions of confined mixtures. This Chapter will summarise the conclusions that can be drawn from this work and detail their implications, as well as relating them to current applications that utilise confined fluids and mixtures. This lets us guide the future work which will be required to thoroughly understand this area in order to make confined fluids more applicable to the processes they are currently exploited in. Therefore, suggestions for future study in order to achieve a firmer grasp of these phenomena are also given.

5.2 Summary of Chapters 2 and 3

These Chapters describe spectroscopic measurements showing a significant depression in the critical temperatures of carbon dioxide, difluoromethane and ethane confined in nanopores. It was found that the pore size has a measurable impact on the depression of the critical temperature, with the smaller pore sizes depressing the critical temperature to a greater extent. The trend of the pore critical temperature versus mean pore diameter was also found to depend on the nature of the adsorbate (see Figure 5.1). In the cases of CO_2 and CH_2F_2 there appears to be a plateau in the pore critical temperature value in pore sizes ranging from *ca.* 5–12 nm. It was proposed that this effect may arise due the fluid-pore interaction potential dominating the pore volume and influencing the phase behaviour. In order to probe this further, these results were compared to those obtained from C_2H_6, a weakly interacting adsorbate.[181] Ethane did not exhibit this plateau in the pore critical temperature. This was due to the fact that the weak interactions of C_2H_6 with the pore wall led to a smaller influence on the critical temperature in the pore sizes ranging between *ca.* 5–12 nm.

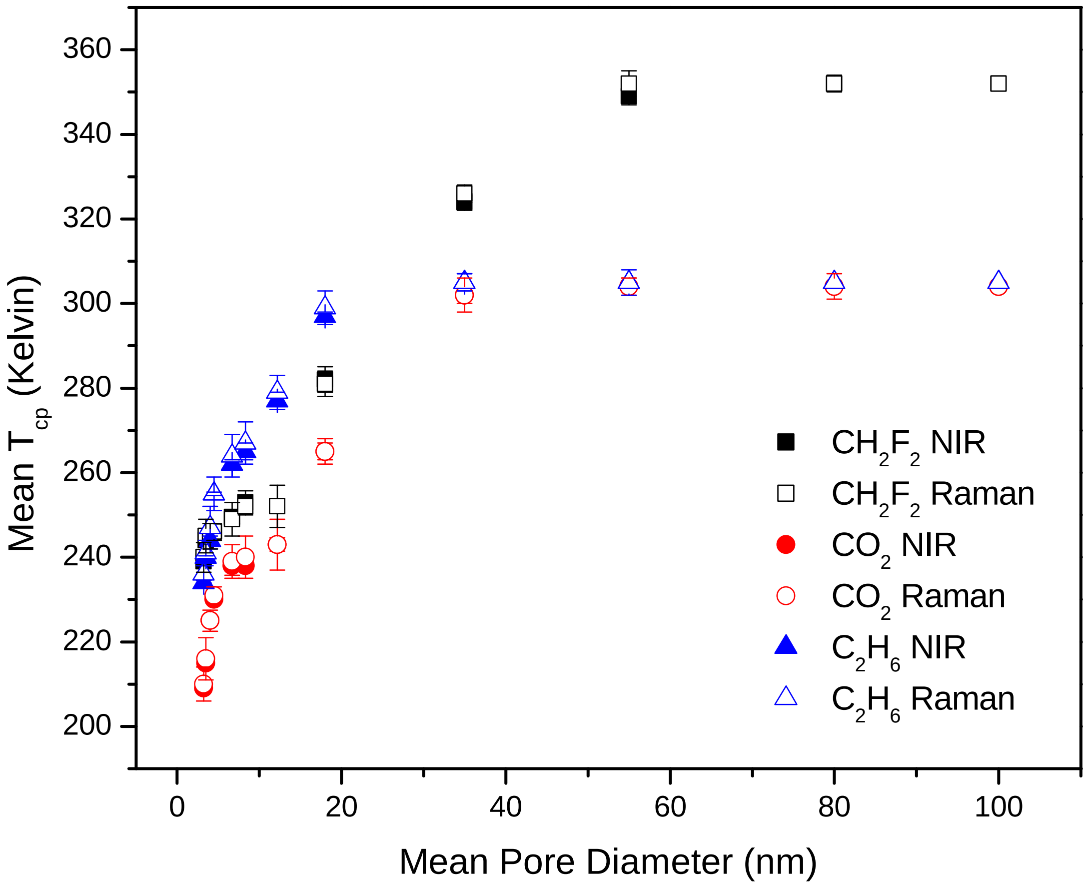

FIGURE 5.1: The mean pore critical temperature (T_{cp}) of CO_2, CH_2F_2 and C_2H_6 as a function of mean pore diameter, determined by both NIR and Raman spectroscopy.

When ΔT_{rp} is plotted against inverse pore diameter it reveals a non-linear trend consisting of multiple linear regimes (see Figure 5.2). These results were in contrast to those predicted by early scaling theory and experimental work which showed a linear relationship between ΔT_c versus inverse pore diameter.[85,139–141]

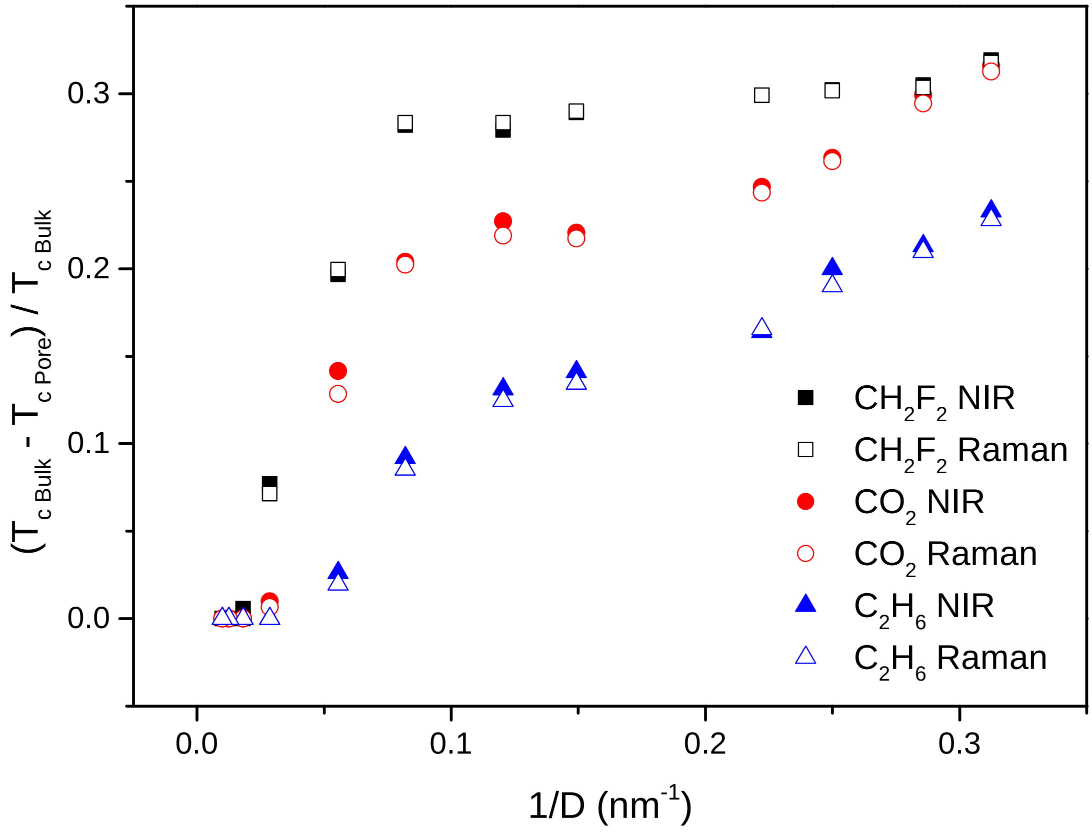

FIGURE 5.2: The decrease of reduced pore critical temperature (ΔT_{rp}) for CH_2F_2, CO_2, and C_2H_6 as a function of the inverse pore diameter, determined by both NIR and Raman spectroscopy.

When this relationship is examined it shows that the extent of the depression in critical temperature ranges from the most polar and highest dielectric fluid, CH_2F_2, to the least polar and lowest dielectric fluid, C_2H_6, across the pore size range. This suggests that the polarity and polarisability of the molecule, and therefore its ability to interact strongly with the functional groups on the walls of the pore, influence the extent to which its critical temperature is depressed. The non-linear relationship of ΔT_{rp} versus the inverse pore diameter was also found to depend on the polarity or polarisability of the molecule and therefore its interaction potential with the pore wall. CH_2F_2 was found to exhibit the least linear trend and C_2H_6 was found to have the most linear. This effect is proposed to be due to the constant magnitude of the fluid-pore potential despite the changing pore diameter. At the smallest of pore sizes the wall potentials will overlap increasing their effect on the fluid in the whole pore volume. However, as the pore diameter increases this influence quickly decreases with fewer molecules in the centre of the pore being attracted to the pore wall. At the largest pore sizes a small proportion of the molecules will be attracted to this potential, leaving the majority of the pore fluid uninfluenced by this potential. This effect results in a non-linear change in the density difference between coexisting gas and liquid phases in the pore (a key factor of critical temperature) as the pore size increases, resulting in a non-linear change in critical temperature.[145,187,188]

Finally, Chapter 3 presents theoretical work to support these results. This was achieved through the use of grand canonical Monte Carlo simulations on CO_2 in pores ranging from 3–8 nm in size. These calculations exhibited a significant depression in the T_c of CO_2 in agreement with the experimental work. The trend of T_{cp} versus pore diameter also behaved in a similar manner to that measured by experiment. To investigate the effect of the fluid-pore wall potential on the T_{cp}, calculations of the pore critical temperature of CO_2 confined in a pores ranging between 3–7 nm in size with no fluid-wall potential were carried out. The pore critical temperature was shifted to a higher value showing that the interaction potential plays a significant role in the extent a fluid's T_c is depressed in a pore. The trend of CO_2 T_{cp} versus pore diameter for the neutrally charged pores was also more linear in its dependence when compared to those with a potential.

This indicates that the trend of T$_{cp}$ with pore size is indeed dependant on the magnitude of the pore-fluid interaction potential.

5.3 Implications and Future Work of Chapters 2 and 3

Chapters 2 and 3 show that vibrational spectroscopy in the form of NIR and Raman spectroscopy can be used to probe the critical parameters of fluids confined in pores. These new approaches have been shown to be a reliable and relatively convenient method to examine the critical temperatures of fluids confined in a large range of pore sizes and types, suggesting they are beneficial for future use of study in this area. Chapter 3 presents a theoretical approach to determine a confined fluid's critical temperature through the use of grand canonical Monte Carlo simulations. These simulations have provided a reliable method of calculating the critical point in pores that exhibit an influence on the confined fluid through an interaction potential between the fluid and the pore wall. This model may therefore prove useful for future investigations in this area. The observed depression in the critical temperature of the fluids examined in this study imply that the critical behaviour of these fluids can be exploited under conditions not currently used in some processes, such as supercritical fluid electrodeposition. An example of this is the fact that the bulk critical parameters of the electrolyte bath have been used to deposit within nanopores, usually well above the critical point of the mixture.[45,47] These findings suggest that milder conditions (*e.g.* pressure and temperature) could be used to achieve the same result. The results presented also establish a link between the depression in the critical temperature with the dielectric properties or binding affinity of the fluid to the pore wall. This knowledge therefore, will aid in electrolyte bath solvent choice, where previously unfavoured solvents, due to their harsh critical parameters, may become viable. This may provide access to fluids with improved conductivity or dielectric properties. The established link between the extent of the depression in critical temperature and pore size also has implications on processes such as gas storage and oil extraction, where the amount of gas that can be stored or oil extracted depends on the phase of the substance injected into the rock or coal.[62,63] This knowledge allows for the selection of geological areas which present pore sizes allowing gas to be stored or oil to be extracted efficiently. In terms of confined catalysis the depression of the critical parameters implies that the reactants may be in a single homogeneous phase even at low temperatures, with very low degrees of wetting on the pore wall. This may improve the miscibility and diffusivity of reactant in the pore.

In order to obtain a firmer grasp on the critical behaviour of confined fluids, therefore expanding their applications, more work is needed in this area. Firstly, a study of how the critical temperature of a mixture changes within pores is needed to determine if the behaviour observed in pure fluids carries over to a real world system. An example is an electrolyte bath used in supercritical fluid electrodeposition or mixtures in a geological setting relevant to gas storage or extraction, where many components exist. Secondly, a study of a larger range of adsorbents or pore types needs to be carried out to further explore the relationship of the fluid-pore interaction potential and its role in depressing the fluid's critical temperature. This will allow for the optimum selection of both fluid and pore type depending on the application. This could be achieved through the selection of pore types with pore walls consisting of other functional groups that will provide different relative charges throughout the lattice and therefore coulombic interaction strengths or hydrophillicity. Thirdly, a larger range of fluids need to be studied to establish a more quantitative link between the fluid properties and the effect on the critical temperature when confined in pores. This will allow for more appropriate fluid choices for processes such as supercritical fluid electrodeposition.

Finally, in order to elucidate the fundamental behaviour of confined fluids further theoretical work is required. This would be in the form of modelling a larger range of pore sizes to confirm the experimental results that indicate a much greater rate of T_{cp} increase with pore size in pores larger than 12 nm, after the observed plateau in T_{cp}. This would be useful as these distinct regimes in the trend are thought to be due to the fact that a constant fluid-wall potential exists on the surface regardless of pore diameters. This may prove difficult however as the GCMC simulations are computationally very expensive due to the large number of molecules required in the simulation. This problem was apparent even for the pore size range studied in this Thesis. Further calculations of the T_{cp} of CO_2 in pores without an attractive potential are also required. This is in order to compare and contrast the results of those obtained for attractive pores and to explore further the effect of the fluid-pore potential on the T_{cp} versus pore diameter relationship. The addition of other fluids would also enable the influence of the pore-fluid potential and fluid type to be probed further and allow any unique behaviour in the T_{cp} versus mean pore diameter relationship to be determined, due to the fluid's unique physical properties. A further examination of the pore fluid inhomogeneity using GCMC is also required. This study of the microscopic properties of the fluid may provide a more detailed explanation of the unique phase characteristics exhibited by the pore confined fluids.

5.4 Summary of Chapter 4

The compositions of binary mixtures have been studied in nanopores with pore sizes ranging from 3.2–18 nm. In the case of the CO_2/CH_3CN mixtures it was found that there was a significant enhancement of the CH_3CN component across all bulk compositions and in all pore sizes studied (see Figure 5.3). The enhancement of CH_3CN was found to be greatest in the mixtures containing the lowest concentrations of CH_3CN indicating that layering of CH_3CN molecules on the pore wall is a major factor influencing the pore mixture composition.[218] The extent of the enhancement was also found to decrease with increasing pore size. This suggests that the constant magnitude of the component-pore potential, which is responsible for this selectivity, loses its dominating influence over the whole pore volume in the larger pores.[218]

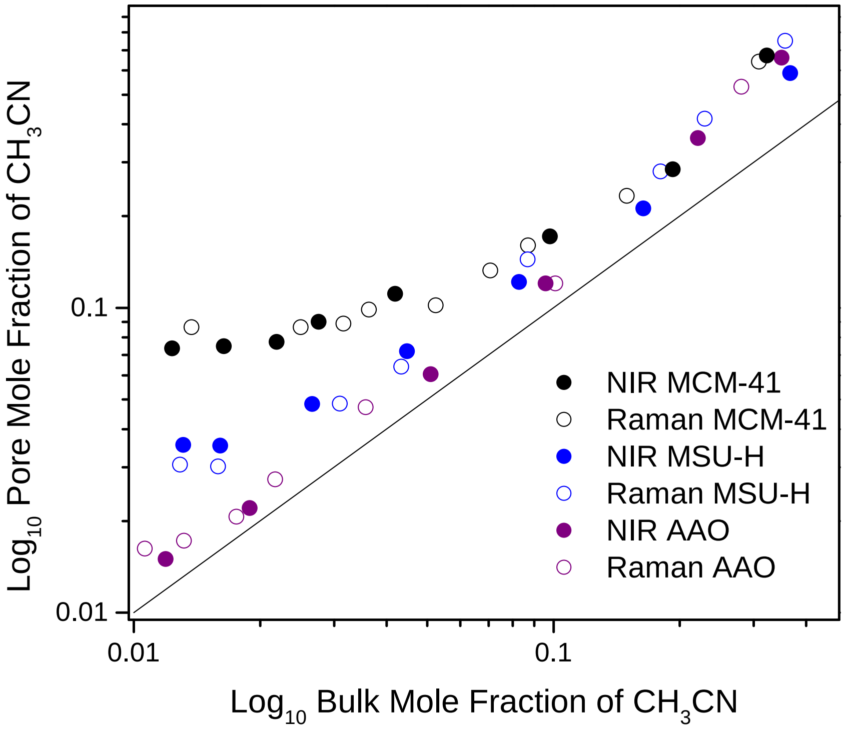

FIGURE 5.3: The pore confined mole fraction of CH_3CN confined in 3.2, 8.3 and 18 nm pores, as a function of bulk CH_3CN mole fraction determined by NIR and Raman. The black line indicates the mole fraction value if the bulk and the confined mixtures are of an equivalent composition.

A second binary mixture consisting of CH_2F_2/TBA.BF_4 was also examined. As before, a range of porous materials was used and a very large enhancement of the TBA.BF_4 component in the pore was observed, across all pore sizes and bulk mixture compositions (see Figure 5.4). The greatest enhancement was again observed in the smallest pores. For this mixture the extent of TBA.BF_4 enhancement was greater than that found for CH_3CN in the CO_2/CH_3CN mixture. This is probably due to the TBA.BF_4 interacting more strongly with the pore wall compared to CH_3CN, due to the dielectric properties of the molecule creating a stronger interaction potential with the pore wall and its relative charges.[216–218,228]

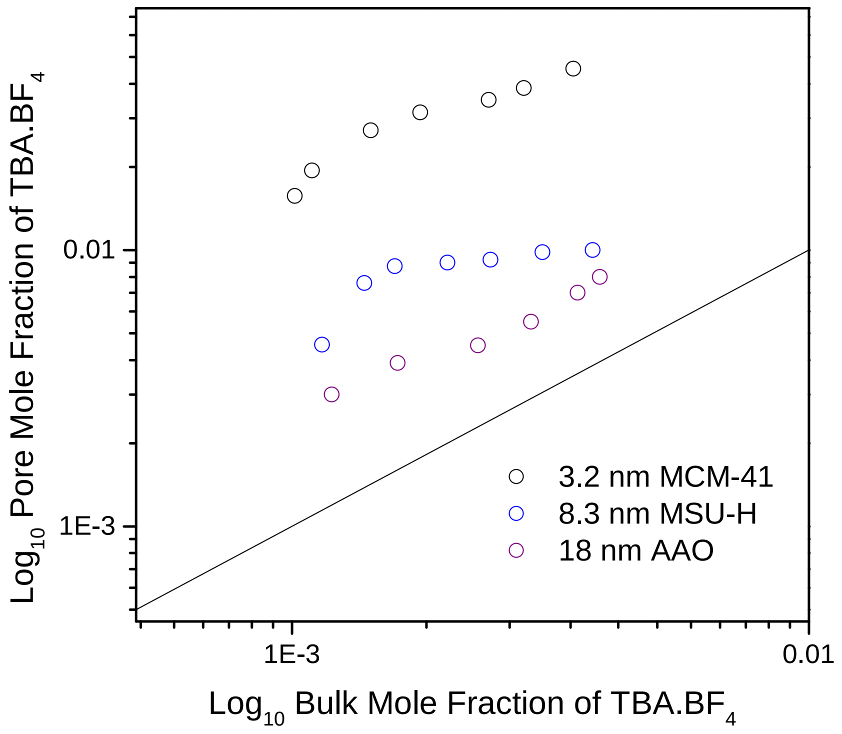

FIGURE 5.4: The pore confined mole fraction of TBA.BF$_4$ as a function of bulk TBA.BF$_4$ mole fraction determined by Raman spectroscopy. The black line indicates the mole fraction value if the bulk and the confined mixtures are of an equivalent composition.

5.5 Implications of Chapter 4 and Future Work

The results presented in this Chapter offer the first fundamental examination of mixture composition change for supercritical fluid electrodeposition relevant mixtures confined in nanopores. This work has developed a simple, robust and reliable approach using vibrational spectroscopy to probe mixture composition in the confines of a pore, as traditional phase measurements in this environment can prove difficult or impossible. This work shows therefore, that vibrational spectroscopy is an ideal approach for future confined mixture composition studies.

The results obtained through this study also have important implications relating to supercritical fluid electrodeposition in nanopores. Firstly, enhancement of the polar CH_3CN and $TBA.BF_4$ components suggest improved conductivity and ion solubility, with the increased presence of these species possibly increasing the dielectric constant of the mixture in the pore.[36,45] Secondly, due to the increased uptake of these components, it may be possible to to carry out supercritical fluid electrodeposition in nanoporous templates with lower concentrations of co-solvents or electrolytes, making the process much more efficient in terms of reagent quantity. The selectivity of mixture components observed in this Thesis also has implications in confined catalysis where reagent selectivity in the pores will change the conditions for reactions taking place within pores, possibly influencing yields and product formation. Finally, these results indicate that certain components of mixtures, such as those found in geologically stored flue gas, will preferentially adsorb into pores and therefore perhaps be stored more efficiently than the others. This may depend on mixture composition, conditions and pore size. Therefore these factors need to be considered to make this process more efficient.

Despite this progress, further work is required in order to fully understand and thus optimise supercritical fluid electrodeposition in nanopores. Study of pore confined tertiary or quaternary mixture composition is required, as supercritical fluid electrodeposition often takes place in a system with a multitude of components including the ions that are to be deposited. It would be of interest to determine how the presence of these components will affect electrolyte, co-solvent, and solvent uptake into the pore. The pore uptake of other commonly used electrolytes in the supercritical fluid electrodeposition process should also be studied. This is in order to establish a relationship between the structure and chemistry of the electrolyte molecule, and any selectivity the nanopores exhibit for these compounds. Ion solubility measurements in nanopores also need to be carried out in order to ascertain the influence of pore mixture component enhancement on the solubility of the ions to be deposited. Pore conductivity measurements in the presence of mixtures are also of interest, enabling the relationship between mixture component selectivity and conductivity to be determined. This would confirm whether the pronounced uptake of the TBA.BF_4 into the pores does indeed increase the conductivity. This would offer insights into the ability of the adsorbed electrolyte to carry charge and therefore the nature of the relationship between the pore and the electrolyte in its adsorbed state. Furthermore other mixtures relevant to both confined catalysis and gas storage need to be studied in pores to establish the extent of the mixture component selectivity in these systems, along with adsorbents relevant to these applications.

Finally, the use of theoretical studies to model these binary mixtures relevant to supercritical fluid electrodeposition need to be carried out. This is in order to gain a fundamental understanding of the physical properties of these confined mixtures and the effect of the fluid-pore interface, selectivity and inhomogeneity on these properties. These studies will help to determine the knock-on effects of these factors on applications for which these confined mixtures are to be used.

Chapter 6

Experimental

6.1 Introduction

This Chapter will describe the experimental procedure used to obtain the results described in this Thesis. Although the majority of the equipment has been used elsewhere in other studies, the work in this Thesis required the use of novel combinations of equipment to carry these experiments for the first time.

6.2 Near-Infrared Spectroscopic Measurements

Near-infrared spectra were recorded using a Thermo Scientific; Nicolet 6700 FTIR spectrometer equipped with a liquid nitrogen cooled Thermo-Nicolet InSb detector, quartz beam splitter and white light source allowing spectra to be recorded in the near-infrared range. Measurements were taken using Thermo-Nicolet's OMNIC 7 program with an averaged 32 scans per spectrum and with a resolution of 4 cm^{-1} in the 2800-10000 cm^{-1} range.

6.3 Raman Spectroscopic Measurements

Raman spectra were recorded using a Kaiser RamanRxn2^{TM} multi-channel Raman analyzer with a 785 nm laser wavelength. The fibre optic Raman probe was fitted with a NCO-3.0-NIR optic system that has a 7.5 cm laser focal length. All spectra were obtained by averaging 60 collections with a 1 second laser exposure time. The laser power was set to a constant 40 mW.

6.4 Low Temperature Near-Infrared and Raman Experiments

Low temperature phase behaviour experiments were carried out using the CryoTiger$^{®}$ cold end, connected to a high pressure cell. The cell consisted of of a machined copper body fitted with CaF_2 windows for near-infrared measurements or quartz windows used for Raman investigations sealed into the cell body with an epoxy resin adhesive. The cell connects to the cold end using a machined "dovetail" joint, forming the high-pressure-low-temperature (HPLT) cryostat used in this study, as described by Calladine *et al.*[240,241] The path length of the cell is *ca.* 2 mm and the cell can withstand pressures up to 2500 psi in a temperature range of 77–310 K. The two halves of the cell sealed together with a 0.5 mm thick lead gasket. The face of the cell is fitted with inlet and outlet ports used to fill and evacuate the cell with the desired species which are made out of 1/16 inch steel pipe attached to the rest of the apparatus using 1/16 inch fittings (Swagelok®) (see figure 6.1).

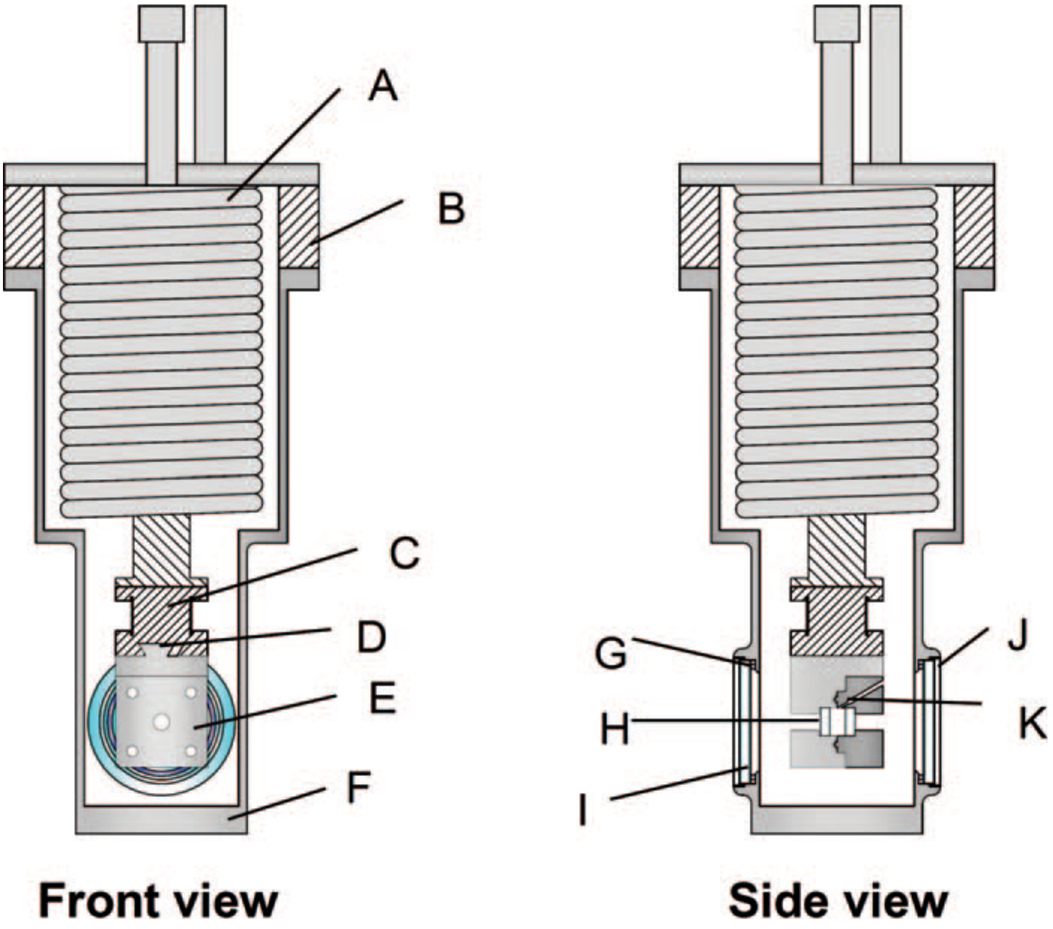

FIGURE 6.1: Schematic representation of the HPLT spectroscopic cell and cryostat: **(A)** CryoTiger® cold end, **(B)** stainless steel support collar (with vacuum port, electronics feed through, and gas/solution inlet/outlet pipes), **(C)** copper heating block containing a resistive heating band and silicon diode thermocouple (not shown), **(D)** “dovetail” slide mount (and stainless steel wedge) on top of **(E)** HPLT copper cell, (F) stainless steel vacuum shroud, **(G)** O-ring, **(H)** and **(I)** CaF2 / quartz windows, **(J)** PEEK shroud window holder and **(K)** 1/16 inch diameter gas/solution inlet holes. Figure taken and adapted from reference 241

.

The inlet of the cell is fitted to an SSI (Scientific Systems Inc.) valve that is used to introduce the substance into the cell *via* a connected Teledyne Technologies Inc. ISCO 260 D syringe pump and vacuum pump (connected *via* a T-piece) that can be used to achieve vacuum conditions in the system. The outlet port is connected to a 1/16 inch steel pipe with a T-piece that is joined to an STIF pressure transducer (RDP Electrics Ltd.), with a range of 0–3000 psi, to measure the pressure of the system and an HiP (High Pressure Equipment Co.) valve that is used as a release to de-pressurise the cell (Figure 6.2). The cell was evacuated before each experiment. This vacuum condition was then set as the zero value on the pressure monitor to represent the lack of any contained species. The syringe pump containing the fluid was at a continuous flow rate of 0.05 ml / min. In the case of the near-infrared measurements, the spectra were recorded continuously at 50 second intervals along with pressure readings as the substance was slowly flowed into the cell with the syringe pump. All near-infrared spectra used were processed against a single beam spectrum of the empty cell under vacuum as the background reference. All Raman measurements where collected at 2 minute intervals with the pressure recording times adjusted accordingly.

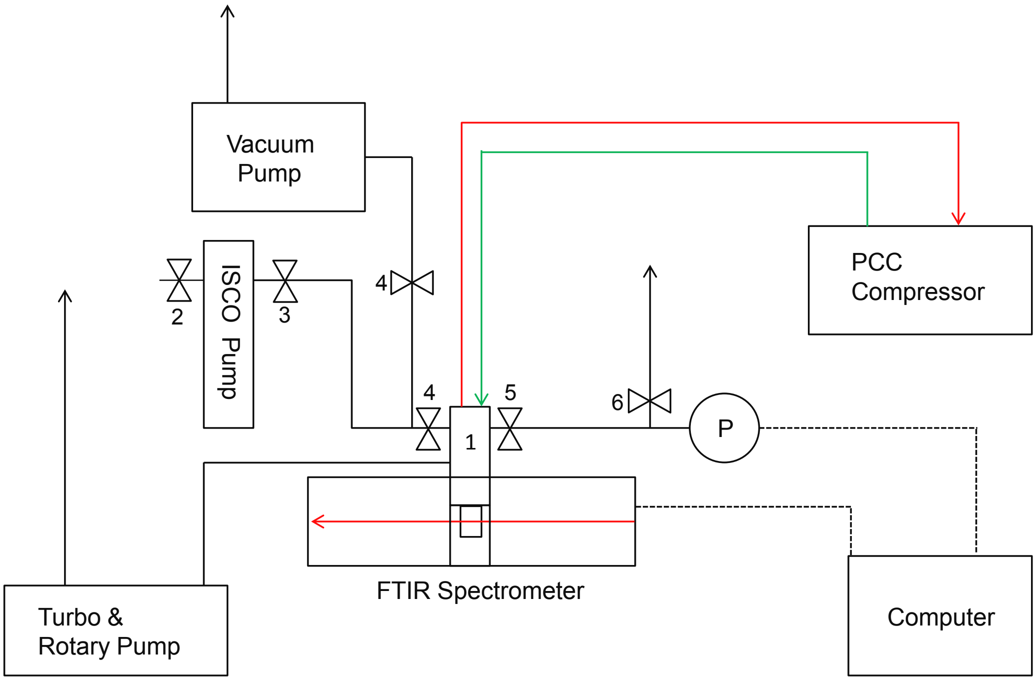

FIGURE 6.2: Schematic representation of the low temperature near-infrared experimental setup: **(1)** CryoTiger® cold end, **(2–6)** valves, **(P)** pressure transducer, **(dotted line)** USB connection, **(Green)** send, **(Red)** return, **(Arrow)** extraction pipe. In the case of the Raman measurements, the probe was mounted next to this apparatus allowing the cell to remain situated in the FTIR spectrometer.

6.5 Spectroscopic Measurements on Mixtures

Mixtures were prepared by weight in a variable volume view cell detailed by Licence *et al.*[242] and stirred with an internal magnetic stir bar under one phase conditions to ensure a fully homogeneous fluid (Figure 6.3). The temperature of the mixture was controlled by the six cartridge heater embedded in the cell body and the pressure regulated by changing the internal volume of the view cell *via.* the back window, moved by a hydraulic piston. The front window allowed for the observation of the mixture, ensuring it was in a single phase, and the collection of Raman Spectra.

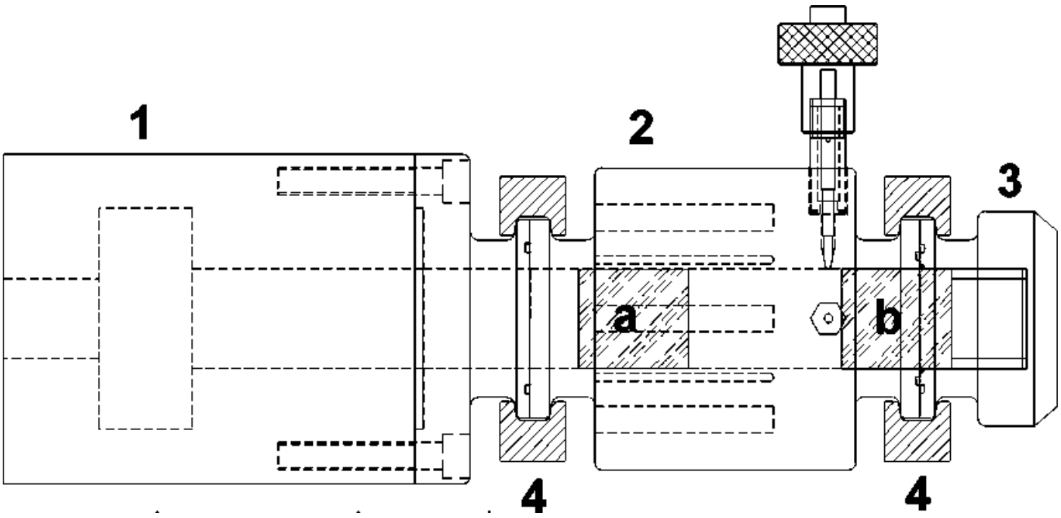

FIGURE 6.3: Diagram of the high pressure view cell. It consists of a hydraulically driven ram that alters the position of a dynamically sealed sapphire piston **(a)** within the cell (thereby changing its internal volume). The cell is sealed at the other end by a static sapphire window **(b)**, held in a removable window holder with a rubber O-ring. The main components of the cell, hydraulic unit **(1)**, cell body **(2)** and window holder **(3)** are assembled with a pair of interchangeable clamps **(4)** both of which are secured with a fail-safe mechanism. Reproduced from reference 242.

The mixture could then be flowed from the view cell through a preheated spectroscopy cell containing the porous material. NIR or Raman spectroscopic measurements of the mixture could then take place in this cell (Figure 6.4).

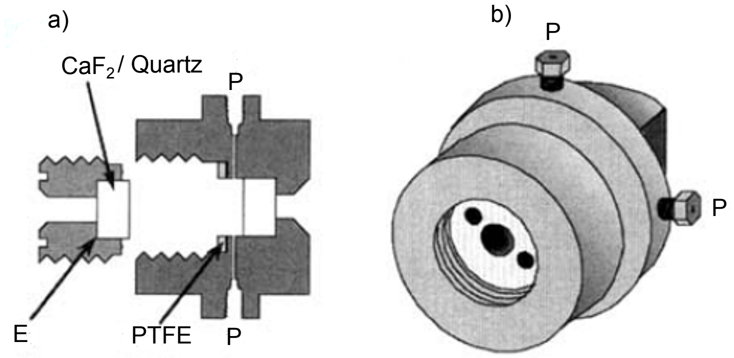

FIGURE 6.4: **a)** Cross-sectional and **b)** external view of high pressure cell used in the spectroscopic mixture experiments. **E** indicates the epoxy resin used to seal the window to the body of the cell, consisting of either low temperature epoxy resin or high temperature glue, depending on the temperature of the mixture studied. **P** are the 1/16th" SSI ports. Adapted from reference 243.

The mixture was then flowed out of the cell and vented *via* a Jasco Model 880-81 model BPR (back pressure regulator). A schematic of the experimental apparatus is shown in Figure 6.5.

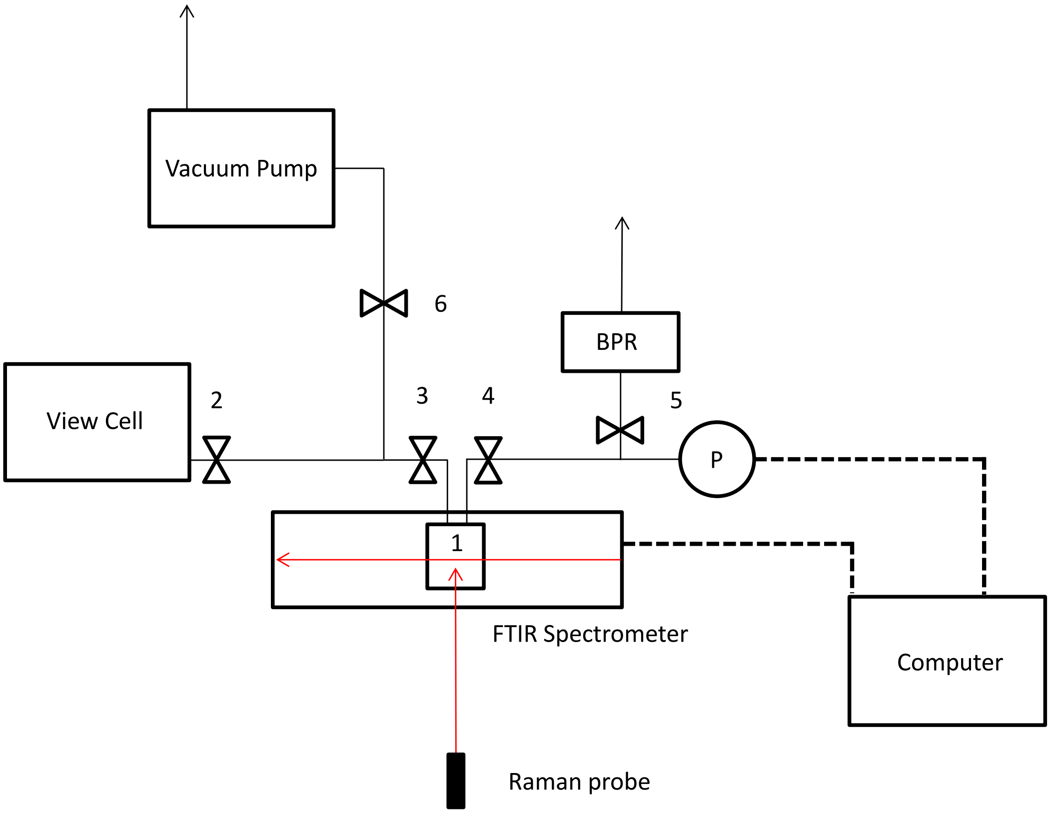

Figure 6.5: Schematic representation of the experimental setup used to determine mixture composition: **(1)** spectroscopy cell, **(2–6)** valves, **(P)** pressure transducer, **(dotted line)** USB connection and **(Arrow)** extraction pipe.

6.6 Materials

6.6.1 Materials Used in Chapter 2 and 3

The fluids used for confinement studies were obtained in the form of gases and used as received from the manufacturer. These gases included BOC supercritical fluid (SCF) grade carbon dioxide, Mexichem Fluor Inc. difluoromethane and Air Products ethane. The 3.2 nm MCM-41[92,244] (Mobil^{TM} Crystalline Materials-41) and 8.3 nm MSU-H[245] (large pore hexagonal) silica were used as received from the manufacturer (Sigma-Aldrich). The 3.5 nm, 4.0 nm and 4.5 nm MCM-41 were synthesised and provided courtesy of Beatrice Adeniran and Wantana Sangchoom and the 6.7 nm and 12.2 nm aluminosilicates were produced by Erik Masika (Mokaya Group, University of Nottingham).

The porous materials used in this study include mesostructured silica including four separate MCM-41 (Mobil^{TM} Crystalline Materials-41) samples, one MSU-H (large pore hexagonal) type silica, along with MZBN-100w3hd and MZBN-135w3h aluminosilicates.[246] All pore size measurements were obtained using gas soprtion with NLDFT calculations by the Mokaya Group (see Table 1 and Figures 6.6 and 6.7).[247] Before experiments all samples where prepared by drying under vacuum at *ca.* 313 K for approximately 12 hours.

TABLE 6.1: The porous silica templates used in this study.

Material	Mean Pore Diameter (nm)	Distribution FWHM (nm)	Ref
MCM-41 3.2	3.2	0.5	This Work
MCM-41 3.5	3.5	0.4	This Work
MCM-41 165	4.0	0.6	248
MCM-41 180	4.5	0.9	248
MZBN-100w3hd	6.7	7.4	246
MSU-H	8.3	1.6	This Work
MZBN-135w3h	12.2	8.8	246

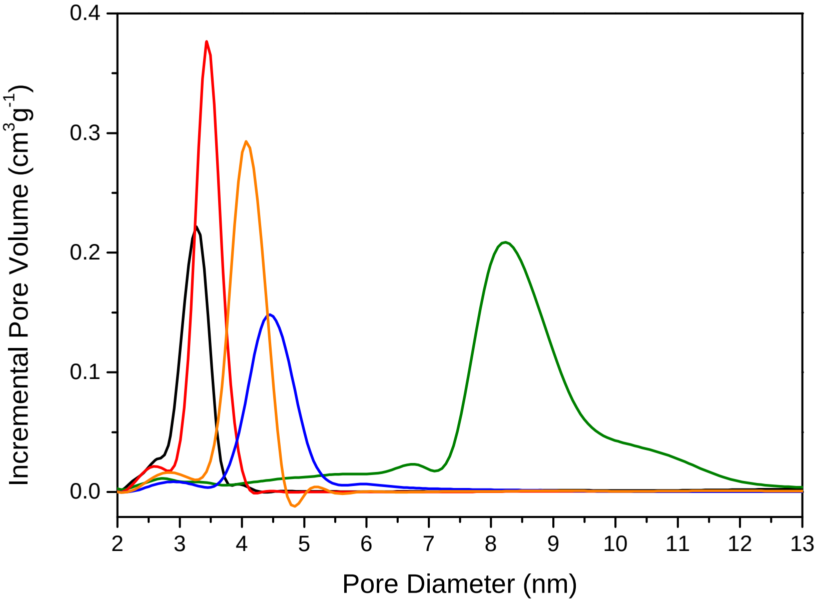

Figure 6.6: Pore size distributions of the 3.2 nm (black), 3.5 nm (red), 4.0 nm (orange) and 4.5 nm (blue) MCM-41 and 8.3 nm (green) MSU-H silica, calculated from gas sorption data, using NLDFT calculations.

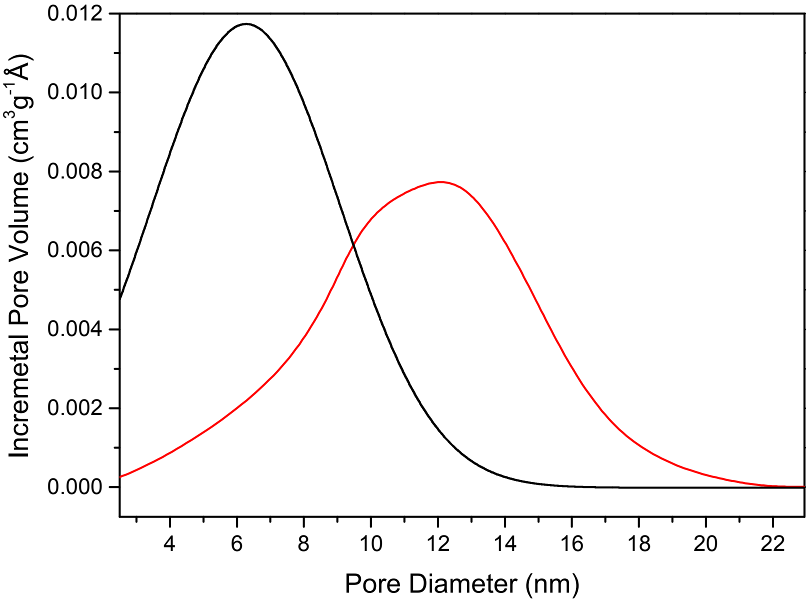

Figure 6.7: Pore size distributions of the 6.7 nm (black), 12.2 nm (red) aluminosilicates calculated from gas sorption data, using NLDFT calculations.

The larger pore anodic alumina oxide templates where obtained from Synkera

Inc. and were used as received. The manufacturer stated mean pore diameters are given in Table 6.2.

TABLE 6.2: The porous anodic alumina templates used in this study.

Material	Mean Pore Diameter (nm)
SM-18-100-13	18
SM-35-100-13	35
SM-55-100-13	55
SM-80-100-13	80
SM-100-100-13	100

6.6.2 Materials Used in Chapter 4

The fluids used for composition studies were obtained in the form of gasses used as received from the manufacturer (BOC, supercritical fluid (SCF) grade carbon dioxide and Mexichem Fluor Inc., difluoromethane) and liquid Acetonitrile (VWR Prolobo®, 99.9 % purity). The tetrabutylammonium tetrafluoroborate (TBA.BF_4) was used as received (Fluka®, electrochemical analysis grade $\geq$ 99.0 % purity). The 3.2 nm MCM-41[92,244] and 8.3 nm MSU-H[245] silica were used as received from the manufacturer (Sigma-Aldrich) as was the 18 nm SM-18-100-13 anodic alumina templates (Synkera Inc.). Fresh silica was placed into the cell before each experiment as a significant amount of CH_3CN or TBA.BF_4 was left in the pore after de-pressuring the system. The pore confinement of CO_2/CH_3CN in anodic alumina again left residual CH_3CN in the pores. The templates were recovered and purged by oven drying for *ca.* 8 hours at *ca.* 368 K and left under vacuum in the heated spectroscopy cell overnight at 323 K allowing them to be reused. To ensure they were fully purged a Raman spectrum of the template was recorded with a 1 second exposure time for 200 collections. The disappearance of the CH_3CN peaks indicates that the sample is fully purged of the CH_3CN that remained in the pores from the previous mixture. Figure 6.8 shows the Raman spectrum of the anodic alumina templates before and after this purging process.

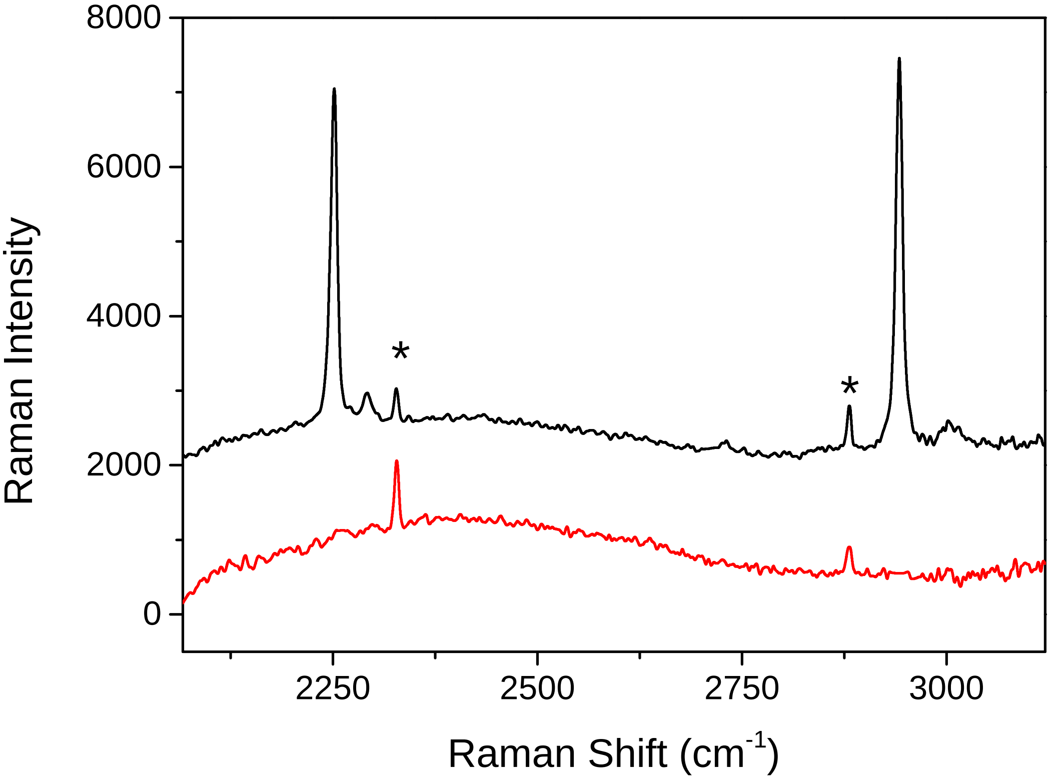

FIGURE 6.8: Raman spectrum of the anodic alumina template before and after the purging process, the spectrum displays how the CH_3CN Raman bands disappear after the CH_3CN is removed. The starred points indicate stray light.

$TBA.BF_4$ also contaminated the anodic alumina samples after experiments using the $CH_2F_2/TBA.BF_4$ mixture. The solid $TBA.BF_4$ could not be removed by washing with ethanol, heating under a vacuum and purging with supercritical CH_2F_2, therefore fresh unused SM-18-100-13 templates were used before each experiment. Figure 6.9 shows the Raman spectrum of a TBA.BF$_4$ contaminated anodic alumina template before and after the attempted purging.

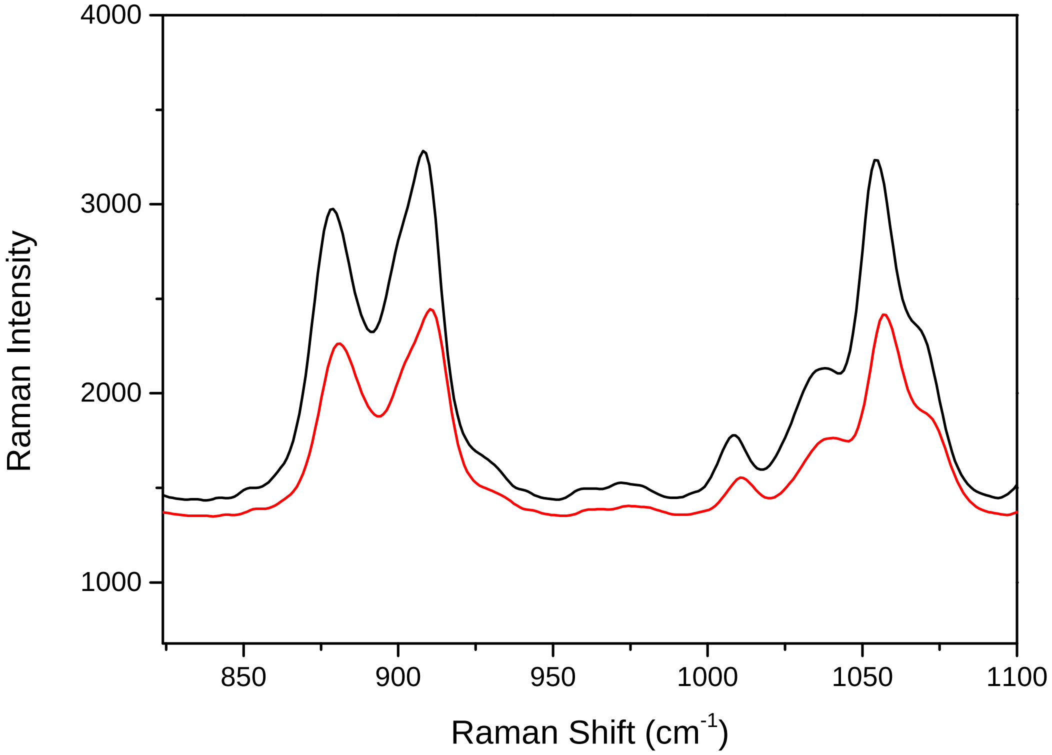

FIGURE 6.9: Raman spectra of anodic alumina templates containing residual TBA.BF$_4$ before **(black)** and after **(red)** attempted purging. The TBA.BF$_4$ clearly resides in the pores after this process.

References

[1] R. M. Smith, *Pure Appl. Chem.*, 1993, **65**, 2397–2403.

[2] J. A. Darr and M. Poliakoff, *Chem. Rev.*, 1999, **99**, 495–542.

[3] T. G. Squires, C. G. Venier and T. Aida, *Fluid Phase Equilibr.*, 1983, **10**, 261–268.

[4] H. Tiltscher and H. Hofmann, *Chem. Eng. Sci.*, 1987, **42**, 959–977.

[5] P. E. Savage, S. Gopalan, T. I. Mizan, C. J. Martino and E. E. Brock, *AIChE J.*, 1995, **41**, 1723–1778.

[6] V. Goodship and E. O. Ogur, *Polymer Processing with Supercritical Fluids*, Smithers Rapra Publishing, Shrewsbury, 2004.

[7] M. Türk, *Particle Formation with Supercritical Fluids: Challenges and Limitations*, Elsevier, Oxford, 2014.

[8] P. M. Chaikin, *Principles of Condensed Matter Physics*, Cambridge University Press, Cambridge, 2000.

[9] K. Binder, *Rep. Prog. Phys.*, 1987, **50**, 783–859.

[10] E. W. Lemmon, M. O. McLinden and D. G. Friend, *ThermoPhysical Properties of Fluid Systems*, Nist Chemistry WebBook, NIST Standered Reference Number 69. National Institute of Standards and Technology, Gaithersburg MD, 20899, http://webbook.nist.gov/chemistry/fluid/, (Accessed Sep 2015).

[11] G. Jeager, *Arch. Hist. Exact Sci.*, 1998, **53**, 51–81.

[12] R. Hołyst and A. Poniewierski, *Thermodynamics for Chemists, Physicists and Engineers*, Springer Science & Business Media, Dordrecht, 2012.

[13] R. Batterman, *The Oxford Handbook of Philosophy of Physics*, Oxford University Press, Oxford, 2013.

[14] J. Sengers, R. Kayser, C. Peters and H. White, *Equations of State for Fluids and Fluid Mixtures*, Elsevier, Oxford, 2000, vol. 5.

[15] G. Rother, D. Woywod, M. Schoen and G. H. Findenegg, *J. Chem. Phys.*, 2004, **120**, 11864–11873.

[16] P. Davies, *The New Physics*, Cambridge University Press, Cambridge, 1992.

[17] C. Stenland and B. M. Pettitt, *J. Chem. Educ.*, 1995, **72**, 560–564.

[18] E. Stahl, W. Schilz, E. Schütz and E. Willing, *Angew. Chem. Int. Ed. Engl.*, 1978, **17**, 731–738.

[19] P. Hubert and O. G. Vitzthum, *Angew. Chem. Int. Ed. Engl.*, 1978, **17**, 710–715.

[20] E. Klesper, *Angew. Chem. Int. Ed. Engl.*, 1978, **17**, 738–746.

[21] R. Eggers, *Angew. Chem. Int. Ed. Engl.*, 1978, **17**, 751–754.

[22] J. F. Brennecke and C. A. Eckert, *AIChE Journal*, 1989, **35**, 1409–1427.

[23] K. W. Hutchenson and N. R. Foster, *Innovations in Supercritical Fluids*, American Chemical Society, Washington, D.C., 1995.

[24] Z. Xinli, H. Xiaoling, G. Ping and L. Guozheng, *J. Supercrit. Fluids*, 2009, **49**, 111–116.

[25] H. Lv, F. Meng, M. Zhang, Z. Geng and Y. Sun, *Chem. Eng. Sci.*, 2015, **135**, 285–293.

[26] Y. Liang, C. Zhen, D. Zou and D. Xu, *J. Am. Chem. Soc.*, 2004, **126**, 16338–16339.

[27] P. Atkins and J. D. Paula, *Atkins' Physical Chemistry*, Oxford University Press, 8th edn., 2006.

[28] M. Schlesinger and M. Paunovic, *Modern Electroplating*, Wiley, Hoboken, 5th edn., 2010.

[29] M. Paunovic and M. Schlesinger, *Fundamentals of Electrochemical Deposition*, Wiley, Hoboken, 2nd edn., 2006.

[30] R. M. Crooks, F. R. F. Fan and A. J. Bard, *J. Am. Chem. Soc.*, 1984, **106**, 6851–6852.

[31] R. M. Crooks and A. J. Bard, *J. Phys. Chem.*, 1987, **91**, 1274–1284.

[32] A. C. McDonald, F. R. F. Fan and A. J. Bard, *J. Phys. Chem.*, 1986, **90**, 196–202.

[33] J. Ke, W. Su, S. M. Howdle, M. W. George, D. Cook, M. Perdjon-Abel, P. N. Bartlett, W. Zhang, F. Cheng, W. Levason, G. Reid, J. Hyde, J. Wilson, D. C. Smith, K. Mallik and P. Sazio, *Proc. Natl. Acad. Sci. U.S.A.*, 2009, **106**, 14768–14772.

[34] D. Cook, P. N. Bartlett, W. Zhang, W. Levason, G. Reid, J. Ke, W. Su, M. W. George, J. Wilson, D. Smith, K. Mallik, E. Barrett and P. Sazio, *Phys. Chem. Chem. Phys.*, 2010, **12**, 11744–11752.

[35] A. P. Abbott, C. A. Eardley, J. C. Harper and E. G. Hope, *J. Electroanal. Chem.*, 1998, **457**, 1–4.

[36] A. P. Abbott and C. A. Eardley, *J. Phys. Chem. B*, 2000, **104**, 9351–9355.

[37] P. N. Bartlett, D. A. Cook, M. W. George, A. L. Hector, J. Ke, W. Levason, G. Reid, D. C. Smith and W. Zhang, *Phys. Chem. Chem. Phys.*, 2014, **16**, 9185–9668.

[38] A. W. Verkerk, E. L. V. Goetheer, L. J. P. van den Broeke and J. T. F. Keurentjes, *Langmuir*, 2002, **18**, 6807–6812.

[39] J. L. Dickson, G. Gupta, T. S. Horozov, B. P. Binks and K. P. Johnston, *Langmuir*, 2006, **22**, 2161–2170.

[40] M. Hayyan, F. S. Mjalli, M. A. Hashim, I. M. AlNashef and T. X. Mei, *J. Ind. Eng. Chem.*, 2013, **19**, 106–112.

[41] J. M. Blackburn, D. P. Long, A. Cabañas and J. J. Watkins, *Science*, 2001, **294**, 141–145.

[42] I. Souvignet and S. V. Olesik, *Anal. Chem.*, 1998, **70**, 2783–2788.

[43] J. Ke, P. N. Bartlett, D. Cook, T. L. Easun, M. W. George, W. Levason, G. Reid, D. Smith, W. Su and W. Zhang, *Phys. Chem. Chem. Phys.*, 2012, **14**, 1517–1528.

[44] *The Science of SCFED*, http://www.scfed.net/scfedscience2.php, (Accessed Aug 2016).

[45] J. Ke, W. Su, S. M. Howdle, M. W. George, D. Cook, M. Perdjon-Abel, P. N. Bartlett, W. Zhang, F. Cheng, W. Levason, G. Reid, J. Hyde, J. Wilson, D. C. Smith, K. Mallik and P. Sazio, *Proc. Natl. Acad. Sci. U.S.A.*, 2009, **106**, 14768–14772.

[46] M. Atobe, N. Yoshida, K. Sakamoto, K. Sugino and T. Fuchigami, *Electrochim. Acta*, 2013, **87**, 409–415.

[47] P. N. Bartlett, M. Perdjon-Abel, D. Cook, G. Reid, W. Levason, F. Cheng, W. Zhang, M. W. George, J. Ke, R. Beanland and J. Sloan, *ChemElectroChem*, 2014, **1**, 187–194.

[48] K. Jain, C. Willson and B. Lin, *IEEE Electron Device Lett.*, 1982, **3**, 53–55.

[49] C. W. Gwyn, R. Stulen, D. Sweeney and D. Attwood, *J. Vac. Sci. Technol., B*, 1998, **16**, 3142–3149.

[50] R. Feder, E. Spiller and J. Topalian, *Polym. Eng. Sci.*, 1977, **17**, 385–389.

[51] S. H. Park, D. O. Shin, B. H. Kim, D. K. Yoon, K. Kim, S. Y. Lee, S.-H. Oh, S.-W. Choi, S. C. Jeon and S. O. Kim, *Soft Matter*, 2010, **6**, 120–125.

[52] R. Xu, W. Pang, J. Yu, Q. Huo and J. Chen, *Chemistry of Zeolites and Related Porous Materials: Synthesis and Structure*, John Wiley & Sons, Singapore, 2007.

[53] Y. Xia, P. Yang, Y. Sun, Y. Wu, B. Mayers, B. Gates, Y. Yin, F. Kim and H. Yan, *Adv. Mater.*, 2003, **15**, 353–389.

[54] K. I. Popov, S. S. Djokic, N. D. Nikolic and V. D. Jovic, *Morphology of Electrochemically and Chemically Deposited Metals*, Springer International Publishing, Zurich, 2016.

[55] J. Bisquert, P. Cendula, L. Bertoluzzi and S. Gimenez, *J. Phys. Chem. Lett.*, 2014, **5**, 205–207.

[56] F. G. Keyes and J. G. Kirkwood, *Phys. Rev.*, 1930, **36**, 754–761.

[57] A. P. Abbott, S. Corr, N. E. Durling and E. G. Hope, *J. Phys. Chem.*, 2004, **108**, 4922–4926.

[58] J. Jun and P. S. Fedkiw, *J. Electroanal. Chem.*, 2001, **515**, 113–122.

[59] H. Yan, T. Sato, D. Komago, A. Yamaguchi, K. Oyaizu, M. Yuasa and K. Otake, *Langmuir*, 2005, **21**, 12303–12308.

[60] M. L. Kijevcanin, I. S. A. Ribeiro, A. G. M. Ferreira and I. M. A. Fonseca, *J. Chem. Eng. Data*, 2003, **48**, 1266–1270.

[61] W. Liu, X. Yan, J. Lang and Q. Xue, *J. Mater. Chem.*, 2012, **22**, 8853–8861.

[62] Y. Melnichenko, A. Radlinski, M. Mastalerz, G. Cheng and J. Rupp, *Int. J. Coal. Geol.*, 2009, **77**, 69–79.

[63] Y. B. Melnichenko, H. Mayama, G. Cheng and T. Blach, *Langmuir*, 2010, **26**, 6374–6379.

[64] H. E. Ross, P. Hagin and M. D. Zoback, *Int. J. Greenh. Gas Con.*, 2009, **3**, 773–786.

[65] M. Gruszkiewicz, M. Naney, J. Blencoe, D. Cole, J. Pashin and R. Carroll, *Int. J. Coal Geol.*, 2009, **77**, 23–33.

[66] M. Andrew, B. Bijeljic and M. J. Blunt, *Adv. Water Resour.*, 2014, **68**, 24–31.

[67] X. Li and X. Fan, *Energy Procedia*, 2014, **61**, 2712–2715.

[68] S.-Y. Hsu and M. Hilpert, *Adv. Water Resour.*, 2015, In Press DOI:10.1016/j.advwatres.2015.08.004.

[69] S. Bachu, *Int. J. Greenh. Gas. Con.*, 2015, **40**, 188–202.

[70] J. Ge, Q. Zhang, T. Zhang and Y. Yin, *Angew. Chem. Int. Ed.*, 2008, **47**, 8924–8928.

[71] J. Gao, J. Xu, S. Wen, J. Hu and H. Liu, *Micropor. Mesopor. Mat.*, 2015, **207**, 149–155.

[72] K. Morishige, H. Fujii, M. Uga and D. Kinukawa, *Langmuir*, 1997, **13**, 3494–3498.

[73] K. Morishige and M. Shikimi, *J. Chem. Phys.*, 1998, **108**, 7821–7824.

[74] K. Morishige and M. Ito, *J. Chem. Phys.*, 2002, **117**, 8036–8041.

[75] C. G. V. Burgess, D. H. Everett and S. Nuttall, *Pure Appl. Chem*, 1989, **61**, 1845–1857.

[76] W. D. Machin, *Langmuir*, 1999, **15**, 169–173.

[77] M. Thommes and G. H. Findenegg, *Langmuir*, 1994, **10**, 4270–4277.

[78] D. G. Jones and H. M. Fretwell, *J. Phys.: Condens. Matter*, 2003, **15**, 4709–4715.

[79] M. Dvoyashkin, R. Valiullin, J. Kärger, W.-D. Einicke and R. Gläser, *J. Am. Chem. Soc.*, 2007, **129**, 10344–10345.

[80] H. Omi, B. Nagasaka, K. Miyakubo, T. Ueda and T. Eguchi, *Phys. Chem. Chem. Phys.*, 2004, **6**, 1299–1303.

[81] S. De, Y. Shapir, E. H. Chimowitz and V. Kumaran, *AIChE J.*, 2001, **47**, 463–473.

[82] P. López-Aranguren, L. F. Vega, C. Domingo and E. H. Chimowitz, *AIChE J.*, 2012, **58**, 3597–3600.

[83] Y. Hiejima and M. Yao, *J. Phys.: Condens. Matter*, 2004, **16**, 7903–7908.

[84] E. Roduner, *Nanoscopic Materials*, The Royal Society of Chemistry, Cambridge, 2nd edn., 2014.

[85] M. E. Fisher and H. Nakanishi, *J. Chem. Phys.*, 1981, **75**, 5857–5863.

[86] D. M. Antonelli and J. Y. Ying, *Curr. Opin. Colloid Interface Sci.*, 1996, **1**, 523–529.

[87] A. Lopes, P. Martins and S. Lanceros-Mendez, *Prog. Surf. Sci.*, 2014, **89**, 239–277.

[88] K. O'Malley, A. Gil and T. Curtin, *Micropor. Mesopor. Mat.*, 2014, **191**, 48–58.

[89] S. Iijima, *Nature*, 1991, **354**, 56–58.

[90] S. D. Kirik, V. A. Parfenov and S. M. Zharkov, *Micropor. Mesopor. Mat.*, 2014, **195**, 21–30.

[91] N. Floquet, J. Coulomb and G. André, *Micropor. Mesopor. Mat.*, 2004, **72**, 143–152.

[92] J. S. Beck, J. C. Vartuli, W. J. Roth, M. E. Leonowicz, C. T. Kresge, K. D. Schmitt, C. T. W. Chu, D. H. Olson and E. W. Sheppard, *J. Am. Chem. Soc.*, 1992, **114**, 10834–10843.

[93] C. T. Kresge, M. E. Leonowicz, W. J. Roth, J. C. Vartuli and J. S. Beck, *Nature*, 1992, **359**, 710–712.

[94] H. Masuda and K. Fukuda, *Science*, 1995, **268**, 1466–1468.

[95] T. T. Xu, R. D. Piner, and R. S. Ruoff, *Langmuir*, 2003, **19**, 1443–1445.

[96] P. I. Ravikovitch, S. C. O. Domhnaill, A. V. Neimark, F. Schueth and K. K. Unger, *Langmuir*, 1995, **11**, 4765–4772.

[97] K. S. W. Sing, D. H. Everett, R. A. W. Haul, L. Moscou, R. A. Pierotti, J. Rouquerol and T. Siemeiniewska, *Pure Appl. Chem.*, 1985, **57**, 603–619.

[98] A. G. Foster, *Trans. Faraday Soc.*, 1932, **28**, 645–657.

[99] L. H. Cohan, *J. Am. Chem. Soc.*, 1938, **60**, 433–435.

[100] M. W. Cole and W. F. Saam, *Phys. Rev. Lett.*, 1974, **32**, 985–988.

[101] P. C. Ball and R. Evans, *Langmuir*, 1989, **5**, 714–723.

[102] S. Lowell, J. Shields, M. Thomas and M. Thommes, *Characterization of Porous Solids and Powders: Surface Area, Pore Size and Density*, Springer Science & Business Media, Dordrecht, 2004.

[103] E. P. Barrett, L. G. Joyner and P. P. Halenda, *J. Am. Chem. Soc.*, 1951, **73**, 373–380.

[104] J. Rouquerol, D. Avnir, C. W. Fairbridge, D. H. Everett, J. M. Haynes, N. Pernicone, J. D. F. Ramsay, K. S. W. Sing and K. K. Unger, *Pure Appl. Chem.*, 1994, **66**, 1739–1758.

[105] A. V. Neimark, *Langmuir*, 1995, **11**, 4183–4184.

[106] P. I. Ravikovitch, A. Vishnyakov and A. V. Neimark, *Phys. Rev. E*, 2001, **64**, 011602.

[107] A. A. Novitskiy, J. Ke, G. Comak, M. Poliakoff and M. W. George, *Appl. Spectrosc.*, 2011, **65**, 885–891.

[108] C. Yonker, J. Linehan and J. Fulton, *J. Supercrit. Fluids*, 1998, **14**, 9–16.

[109] M. Buback, J. Schweer and H. Tups, *Ber. Bunsenges. Phys. Chem.*, 1985, **89**, 545–550.

[110] M. Buback, *J. Mol. Struct.*, 1995, **347**, 113–129.

[111] M. Buback, J. Schweer and H. Tups, *Z. Naturforsch.*, 1985, **41a**, 505–511.

[112] M. Buback, J. Schweer and H. Tups, *Physica B+C*, 1986, **139–140**, 544–546.

[113] V. G. Arakcheev, V. N. Bagratashvili, A. A. Valeev, V. M. Gordiyenko, V. V. Kireev, V. B. Morozov, A. N. Olenin, V. K. Popov, V. G. Tunkin and D. V. Yakovlev, *J. Raman Spectrosc.*, 2003, **34**, 952–956.

[114] S. Roy, J. R. Gord and A. K. Patnaik., *Prog. Energy Combust. Sci.*, 2010, **36**, 280–306.

[115] M. S. Schneider, J. D. Grunwaldt and A. Baiker, *Langmuir*, 2004, **20**, 2890–2899.

[116] V. G. Arakcheev, V. N. Bagratashvili, S. A. Dubyanskiy, V. B. Morozov, A. N. Olenin, V. K. Popov, V. G. Tunkin, A. A. Valeev and D. V. Yakovlev, *J. Raman Spectrosc.*, 2008, **39**, 750–755.

[117] V. Arakcheev, A. Valeev, V. Morozov and A. Olenin, *Laser Phys.*, 2008, **18**, 1451–1458.

[118] I. Afara, S. Singh and A. Oloyede, *Med. Eng. Phys.*, 2013, **35**, 88–95.

[119] E. Keller, A. Nadler, H. Alkadhi, S. S. Kollias, Y. Yonekawa and P. Niederer, *NeuroImage*, 2003, **20**, 828–839.

[120] G. L. Alexandrino and R. J. Poppi, *Anal. Chim. Acta*, 2013, **765**, 37–44.

[121] J. M. Balage, S. da Luz e Silva, C. A. Gomide, M. de Nadai Bonin and A. C. Figueira, *Meat Sci.*, 2015, **108**, 37–43.

[122] G. Giovanelli, N. Sinelli, R. Beghi, R. Guidetti and E. Casiraghi, *Postharvest Biol. Tech.*, 2014, **87**, 13–20.

[123] Y. Yagi, H. Tsugane, H. Inomata and S. Saito, *J. Supercrit. Fluids*, 1993, **6**, 139–142.

[124] D. C. Harris and M. D. Bertolucci, *Symmetry and Spectroscopy*, Dover Publications, New York, 1989.

[125] M. Schmitt and J. Popp, *J. Raman Spectrosc.*, 2006, **37**, 20–28.

[126] H. Abramczyk, B. Brozek-Pluska, J. Surmacki, J. Jablonska-Gajewicz and R. Kordek, *Prog. in Biophys. Mol. Bio.*, 2012, **108**, 74–81.

[127] F. B. Legesse, A. Medyukhina, S. Heuke and J. Popp, *Comput. Med. Imag. Graph.*, 2015, **43**, 36–43.

[128] B. Schrader, H. Klump, K. Schenzel and H. Schulz, *J. Mol. Struct.*, 1999, **509**, 201–212.

[129] B. Kolozsvari, S. Firth and A. Saiardi, *Mol. Plant*, 2015, **8**, 826–828.

[130] M. S. Ruiz, H. Yasuor, A. Ben-Gal, U. Yermiyahu, Y. Saranga and R. Elbaum, *Sci. Hortic.*, 2015, **192**, 244–249.

[131] O. V. Andreeva, V. G. Arakcheev, V. N. Bagratashvili, V. B. Morozov, V. K. Popov and A. A. Valeev, *J. Raman Spectrosc.*, 2011, **42**, 1747–1753.

[132] B. K. Peterson, G. S. Heffelfinger, K. E. Gubbins and F. van Swol, *J. Chem. Phys.*, 1990, **93**, 679–685.

[133] P. B. Balbuena and K. E. Gubbins, *Langmuir*, 1993, **9**, 1801–1814.

[134] M. Miyahara and K. E. Gubbins, *J. Chem. Phys.*, 1997, **106**, 2865–2880.

[135] K. Binder, *Ferroelectrics*, 1987, **73**, 43–67.

[136] H. Bock and M. Schoen, *Phys. Rev. E*, 1999, **59**, 4122–4136.

[137] P. Röcken, A. Somoza, P. Tarazona and G. Findenegg, *J. Chem. Phys.*, 1998, **108**, 8689–8697.

[138] T. W. Rosch and J. R. Errington, *J. Phys. Chem. B*, 2008, **112**, 14911–14919.

[139] H. Nakanishi and M. E. Fisher, *J. Chem. Phys.*, 1983, **78**, 3279–3293.

[140] R. Evans, U. M. B. Marconi and P. Tarazona, *J. Chem. Soc., Faraday Trans. 2*, 1986, **82**, 1763–1787.

[141] R. Evans, U. M. B. Marconi and P. Tarazona, *J. Chem. Phys.*, 1986, **84**, 2376–2399.

[142] J. P. Fraissard, *Physical Adsorption: Experiment, Theory, and Applications*, Springer Netherlands, Dordrecht, 1997, vol. 491.

[143] S. Jana, J. K. Singh and S. K. Kwak, *J. Chem. Phys.*, 2009, **130**, 214707.

[144] S. K. Singh, A. Sinha, G. Deo and J. K. Singh, *J. Phys. Chem. C*, 2009, **113**, 7170–7180.

[145] S. K. Singh, A. K. Saha and J. K. Singh, *J. Phys. Chem. B*, 2010, **114**, 4283–4292.

[146] M. Y. Lin, S. K. Sinha, J. M. Drake, X.-l. Wu, P. Thiyagarajan and H. B. Stanley, *Phys. Rev. Lett.*, 1994, **72**, 2207–2210.

[147] Y. B. Melnichenko, G. D. Wignall, D. R. Cole and H. Frielinghaus, *J. Chem. Phys.*, 2006, **124**, 204711.

[148] A. Bondi, *J. Phys. Chem.*, 1964, **68**, 441–451.

[149] R. Humauyn and D. L. Tomasko, *AIChE J.*, 2000, **46**, 2065.

[150] N. C. Gallego, L. He, D. Saha, C. I. Contescu and Y. B. Melnichenko, *J. Am. Chem. Soc.*, 2011, **133**, 13794–13797.

[151] Y. Hiejima, M. Kanakubo, T. Aizawa, Y. Kurata and Y. Ikushima, *Chem. Phys. Lett.*, 2005, **408**, 344–347.

[152] A. K. Jameson, C. J. Jameson and H. S. Gutowsky, *J. Chem. Phys.*, 1970, **53**, 2310–2321.

[153] M. Thommes, G. H. Findenegg and H. Lewandowski, *Berich. Bunsen Gesell.*, 1994, **98**, 477–481.

[154] A. de. Keizer, T. Michalskis and G. H. Findenegg, *Pure Appl. Chem.*, 1991, **63**, 1495–1502.

[155] M. Thommes, R. Köhn and M. Fröba, *Appl. Surf. Sci.*, 2002, **196**, 239–249.

[156] K. Morishige and N. Tateishi, *J. Chem. Phys.*, 2003, **119**, 2301–2306.

[157] W. D. Machin, *Phys. Chem. Chem. Phys.*, 2003, **5**, 203–207.

[158] J. W. Mc Bain, *J. Am. Chem. Soc.*, 1932, **57**, 699.

[159] M. S. Gruszkiewicz, G. Rother, D. J. Wesolowski, D. R. Cole and D. Wallacher, *Langmuir*, 2012, **28**, 5070–5078.

[160] S. Kittaka, T. Iwashita, A. Serizawa, M. Kranishi, S. Takahara, Y. Kuroda, T. Mori and T. Yamaguchi, *J. Phys. Chem. B*, 2005, **109**, 23162–23169.

[161] S. Kittaka, M. Kuranishi, S. Ishimaru and O. Umahara, *J. Chem. Phys.*, 2007, **126**, 091103.

[162] L. A. Weber, *J. Chem. Phys.*, 1976, **65**, 446–449.

[163] D. F. Swinehart, *J. Chem. Educ.*, 1962, **39**, 333–335.

[164] A. Kordikowski, D. G. Robertson and M. Poliakoff, *Anal. Chem.*, 1996, **68**, 4436–4440.

[165] D. N. Sathyanarayana, *Vibrational Spectroscopy: Theory and Applications*, New Age International, New Delhi, 2007.

[166] A. Burneau and C. Carteret, *Phys. Chem. Chem. Phys.*, 2000, **2**, 3217–3226.

[167] N. Tasinato, G. Regini, P. Stoppa, A. P. Charmet and A. Gambi, *J. Chem. Phys.*, 2012, **136**, 214302.

[168] A. Bai, C.-C. Hu, Y.-F. Yang and C.-C. Lin, *Electrochimica Acta*, 2008, **53**, 2258–2264.

[169] F. Schüth, *Mesoporous Crystals and Related Nano-Structured Materials: Proceedings of the Meeting on Mesoporous Crystals and Related Nano-Structured Materials, Stockholm, Sweden, 1-5 June 2004*, Elsevier, Amsterdam, 2004, vol. 148.

[170] J. O. Hirschfelder, C. F. Curtiss and R. B. Bird, *Molecular Theory of Gases and Liquids*, Wiley, Hoboken, 1964.

[171] I. Brovchenko and A. Oleinikova, *J. Phys. Chem. B*, 2011, **115**, 9990–10000.

[172] P. V. Rysselberghe, *J. Phys. Chem.*, 1931, **36**, 1152–1155.

[173] Y. He and N. A. Seaton, *Langmuir*, 2006, **22**, 1150–1155.

[174] R. Redón, A. Vázquez-Olmos, M. E. Mata-Zamora, A. Ordóñez-Medrano, F. Rivera-Torres and J. M. Saniger, *Rev. Adv. Mater. Sci.*, 2006, **11**, 79–87.

[175] L. Pauling, *Am. Mineral.*, 1980, **65**, 321–323.

[176] C. A. Koh, T. Montanari, R. I. Nooney, S. F. Tahir and R. E. Westacott, *Langmuir*, 1999, **15**, 6043–6049.

[177] S. D. Moon, *Bull. Korean Chem. Soc*, 2012, **33**, 2553.

[178] M. L. Hair, *J. Non-Cryst. Solids*, 1975, **19**, 299–309.

[179] M. R. Alexander, G. Beamson, P. Bailey, T. C. Q. Noakes, P. Skeldon and G. E. Thompson, *Surf. Interface Anal.*, 2003, **35**, 649–657.

[180] D. R. James, L. G. Christophorou and R. A. Mathis, *Gaseous Dielectrics II: Proceedings of the Second International Symposium on Gaseous Dielectrics, Knoxville, Tennessee, U.S.A., March 9–13, 1980*, Pergamon Press, New York, 1980.

[181] A. C. Dewitt, K. W. Herwig and S. J. Lombardo, *Adsorption*, 2005, **11**, 491–499.

[182] M. R. Mello, D. Phanon, G. Q. Silveira, P. L. Llewellyn and C. M. Ronconi, *Micropor. Mesopor. Mat.*, 2011, **143**, 174–179.

[183] *CRC Handbook of Chemistry and Physics*, ed. R. C. Weast, The Chemical Rubber Co., Cleveland, 53rd edn., 1972–1973.

[184] A. P. Abbott, C. A. Eardley and R. Tooth, *J. Chem. Eng. Data*, 1999, **44**, 112–115.

[185] M. H. M. Herman, *Mol. Phys.*, 1998, **94**, 829–838.

[186] H. Grüll and D. Woermann, *J. Chem. Phys.*, 1996, **105**, 2527–2532.

[187] L. J. V. Poolen, C. D. Holcomb and V. G. Niesen, *Fluid Phase Equilibr.*, 1997, **129**, 105–111.

[188] J. K. Singh, J. Adhikari and S. K. Kwak, *Fluid Phase Equilibr.*, 2006, **248**, 1–6.

[189] F. El-Diasty, *Vib. Spectrosc.*, 2011, **55**, 1–37.

[190] S. Roy, J. R. Gord and A. K. Patnaik, *Prog. Energ. Combust. Sci.*, 2010, **36**, 280–306.

[191] J. Yi and J. Jonas, *J. Phys. Chem.*, 1996, **100**, 16789–16793.

[192] J.-P. Korb, A. Delville, S. Xu, G. Demeulenaere, P. Costa and J. Jonas, *J. Chem. Phys.*, 1994, **101**, 7074–7081.

[193] Y. Shao and T. W. Zerda, *J. Phys. Chem. B*, 1998, **102**, 3387–3394.

[194] S. Tjong, *Mat. Sci. Eng. R-Rep*, 2003, **41**, 1–60.

[195] B. K. Peterson, K. E. Gubbins, G. S. Heffelfinger, U. Marini Bettolo Marconi and F. van Swol, *J. Chem. Phys.*, 1988, **88**, 6487–6500.

[196] P. I. Ravikovitch, G. L. Haller and A. V. Neimark, *Adv. Colloid Interface Sci.*, 1998, **76–77**, 203–226.

[197] B. Peng and Y.-X. Yu, *J. Phys. Chem. B*, 2008, **112**, 15407–15416.

[198] K. Binder and D. P. Landau, *J. Chem. Phys.*, 1992, **96**, 1444–1454.

[199] K. S. Page and P. A. Monson, *Phys. Rev. E*, 1996, **54**, 6557–6564.

[200] L. Sarkisov, and P. A. Monson, *Langmuir*, 2000, **16**, 9857–9860.

[201] P. Kowalczyk, H. Tanaka, K. Kaneko, A. P. Terzyk and D. D. Do, *Langmuir*, 2005, **21**, 5639–5646.

[202] A. Vishnyakov, E. M. Piotrovskaya, E. N. Brodskaya, E. V. Votyakov and Y. K. Tovbin, *Langmuir*, 2001, **17**, 4451–4458.

[203] J. K. Singh and S. K. Kwak, *J. Chem. Phys.*, 2007, **126**, 024702.

[204] A. Lang, G. Kahl, C. N. Likos, H. Lowen and M. Watzlawek, *J. Phys. Condens. Matter*, 1999, **11**, 10143–10161.

[205] *Handbook of Raman Spectroscopy: From the Research Laboratory to the Process Line*, ed. I. R. Lewis and H. Edwards, Marcel Dekker, New York, 2001.

[206] Y. Kawakami, J. Yamamoto and H. Kagi, *Appl. Spectrosc.*, 2003, **57**, 1333–1339.

[207] Y. Nardon and Y. Larher, *Surf. Sci.*, 1974, **42**, 299–305.

[208] I. Suzuki and T. Shimanouchi, *J. Mol. Spectrosc.*, 1973, **46**, 130–145.

[209] D. Bermejo, J. Santos, P. Cancio, J. M. Fernandez-Sanchez and S. Montero, *J. Chem. Phys.*, 1992, **97**, 7055–7063.

[210] K. V. Helvoort, W. Knippers, R. Fantoni and S. Stolte, *Chem. Phys.*, 1987, **111**, 445–465.

[211] K. K. Unger, *Porous Silica*, Elsevier, Amsterdam, 1979, vol. 16.

[212] O. I. Malyi, P. Thiyam, M. Bostrom and C. Persson, *Phys. Chem. Chem. Phys.*, 2015, **17**, 20125–20133.

[213] J. G. Harris and K. H. Yung, *J. Phys. Chem.*, 1995, **99**, 12021–12024.

[214] B. G. Korenav, *Bessel Functions and Their Applications*, Chapman & Hall / CRC Press, Boca Raton, 2002.

[215] H. Greberg and G. N. Patey, *J. Chem. Phys.*, 2001, **114**, 7182–7188.

[216] W. Wang, X. Peng and D. Cao, *Environ. Sci. Technol.*, 2011, **45**, 4832–4838.

[217] M. Sliwinska-Bartkowiak, S. L. Sowers and K. E. Gubbins, *Langmuir*, 1997, **13**, 1182–1188.

[218] D. Woywod, S. Schemmel, G. Rother, G. H. Findenegg and M. Schoen, *J. Chem. Phys.*, 2005, **122**, 124510.

[219] S. G. Ash, D. H. Everett and G. H. Findenegg, *Trans. Faraday Soc.*, 1970, **66**, 708–722.

[220] S. Dietrich and M. Schick, *Phys. Rev. B*, 1986, **33**, 4952–4968.

[221] M. Sliwinska-Bartkowiak, B. Szurkowski and T. Hilczer, *Chem. Phys. Lett.*, 1983, **94**, 609–613.

[222] K. Zboinski, *Chem. Phys. Lett.*, 1976, **39**, 336–338.

[223] J. S. Hølye and G. Stell, *J. Chem. Phys.*, 1984, **81**, 3200–3210.

[224] H. Grüll and D. Woermann, *J. Chem. Phys.*, 1997, **106**, 732–737.

[225] B. J. Frisken, D. S. Cannell, M. Y. Lin and S. K. Sinha, *Phys. Rev. E*, 1995, **51**, 5866–5879.

[226] S. Schemmel, G. Rother, H. Eckerlebe and G. H. Findenegg, *J. Chem. Phys.*, 2005, **122**, 244718.

[227] D. Nicholson and K. E. Gubbins, *J. Chem. Phys.*, 1996, **104**, 8126–8134.

[228] A. V. Shevade, S. Jiang and K. E. Gubbins, *J. Chem. Phys.*, 2000, **113**, 6933–6942.

[229] P. T. M. Nguyen, D. D. Do and D. Nicholson, *J. Phys. Chem. C*, 2012, **116**, 13954–13963.

[230] A. P. Abbott and C. A. Eardley, *J. Phys. Chem. B*, 1999, **103**, 6157–6159.

[231] C. P. Rinsland, S. W. Sharpe and R. L. Sams, *J. Quant. Spectrosc. Radiat. Transfer*, 2005, **96**, 271–280.

[232] J. J. Andueza, R. Ouillon, J. P. P. Lucarre and P. Ranson, *J. Raman Spectrosc.*, 1995, **26**, 643–652.

[233] P. Neelakantan, *Proc. Ind. Acad. Sci., A,*, 1964, **60**, 422–424.

[234] T. S. Reighard, S. T. Lee and S. V. Olesik, *Fluid Phase Equilibr.*, 1996, **123**, 215–230.

[235] V. Rajakumar, N. Krishnamurthy, V. Ramakrishnan and J. Kumar, *J. Raman Spectrosc.*, 1992, **23**, 75–79.

[236] E. K. Plyler and M. A. Lamb, *J. Res. Nat. Bur. Stand.*, 1950, **45**, 204–208.

[237] T. Uchida, R. Ohmura and A. Hori, *J. Phys. Chem. A*, 2010, **114**, 317–323.

[238] D. S. Dao, H. Yamada and K. Yogo, *Ind. Eng. Chem. Res.*, 2013, **52**, 13810–13817.

[239] P. A. Steiner and W. Gordy, *J. Mol. Spectrosc.*, 1966, **21**, 291–301.

[240] J. A. Calladine, *Ph.D. thesis*, University of Nottingham, 2010.

[241] J. A. Calladine, A. Love, P. A. Fields, R. G. M. Wilson and M. W. George, *Appl. Spectrosc.*, 2014, **68**, 324–331.

[242] P. Licence, M. P. Dellar, R. G. M. Wilson, P. A. Fields, D. Litchfield, H. M. Woods, M. Poliakoff and S. M. Howdle, *Rev. Sci. Instrum.*, 2004, **75**, 3233–3236.

[243] M. Poliakoff, S. M. Howdle and S. G. Kazarian, *Angew. Chem. Int. Ed. Engl.*, 1995, **34**, 1275–1295.

[244] B. G. Trewyn, I. I. Slowing, S. Giri, H.-T. Chen and V. S.-Y. Lin, *Acc. Chem. Res.*, 2007, **40**, 846–853.

[245] S. S. Kim, A. Karkamkar, T. J. Pinnavaia, M. Kruk and M. Jaroniec, *J. Phys. Chem. B*, 2001, **105**, 7663–7670.

[246] E. Masika and R. Mokaya, *Chem. Mater.*, 2011, **23**, 2491–2498.

[247] J. Olivier, W. Conklin and M. Szombathely, in *Characterization of Porous Solids III*, ed. K. S. J. Rouquerol, F. Rodríguez-Reinoso and K. Unger, Elsevier, Amsterdam, 1994, vol. 87.

[248] W. Sangchoom and R. Mokaya, *J. Mater. Chem.*, 2012, **22**, 18872–18878.